ASME
SETTING THE STANDARD



**Transactions of the ASME, Journal of Fluids Engineering** (ISSN 0098-2202) is published monthly by The American Society of Mechanical Engineers, Three Park Avenue, New York, NY 10016. Periodicals postage paid at New York, NY and additional mailing offices.
POSTMASTER: Send address changes to Transactions of the ASME, Journal of Fluids Engineering, c/o THE AMERICAN SOCIETY OF MECHANICAL ENGINEERS, 22 Law Drive, Box 2300, Fairfield, NJ 07007-2300.
**CHANGES OF ADDRESS** must be received at Society headquarters seven weeks before they are to be effective. Please send old label and new address.
**STATEMENT from By-Laws.** The Society shall not be responsible for statements or opinions advanced in papers or ... printed in its publications (B7.1, Par. 3).


# Journal of Fluids Engineering

Published Monthly by ASME

VOLUME 130 • NUMBER 5 • MAY 2008

## RESEARCH PAPERS

### Flows in Complex Systems



### Fundamental Issues and Canonical Flows



### Multiphase Flows



### Techniques and Procedures



(Contents continued on inside back cover)

This journal is printed on acid-free paper, which exceeds the ANSI Z39.48-1992 specification for permanence of paper and library materials. ♾™
♻ 85% recycled content, including 10% post-consumer fibers.

(**Contents continued**)

**Journal of Fluids Engineering** **Volume 130, Number 5** **MAY 2008**

## TECHNICAL BRIEFS



The ASME Journal of Fluids Engineering is abstracted and indexed in the following:

*Applied Science & Technology Index, Chemical Abstracts, Chemical Engineering and Biotechnology Abstracts (Electronic equivalent of Process and Chemical Engineering), Civil Engineering Abstracts, Computer & Information Systems Abstracts, Corrosion Abstracts, Current Contents, Ei EncompassLit, Electronics & Communications Abstracts, Engineered Materials Abstracts, Engineering Index, Environmental Engineering Abstracts, Environmental Science and Pollution Management, Excerpta Medica, Fluidex, Index to Scientific Reviews, INSPEC, International Building Services Abstracts, Mechanical & Transportation Engineering Abstracts, Mechanical Engineering Abstracts, METADEX (The electronic equivalent of Metals Abstracts and Alloys Index), Petroleum Abstracts, Process and Chemical Engineering, Referativnyi Zhurnal, Science Citation Index, SciSearch (The electronic equivalent of Science Citation Index), Shock and Vibration Digest, Solid State and Superconductivity Abstracts, Theoretical Chemical Engineering*

# An Experimental Study of the Laminar Flow Separation on a Low-Reynolds-Number Airfoil

**Hui Hu**
Assistant Professor
e-mail: huhui@iastate.edu

**Zifeng Yang**
Graduate Student

Department of Aerospace Engineering,
Iowa State University,
Ames, IA 50011

*An experimental study was conducted to characterize the transient behavior of laminar flow separation on a NASA low-speed GA (W)-1 airfoil at the chord Reynolds number of 70,000. In addition to measuring the surface pressure distribution around the airfoil, a high-resolution particle image velocimetry (PIV) system was used to make detailed flow field measurements to quantify the evolution of unsteady flow structures around the airfoil at various angles of attack (AOAs). The surface pressure and PIV measurements clearly revealed that the laminar boundary layer would separate from the airfoil surface, as the adverse pressure gradient over the airfoil upper surface became severe at AOA $\geq$ 8.0 deg. The separated laminar boundary layer was found to rapidly transit to turbulence by generating unsteady Kelvin–Helmholtz vortex structures. After turbulence transition, the separated boundary layer was found to reattach to the airfoil surface as a turbulent boundary layer when the adverse pressure gradient was adequate at AOA $<$ 12.0 deg, resulting in the formation of a laminar separation bubble on the airfoil. The turbulence transition process of the separated laminar boundary layer was found to be accompanied by a significant increase of Reynolds stress in the flow field. The reattached turbulent boundary layer was much more energetic, thus more capable of advancing against an adverse pressure gradient without flow separation, compared to the laminar boundary layer upstream of the laminar separation bubble. The laminar separation bubble formed on the airfoil upper surface was found to move upstream, approaching the airfoil leading edge as the AOA increased. While the total length of the laminar separation bubble was found to be almost unchanged ($\sim$20% of the airfoil chord length), the laminar portion of the separation bubble was found to be slightly stretched, and the turbulent portion became slightly shorter with the increasing AOA. After the formation of the separation bubble on the airfoil, the increase rate of the airfoil lift coefficient was found to considerably degrade, and the airfoil drag coefficient increased much faster with increasing AOA. The separation bubble was found to burst suddenly, causing airfoil stall, when the adverse pressure gradient became too significant at AOA $>$ 12.0 deg.*
[DOI: 10.1115/1.2907416]

## 1 Introduction

Low-Reynolds-number airfoil aerodynamics is important for both military and civilian applications. These applications include propellers, sailplanes, ultralight man-carrying/man-powered aircraft, high-altitude vehicles, wind turbines, unmanned aerial vehicles (UAVs), and microAir vehicles (MAVs). Nondimensional chord Reynolds number ($Re_C$) is defined as the cruise speed multiplied by the mean wing chord and divided by the kinematic viscosity of air. For the applications listed above, the combination of small length scale and low flight velocities results in flight regimes with low wing-chord Reynolds number (i.e., chord Reynolds numbers, $Re_C$, ranging from 10,000 to 500,000).The aerodynamic design methods and principles developed over the past 40 years have produced efficient airfoils for conventional, large-scale, high-speed aircraft whose chord Reynolds numbers are usually in the range of $10^6$–$10^9$. It is well known that the aerodynamic performance of airfoils that are optimal for conventional, large-scale and high-speed aircraft (therefore, high chord Reynolds number) significantly degrades when used for low-Reynolds-number applications where the chord Reynolds numbers are several orders smaller. While conventional airfoil design principles usually either neglect viscous effects or restrict its influence to a very thin region near the airfoil surface at high Reynolds numbers, the predominance of viscous effects in low-Reynolds-number applications would result in boundary layers rapidly growing and easily separating from the surfaces of airfoils.

It is well known that the boundary layers on low-Reynolds-number airfoils remain laminar at the onset of the pressure recovery unless artificially tripped. The behavior of the laminar boundary layers on low-Reynolds-number airfoils significantly affects the aerodynamic performances of the airfoils. Since laminar boundary layers are unable to withstand any significant adverse pressure gradient, laminar flow separation is usually found on low-Reynolds-number airfoils. Postseparation behavior of laminar boundary layers accounts for the deterioration in the aerodynamic performances of low-Reynolds-number airfoils. The deterioration is exhibited by an increase in drag and decrease in lift. Extensive reviews about aerodynamics of low-Reynolds-number airfoils and the dependence of the laminar flow separation phenomena on the chord Reynolds numbers can be found at Tani [1], Carmichael [2], Lissaman [3], Mueller [4] and Gad-el-Hak [5]. It has been suggested that the separated laminar boundary layers would rapidly transit to turbulence, and then reattach to the airfoil surface as a turbulent boundary layer when the adverse pressure gradient over the airfoil surface is adequate [6]. This would result in the formation of a laminar separation bubble, as schematically shown in Fig. 1. As the adverse pressure gradient becomes more severe with the increasing angle of attack, the separation bubble would suddenly burst, which will subsequently result in airfoil stall.

A good physical understanding is essential in order to control

Contributed by the Fluids Engineering Division of ASME for publication in the JOURNAL OF FLUIDS ENGINEERING. Manuscript received April 7, 2007; final manuscript received January 31, 2008; published online April 25, 2008. Assoc. Editor: Hamid Johari.

  

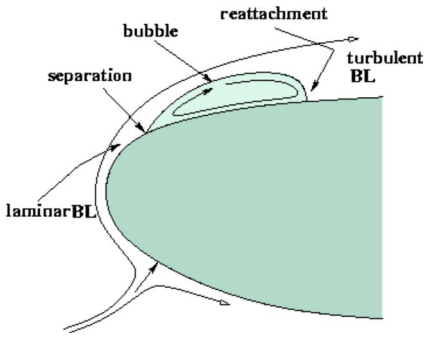


**Fig. 1 Schematic of a laminar separation bubble formed on a low-Reynolds-number airfoil**

the laminar flow separations and suppress the burst of the laminar separation bubbles for better aerodynamic performances of low-Reynolds-number airfoils. This requires a detailed knowledge about transient behavior of the separated laminar boundary layers and the evolution of laminar separation bubbles. Although extensive experimental studies have been conducted to investigate laminar flow separation, transition, and reattachment on low-Reynolds-number airfoils, the majority of those previous studies were carried out by using pointwise flow diagnostic techniques, such as hot-wire anemometry [7–10], hot-film anemometry [11,12] and laser Doppler velocimetry [13–15] to conduct flow velocity measurements at limited points of interest. A common shortcoming of such pointwise flow measurements is the incapability of providing spatial correlation of the unsteady flow structures to effectively reveal the transient behavior of the laminar flow separation. The availability of temporally synchronized and spatially resolved flow field measurements is highly desirable in order to elucidate underlying physics to improve our understanding about the laminar boundary layer separation, transition, and reattachment processes on low-Reynolds-number airfoils. Advanced flow diagnostic techniques, such as particle image velocimetry (PIV), are capable of providing such information.

Surprisingly, only very few experimental studies were recently conducted to provide temporally synchronized and spatially resolved flow field measurements to quantify the transient behavior of the laminar boundary layers on low-Reynolds-number airfoils [16–19]. Very little in the literature can be found to correlate detailed flow field measurements with the airfoil surface pressure measurements to investigate laminar flow separation, transition, and reattachment as well as the evolution of laminar separation bubbles on low-Reynolds-number airfoils. In this study, we conducted a detailed experimental study to characterize the transient behavior of laminar flow separation, transition, and reattachment on a low-Reynolds-number airfoil at $\mathrm{Re}_C=70{,}000$. In addition to mapping the surface pressure distribution around the airfoil with pressure sensors, a high-resolution PIV system was used to make detailed flow field measurements to quantify the occurrence and behavior of laminar boundary layer separation, transition, and reattachment on the low-Reynolds-number airfoil. The detailed flow field measurements were correlated with the surface pressure measurements to elucidate the underlying physics associated with the separation, transition, and reattachment processes of the laminar boundary layer. To the best knowledge of the authors, this is the first effort of its nature. The primary objective of the present study is to gain further insight into the fundamental physics of laminar flow separation, transition, and reattachment as well as the evolution of laminar separation bubble formed on low-Reynolds-number airfoils. In addition, the quantitative surface pressure and flow field measurements will be used as the database for the validation of computational fluid dynamics (CFD) simulations of such complex flow phenomena for the optimum design of low-Reynolds-number airfoils [20].

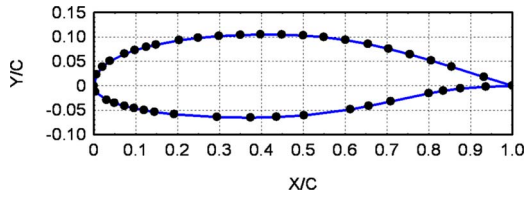


**Fig. 2 GA(W)-1 airfoil geometry and pressure tap locations**

## 2 Experimental Setup and the Studied Airfoil

The experiments were performed in a closed-circuit low-speed wind tunnel located in the Aerospace Engineering Department of Iowa State University. The tunnel has a test section with a 1.0 $\times$ 1.0 $\mathrm{ft}^2$ ($30\times30$ $\mathrm{cm}^2$) cross section and optically transparent walls. The tunnel has a contraction section upstream of the test section with honeycomb, screen structures, and cooling system installed ahead of the contraction section to provide uniform low turbulent incoming flow to enter the test section.

Figure 2 shows the schematic of the airfoil used in the present study: a GA (W)-1 airfoil (also labeled as NASA LS(1)-0417). The GA (W)-1 has a maximum thickness of 17% of the chord length. Compared to standard NACA airfoils, the GA (W)-1 airfoil was especially designed for low-speed general aviation applications with a large leading-edge radius in order to flatten the peak in pressure coefficient near the airfoil nose to discourage flow separation [21]. The chord length of the airfoil model is 101 mm, i.e., $C=101$ mm, for the present study. The flow velocity at the inlet of the test section was set as $U_\infty=10.7$ m/s, which corresponds to a chord Reynolds number of $\mathrm{Re}_c\approx70{,}000$.

The airfoil model is equipped with 43 pressure taps at its median span with the spanwise length of the airfoil being 1.0 ft. The locations of the pressure taps are indicated in Fig. 2. The 43 pressure taps were connected by plastic tubing to 43 channels of a pressure acquisition system (Model DSA3217, Scanivalve Corp). The DSA3217 digital sensor arrays incorporate temperature compensated piezoresistive pressure sensors with a pneumatic calibration valve, RAM, 16 bit A/D converter, and a microprocessor in a compact self-contained module. The precision of the pressure acquisition system is $\pm0.2\%$ of the full scale ($\pm10$ in. $H_2O$). During the experiment, each pressure transducer input was scanned at 400 Hz for 20 s. The pressure coefficient distributions, $C_p=(P-P_\infty)/(\frac{1}{2}\rho U_\infty^2)$, around the airfoil at various angles of attack were measured by using the pressure acquisition system. The lift and drag coefficients ($C_l=l/(\frac{1}{2}\rho U_\infty^2 C)$ and $C_d=d/(\frac{1}{2}\rho U_\infty^2 C)$) of the 2D airfoil were determined by numerically integrating the pressure distribution around the airfoil.

Figure 3 shows the schematic of the experimental setup used for the PIV measurement. The test airfoil was installed in the middle of the test section. A PIV system was used to make flow velocity field measurements along the chord at the middle span of the airfoil. The flow was seeded with $\sim1$ $\mu$m oil droplets. Illumination was provided by a double-pulsed Nd:YAG (yttrium aluminum garnet) laser (NewWave Gemini 200) adjusted on the second harmonic and emitting two laser pulses of 200 mJ at a wavelength of 532 nm with a repetition rate of 10 Hz. The laser beam was shaped into a sheet by a set of mirrors, spherical and cylindrical lenses. The thickness of the laser sheet in the measurement region is about 0.5 mm. A high-resolution 12 bit ($1376\times1040$ pixels) charge-coupled device (CCD) camera was used for PIV image acquisition with the axis of the camera perpendicular to the laser sheet. The CCD camera and the double-pulsed Nd:YAG lasers were connected to a workstation (host computer) via a Digital Delay Generator (Berkeley Nucleonics, Model 565), which controlled the timing of the laser illumination and the image acquisition. In the present study, a careful pretest, which includes testing different seeding methods, applying different paints to the airfoil

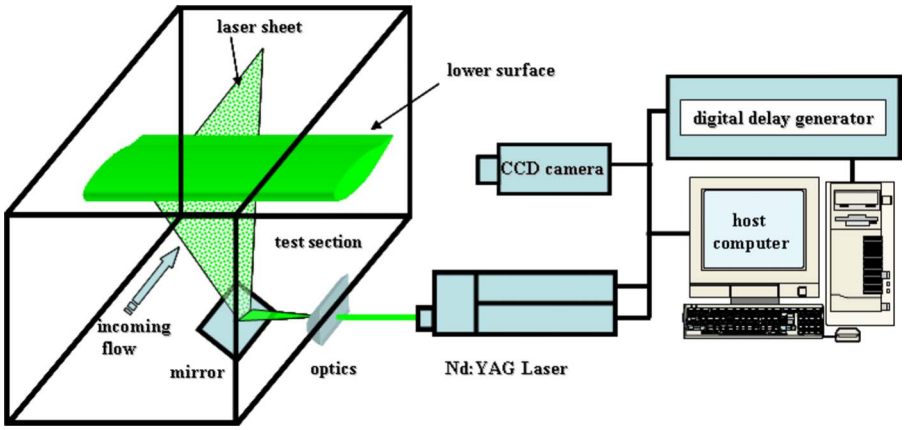


**Fig. 3 Schematic of the experimental setup for the PIV measurements**

model as well as adjusting laser excitation energy level, camera positions, and optic lens arrangements, was conducted in order to minimize the reflection from the airfoil surface for the near wall PIV measurements.

Instantaneous PIV velocity vectors were obtained by a frame to frame cross-correlation technique involving successive frames of patterns of particle images in an interrogation window of 32 $\times$32 pixels. An effective overlap of 50% was employed for PIV image processing. After the instantaneous velocity vectors $(\mathbf{u}_i, \mathbf{v}_i)$ were determined, the spanwise vorticity $(\omega_z)$ could be derived. The time-averaged quantities such as mean velocity $(U,V)$, turbulent velocity fluctuations $(\overline{u'}, \overline{v'})$, normalized Reynolds stress $(\overline{\tau} = -\overline{u'v'}/U_\infty^2)$, and normalized turbulent kinetic energy (TKE $=0.5*(\overline{u'^2}+\overline{v'^2})/U_\infty^2$) were obtained from a cinema sequence of 400 frames of instantaneous velocity fields. The measurement uncertainty level for the velocity vectors is estimated to be within 2% and 5% for the turbulent velocity fluctuations $(\overline{u'}, \overline{v'})$, Reynolds stress, and turbulent kinetic energy calculations. The uncertainty level of the spanwise vorticity data is expected to be within 10.0%. It should be noted that the surface pressure mapping and PIV measurements are designed to acquire statistical data instead of time-resolved measurements due the limited sampling rates of the surface pressure mapping and PIV measurements.

## 3 Experimental Results and Discussions

**3.1 Measured Surface Pressure Distribution Around the Airfoil.** Figure 4 shows the measured surface pressure coefficient distributions around the GA (W)-1 airfoil as the angle of attack changes from 6.0 deg to 14.0 deg. While the surface pressure distribution on the lower surface of the airfoil does not notably change with the increasing angle of attack (up to 12.0 deg), the surface pressure distribution on the upper surface of the airfoil was found to significantly vary at different angles of attack. As the angle of attack (AOA) was relatively small (i.e., AOA $<$ 8.0 deg), the surface pressure coefficient profiles along the airfoil upper surface were found to rapidly reach their negative peaks at locations quite near to the airfoil leading edge, then the surface pressure gradually and smoothly recovered over the upper surface of the airfoil up to the airfoil trailing edge. As the AOA increases to 8.0 $\leq$ AOA $<$ 12.0 deg, a distinctive characteristic of the surface pressure coefficient profiles is the existence of a region of nearly constant pressure (i.e., pressure plateau region) at $X/C \approx 0.05-0.25$. Sudden increase in surface pressure coefficient was found following the pressure plateau region. Further downstream, the surface pressure was found to gradually and smoothly recover, which is similar as those cases with relatively low AOAs. Such a characteristic of the surface pressure profiles is actually closely related to laminar flow separation and the formation of laminar separation bubbles on low-Reynolds-number airfoils.

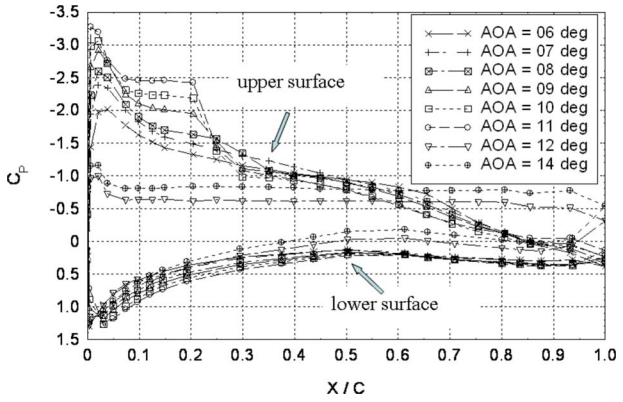


**Fig. 4 Surface pressure distribution profiles around the airfoil**

As schematically illustrated in Fig. 5, Russell [22] suggested a theoretic model to characterize the laminar separation bubbles formed on low-Reynolds-number airfoils. Based on the theoretic model of Russell [22], the critic points (the separation, transition, and reattachment points) of a laminar separation bubble formed on a low-Reynolds-number airfoil can be determined from the surface pressure measurements. The separation point refers to the location from where the laminar boundary layer separates from the airfoil surface. The transition point refers to the onsite point at where the separated laminar boundary layer begins to transit to turbulence. The reattachment point refers to the location where the separated boundary layer reattaches to the airfoil surface after transition. As suggested by Russell [22], a laminar separation bubble formed on a low-Reynolds-number airfoil includes two portions: a laminar portion and a turbulent portion. The location of the pressure plateau is coincident with that of the laminar portion of the separation bubble. The starting point of the pressure plateau indicates the location where the laminar boundary layer separates from the airfoil surface (i.e., the separation point). Since the transition of the separated laminar boundary layer to turbulence will result in a rapid pressure rise brought about by fluid entrainment, the termination of the pressure plateau can be used to locate the transition point, at where the transition of the separated laminar boundary layer to turbulence begins to occur. The pressure rise due to the turbulence transition often overshoots the invisicid pressure that exists at the reattachment location. Therefore, the location of the point of equality between the actual and inviscid surface pressure marks the location of reattachment (i.e., the reattachment point).

Following the work of Russell [22], the locations of the critic

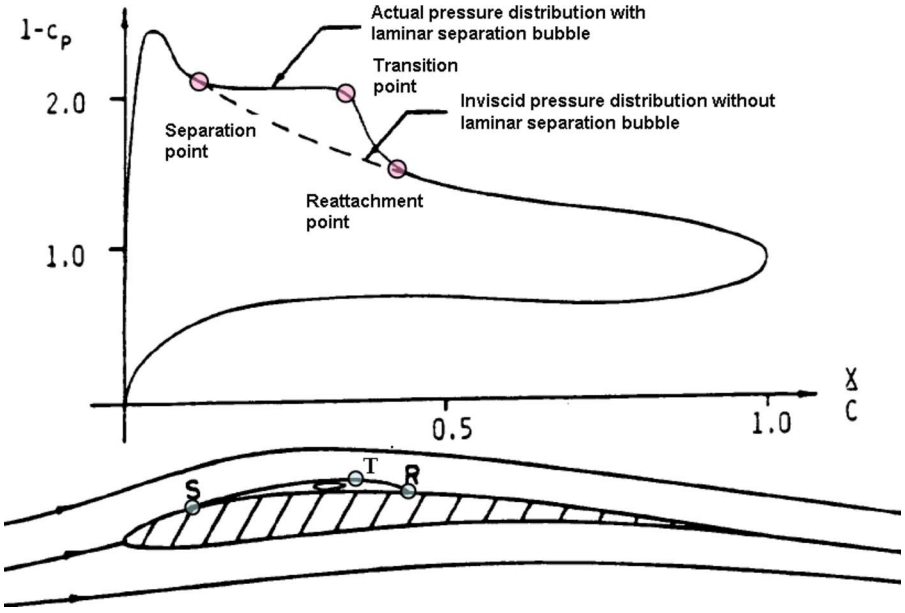


**Fig. 5 Pressure distribution on an airfoil with laminar separation bubble (Russell [22])**

points (the separation, transition, and reattachment points) of laminar separation bubbles at different AOAs were estimated based on the measured airfoil surface pressure profiles given in Fig. 4. A summation of the locations of separation, transition, and reattachment points on the GA(W)-1 airfoil at different AOAs is given in Fig. 6. The uncertainties of the estimated locations of the critical points is about 2.0% of chord length due to the limited numbers of the pressure taps available in the region, which are shown in the figure as the error bars. As the AOA increases, the laminar separation bubble was found to move upstream to approach the airfoil leading edge. The total length of the separation bubble (i.e., the distance between the separation and reattachment points), which is about 20% of the chord length, was found to be almost unchanged regardless of the angles of attack. Following the terminology used by Horton [6], the length of the laminar portion of the separation bubble is defined as the distance between the separation point and the transition point, and the turbulent portion length corresponds to the distance between the transition point and the reattachment point. From the experimental results given in Fig. 6, it can be seen that, while the length of the laminar portion of the separation bubble was found to slightly increase as the AOA increases, the turbulent portion became slightly shorter with the increasing AOA.

As the AOA became greater than 12.0 deg, the magnitude of the negative pressure coefficient peak near the airfoil leading edge was found to significantly decrease. As shown in Fig. 4, the surface pressure over most of the airfoil upper surface was found to be nearly constant. Such a surface pressure distribution indicates that airfoil is in stalled state [23–25], which is confirmed from the PIV measurements given in Fig 7.

**3.2 PIV Measurement Results.** While the surface pressure measurements can be used to quantify the global characteristics of the laminar separation bubble formed on the low-Reynolds-number airfoil, quantitative flow field measurements taken by using a high-resolution PIV system can reveal much more details

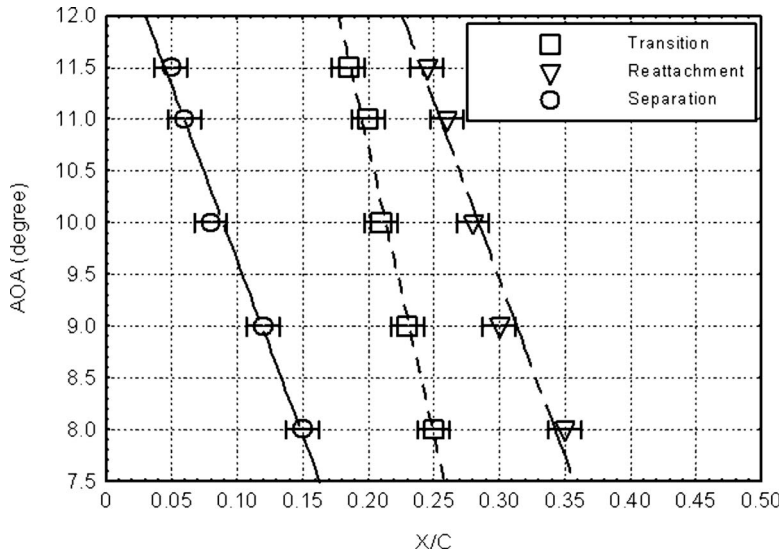


**Fig. 6 The estimated locations of the separation points, transition points, and reattachment points at various AOAs**

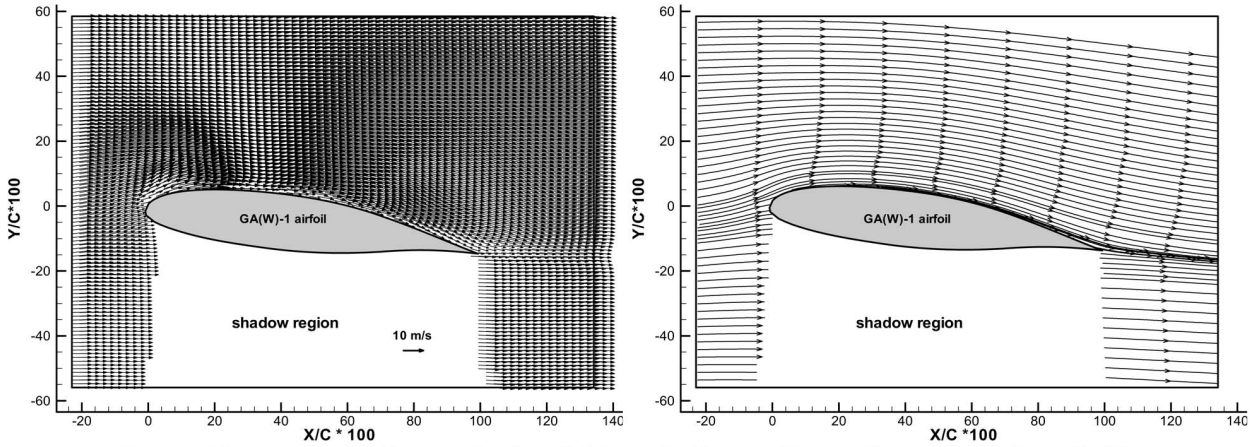


a. Ensemble-averaged flow velocity field b. Streamlines of the mean flow field

A. AOA = 6.0 degrees

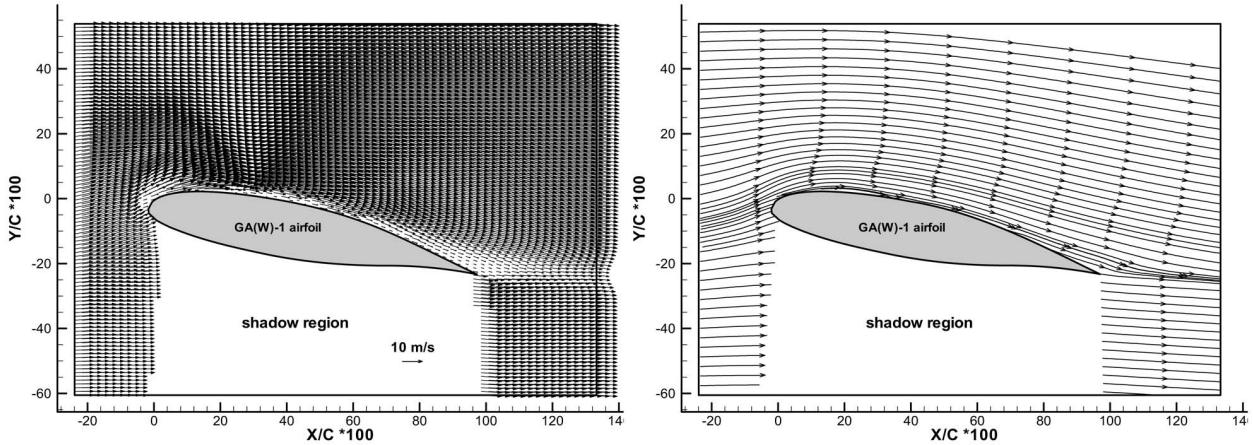


a. Ensemble-averaged flow velocity field b. Streamlines of the mean flow field

B. AOA = 10.0 degrees

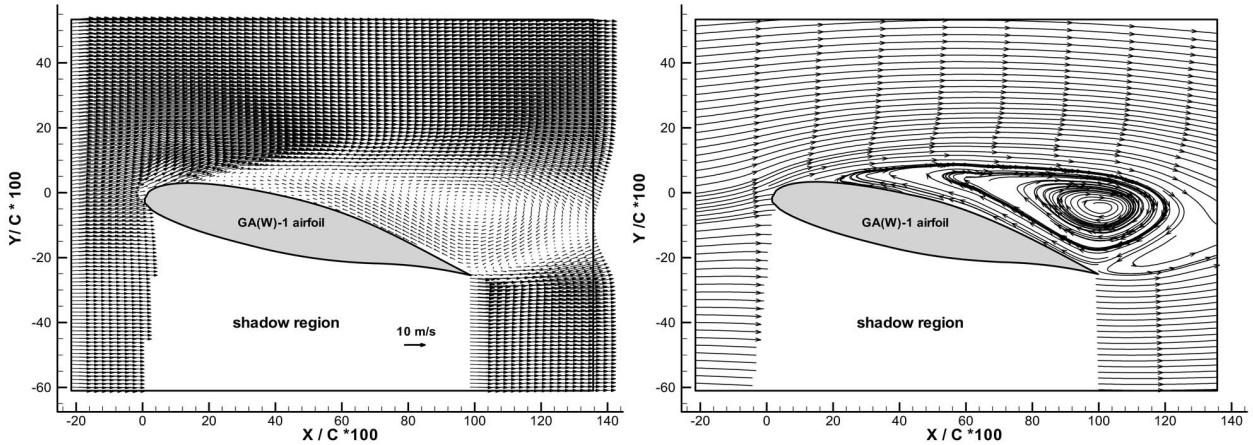


a. Ensemble-averaged flow velocity field b. Streamlines of the mean flow field

C. AOA = 12.0 degrees

**Fig. 7 PIV measurement results at various AOAs**

about the transient behavior of laminar flow separation and the evolution of a laminar separation bubble formed on the airfoil. In the present study, PIV measurements were conducted at three spatial resolution levels: a coarse level to visualize the global features of the flow structures around the airfoil at various AOAs with the measurement window size being about $160 \times 120$ mm$^2$, a refined level to reveal the transient behavior of the laminar flow separation process near the nose of the airfoil with a measurement window size of about $40 \times 20$ mm$^2$, and a superfine level to elucidate the details about the turbulence transition and the reattachment of the separated boundary layer to the airfoil surface at the rear portion of the separation bubble with a measurement window size of

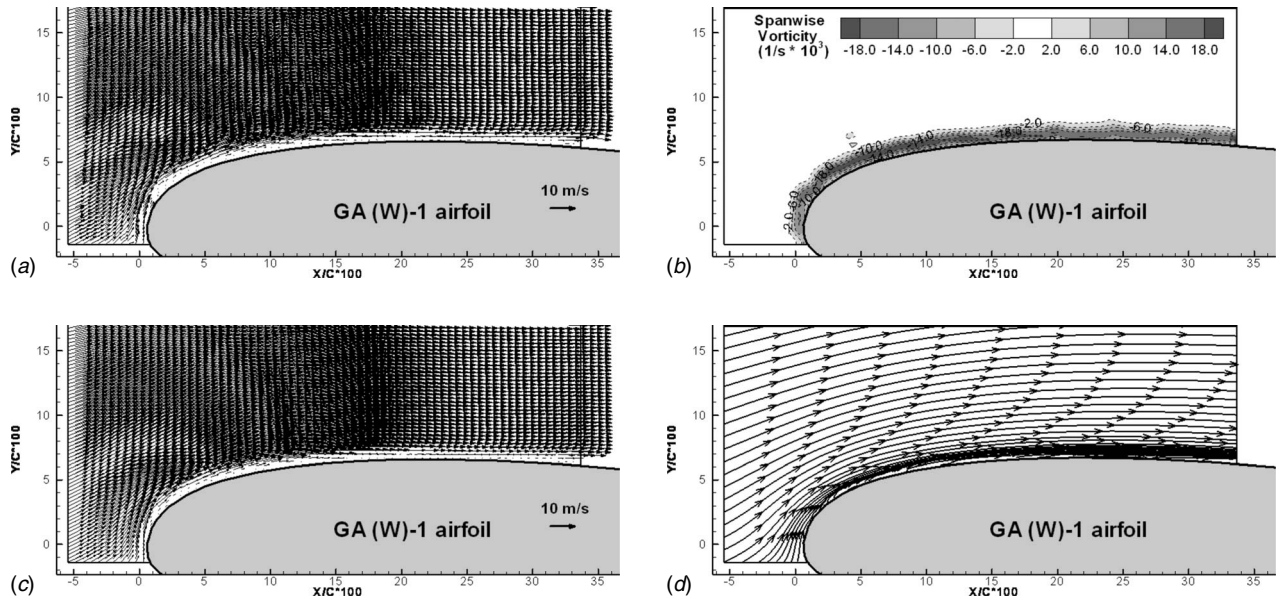


**Fig. 8 PIV measurements near the airfoil leading edge with AOA=6.0 deg; (*a*) instantaneous velocity vectors; (*b*) instantaneous vorticity distribution; (*c*) ensemble-averaged velocity vectors; and (*d*) streamlines of the mean flow**

about $16\times 10$ mm$^2$. The time interval between the double pulsed laser illumination for the PIV measurements was set as $\Delta t$ =40.0 $\mu$s, 14.0 $\mu$s, and 4.0 $\mu$s, respectively. The effective resolutions of the PIV measurements (i.e., grid sizes) were $\Delta/C$ =0.018, 0.0045, and 0.0018, respectively.

Figure 7 shows the PIV measurement results at the coarse resolution level. As clearly revealed by the ensemble-averaged velocity distribution and the streamlines of the mean flow around the airfoil, incoming flow streams faithfully follow the streamlined profile of the airfoil when the AOA is relatively small (i.e., AOA $<$ 8.0 deg). No flow separation was found on the airfoil upper surface when the adverse pressure gradient is rather mild at relatively small AOAs. Since the flow streams can firmly attach to the airfoil surface, they smoothly leave the airfoil at the trailing edge, which results in a very small wake region (i.e., the region with velocity deficits) downstream of the airfoil. The small wake region downstream of the airfoil indicates a small aerodynamic drag force acting on the airfoil, which is confirmed from the drag coefficient measurement results given in Fig. 12.

As the AOA increases to 8.0–11.0 deg, the surface pressure measurement results given in Fig. 4 indicate that a laminar separation bubble would be generated on the upper surface of the airfoil. However, since the height of the separation bubble is very small (only $\sim$1.0% of the chord length based on the refined PIV measurement results shown in Figs. 9 and Fig. 10), the laminar separation bubble cannot be clearly revealed from the PIV measurement results shown in Fig. 7(*B*) due to the limited spatial resolution of the PIV measurements (i.e., $\Delta/C\approx 0.018$). It has been suggested that the separated laminar boundary layer would firmly reattach to the airfoil upper surface at the downstream of

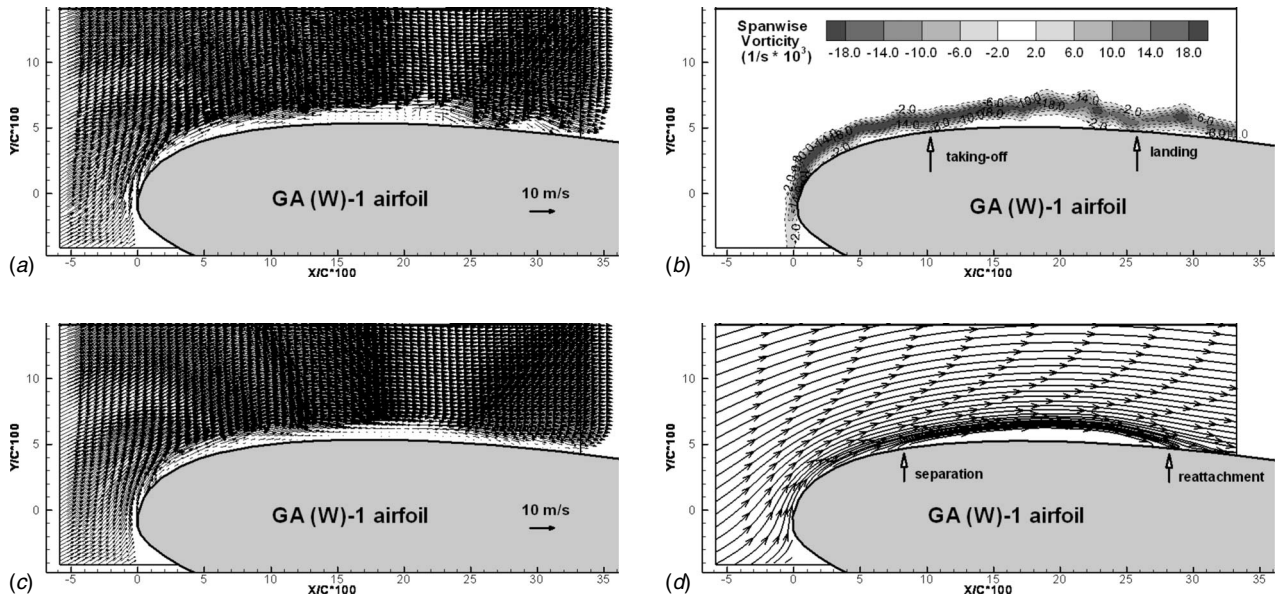


**Fig. 9 PIV measurements near the airfoil leading edge with AOA=10.0 deg; (*a*) instantaneous velocity vectors; (*b*) instantaneous vorticity distribution; (*c*) ensemble-averaged velocity vectors; and (*d*) streamlines of the mean flow**

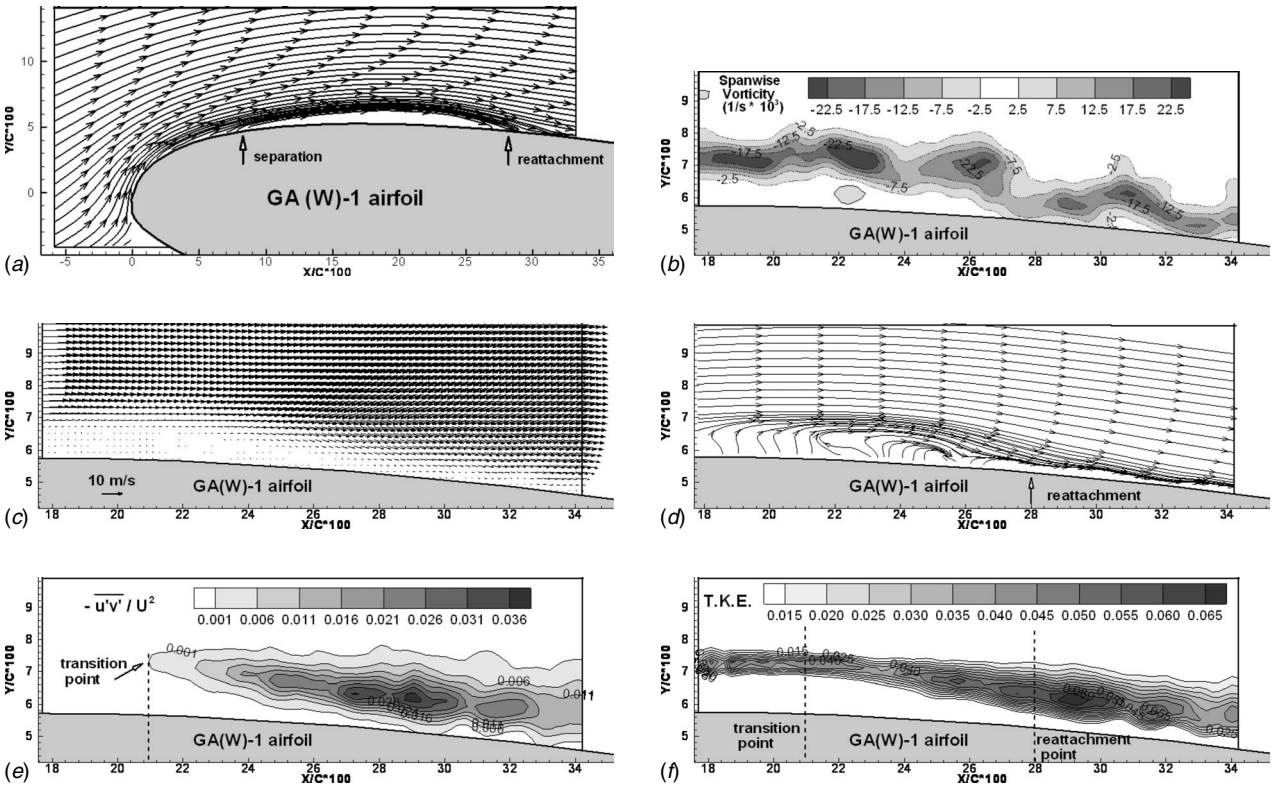


**Fig. 10 PIV measurement results at the rear portion of the separation bubble with AOA=10.0 deg; (*a*) instantaneous velocity field; (*b*) instantaneous vorticity distribution; (*c*) ensemble-averaged velocity field; (*d*) streamlines of the mean flow; (*e*) normalized Reynolds stress distribution; and (*f*) normalized turbulent kinetic energy distribution**

the reattachment point all the way to the airfoil trailing edge [6,22,23]. The mean velocity vectors and streamlines of the mean flow shown in Fig. 7(*B*) reveal that incoming flow streams smoothly leave the airfoil at the trailing edge at AOA=10.0 deg, which confirms the reattachment of the separated boundary layer to the airfoil upper surface downstream of the laminar separation bubble. As a result of the reattachment of the separated boundary layer, the wake region downstream of the airfoil was found to be reasonably small even though a separated bubble was already formed on the airfoil upper surface. Compared to those cases at smaller AOAs (such as the case shown in Figs. 7(*A*) with AOA =6.0 deg), the size of the wake region for the cases with the separation bubbles generated on the airfoil upper surface becomes slightly larger, indicating a slightly increased aerodynamic drag force acting on the airfoil, which is confirmed from the airfoil drag coefficient measurement results given in Fig. 12.

The adverse pressure gradient over the upper surface of the airfoil becomes more and more severe as the AOA increases. The surface pressure measurement results given in Fig. 4 indicate that the separation bubble would burst, eventually causing airfoil stall when the AOA becomes greater than 12.0 deg. The large-scale flow separation over almost the entire upper surface of the airfoil due to the burst of the laminar separation bubble is visualized clearly and quantitatively from the PIV measurement results given in Fig. 7(*C*). The large-scale flow separation on the airfoil upper surface resulted in the formation of a very large recirculation bubble in the wake the airfoil. As a result, the size of the wake region (i.e., the region with velocity deficit) downstream the airfoil was found to dramatically increase, which indicates a significant increase of the aerodynamic drag force acting on the airfoil, again quantitatively confirmed for the measured drag coefficient data given in Fig. 12.

Although the PIV measurement results given in Fig. 7 clearly reveal the global features of the flow structures around the airfoil, further details about the transient behavior of the laminar flow separation and evolution of the separation bubble formed on the low-Reynolds-number airfoil cannot be clearly seen due to the limited spatial resolution of the PIV measurements. In order to provide further insights to elucidate underlying physics associated with the laminar flow separation process on low-Reynolds-number airfoils, refined PIV measurements near the nose of the airfoil with much higher spatial resolution ($\Delta/C \approx 0.0045$) were made. The measurement results are shown in Figs. 8, 9, and 11 with the AOA being 6.0 deg, 10.0 deg, and 12.0 deg, respectively.

The laminar boundary layer around the airfoil was clearly visualized as a thin vortex layer affixing to the airfoil upper surface in the typical instantaneous velocity field and the corresponding vorticity distribution shown in Fig. 8. The laminar boundary layer was found to be firmly attached to the airfoil surface when the adverse pressure gradient over the airfoil upper surface is rather mild at relatively small AOA (i.e., AOA $<$ 8.0 deg). The ensemble-averaged velocity field and the streamlines of the mean flow also confirmed that the incoming fluid streams would smoothly flow to follow the streamlined profile of the airfoil when the AOA is relatively small.

As indicated by the surface pressure measurement results described above, a laminar separation bubble would be generated on the airfoil when the AOA became relatively high (i.e., AOA $\approx$ 8.0–12.0 deg). The typical instantaneous velocity field and the corresponding vorticity distribution given in Fig. 9 clearly show that the laminar boundary layer (i.e., the thin vortex layer over the airfoil upper surface) would be "taking off" from the airfoil upper surface at first, and then "landing" on the airfoil upper surface again further downstream. The separation of the laminar boundary layer from the airfoil upper surface and the reattachment of the separated boundary layer can be much more clearly seen from the ensemble-averaged velocity field and the corresponding mean

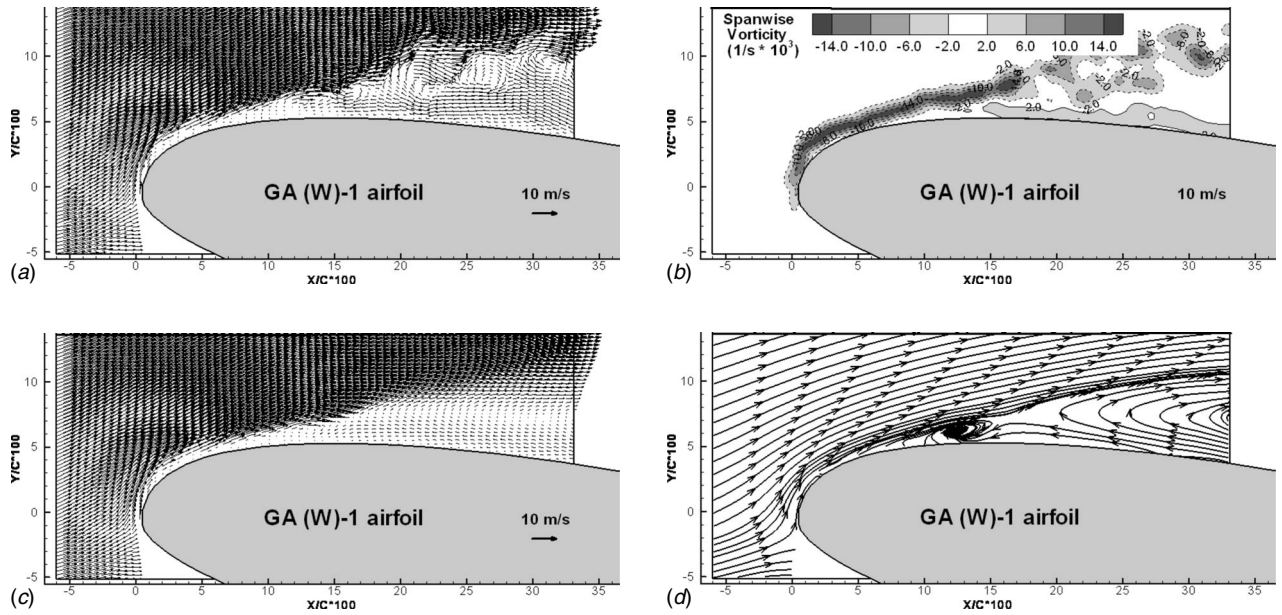


**Fig. 11 PIV measurements near the airfoil leading edge with AOA=12.0 deg; (*a*) instantaneous velocity vectors; (*b*) instantaneous vorticity distribution; (*c*) ensemble-averaged velocity vectors; and (*d*) streamlines of the mean flow**

flow streamlines. Based on the PIV measurement results shown in Fig. 9, the location of the separation point (i.e., from where the laminar boundary layer begins to separate from the airfoil surface) was found to be in the neighborhood of $X/C \approx 0.08$, which agrees with the starting point of the "pressure plateau" of the measured surface pressure distribution at 10.0 deg AOA. The reattachment point (i.e., at where the separated boundary layer reattaches to the airfoil surface) was found to be in the neighborhood of $X/C \approx 0.28$, which also agrees well with the estimated location of the reattachment point based on the surface pressure measurements. The laminar separation bubble, which sits in the region between the separation point and the reattachment point, is clearly visualized from the PIV measurement results. While the length of the separation bubble is about 20% of the chord length, the height of the laminar separation bubble is found to be only about 1% of the chord length.

In order to provide further insight into the fundamental physics associated with the turbulent transition and reattachment of the separated laminar boundary layer, PIV measurements with superfine spatial resolution ($\Delta/C \approx 0.0018$) were made at the rear portion of the laminar separation bubble. The measurement results are shown in Fig. 10 with the airfoil AOA being 10.0 deg.

The PIV measurement results given in Fig. 9 clearly show that the laminar boundary layer would separate from the airfoil upper surface at $X/C \approx 0.08$ due to the severe adverse pressure gradient at 10.0 deg AOA. The instantaneous velocity field and corresponding vorticity distribution given in Fig. 10 reveal that the separated laminar boundary layer behaved more like a free shear layer after separation, which is highly unstable; therefore, rolling up of unsteady vortex structures due to the Kelvin–Helmholtz instabilities and transition to turbulent flow would be readily realized. After the separated laminar boundary layer transits to turbulent flow, the increased entrainment of the turbulent flow made the separated boundary layer reattach to the airfoil upper surface as a turbulent boundary layer, which consequently resulted in the formation of a laminar separation bubble on the airfoil. The reattachment of the separated boundary layer to the airfoil upper surface and consequent formation of the laminar separation bubble can be more clearly seen from the ensemble-averaged velocity field and the streamlines of the mean flow shown in Figs. 10(*c*) and 10(*d*).

Figure 10(*e*) shows the distribution of the measured normalized Reynolds stress ($-\overline{u'v'}/U_\infty^2$) near the rear portion of the laminar separation bubble. It can be clearly seen that the transition process of the laminar boundary layer is accompanied by the significant increase of Reynolds stress in the flow field. It should be noted that only the contour lines of the normalized Reynolds stress above a critical value of 0.001 are shown in the Fig. 10(*e*). This critical value has been chosen in the literature to locate the onset of the turbulent transition in separated shear layers [10,17,19]. Following the work of Ol et al. [17], the transition onset position was estimated as the streamwise location where the normalized Reynolds stress first reaches a value of 0.001. The transition onset position at 10.0 deg AOA was found to be located in the neighborhood of $X/C \approx 0.21$ based on the measured Reynolds stress distribution shown in Fig. 10(*e*). The estimated location was found to agree well with the estimation of the transition point given in Fig. 5, which is based on the surface pressure measurements.

The measured turbulent kinetic energy ($\mathrm{TKE}=0.5*(\overline{u'^2}+\overline{v'^2})/U_\infty^2$) distribution at the rear part of the laminar separation bubble is given in Fig. 10(*f*). It can be clearly seen that the regions with higher TKE was found to be confined in a thin layer in the upstream of the transition point due to the laminar nature of the separated laminar boundary layer. The contour lines of the regions with higher TKE were found to rapidly diverge after the separated laminar boundary layer began to transit to turbulence (i.e., downstream of the transition point). The measured TKE distribution also shows that the regions with higher TKE can be quite close to the airfoil surface wall downstream of the reattachment point (i.e., downstream of location $X/C \approx 0.28$). This confirms that the reattached turbulent boundary layer can entrain more high-speed fluid from outside to the near wall region to make the near wall flow much more energetic compared to the laminar boundary layer upstream of the laminar separation bubble. Therefore, the turbulent boundary layer is much more capable of advancing against an adverse pressure gradient without flow separation. As a result, the reattached turbulent boundary layer can stay attached to the airfoil surface from the reattachment point to the trailing edge of the airfoil, which was confirmed in the PIV measurement results given above.

As the AOA increases to 12.0 deg and higher, the adverse pressure gradient over the upper surface of the airfoil becomes much more significant, and the separation bubble was found to eventu-

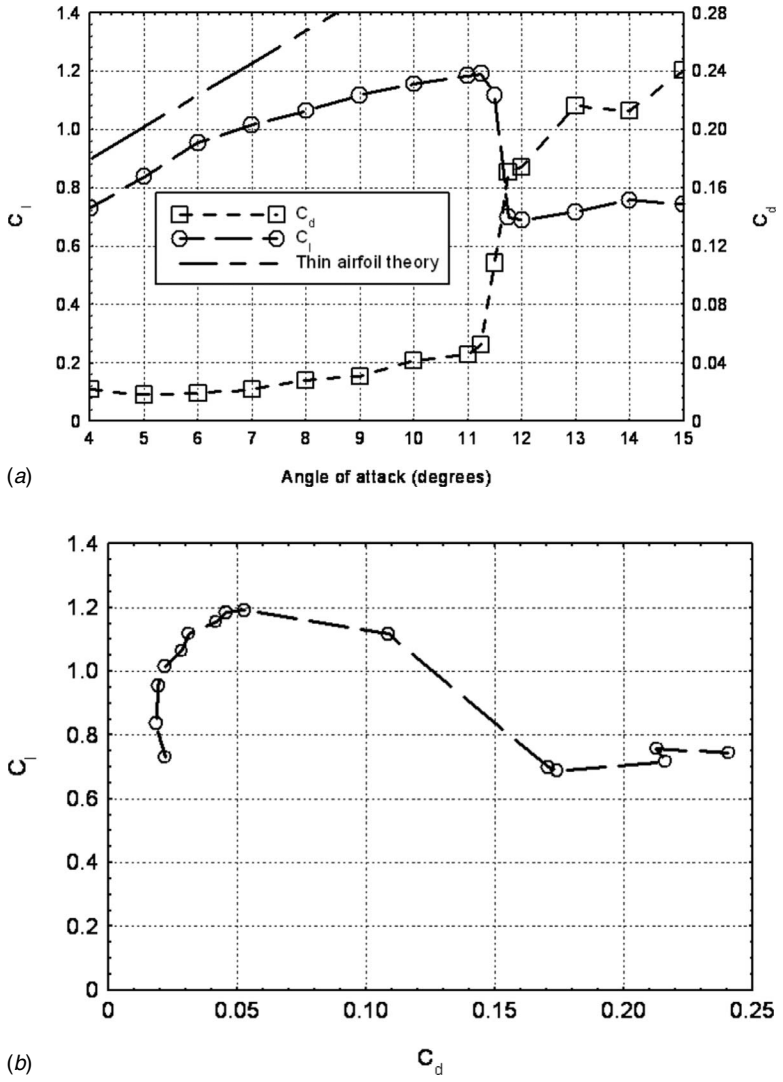


**Fig. 12 The measured airfoil lift and drag coefficients; (*a*) airfoil lift and drag coefficients vs. angle of attack; and (*b*) lift-drag polar dot**

ally burst. As clearly revealed in the instantaneous PIV measurement results given in Fig. 11, the laminar boundary layer was found to separate from the upper surface of the airfoil very near to the airfoil leading edge due to the significant adverse pressure gradient. Although the separated laminar boundary layer was still found to rapidly transit to turbulence by rolling up unsteady vortex structures due to the Kelvin–Helmholtz instabilities, the separated boundary layer could not reattach to the airfoil upper surface anymore due to the much more significant adverse pressure gradient when the AOA became 12 deg and higher. Large-scale flow separation was found to take place over almost entire airfoil upper surface, and the airfoil completely stalled. The airfoil stall is clearly visualized from the PIV measurement results.

**3.3 Lift and Drag Coefficients of the Airfoil.** The lift and drag coefficients of the airfoil at various AOA were determined by numerically integrating the measured surface pressure distribution around the 2D airfoil model used in the present study. Figure 12 shows the profiles of the measured lift and drag coefficients as the functions of the AOA and a lift-drag polar plot. For reference, the predicted increase rate of the airfoil lift coefficient (i.e., $dC_l/d\alpha = 2\pi$) based on thin airfoil theory [26] is also shown in the figure.

As revealed from the measured surface pressure distributions and PIV measurement results discussed above, the laminar boundary layer was found to firmly attach to the airfoil surface all the way from the airfoil leading edge to the trailing edge when the adverse pressure gradient over the upper surface of the airfoil is rather mild at relatively small AOA (i.e., AOA $\leq$ 6.0 deg). Therefore, the airfoil drag coefficient of the airfoil was found to be very small. The airfoil lift coefficient of the airfoil was found to increase almost linearly with the increasing AOA. The increase rate of the airfoil lift coefficient was found to be almost the same as the prediction based on thin airfoil theory (i.e., $dC_l/d\alpha = 2\pi$) at relatively small AOA when no laminar separation bubble was formed on the airfoil.

The adverse pressure gradient on the airfoil upper surface becomes more and more severe as the AOA increases. Since the laminar boundary layer on the airfoil is unable to withstand the severe adverse pressure gradient [2,3], it will separate from the airfoil upper surface, the and laminar flow separation occurs as the AOA relatively becomes large (i.e., AOA $\geq$ 8 deg for the present study). The laminar flow separation is evident as the pressure plateau in the measured surface pressure distributions and clearly visualized in the PIV measurement results given above. The separated laminar boundary layer was found to be able to reattach to the upper surface of the airfoil as a turbulent boundary layer after turbulence transition at adequate AOAs (i.e., 8.0 deg $\leq$ AOA $<$ 12.0 deg). This results in the formation of a laminar separation bubble on the airfoil upper surface. The airfoil lift coefficient was

found to keep on increasing with the AOA. However, the increase rate of the airfoil lift coefficient was found to considerably degrade due to the formation of a laminar separation bubble. The drag coefficient of the airfoil was found to increase faster with the increasing AOA when the laminar separation bubble was formed on the airfoil. The adverse gradient over the airfoil upper surface became so significant at AOA $\geq$ 12.0 deg that the laminar separation bubble was found to burst. The separated laminar boundary layer was not able to reattach to the airfoil upper surface anymore. As visualized in the PIV measurements given above, large-scale flow separation was found to take place over almost the entire airfoil upper surface, and the airfoil was found to completely stall. As a result, the lift coefficient of the airfoil was found to dramatically drop and the drag coefficient was found to significantly increase with the increasing AOA.

## 4 Conclusion

An experimental investigation was carried out to study the transient behavior of the laminar flow separation on a NASA low-speed GA (W)-1 airfoil at the chord Reynolds number of $Re_C$ =70,000. In addition to conducting surface pressure distribution mapping around the airfoil, a high-resolution PIV system was used to make detailed flow field measurements to quantify the occurrence and behavior of laminar boundary layer separation, transition, and reattachment at various AOAs. The detailed flow field measurements were correlated with the surface pressure measurements to elucidate the underlying physics associated with the separation, transition, and reattachment processes of the laminar boundary layer on the low-Reynolds-number airfoil.

The surface pressure mapping and detailed PIV measurements clearly revealed that the laminar boundary layer would stay firmly attached to the airfoil surface as the adverse pressure gradient over the airfoil upper surface was rather mild at relatively small AOA (i.e., AOA $<$ 8.0 deg). As the AOA became greater than 8.0 deg, the increased adverse pressure gradient caused the laminar boundary layer to separate from the airfoil upper surface. The separated laminar boundary layer was found to rapidly transit to turbulent flow by generating unsteady Kelvin–Helmholtz vortex structures. When the adverse pressure gradient was adequate (i.e., AOA $<$ 12.0 deg), the separated laminar boundary layer was found to be able to reattach to the upper surface of the airfoil as a turbulent boundary layer. As a result, a laminar separation bubble was formed on the airfoil. The length of the laminar separation bubble was found to be about 20% of the airfoil chord length and its height only about 1% of the chord length. While the total length of the laminar separation bubble was found to be almost unchanged regardless the AOA, the length of the laminar portion of the separation bubble was found to slightly increase, and the turbulent portion became slightly shorter with the increasing AOA. The separation bubble was found to move upstream to approach airfoil leading edge as the AOA increased. The laminar separation bubble was found to burst, causing airfoil stall, when the adverse pressure gradient became very significant at AOA $\geq$ 12.0 deg.

The detailed PIV measurements elucidated many details about the transient behavior of the laminar boundary layer separation, transition, and reattachment on the low-Reynolds-number airfoil. The transition process of the separated laminar boundary layer was found to be accompanied by the significant increase of Reynolds stress in the flow field. The measured TKE distributions clearly revealed that the reattached turbulent boundary layer was much more energetic, thus more capable of advancing against an adverse pressure gradient without flow separation, compared to the laminar boundary layer upstream the separation bubble. As a result, the reattached turbulent boundary layer was found to stay firmly attached to the airfoil surface from the reattachment point to the trailing edge of the airfoil. The critic points (i.e., separation, transition, and reattachment points) of the separation bubble identified from the PIV measurements were found to agree well with those estimated based on the surface pressure measurements.

The lift coefficient of the airfoil was found to linearly increase with the increasing AOA when the AOA is relatively small, while the drag coefficient of the airfoil was found to be very small. After the formation of the laminar separation bubble on the airfoil at AOA $\geq$ 8.0 deg, the increase rate of the airfoil lift coefficient was found to considerably degrade and the airfoil drag coefficient was found to increase much faster with increasing AOA. As the AOA became much higher (i.e., AOA $\geq$ 12.0 deg), where the separation bubble was found to burst to cause airfoil stall, the lift coefficient of the airfoil was found to dramatically drop, and the airfoil drag coefficient was found to significantly increase.

## Acknowledgment

The authors want to thank Mr. Bill Rickard, Mr. De Huang, and Mr. Masatoshi Tamai of Iowa State University for their help in conducting the experiments. The support of National Science Foundation CAREER program under Award No. CTS-0545918 is gratefully acknowledged.

## References

[1] Tani, I., 1964, "Low Speed Flows Involving Bubble Separations," Prog. Aeronaut. Sci., Vol. **5**, pp. 70–103.
[2] Carmichael, B. H., 1981, "Low Reynolds Number Airfoil Survey," NASA CR-165803, Vol. 1.
[3] Lissaman, P. B. S., 1983, "Low-Reynolds-Number Airfoils," Annu. Rev. Fluid Mech., **15**, pp. 223–239.
[4] J. T. Mueller, ed., 2001, *Fixed and Flapping Wing Aerodynamics for Micro Air Vehicle Applications*, Progress in Astronautics and Aeronautics, Vol. 195, AIAA.
[5] Gad-el-Hak, M., 2001, "Micro-Air-Vehicles: Can They be Controlled Better," J. Aircr., **38**(3), pp. 419–429.
[6] Horton, H. P., 1968, Laminar Separation in Two and Three-Dimensional Incompressible Flow, Ph.D. thesis, University of London.
[7] Hatman, A., and Wang, T., 1999, "A Prediction Model for Separated Flow Transition," ASME J. Turbomach., **121**, pp. 594–602.
[8] Johnson, M. W., 1994, "A Bypass Transition Model for Boundary Layers," ASME J. Turbomach., **116**, pp. 759–764.
[9] Solomon, W. J., Walker, G. J., and Gostelow, J. P., 1996, "Transition Length Prediction for Flows With Rapidly Changing Pressure Gradients," ASME J. Turbomach., **118**, pp. 744–751.
[10] Volino, R. J., and Hultgren, L. S., 2001, "Measurements in Separated and Transitional Boundary Layers Under Low-Pressure Turbine Airfoil Conditions," ASME J. Turbomach., **123**, pp. 189–197.
[11] Haueisen, V., Henneke, D. K., and Schröder, T., 1997, "Measurements With Surface Mounted Hot Film Sensors on Boundary Layer Transition in Wake Disturbed Flow," AGARD CP-598.
[12] Zhong, S., Kittichaikarn, C., Hodson, H. P., and Ireland, P. T., 2000, "Visualization of Turbulent Spots Under the Influence of Adverse Pressure Gradients," Exp. Fluids, **28**, pp. 385–393.
[13] FItzgerald, E. J., and Mueller, T. J., 1990, "Measurements in a Separation Bubble on an Airfoil Using Laser Velocimetry," AIAA J., **28**(4), pp. 584–592.
[14] Brendel, M., and Mueller, T. J., 1987, "Boundary Layer Measurements on an Airfoil at Low Reynolds Numbers," AIAA Paper No. 87-0495.
[15] O'Meara, M. M., and Mueller, T. J., 1987, "Laminar Separation Bubble Characteristics on an Airfoil at Low Reynolds Numbers," AIAA J., **25**(8), pp. 1033–1041.
[16] Lang, M., Rist, U., and Wagner, S., 2004, "Investigations on Controlled Transition Development in a Laminar Separation Bubble by Means of LDA and PIV," Exp. Fluids, **36**, pp. 43–52.
[17] Ol, M. V., Hanff, E., McAuliffe, B., Scholz, U., and Kaehler, C., 2005, "Comparison of Laminar Separation Bubble Measurements on a Low Reynolds Number Airfoil in Three Facilities," *35th AIAA Fluid Dynamics Conference and Exhibit*, Toronto, Ontario, June 6–9, AIAA Paper 2005-5149.
[18] Raffel, M., Favier, D., Berton, E., Rondot, C., Nsimba, M., and Geissler, M., 2006 "Micro-PIV and ELDV Wind Tunnel Investigations of the Laminar Separation Bubble Above a Helicopter Blade Tip," Meas. Sci. Technol., **17**, pp. 1652–1658.
[19] Burgmann, S., Brücker, S., Schröder, W., 2006, "Scanning PIV Measurements of a Laminar Separation Bubble," Exp. Fluids, **41**, pp. 319–326.
[20] Gao, H., Hu, H., and Wang, Z. J., 2008, "Computational Study of Unsteady Flows Around Dragonfly and Smooth Airfoils at Low Reynolds Numbers," *46th AIAA Aerospace Sciences Meeting and Exhibit*, Reno, NV, Jan. 7–10, AIAA Paper No. 2008-0385.

[21] McGee, R. J., and Beasley, W. D., 1973, "Low-Speed Aerodynamics Characteristics of a 17-Percent-Thick Airfoil Section Designed for General Aviation Applications," NASA TN D-7428.
[22] Russell, J., 1979, "Length and Bursting of Separation Bubbles: A Physical Interpretation," Science and Technology of Low Speed Motorless Flight, NASA Conference Publication 2085, Part 1.
[23] Shum, Y. K., and Marsden, D. J., 1994, "Separation Bubble Model for Low Reynolds Number Airfoil Applications," J. Aircr., **31**(4), pp. 761–766.
[24] Yaruseych, S., Sullivan, P. E., and Kawall, J. G., 2006, "Coherent Structure in an Airfoil Boundary Layer and Wake at Low Reynolds Numbers," Phys. Fluids, **18**, 044101.
[25] Lin, J. C. M., and Pulley, L. L., 1996, "Low-Reynolds-Number Separation on an Airfoil," AIAA J., **34**(8), pp. 1570–1577.
[26] Anderson, J. D., 2005, *Fundamentals of Aerodynamics*, 4th ed., McGraw-Hill Higher Education, New York.

# Computational Modeling and Simulation of a Single-Jet Water Meter

**Gorka S. Larraona**
**Alejandro Rivas**
**Juan Carlos Ramos**

Thermal and Fluids Engineering Division,
Mechanical Engineering Department,
Tecnun (University of Navarra),
Manuel de Lardizábal 13,
20018 San Sebastián, Spain

*A single-jet water meter was modeled and simulated within a wide measuring range that included flow rates in laminar, transitional, and turbulent flow regimes. The interaction between the turbine and the flow, on which the operating principle of this kind of meter is based, was studied in depth from the detailed information provided by simulations of the three dimensional flow within the meter. This interaction was resolved by means of a devised semi-implicit time-marching procedure in such a way that the speed and the position of the turbine were obtained as part of the solution. Results obtained regarding the turbine's mean rotation speed, measurement error, and pressure drop were validated through experimental measurements performed on a test rig. The role of mechanical friction on the performance of the meter at low flow rates was analyzed and interesting conclusions about its influence on the reduction of the turbine's rotation speed and on the related change in the measurement error were drawn. The mathematical model developed was capable of reproducing the performance of the meter throughout the majority of the measuring range, and thus was shown to be a very valuable tool for the analysis and improvement of the single-jet water meter studied.* [DOI: 10.1115/1.2911679]

*Keywords: single-jet water meter, CFD, fluid-structure interaction, measurement error, pressure drop, mechanical friction*

## 1 Introduction

Single-jet meters are widely used for measuring water consumption in industrial, commercial, and residential applications. Their broad measuring range and remarkable low-flow sensibility, along with their long-term durability, make single-jet water meters a cost-effective choice for general billing purposes. Basically, they consist of a turbine contained in a chamber that rotates due to the torque imparted by a jet—formed as the flow enters the chamber—that impacts several of its vanes (Fig. 1). The speed at which the turbine rotates is expected to be proportional to the flow rate, so that the number of revolutions that the turbine turns is thereby proportional to the water volume delivered through the meter. The proportionality constant is usually known as the *meter factor* K (given in revolutions per volume unit) and it is determined for each meter design by experimental calibration.

However, the speed of the turbine is not exactly proportional to the flow rate and hence there exists a deviation between the volume registered by the meter—as $K^{-1}$ times the number of revolutions given by the turbine—and the actual water volume delivered through it. This error in volume measurement depends on the flow rate and its variation throughout the measuring range of the meter is represented in the so-called *error curve* (Fig. 1). Manufacturers provide this curve together with the pressure drop curve, showing that the meter meets the requirements of the applicable standard (e.g., ISO, AWWA) regarding accuracy and maximum pressure drop.

Despite their simple operating principle, single-jet meters are difficult to theoretically analyze. On the one hand, the driving torque exerted by the jet depends on the position of the turbine, and it can hardly be quantified due to the complex interference that exists between the vanes impacted. On the other hand, the turbine is not likely to rotate with constant speed owing to the variable torque exerted by the jet, so it is also complicated to estimate the retarding torque produced upon the vanes of the turbine that are not impacted by the jet and which drag water. In addition, there is a nonhydraulic torque related to mechanical friction that acts against the rotation of the turbine. This torque is also difficult to quantify, although it is known to be significant only in the lower part of the measuring range [1], where it is responsible for the steep decline that is often observed in the error curve (see Fig. 1). In one of the few studies found in the bibliography, Chen [2] proposed a very simplified theoretical model for these forms of torque that assumes that the turbine rotates at a strictly constant speed for a given flow rate and that there is no interference between the vanes impacted by the jet. Moreover, it accepts that the torque on each vane is constant regardless of the position of the turbine and only depends on whether the vane is impacted by the jet or if it drags water. With these hypotheses and introducing an empirical constant to the model, he was able to reproduce the error curve of a specific design. However, the model is not capable of predicting the effect of the main design parameters on the performance of the meter, and therefore it cannot be employed for design purposes.

Due to the lack of a solid theoretical basis, the design and improvement of single-jet water meters have been mainly achieved so far by means of the experience gathered by each manufacturer in costly experimental procedures. This methodology involves building expensive prototypes and a large number of tests, which are limited to assessing the error and pressure drop curves of the new meter designs. Therefore, improvements in performance obtained with this methodology are often difficult to interpret and are not universally applicable.

Alternatively, computational fluid dynamics (CFD) techniques have been successfully employed for the study of several types of flow meters that, such as single-jet meters, have an operating principle based on the interaction between the flow and a moving element. Buckle et al. [3] studied the laminar flow around the float of a variable area flow meter and found reasonable agreement between the computed velocities and the Laser Doppler Anemometry (LDA) measurements they performed. They concluded [4]

Contributed by the Fluids Engineering Division of ASME for publication in the JOURNAL OF FLUIDS ENGINEERING. Manuscript received June 13, 2007; final manuscript received February 5, 2008; published online April 25, 2008. Assoc. Editor: Yu-Tai Lee.

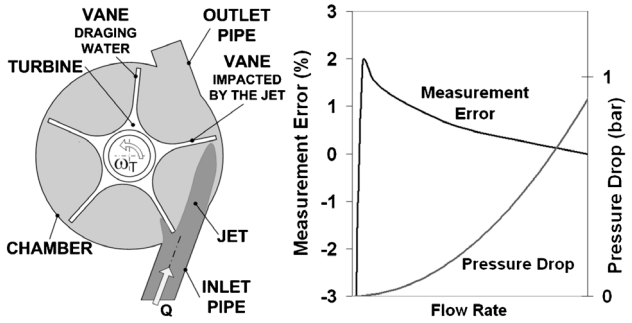


**Fig. 1 Single-jet water meter: schematic of the operating principle (left) and typical error and pressure drop curves (right)**

**Table 1 Summary of studied flow rates and corresponding pipeline Reynolds number and expected mean turbine speed ($\bar{\omega}_{T,\text{expected}} = 2\pi KQ/3600$, where $Q$ is the flow rate in l/h)**

| Flow rate (1/h) | $\text{Re}_{\text{pipeline}}$ | $\bar{\omega}_{T,\text{expected}}$ (rad/s) |
|---|---|---|
| 15 | 352 | 0.95 |
| 22.5 | 528 | 1.42 |
| 30 | 704 | 1.90 |
| 60 | 1410 | 3.80 |
| 120 | 2820 | 7.60 |
| 300 | 7040 | 19.0 |
| 450 | 10,600 | 28.5 |
| 750 | 17,600 | 47.5 |
| 1500 | 35,200 | 95.0 |
| 3,000 | 70,400 | 190 |

that the discrepancies were probably due to the asymmetry in the experimental flow. Xu [5] studied the flow around an isolated blade of an axial turbine flow meter and calculated the torque exerted by the flow on a radial section of the blade at different angles of attack and flow rates. These torques were later introduced in an analytical model of the flow meter [6] that also included all other torques applied to the turbine (e.g., bearing friction). The prediction of the error curve of the flow meter showed good agreement with the curve experimentally obtained. Aboury et al. [7] worked on an oscillating-piston water meter model. They used a deforming mesh and an implicit fluid-rigid body interaction algorithm and were able to quite accurately predict the error curve of the meter.

In the present study, the CFD based procedure described by Sánchez and Rivas [8] has been followed to develop a computational model for studying the performance of a single-jet water meter throughout a wide measuring range, which includes flow rates in laminar, transitional, and turbulent flow regimes. A semi-implicit time-marching procedure has been devised to resolve the complex interaction that exists between the flow and the turbine. This interaction has been studied in detail and the torques and turbine speed involved, which depend on the turbine position, have been calculated, so that valuable information for design purposes has been obtained. Results obtained regarding the turbine's mean rotation speed, measurement error, and pressure drop have been validated through experimental measurements performed on several units of the meter. The effect of mechanical friction on the lower part of the measuring range has been analyzed by considering different constant values of the associated retarding torque. The computational model is capable of reproducing the performance of the meter in this range when a specific amount of friction is considered.

## 2 Description of the Meter Studied

The meter studied (Fig. 2) is a noncommercial design that has been built following industry standards and can be considered as prototypical of a single-jet water meter for residential applications. Its five-vane turbine is contained in a cylindrical chamber that is enclosed by two ribbed plates above and below. The turbine is mounted on a pivot bearing and it has a magnet to transmit the number of revolutions by a magnetic coupling to the mechanical register located in a watertight enclosure. The gear ratio of the register is such that 1 litre is recorded whenever the turbine has turned 36.27 revolutions; thus the meter factor $K$ is 36.27 rev/l. Both inlet and outlet pipes have straight ends that are aligned with the axis of the pipeline, but they are angled as they approach the chamber. In the case of the inlet pipe, the internal diameter is progressively reduced and the inlet strainer has been removed for simplicity.

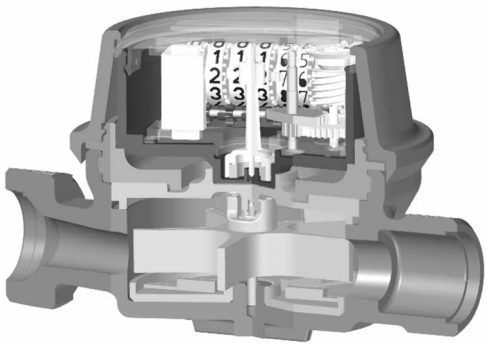

**Fig. 2 Geometry of the single-jet water meter studied**

The measuring range of single-jet water meters in residential applications usually expands from 15 l/h to 3000 l/h. Ten different flow rates within this range have been studied, so as to provide sufficient data to determine the overall performance of the meter. Table 1 shows the flow rates studied together with the corresponding Reynolds number based on the pipeline's internal diameter (15 mm) and the expected mean turbine speed, which is the result of the established meter factor. Taking into account the pipeline's Reynolds number, the flow within the meter is expected to be fully turbulent from 300 l/h. At lower flow rates, the flow might enter the meter in laminar regime and undergo a transition to turbulent regime inside. This transitional regime is more likely to happen in the case of 120 l/h and 60 l/h, even more so if the diameter reduction in the inlet pipe is taken into account. Because of this uncertainty about the possible transition to turbulence within the meter, simulations of flow rates up to 120 l/h have been performed considering the flow both in laminar and transitional regimes. Higher flow rates have only been simulated as fully turbulent.

## 3 Mathematical Model

Since the operating principle of the single-jet water meter is based on the interaction between the flow and the turbine, both water flow and turbine rotation have to be modeled and coupled in order to simulate the performance of the meter. The mathematical model developed considers the two-way coupling.

- Flow to turbine: The torque exerted by the flow is included in the differential equations that define the rotation of the turbine (Sec. 3.2). At each instant, the torque is computed and the speed and position of the turbine recalculated by integrating these equations.
- Turbine to flow: Time dependent position and speed of the turbine are included in the computation of the water flow. On the one hand, the domain in which the water flow is calculated is variable in time and accommodates the position of the turbine at each instant (Sec. 3.1). On the other hand, the velocities of water particles in contact with the

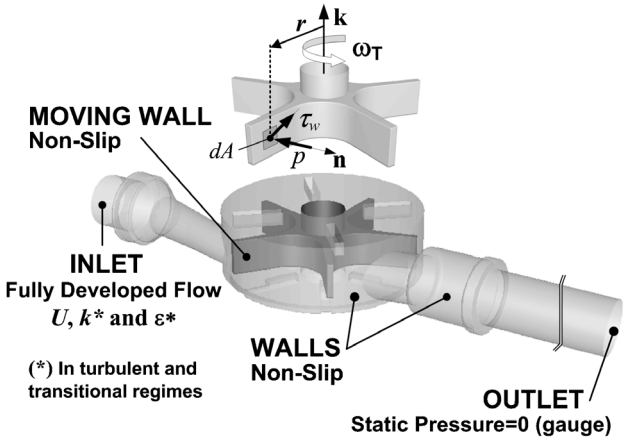


**Fig. 3 Flow domain and boundary conditions. (Pressure and shear forces exerted by the flow on the turbine are also depicted.)**

turbine are set at each instant to those of the turbine points by the nonslip boundary condition (Sec. 3.3).

As a result of solving the interaction between the turbine and the water flow, the variations of both the torque exerted by the flow and the rotation speed of the turbine will be obtained. They are expected to periodically vary since the five-vane turbine recovers the same position each 72 deg ($2\pi/5$ rad).

**3.1 Flow Domain.** The flow domain (Fig. 3) is defined as the volume delimited by the internal geometry of the meter, the turbine, and two sections of the pipeline to which the meter is threaded in its normal installation. As explained before, the flow domain is variable in time because the turbine rotates and occupies a different position at each instant. The pipeline has an internal diameter of 15 mm, and its sections before and after the meter are 15 mm and 90 mm long, respectively; these sections are considered long enough for the boundary conditions prescribed at their ends to be realistic (see Sec. 3.3).

### 3.2 Governing Equations

*Water Flow*. The flow within the meter is considered incompressible. Different forms of the Navier–Stokes equations are used depending on whether the flow rate simulated is considered as being in a laminar, transitional, or fully turbulent regime. When the flow is considered laminar, the unsteady Navier–Stokes equations are employed, which in vector form can be written as

$$\nabla \cdot \mathbf{u} = 0 \tag{1}$$

$$\frac{\partial \mathbf{u}}{\partial t} + \nabla \cdot (\mathbf{u}\mathbf{u}) = -\frac{1}{\rho}\nabla p + \nabla \cdot [\nu(\nabla \mathbf{u} + \nabla \mathbf{u}^T)] \tag{2}$$

On the other hand, the unsteady Reynolds averaged Navier–Stokes (URANS) equations are used when the flow is considered transitional or fully turbulent. Since the Boussinesq hypothesis [9] is adopted, these equations are as follows:

$$\nabla \cdot \mathbf{U} = 0 \tag{3}$$

$$\frac{\partial \mathbf{U}}{\partial t} + \nabla \cdot (\mathbf{U}\mathbf{U}) = -\frac{1}{\rho}\nabla P + \nabla \cdot \left\{ (\nu + \nu_t)[\nabla \mathbf{U} + \nabla \mathbf{U}^T] - \frac{2}{3}k\mathbf{I} \right\} \tag{4}$$

In these equations, the magnitudes that appear in capitals refer to ensemble averaged values; $\nu_t$ and $k$ stand for kinematic eddy viscosity and turbulence kinetic energy, respectively, and they have to be calculated using a turbulence model. The two-layer approach of Chen and Patel [10] has been used for this aim, combining the two-equation realizable $k$-$\varepsilon$ model [11] with the one-equation model of Wolfshtein [12], which is more suitable for reproducing viscous effects close to solid walls. Both models solve the same transport equation for $k$ but calculate $\varepsilon$ and $\nu_t$ in a different way. A smooth merging between the results of the two models is achieved by means of the blending functions proposed by Jongen and Marx [13].

The computation of transitional flows is currently an active topic of research. Customary turbulence models fail even in the prediction of the simplest case, so some specific models or modifications to the usual models have been proposed for the different types of transition [14,15]. Neither the realizable $k$-$\varepsilon$ model nor the Wolfshtein model is suitable for accurately predicting the onset of transition from laminar to turbulent regime, although the latter can be tuned for transitional boundary layer calculations as explained by Rodi [16]. Therefore, simulations of the lower flow rates in transitional regime cannot be expected to reproduce turbulent quantities, such as $\nu_t$ and $k$, accurately. However, the impact of this restraint on the prediction of the integral quantities of interest, such as the rotation speed of the turbine, can be expected to be limited. The latter will be assessed comparing the results obtained with experimental measurements.

*Turbine Rotation*. Considering the turbine as a rigid body, its rotation is governed by the following system of ordinary differential equations:

$$I_T \frac{d\omega_T}{dt} = T_F - T_{\mathrm{PB}} - T_R \tag{5a}$$

$$\frac{d\varphi_T}{dt} = \omega_T \tag{5b}$$

where $I_T$ is the turbine's inertia moment, $\omega_T$ and $\varphi_T$ are its rotation speed and angular position, and $T_F$, $T_{\mathrm{PB}}$, and $T_R$ are the torques produced by the flow about the axis of the turbine, the pivot bearing, and the registration system, respectively.

The torque imparted by the flow ($T_F$) is the sum of the driving torque due to the impact of the jet on some of the vanes and the retarding torque due to the fact that the rest of the turbine drags water. Its magnitude depends on both the position and the speed of the turbine and it increases with the flow rate since both the momentum flux of the jet and the speed with which the turbine drags water become greater. This torque is calculated at each time step by integrating the torque of the pressure and shear forces about the rotation axis ($\mathbf{k}$) along the surface of the turbine ($A_T$) (see Fig. 3):

$$T_F = \left[ \int\int_{A_T} \mathbf{r} \wedge (-p\mathbf{n} + \boldsymbol{\tau}_\mathbf{w}) dA \right] \cdot \mathbf{k} \tag{6}$$

On the other hand, the torques produced by the pivot bearing ($T_{\mathrm{PB}}$) and the registration system ($T_R$) are owing to mechanical friction and always oppose the turning of the turbine, thereby slowing it down. The former is due to the contact that exists between the turbine and the pivot bearing around which it rotates. The latter is the torque needed to overcome the friction between the gears of the mechanical register and is transmitted to the turbine by the magnetic coupling. These two torques are not easy to model and will be combined into a single term: *mechanical resistance torque* ($T_{\mathrm{MR}}$), which encompasses the effect of mechanical friction overall. Since the effect of mechanical friction has been reported to be of importance only in the lower part of the measuring range [1,17], mechanical resistance torque can be expected to be significant compared to the torque exerted by the flow only at low flow rates, where this torque is rather small. Because of the uncertainty about the magnitude that the mechanical resistance torque may have, different possible values will be considered in

**Table 2 Numerical schemes used in simulations**

| Transport equation terms | Numerical scheme | Refs. |
|---|---|---|
| Unsteady | Second order | |
| Diffusive | Second order centered | |
| Convective | Second order upwind | [21] |
| Source | Midpoint rule integration | |
| Pressure-correction algorithm | SIMPLEC | [22] |
| Velocity interpolation in continuity equation | Rhie-Chow | [23] |

the simulations of flow rates up to 120 l/h. This torque will not be regarded, however, in the simulations of higher flow rates.

**3.3 Boundary Conditions.** Boundary conditions for the water flow are applied at the walls of the meter and the pipes, at the surface of the turbine, and at the ends of the pipe sections (Fig. 3). In the case of the walls and the surface of the turbine, the nonslip velocity condition is imposed so that the fluid has the same velocity as the wall. In the simulations in transitional and turbulent regimes, they have been considered as smooth walls for shear stress calculation.

At the inlet, profiles corresponding to fully developed flow are prescribed for the velocity and—in the case of flows in turbulent regime—for the turbulence kinetic energy ($k$), and its dissipation rate ($\varepsilon$). In simulations in transitional regime, the velocity profile is that of the fully developed laminar flow and $k$ and $\varepsilon$ are set at very small constant values that make the turbulent viscosity ratio ($\nu_t/\nu$) of the order of $10^{-5}$. Fully developed flow profiles have been obtained by means of a separate simulation of the corresponding flow rate in an infinite 15 mm diameter pipe, following the method described by Murthy and Mathur [18].

At the outlet, only the value of the static pressure is specified; the remaining flow variables are extrapolated from within the flow domain itself. The value given is zero gauge pressure. Since the flow has been modeled as being incompressible, only pressure gradients are significant, so any other constant value prescribed would lead exactly to the same result but with a shift in the pressure field of this constant value. The election of zero gauge pressure helps minimize the round-off error in the calculations [19].

Initial conditions are also to be equally provided for the flow variables and for the position and speed of the turbine. They are described below where the full process of initialization is explained (Sec. 4.2).

## 4 Numerical Simulation of the Mathematical Model

The unstructured CFD code FLUENT V.6.3 has been used to numerically solve the mathematical model. The time-marching procedure used for resolving the interaction between the turbine and the flow has been implemented with the help of the user defined functions of the code. FLUENT uses the finite volume method [19] to discretize the flow-governing equations with a collocated variable arrangement. The equations are integrated in each mesh cell and the resulting integrals approximated using a multidimensional linear reconstruction approach [20]. Numerical schemes used in the simulations are listed in Table 2.

**4.1 Flow Domain and Time Discretization.** The flow domain has been discretized by means of an 815,000 hexahedral element mesh (Fig. 4). A cylindrical sliding mesh zone has been defined, which rotates together with the turbine while it slides past the mesh of the rest of the domain. Consequently, the discretized flow-governing equations are modified within this sliding mesh zone to account for the velocity of the cell faces. The nonconformal interface that exists between the rotating and the static mesh zones is treated employing the method described by Mathur [24], which avoids the need for interpolation and preserves the order of the numerical schemes at the interface.

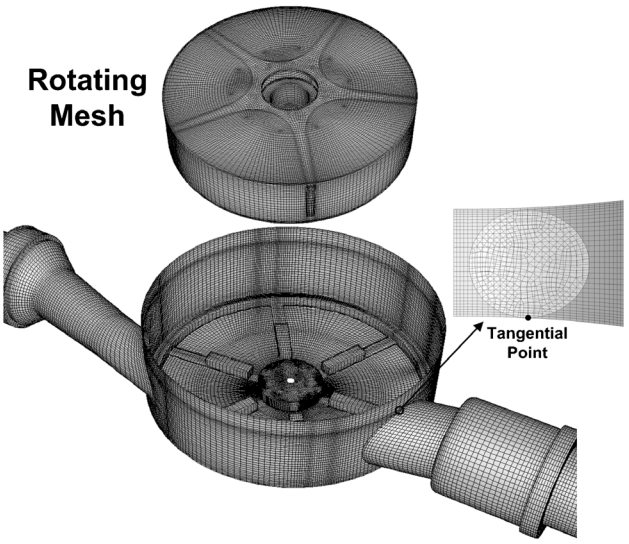


**Fig. 4 Computational mesh with details of the moving mesh zone and the nonconformal mesh connecting the chamber and the outlet pipe**

A nonconformal interface has also been used at the intersection of the chamber and the outlet pipe because there is a tangential point between them that would otherwise make the mesh of very poor quality. This procedure was not necessary at the intersection of the inlet pipe and the chamber since there is no tangency; there the mesh is fully conformal. Mesh points have been clustered near the walls of the chamber and the turbine to correctly resolve the boundary layers involved in the turbine-flow interaction. However, since boundary layers become thinner as the flow rate increases, a worse resolution of the boundary layers and larger values of $y^+$ at wall-adjacent cells have to be anticipated in the case of the highest flow rates.

The time step size ($\Delta t$) has been set for each simulation so that approximately 1200 integration steps ($N_{\text{steps}}$) are given in each revolution of the turbine (Eq. (7)). Specifically, it has been $\Delta t = 5 \times 10^{-3}$ s in the simulation with a flow rate of 15 l/h and $\Delta t = 2.5 \times 10^{-5}$ s in the simulation with 3000 l/h. With the time step size so calculated, the turbine turns $\Delta\varphi_T \approx 0.3$ deg on average between two consecutive time steps. This angle of rotation is fairly smaller than the angle that Benra [25] recommended for a realistic unsteady simulation of the flow within a pump, and thus it is judged to be small enough to provide accurate results in this particular case.

$$\Delta t = \frac{2\pi}{N_{\text{steps}} \bar{\omega}_{T,\text{expected}}} \tag{7}$$

**4.2 Initialization of the Simulations.** A steady solution was first obtained prior to each simulation with the turbine set at a specific motionless position. The transient simulation was then initiated with the values of the flow variables obtained and the rotation speed of the turbine being progressively increased until the value expected for the corresponding flow rate was reached (see Table 1). Five time steps with linearly increasing speed were enough to reach the desired value in all cases. The rotation speed was maintained constant until the flow became almost periodic after the turbine had completed two turns. Thereafter, the speed and the position of the turbine were calculated at each time step following the time-marching procedure described below.

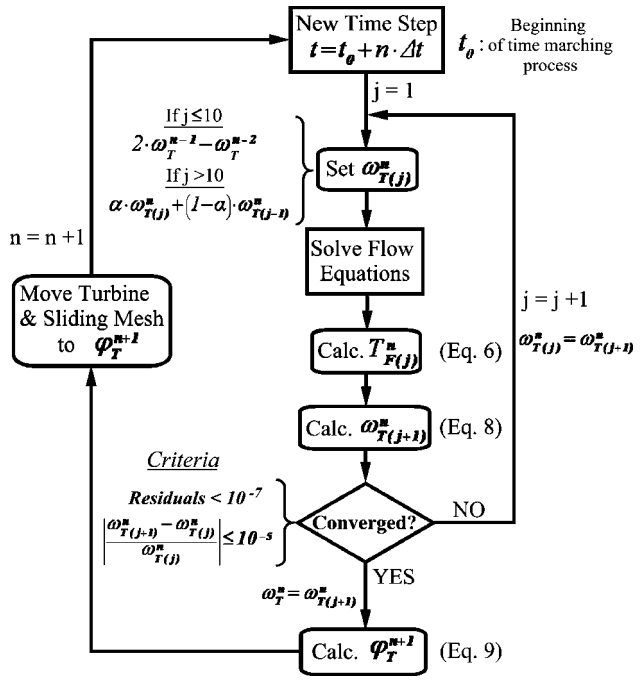


**Fig. 5 Flow diagram of the semi-implicit time-marching procedure devised to handle turbine-flow interaction**

**4.3 Numerical Procedure to Handle Turbine-Flow Interaction.** A semi-implicit time-marching procedure has been devised to deal with turbine-flow interaction (Fig. 5). Actually, the inertia moment of the turbine is very low and its rotation speed has shown to be very sensitive to the torque exerted by the flow. This makes the required time step size extremely small in order for the explicit time marching to be stable. The proposed time-marching procedure implicitly treats the turbine's rotation speed to overcome this restriction. The position, however, is explicitly treated. The procedure follows the steps described below:

(1) The rotation speed of the turbine is set at the beginning of each iteration step ($j$). In the first ten steps ($j \leqslant 10$), the rotation speed is maintained constant with the value obtained by linear extrapolation of the speeds at the last two time steps. From then on ($j > 10$), the rotation speed calculated in the previous iteration step (see Eq. (8)) is underrelaxed and imposed on the turbine. A relaxation factor of $\alpha=0.3$ has been used.

(2) Once the rotation speed of the turbine has been established, the flow-governing equations are solved by means of the pressure-correction algorithm SIMPLEC, using an implicit point Gauss–Seidel method accelerated by an algebraic multigrid strategy.

(3) Next, the torque exerted by the flow is calculated with the values of velocity and pressure just obtained. This value is then used to compute the rotation speed for the next iteration step by integrating Eq. (5*a*) with the second order scheme:

$$\omega_{T(j+1)}^n = \frac{4}{3}\omega_T^{n-1} - \frac{1}{3}\omega_T^{n-2} + \frac{2}{3}\frac{\Delta t}{I_T}(T_{F(j)}^n - T_{\mathrm{MR}}) \qquad (8)$$

When mechanical resistance torque ($T_{\mathrm{MR}}$) is considered, i.e., in flow rates up to 120 l/h, it is regarded as independent of the rotation speed, so it is not recomputed in each iteration step.

(4) Convergence is judged by checking (i) that the scaled residuals of the flow-governing equations in the iterative process are below $10^{-7}$ and (ii) that the variation of the rotation speed in two consecutive iteration steps is less than a 0.001%. Both requirements are usually met after 25 iteration steps.

(5) Once convergence is achieved, the rotation speed of the turbine is set to the last value calculated and its position in the next time step is calculated with Eq. (9). The sliding mesh is then moved to the new position and a new time step begins.

$$\varphi_T^{n+1} = \frac{4}{3}\varphi_T^n - \frac{1}{3}\varphi_T^{n-1} + \frac{2}{3}\Delta t\omega_T^n \qquad (9)$$

This procedure has two important advantages. First, the sliding mesh is only moved at the end of the time step, once the iteration process has been converged. The fully implicit approach, as that proposed by Aboury et al. [7], requires the readjustment of the position of the turbine within the iterative process of each time step, which makes the calculation more costly. Second, the implicit treatment of the turbine's speed guarantees that energy conservation in the fluid-solid interface is accomplished. As noted by Le Tellec and Mouro [26], this characteristic is essential both for preserving stability and ensuring the long-term accuracy of the numerical computation.

**4.4 Convergence and Verification of the Simulations.** Once the time-marching procedure is started it, nearly takes three complete revolutions of the turbine for each simulation to reach a periodic flow solution. Thereafter, the torque exerted by the flow and the rotation speed of the turbine repeat each time period $T$, which is the time needed for the turbine to complete 72 deg and recover the same position. However, in the case of flow rates ranging from 30 l/h to 120 l/h, the simulations performed assuming a laminar flow regime did not reach a periodic flow solution. Indeed, the nonperiodicity was more marked as the flow rate increases. This fact has been judged as an indicator that the flow is actually in transitional regime at these flow rates, and therefore, only the periodic torque and speed results obtained in this regime have been considered. On the other hand, simulations with 15 l/h and 22.5 l/h performed considering a laminar flow regime did reach a periodic flow solution. This fact would confirm that the flow is actually laminar at these two flow rates. Consequently, the results obtained from these simulations have been considered instead of those obtained assuming a transitional flow regime. In any case, the results obtained in both regimes showed minimum differences with regard to the torque exerted by the flow and the turbine's rotation speed.

The simulations have been considered as converged once the mean rotation speed of the turbine does not change more than 0.01% from period to period. A runtime of nearly 900 h in a PC with a 2.8 GHz Intel processor was typically necessary to attain this level of convergence. As will be shown below, the variation of the torque exerted by the flow and the turbine's rotation speed in each period is quite smooth, so the numerical dispersion related to time integration is believed to be rather low.

All simulations have been repeated in a coarser mesh of 410,000 elements in order to estimate the discretization error. This mesh has been obtained applying a coarsening factor of 1.25 in each coordinate direction of the original mesh. Accordingly, the time step size used in the simulations has been 1.25 times larger. The discretization error corresponding to the mean rotation speed of the turbine has been estimated by the *extrapolated relative error* proposed by Celik and Karatekin [27], using the formal order of accuracy of the numerical schemes employed. The estimated discretization error is below 1% in the case of the simulations up to 300 l/h. It is higher in the simulations of flow rates between 450 l/h and 3000 l/h, but it is still small, the highest errors estimated being those of 1500 l/h and 3000 l/h, which are 2.3% and 1.7% respectively.

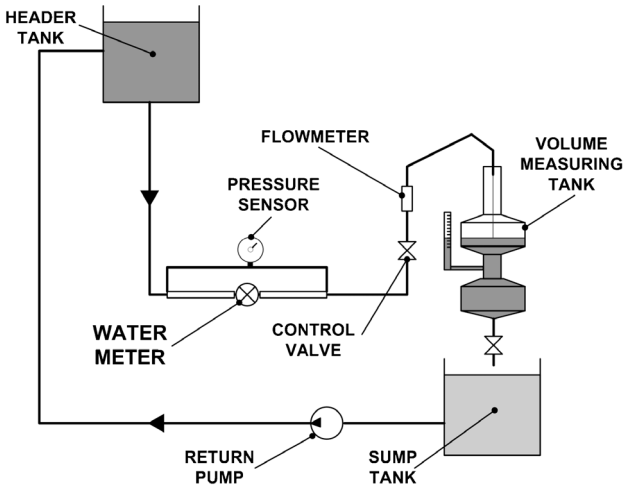


**Fig. 6 Schematic of the experimental test rig**

## 5 Experimental Measurements for Model Validation

Experimental measurements have been carried out in a calibration facility (Fig. 6). It includes a constant head tank that allows a steady water flow to pass through the meter by gravity, a series of control valves and variable area flow meters to establish the desired flow rate and a volume measuring tank into which the water is discharged. The meter is threaded to a horizontal pipe with an internal diameter of 15 mm. The pipe section before the meter is 250 mm long and is in turn preceded by a large radius bend; hence, the flow is expected to be fully developed when it enters the meter.

Three units of the meter have been constructed and tested in order to obtain the error curve, the mean rotation speed of the turbine, and the pressure drop. The results for each flow rate have been obtained by averaging the measurements of the three runs carried out with each unit. The dispersion of the data obtained in different runs and different units was rather small. The difference was less than 0.2% between data from the same unit and nearly 0.7% between data from different units.

Error in volume measurement is determined allowing a certain amount of water to pass through the meter and comparing the volume registered by the meter with the actual volume that is ascertained in the measuring tank. In the case of flow rates between 15 l/h and 120 l/h, a 10 l tank is used, whereas in the case of higher flow rates, a 100 l tank is utilized. Both tanks have a calibrated sight glass for reading water volume in their upper part. The time needed for total water volume to pass through the meter was also measured in each experiment and it helped assess the flow rate indicated by the flow meter by dividing the actual volume that had passed through the meter by the elapsed time. The error curve of the meter has been obtained performing measurements of the ten flow rates studied. The overall uncertainty in the error has been calculated to be $\pm 0.3\%$.

Mean rotation speed of the turbine for a given flow rate is inferred from the indication of the meter's register. The number of revolutions given by the turbine in an experiment is calculated multiplying the registered volume by the meter factor $K$. The mean rotation speed is then obtained dividing the number of revolutions by the time elapsed in the experiment.

Finally, pressure drop is measured in the case of the highest flow rates, namely, 450 l/h, 750 l/h, 1500 l/h, and 3000 l/h, using a differential pressure sensor connected to two pressure tapings that are located 200 mm before and 150 mm after the water meter, respectively. The pressure sensor has an uncertainty of $\pm 1\%$ of the full-scale reading, which is 2 bars. Pressure losses provoked by the pipe sections that are not included in the mathematical model have been estimated and subtracted from the measurements. The pipes have a very low roughness and have been considered as being hydraulically smooth, so their friction factor has been calculated using the Blasius formula [28]. The subtracted pressure losses represent about 4% of the measured value at all four flow rates.

## 6 Results and Discussion

**6.1 Study of the Turbine-Flow Interaction.** The numerical simulation of the flow within the single-jet water meter with different flow rates has allowed a detailed analysis of the interaction between the flow and the turbine. For example, Figs. 7–9 show some of the results obtained in the simulation of a flow rate of 3000 l/h. For this study, the initial position of the turbine ($\varphi_T = 0$ deg) has been arbitrarily defined as that in which one of the vanes impacted by the jet is perpendicular to the pipeline axis. Additionally, the side of each vane that is directly impacted by the jet when both come into contact is designated as the front side, and the opposite side as the back side.

In Fig. 7, the calculated distributions of the velocity and the static pressure in the midheight plane perpendicular to the turbine axis are represented at six different positions of the turbine. They show the complex interaction that exists between the flow and the turbine, and especially between the jet and the two vanes that are impacted by it. As the turbine rotates, Vane 1 comes into contact with the jet and interferes with Vane 2, which progressively losses the influence of the jet. In this process, the jet accelerates near the tip of Vane 1 at the early positions ($\varphi_T = 12-24$ deg), producing a low-pressure zone at the back side of the vane. In further positions, however, there is a pressure increase in the region between the back side of Vane 1 and the front side of Vane 2 ($\varphi_T = 36-48$ deg). It seems to be produced by the fact that a piece of high-velocity fluid coming from the jet becomes confined within this region and gradually decelerates. The low-pressure vortex that is formed at the front of Vane 1 as a result of the high-shear layer produced between the flow carried by the turbine and the jet sliding across the front side of the vane is also noticeable. The depression related to this vortex has been found to be more important as the flow rate increases.

It is important to note that the pressure difference between the inlet and the outlet of the meter is not constant but varies with the position of the turbine. Figure 8 shows that the pressure difference is the lowest at the initial position considered and has its largest value at 14 deg, approximately. This variable pressure difference is generated, not only by the hydraulic losses but also by the energy interchange that exists between the turbine and the flow in the chamber. Actually, it is the pressure at the inlet, which varies, since the pressure at the outlet has been set constant. This fact explains the variation of the pressure distribution in the inlet pipe observed in Fig. 7. The pressure distribution in the outlet pipe, however, is maintained nearly unchanged apart from the region close to the intersection with the chamber, where it is somewhat influenced by the passing of the vanes. This intersection is quite abrupt and the flow considerably accelerates when it turns to leave the chamber, forming a region with a negative gauge pressure. This depression becomes more significant as the flow rate increases, being as high as $-100$ kPa relative to the imposed outlet pressure (i.e., zero gauge) in the case of the highest flow rate. Since the outlet pressure would typically be between 500 kPa and 600 kPa in actual working conditions, the possible appearance of cavitation at this point can be dismissed.

The torques exerted by the flow on each of the five vanes of the turbine in a period are illustrated in Fig. 9(*a*). As expected, the only vanes that provided a driving (positive) torque are those impacted by the jet, i.e., Vanes 1 and 2, although it is not the case at their early and late positions, respectively. The remaining three vanes do not come into contact with the jet and they exclusively drag water; hence, they are given only a retarding (negative) torque. It is interesting to point out that it has been verified that

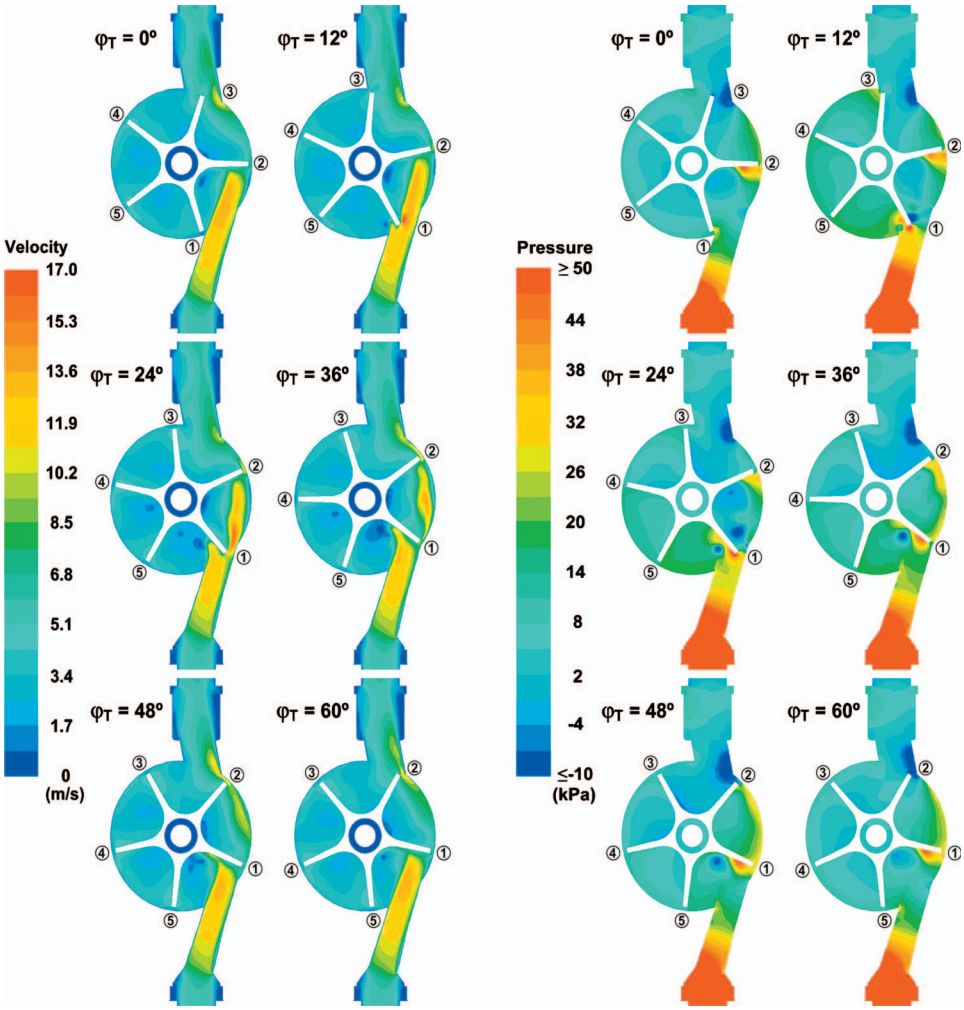


**Fig. 7 Detail of the flow with 3000 l/h. Velocity (left) and static pressure (right) in a mid-height plane at different positions of the turbine.**

the torques on the five vanes are mainly produced by pressure forces, the shear forces contributing less than 1% at virtually all the positions. The torques imparted to each of the five vanes have been added together to compute the total torque produced by the flow ($T_F$). This torque is the only one applied upon the turbine in the simulation because the mechanical resistance torque ($T_{MR}$) has been neglected in this case, as is the case in the remaining simulations of flow rates above 120 l/h. Figure 9(*b*) depicts the variations of the total torque and the rotation speed of the turbine in a period. The sign of the total torque points out whether the sum of the torques on the vanes (and $T_{MR}$ when considered) results in a driving or a retarding torque, and thus whether the turbine accelerates or decelerates. The peak to peak variation of the rotation speed is as much as 20% of its mean value in the period (188 rad/s in this case), as a result of the highly variable torque exerted by the flow and the low inertia moment that the turbine has. Logically, the peaks in rotation speed arise when all the driving and retarding torques applied upon the turbine cancel out and the total torque is zero. Another characteristic of the total torque applied upon the turbine that could be anticipated is that its average in one period is zero. This feature is needed for the turbine's rotation movement to be periodic.

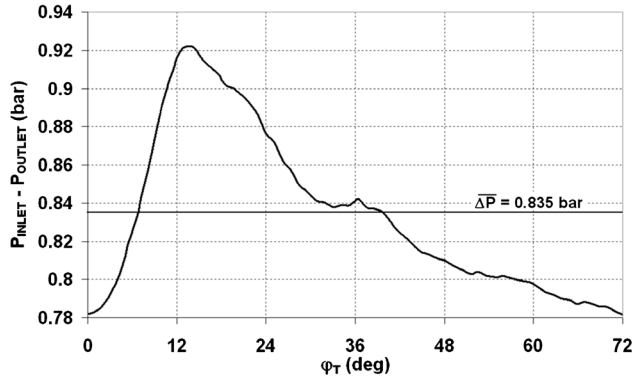


**Fig. 8 Static pressure variation between the outlet and the inlet of the meter during a period ($Q$=3000 l/h)**

As is clearly shown in Fig. 9, the computed driving and retarding torques and turbine's rotation speed are far from the assumptions of unchanging torque upon each vane and constant speed of the turbine that are made in the simple analytical model proposed by Chen [2]. In the case of Vanes 3, 4, and 5, the variation of the retarding torque that they receive is related to both the change in the turbine's rotation speed and the proximity of either the inlet or outlet pipes. Apart from the early positions of Vane 3, in which it faces the effects of the flow exiting from the outlet pipe, the retarding torques provided to these three vanes increase with the speed of the turbine and reach the maximum very close to the position at which the rotation speed of the turbine is the highest ($\varphi_T \approx 42$ deg). Moreover, the torques are approximately the same

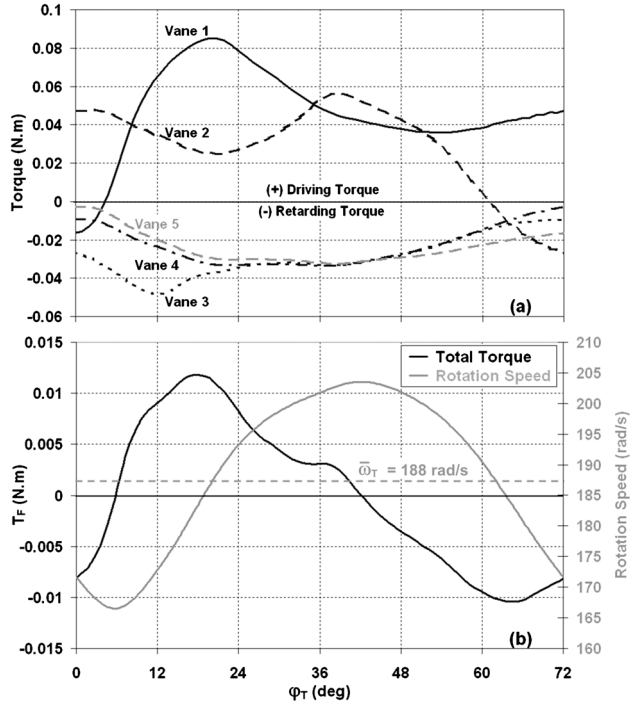


**Fig. 9 Periodical turbine-flow interaction (*Q*=3000 l/h): (*a*) torque exerted on each vane and (*b*) total torque and rotation speed of the turbine**

in the range $\varphi_T$=30–48 deg, in which both Vane 3 and Vane 5 are far from the outlet and inlet pipes, respectively. Out of this range, the effect of the outlet pipe on the torque received by Vane 3 is noticeable, with a significant maximum value at $\varphi_T$=12 deg that is produced by a high pressure zone appearing at its back side when it is about to finish passing across the pipe. The effect of the inlet pipe on the torque upon Vane 5 from $\varphi_T$=48 deg on is more modest, however, and the torque deviates only moderately from those of Vanes 3 and 4, even when the vane is quite close to the inlet.

The variations of the torques on Vanes 1 and 2 are even more remarkable and clearly depend on the extent in which the vanes are impacted by the jet rather than on the rotation speed of the turbine. At the initial position ($\varphi_T$=0 deg), only Vane 2 is impacted by the jet and solely contributes to the driving torque, which is overcome by the retarding torque provided to the rest of the vanes. As the turbine rotates, Vane 1 comes into contact with the jet and quickly starts to contribute to the driving torque. The steep increase of this vane's torque at the early positions is partly produced by the low-pressure zone produced by the accelerated jet at its back side. Although Vane 1 progressively interferes with Vane 2 and reduces its torque, the overall driving torque received by both vanes increases and prevails over the retarding torque, producing the acceleration of the turbine. The total torque has its maximum at a position of $\varphi_T$=18 deg approximately, just before the driving torque provided to Vane 1 has its highest value ($\varphi_T \approx$20 deg). Although in subsequent positions this vane takes up a bigger portion of the jet, the pressure at its back side increases and the driving torque that it receives diminishes. Simultaneously, the driving torque produced on Vane 2 recovers and reaches its maximum (at $\varphi_T$=40 deg approximately) in spite of the interference of Vane 1 that progressively blocks the jet. This growth is produced because the pressure gradually increases at its front side and diminishes at the back side. Soon after this position, the retarding torque overcomes the driving torque and the turbine starts to slow down. The torque on Vane 2 decreases as this vane get closer to the position of the outlet pipe at $\varphi_T$=60 deg, where the influence of the jet is almost completely lost. The torque applied to Vane 1 that has also been decreasing is recovered to some extent at the end of the period, being the only contributor to the driving torque.

The variations of the torques and the rotation speed just discussed are similar in the case of the other flow rates studied, although there are some differences that result in the expected nonlinearity of the water meter's measurements. The comparison between the results obtained with different flow rates has been carried out by means of the dimensionless form of the torque and the rotation speed, which have been defined as

$$\Psi = \frac{T_F}{\rho Q V d} \tag{10}$$

$$\Omega = \frac{\omega_T}{V/d} \tag{11}$$

where $V$ and $d$ are, respectively, the mean velocity of the jet as it enters the chamber and the distance between the axis of the jet and the rotation axis (**k**). Both dimensionless torque and rotation speed have been plotted in Fig. 10 versus the position of the turbine for the ten flow rates studied. The results correspond to simulations in which the friction torque has not been considered, since only the effect of the flow rate is to be investigated. Figure 10(*a*) clearly shows that the dimensionless torque curves of the flow rates in turbulent regime almost coincide, and thus that the torque nearly scales with the square of the flow rate. The same can be stated about the curves that correspond to flow rates in transitional regime (30–120 l/h), as can be seen in Fig. 10(*b*). However, the curves of the flow rates in laminar regime (15 l/h and 22.5 l/h) differ somewhat from the curves corresponding to the other flow regimes. Indeed, they posses higher maxima and have a different form between $\varphi_T$=30–48 deg, but almost share with the other curves the positions in which the torque becomes positive ($\varphi_T \approx$6 deg); it has its maximum ($\varphi_T \approx$18 deg), and its minimum ($\varphi_T \approx$67 deg).

The calculated dimensionless mean rotation speed is directly related to the measurement error predicted by the simulation. Actually, the percentage in which the calculated and the expected mean rotation speeds differ is exactly the error made by the meter in the measurement of the water volume that has passed through (see the Appendix):

$$\text{Meas. Error} = \frac{\bar{\Omega}_{\text{calculated}} - \bar{\Omega}_{\text{expected}}}{\bar{\Omega}_{\text{expected}}} \tag{12}$$

Therefore, the nonlinearity of the measurements provided by the meter is clearly shown in Figs. 10(*c*) and 10(*d*), since the difference between the calculated and the expected dimensionless mean rotation speeds varies with the flow rate. The errors in volume measurement corresponding to 3000 l/h and 30 l/h have been indicated in these figures as an example. It is interesting to point out that the way in which the dimensionless rotation speed curves change with the flow rate depends on the flow regime. On the one hand, in turbulent and transitional regimes, the shape of the curve is maintained but the curve itself, in its entirety, shifts up as the flow rate decreases, hence, so does the resultant dimensionless mean rotation speed. The rise, however, is very modest between 60 l/h and 30 l/h and especially between 450 l/h and 300 l/h. On the other hand, in laminar regime, the whole curve does not shift, but only the portion between $\varphi_T$=6–60 deg shifts down as the flow rate decreases, so that the dimensionless mean rotation speed diminishes. Certainly, results with more flow rates in laminar regime would be necessary to assess this trend.

**6.2 Validation of the Mathematical Model.** The mathematical model has been validated by comparing the results of the turbine's mean rotation speed, error in volume measurement, and pressure drop with the experimental measurements obtained in the test rig. The mechanical resistance torque ($T_{\text{MR}}$) has been kept out

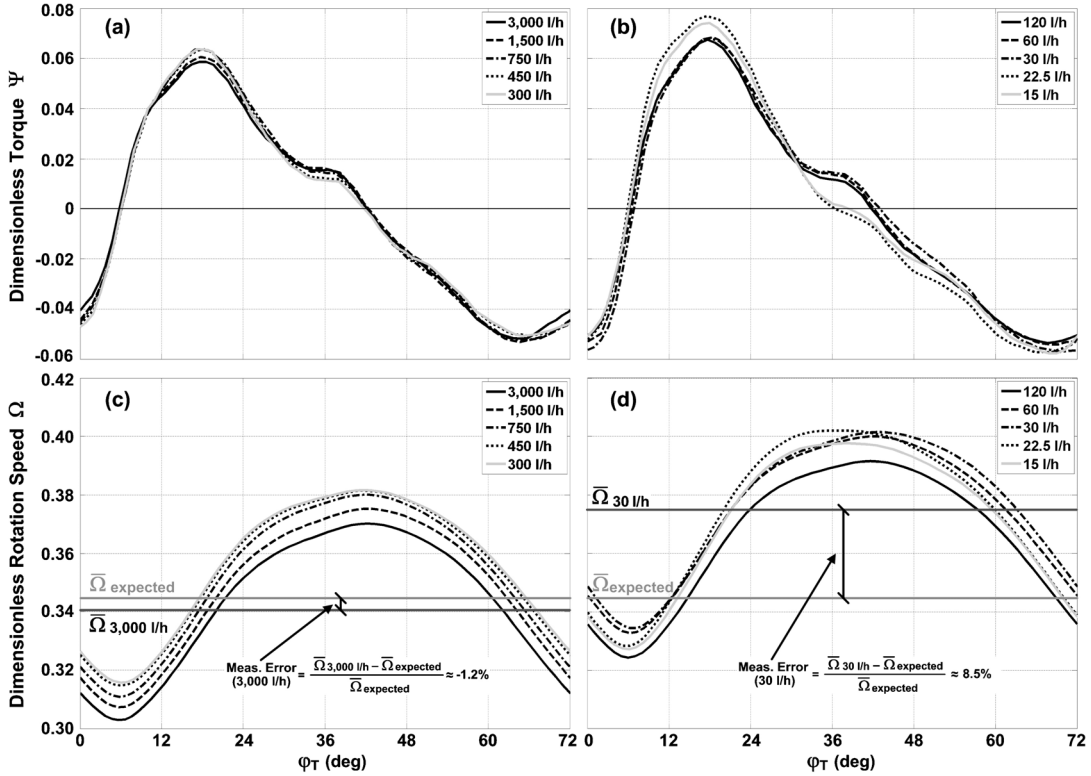


**Fig. 10 Dimensionless torque and rotation speed curves with different flow rates: in turbulent regime ((*a*) and (*c*)) and in transitional and laminar regimes ((*b*) and (*d*))**

of this validation process because its actual value is not known, so the numerical results compared correspond to simulations in which this torque has not been taken into account. For this reason, the results of low flow rates that are affected by mechanical friction should be expected to differ from those measured.

First, the mean rotation speed of the turbine has been calculated in each simulation by averaging the instantaneous speed throughout one period. The obtained mean rotation speeds are compared to those experimentally measured in Fig. 11. As was expected, they have been found to be approximately proportional to the flow rate. Moreover, the agreement between the calculated and the measured speeds is very good for flow rates higher than 22.5 l/h, the difference being 3% at most (at 3000 l/h). The fact that the discrepancy is small in the case of the three flow rates simulated in transitional regime (30 l/h, 60 l/h, and 120 l/h) confirms that the inability of the turbulence models used here to accurately predict the transition to turbulence has little impact on the capacity of the model to forecast the mean rotation speed of the turbine. The deviation found in the case of the two lowest flow rates is higher, especially for 15 l/h, of which the calculated mean rotation speed is 11% higher than the measured one. Interestingly, the mean speeds calculated with these two flow rates are higher than the measured ones, as is the case of 30 l/h and 60 l/h. It is consistent with the fact that mechanical friction, which tends to slow the turbine down, has not been taken into account. In the study about the effect of the friction presented below, it will be confirmed that these calculated speeds get closer to the measured ones when friction is considered.

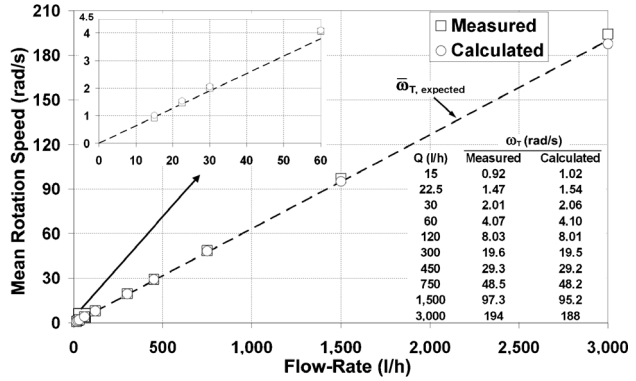


**Fig. 11 Mean rotation speed of the turbine. Measured versus calculated values.**

As discussed above, the pressure drop produced in the meter is not constant in the simulations, but depends on the position of the turbine. The mean pressure drop has been calculated for the flow rates between 450 l/h and 3000 l/h by averaging its value throughout one period. The predictions are in very good agreement with experimental measurements, as is depicted in Fig. 12. Both experimental and numerical results evidence a nearly quadratic variation with the flow rate observed in many references [1].

Finally, the error curve predicted by the mathematical model has been compared to the curve experimentally obtained. Both curves are plotted together in Fig. 13, where the accuracy requirements of the ISO 4064 standard [29] are indicated. The fact that some values of the measurement error do not conform to these requirements is of no importance since the meter studied is a noncommercial prototype. The measurement errors appearing in the calculated error curve have been computed comparing the calculated and the expected dimensionless mean rotation speeds, as was explained above. Therefore, the calculated error curve evidences the different trends that the turbine's dimensionless mean rotation speed exhibits with different flow regimes.

As is shown in Fig. 13, the mathematical model very accurately reproduces the shape of the experimental error curve in the range between 120 l/h and 750 l/h, but deviates from it at lower and

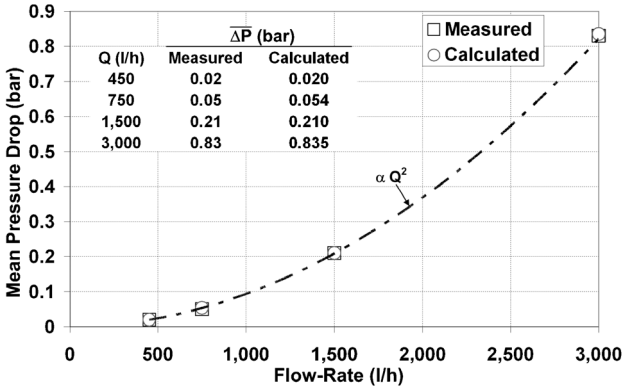


**Fig. 12 Mean pressure drop. Measured versus calculated values.**

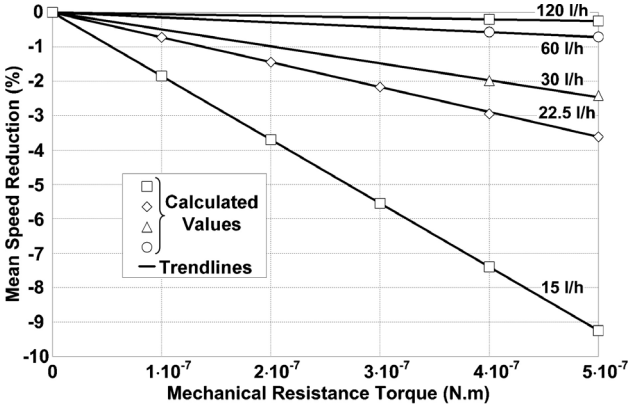


**Fig. 14 Reduction in the mean speed of the turbine as a function of mechanical resistance torque ($T_{MR}$)**

higher flow rates. The deviation to more positive errors (i.e., more volume registered) observed in the case of lower flow rates is consistent with the fact that mechanical friction has not been considered. Actually, in the next section, the mathematical model will be shown capable of reproducing the steep decline observed in the experimental curve when mechanical friction is included.

With regard to the highest flow rates, namely, 1500 l/h and 3000 l/h, the deviation from the measurements might be due to the combination of two causes. On the one hand, the computational mesh is probably not fine enough to accurately calculate the thinner boundary layers found in such high flow rates. The higher discretization error calculated in these simulations and the fact that large values of $y^+$ (up to 30) exist at some wall-adjacent cell zones would confirm this point. On the other hand, the rotation speed of the turbine may be so important at these high flow rates that the centrifugal forces to which the flow is subjected in the chamber might have a significant impact on turbulence. The turbulence models based on the Boussinesq hypothesis, such as the ones employed in this study, are incapable of reproducing the anisotropy of the Reynolds stresses caused by this phenomenon and the result that this anisotropy has on the flow [9]. Therefore, some differences between the calculated and the actual flows and, ultimately, between the calculated and the experimental measurement errors may be expected if the mentioned rotation effects are significant. Nevertheless, these differences seem to be minor in light of the comparison between the calculated and the measured values.

**6.3 Study of the Effect of Mechanical Friction on Meter Performance.** The results presented thus far correspond to simulations in which the retarding torque due to the mechanical friction ($T_{MR}$) has not been considered. The discrepancies found in the lower part of the measuring range between the experimental and the simulated mean rotation speed and measurement error were thus anticipated, because the magnitude of the ignored mechanical resistance torque ($T_{MR}$) is likely to be similar to that produced by the flow ($T_F$) at such a low flow rates. However, the performance of the water meter in the lower part of the measuring range is very important to the designers, since this performance is related to sensitivity, that being the water meter's capability of providing a measure at low flow rates with a margin of error that meets legal requirements. Consequently, the effect of mechanical friction on the turbine's mean rotation speed and the meter's error curve has been analyzed using the mathematical model developed.

The main difficulty in undertaking this analysis is to determine the mechanical resistance torque whether it be experimentally or theoretically. In the present study, however, its magnitude has been estimated as being of the order of $10^{-7}$ N m from the values of $T_F$ calculated in the simulations with 15 l/h and 22.5 l/h when the friction is not regarded. Moreover, its possible dependence on the turbine's speed has been neglected in such a way that its value has been considered constant in each simulation. These two assumptions are based on the fact that the importance of the flow and the mechanical friction on the meter's performance is similar at low flow rates.

In this study, the mathematical model has been simulated with flow rates between 15 l/h and 120 l/h using different values for the mechanical resistance torque ($T_{MR}$) up to $5 \times 10^{-7}$ N m. The values of the turbine's mean rotation speed obtained from these simulations are, obviously, smaller than those obtained when the mechanical resistance torque was not factored in. However, a remarkable result is obtained when the values of the reduction of mean rotation speed are plotted against the values of $T_{MR}$ for a constant value of the flow rate, as has been done in Fig. 14. Interestingly, the reduction of the mean rotation speed is found to be proportional to the value of $T_{MR}$ in which the constant of proportionality is a function of the flow rate. Moreover, the effect of a given constant value of the resistance torque on the mean speed of the turbine notably decreases as the flow rate increases. This trend was expected since $T_F$ is nearly scaled with the square of the flow rate (see Fig. 10) and quickly overcomes the friction torque as the flow rate is increased. Indeed, the speed reduction produced with 120 l/h is very small and it can be predicted to be negligible in the case of higher flow rates. This result is in agreement with the experiments of Arregui et al. [17] that carried out accelerated wear tests on several single-jet water meters of the same size and measuring range of that studied in this work and concluded that the effect of the augmented mechanical friction was only noticeable with flow rates of 120 l/h and below.

Another interesting result is shown when the error curves obtained from the mathematical model considering mechanical fric-

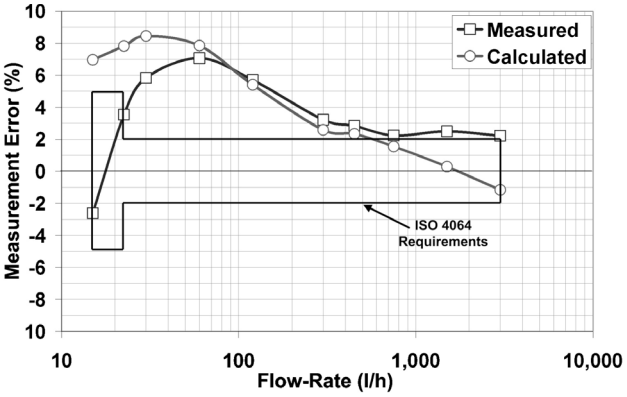


**Fig. 13 Error curve. Measured versus calculated values.**

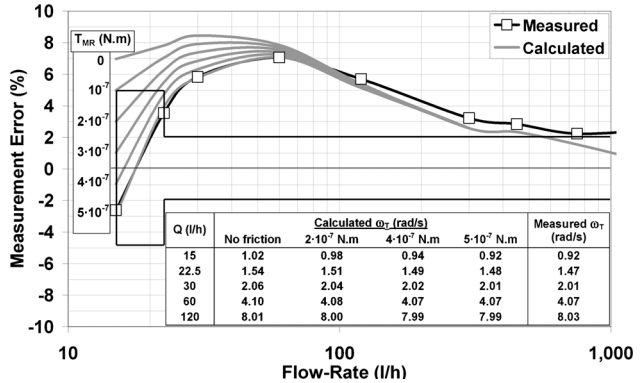


| Q (l/h) | Calculated $\omega_T$ (rad/s) No friction | $2{\cdot}10^{-7}$ N.m | $4{\cdot}10^{-7}$ N.m | $5{\cdot}10^{-7}$ N.m | Measured $\omega_T$ (rad/s) |
|---|---|---|---|---|---|
| 15 | 1.02 | 0.98 | 0.94 | 0.92 | 0.92 |
| 22.5 | 1.54 | 1.51 | 1.49 | 1.48 | 1.47 |
| 30 | 2.06 | 2.04 | 2.02 | 2.01 | 2.01 |
| 60 | 4.10 | 4.08 | 4.07 | 4.07 | 4.07 |
| 120 | 8.01 | 8.00 | 7.99 | 7.99 | 8.03 |

**Fig. 15 Comparison between experimental and calculated values of measurement error and mean rotation speed with different mechanical resistance torques ($T_{MR}$)**

tion are represented. Figure 15 shows the change experienced by the calculated error curve when different constant values of the mechanical resistance torque are considered. The speed reduction produced by this torque implies that less water volume is registered by the meter and therefore makes the measurement error approach, or penetrate deeper into, the negative region. As the value of the torque increases, the calculated error curve tends to reproduce the steep decline observed in the experimental curve and even matches with the latter at a value of $5\times10^{-7}$ N m. These results seem to confirm the initial hypotheses about the magnitude of the mechanical resistance torque and its invariability with the rotation speed of the turbine.

Furthermore, the results obtained in this study could be used by the designers to quantify the effect that a reduction of the mechanical friction would have in the lower part of the error curve. For example, if the related torque is reduced from $5\times10^{-7}$ N m to $2\times10^{-7}$ N m, the measurement error at 15 l/h changes from −3% to +3% and the decline of the error curve is notably minimized.

## 7 Conclusions

The mathematical model developed has allowed a detailed analysis of the performance of a single-jet water meter to be carried out within a wide measuring range, which expanded from 15 l/h to 3000 l/h and included flow rates in laminar, transitional, and turbulent flow regimes. For this end, the simulations of the three dimensional flow within the meter have followed a devised time-marching procedure to resolve the interaction between the flow and the turbine, thus providing the position and the rotation speed as part of the solution. This feature allowed analyzing the error curve of the meter, hence assessing its behavior as a measuring device.

Moreover, the detailed information provided by the simulations made it possible to thoroughly analyze the interaction between the flow and the turbine. This interaction has proven to be very complex since it comprehends the combined effects of the action of the jet over two vanes, the resistance over the remaining vanes that drag water, and the flow exiting from the outlet pipe. The resulting torques exerted by the flow and variable speed of the turbine have been analyzed in detail and have revealed the difficulty of modeling the performance of a single-jet water meter with a simple analytical model. Additionally, the dimensionless torque and rotation speed curves have been presented for different flow rates. In the case of the water meter studied, the changes in these curves as the flow rate varies show different trends depending on the flow regime. The different trends found in the dimensionless rotation speed are directly related to the form of the error curve obtained from the mathematical model.

Three units of the analyzed water meter design have been built and tested in an experimental test rig to validate the mathematical model when the torque produced by the mechanical friction upon the turbine is not considered. The simulated mean values of pressure drop and the turbine's rotation speed have been compared to those experimentally obtained and have been found to be in good agreement. Moreover, the error curve obtained from the mathematical model accurately reproduced the values and the trend of the experimental curve in the range between 120 l/h and 750 l/h, although deviated from it at lower and higher flow rates. These divergences came from different sources. At higher flow rates, the deviation could be related to an insufficient mesh resolution and to the inability of the turbulence model to reproduce the effect of rotation on turbulence. The deviation found at lower flow rates came precisely from the fact that the torque produced by the mechanical friction had been ignored.

When the torque produced by the mechanical friction is taken into account, the trend of the experimental error curve at low flow rates is correctly reproduced by that obtained from the mathematical model. This result has been obtained by undertaking a study in which different constant values of the retarding torque due to the friction have been included in the mathematical model. This study has led to two important conclusions. First, the mean rotation speed of the turbine linearly decreases along the estimated retarding torque value range. Second, it has been confirmed that the effect of mechanical friction is only noticeable at low flow rates (up to 120 l/h in this case). Finally, the study has shown to be valuable for quantifying the effect that an improvement in the mechanical friction would have on the error curve.

To sum up, the present study shows that mathematical modeling and simulation using CFD techniques is a valuable tool for the design of single-jet water meters, even more so if one considers the difficulty of developing a simplified model of their performance and the cost of extracting useful information from the experiments. The encouraging results of this study have led to the application of the proposed methodology in the identification of the most important and influential design parameters, and finally, to produce an optimum design.

## Acknowledgment

This research was carried out with the support of ELSTER Iberconta S.A. and was partially funded by Ministerio de Educación y Ciencia (Spain) through the Programa PROFIT, CIT-020600-2005-023 and by Eusko Jaurlaritza-Gobierno Vasco (Spain) through the Programa SAIOTEK, MERIV002. The authors would like to thank José Bernardo de la Quintana, Jesús Urraca, and David Fuentes for their valuable help. The financial support of Cátedra Fundación Antonio Aranzábal–Universidad de Navarra is gratefully acknowledged.

## Appendix: Relation Between the Mean Rotation Speed of the Turbine and Measurement Error

In the simulations, the error in volume measurement might be calculated as the difference that exists in each period between the actual volume delivered ($V_{\text{actual}}$) and the volume registered by the meter ($V_{\text{regist}}$).

$$\text{Meas. Error} = \frac{V_{\text{regist.}} - V_{\text{actual}}}{V_{\text{actual}}} \tag{A1}$$

However, these volumes are directly related to the calculated and expected turbine's mean rotation speeds, so that the measurement error can be calculated from these values. The relations are shown below.

(1) The actual volume delivered ($V_{\text{actual}}$) equals the time period $T$ times the flow rate established in the simulation.

$$V_{\text{actual}} = TQ \tag{A2}$$

Moreover, the calculated mean rotation speed is related to the time period as

$$T = \frac{2\pi/5}{\bar{\omega}_{T,\text{calc.}}} \tag{A3}$$

Combining Eqs. (A2) and (A3), the relation between the actual volume delivered and the calculated mean rotation speed is found to be

$$V_{\text{actual}} = \frac{2\pi/5}{\bar{\omega}_{T,\text{calc.}}} Q \tag{A4}$$

(2) The volume registered in a period ($V_{\text{regist}}$) is one-fifth of the volume registered in one revolution of the turbine.

$$V_{\text{regist.}} = \frac{1}{5} K^{-1} \tag{A5}$$

Additionally, the expected mean rotation speed is related to the meter factor $K$ as

$$\bar{\omega}_{T,\text{expected}} = 2\pi K Q \tag{A6}$$

Combining Eqs. (A5) and (A6), the relation between the registered volume and the expected mean rotation speed is found to be

$$V_{\text{regist.}} = \frac{2\pi/5}{\bar{\omega}_{T,\text{expected}}} Q \tag{A7}$$

Finally, substitution of Eqs. (A4) and (A7) into Eq. (A1) yields the expression of the measurement error that has been used in the study:

$$\text{Meas. Error} = \frac{\bar{\omega}_{T,\text{calculated}} - \bar{\omega}_{T,\text{expected}}}{\bar{\omega}_{T,\text{expected}}} = \frac{\bar{\Omega}_{\text{calculated}} - \bar{\Omega}_{\text{expected}}}{\bar{\Omega}_{\text{expected}}} \tag{A8}$$

## References


[1] Meinecke, W., 1984, "Measuring Characteristics of Water Meters," Aqua, **4**, pp. 233–237.

[2] Chen, J. S. J., 2000, "On the Design of a Wide Range Mini-flow Paddlewheel Flow Sensor," Sens. Actuators, A, **87**, pp. 1–10.

[3] Buckle, U., Durst, F., Howe, B., and Melling, A., 1992, "Investigation of a Floating Element Flowmeter," Flow Meas. Instrum., **3**, pp. 215–225.

[4] Buckle, U., Durst, F., Kochner, H., and Melling, A., 1995, "Further Investigation of a Floating Element Flowmeter," Flow Meas. Instrum., **6**, pp. 75–78.

[5] Xu, Y., 1992, "Calculation of the Flow Around Turbine Flowmeter Blades," Flow Meas. Instrum., **3**, pp. 25–35.

[6] Xu, Y., 1992, "A Model for the Prediction of Turbine Flowmeter Performance," Flow Meas. Instrum., **3**, pp. 37–43.

[7] Abouri, D., Parry, A., and Hamdouni, A., 2004, "A Stable Fluid Rigid Body Interaction Algorithm: Application to Industrial Problems," *2004 ASME/ISME Pressure Vessels and Piping Conference*, San Diego, CA.

[8] Sánchez, G., and Rivas, A., 2003, "Computational Fluid Dynamics Approach to the Design of a Single-Jet Water-Meter," *Pumps, Electromechanical Devices and Systems Applied to Urban Water Management*, E. Cabrera and E. Cabrera, Jr., eds., Balkema, Lisse, The Netherlands, Vol. 2, pp. 405–413.

[9] Wilcox, D. C., 1998, *Turbulence Modeling for CFD*, DCW Industries, La Canada, CA.

[10] Chen, H. C., and Patel, V. C., 1988, "Near-Wall Turbulence Models for Complex Flows Including Separation," AIAA J., **26**(6), pp. 641–648.

[11] Shih, T.-H., Liou, W. W., Shabbir, A., Yang, Z., and Zhu, J., 1995, "New $k$-$\varepsilon$ Eddy Viscosity Model for High Reynolds Number Turbulents Flows," Comput. Fluids, **24**, pp. 227–238.

[12] Wolfshtein, M., 1969, "The Velocity and Temperature Distribution of One-Dimensional Flow With Turbulence Augmentation and Pressure Gradient," Int. J. Heat Mass Transfer, **12**, pp. 301–318.

[13] Jongen, T., and Marx, Y. P., 1997, "Design of an Unconditionally Stable, Positive Scheme for the $k$-$\varepsilon$ and Two-Layer Turbulence Models," Comput. Fluids, **26**(5), pp. 469–487.

[14] Suzen, Y. B., and Huang, P. G., 2000, "Modeling of Flow Transition Using an Intermittency Transport Equation," ASME J. Fluids Eng., **122**(2), pp. 273–284.

[15] Menter, F. R., Langtry, R. B., Likki, S. R., Suzen, Y. B., Huang, P. G., and Volker, S., 2006, "A Correlation-Based Transition Model Using Local Variables—Part I: Model Formulation," ASME J. Turbomach., **128**(3), pp. 413–422.

[16] Rodi, W., 1991, "Experience With Two-layer Models Combining the $k$-$\varepsilon$ Model With a One-equation Model Near the Wall," AIAA Paper No. 91-0216.

[17] Arregui, F., Cabrera, E. J., Cobacho, R., and García-Serra, J., 2005, "Key Factors Affecting Water Meter Accuracy," Leakage 2005, Halifax, Canada.

[18] Murthy, J. Y., and Mathur, S. R., 1997, "Periodic Flow and Heat Transfer Using Unstructured Meshes," Int. J. Numer. Methods Fluids, **25**, pp. 659–677.

[19] Patankar, S. V., 1980, *Numerical Heat Transfer and Fluid Flow*, Hemisphere, New York.

[20] Barth, T. J., and Jespersen, D., 1989, "The Design and Application of Upwind Schemes on Unstructured Meshes," AIAA Paper No. 89-0366.

[21] Mathur, S., and Murthy, J. Y., 1997, "A Pressure-Based Method for Unstructured Meshes," Numer. Heat Transfer, Part B, **31**(2), pp. 195–215.

[22] Vandoormaal, J. P., and Raithby, G. D., 1984, "Enhancements of the SIMPLE Method for Predicting Incompressible Fluid Flows," Numer. Heat Transfer, **7**, pp. 147–163.

[23] Rhie, C. M., and Chow, W. L., 1983, "Numerical Study of the Turbulent Flow Past an Airfoil With Trailing Edge Separation," AIAA J., **21**(11), pp. 1525–1532.

[24] Mathur, S. R., 1994, "Unsteady Flow Simulations Using Unstructured Sliding Meshes," AIAA Paper No. 94-2333.

[25] Benra, F. K., 2006, "Numerical and Experimental Investigation on the Flow Induced Oscillations of a Single-Blade Pump Impeller," ASME J. Fluids Eng., **128**(4), pp. 783–793.

[26] Le Tallec, P., and Mouro, J., 2001, "Fluid Structure Interaction with Large Structural Displacements," Comput. Methods Appl. Mech. Eng., **190**, pp. 3039–3067.

[27] Celik, I., and Karatekin, O., 1997, "Numerical Experiments on Application of Richardson Extrapolation With Nonuniform Grids," ASME J. Fluids Eng., **119**, pp. 584–590.

[28] White, F. M., 2007, *Fluid Mechanics*, McGraw-Hill, New York.

[29] ISO 4064-1:2005, "Measurement of Water Flow in Fully Charged Closed Conduits—Meters for Cold Potable Water and Hot Water—Part 1: Specifications."

# The Effects of Splitter Plates on Turbulent Boundary Layer on a Long Flat Plate Near the Trailing Edge

**Yoshifumi Jodai**
e-mail: jodai@takamatsu-nct.ac.jp

**Yoshikazu Takahashi**
e-mail: takahasi@takamatsu-nct.ac.jp

Department of Mechanical Engineering,
Takamatsu College of Technology,
761-8058 Takamatsu, Japan

**Masashi Ichimiya**
Department of Mechanical Engineering,
University of Tokushima,
Japan
e-mail: ichimiya@me.tokushima-u.ac.jp

**Hideo Osaka**
Department of Mechanical Engineering,
Yamaguchi University,
Japan
e-mail: ohsaka@po.cc.yamaguchi-u.ac.jp

*An experimental investigation has been made on a turbulent boundary layer near the trailing edge on a long flat plate. The flow was controlled by an additional splitter plate fitted to the trailing edge along the wake centerline. The length of the splitter plate, l, was varied from a half, to five times the trailing edge thickness, h. Measurements of base pressure behind the trailing edge and of mean velocity and pressure distribution in the turbulent boundary layer on the flat plate were made under the freestream zero-pressure gradient. The absolute value of the base pressure coefficient of the long flat plate was considerably smaller than that of the short flat plate without the splitter plate. A significant increase in the base pressure coefficient was achieved with the splitter plate ($l/h \geqq 1$), fitted to the long flat plate. Within an inner layer in the turbulent boundary layer near the trailing edge, the mean velocity increased more than that in the upstream position in the case without the splitter plate. With the splitter plate, however, the base pressure rise made the mean velocity distribution more closely approach that of a fully developed turbulent boundary layer.* [DOI: 10.1115/1.2911683]

*Keywords: flat plate, boundary layer, separation, splitter plate, base pressure*

## 1 Introduction

It has been known that the drag of a bluff body, such as a circular cylinder, depends on the strength of separated vortex (velocity gradient at a boundary layer before separation) affected by the location of the separation point, which is determined by the property of the boundary layer (laminar or turbulent), e.g., Tani [1]. This suggests, therefore, the possibility of upstream boundary-layer control by changing the vortex strength through adjusting base pressure behind the body. As an attempt to this, in the present study, we will investigate the possibility of controlling flow field on a long flat plate owing to the base pressure rise with a splitter plate fitted to the trailing edge of the flat plate. Concerning the boundary-layer control with flow separation at its trailing edge, a method using two dimensional trailing-edge spoilers (Bearman and Trueman [2]) or flaps is not suited to the purpose of our study.

In an important study related to the present study, Bearman [3] used a short flat plate with a $6h$ long (a base height of $h$) and experimentally showed the variation in base pressure on the short flat plate by using a splitter plate fitted to the trailing edge owing to its length $l$. This bluff body model is cited by Apelt and West [4], and we may suppose that the pressure drag is a major contributor to the total drag from reading the related literature (e.g., Schlichting [5]). In a similar work on a circular cylinder with a splitter plate placed along the centerline of the wake, Roshko [6] controlled the vortex formation region behind the cylinder and explained how base pressure rises. In addition, using DNS, Yao and Sandham [7] reported the rise in base pressure coefficient by changing the length of the splitter plate on a flow past the corner of a trailing edge of a flat plate, which has a fully developed turbulent boundary layer, as a result of the flow control. By referring to these results, in contrast to a short flat plate in which the pressure drag plays a major role, by using a long flat plate as in the present study (length of $100h$ and a turbulent boundary layer is formed), investigation of the effects of the base pressure change on the properties of the turbulent boundary layer (such as an influence on skin-friction drag) near the trailing edge will be meaningful. On the other hand, concerning related studies on flow past a backward-facing step, Eaton and Johnston [8] stated that the value of ratio of the boundary-layer thickness at separation to the step height $\delta/h_s$ ($\delta$ as boundary-layer thickness, $h_s$ as step height) is an important parameter, which dictates the flow field (whole separated region) downstream of the step. In addition, Bradshaw and Wong [9] showed that the strength of the perturbation (the fraction of the shear-layer mass flow that is deflected upstream at reattachment), which influences base pressure, can be classified into three categories by the value of $\delta/h_s$. From both results, when the length of the splitter plate $l$ varies at a constant value of $h_s$, the change in $\delta$ on the turbulent boundary layer near the trailing edge or an acceleration (or a deceleration) effect caused by the change of the base pressure is anticipated.

With the above results in mind, the objective of this work is to investigate the properties in the boundary layer near the trailing edge for which the base pressure changes according to the length of the splitter plate, seven types of $l$, fitted to the trailing edge on a long flat plate with a fully developed turbulent boundary layer. The elucidation of the effects of splitter plates mentioned above is expected to improve the stability (e.g., stall) and control of separated vortex on aerofoils at the trailing edge or improve vortex-induced vibration and noise occurring in downstream cascades.

## 2 Experimental Apparatus and Techniques

**2.1 Configuration of Flow Field and Coordinate System.** A wind tunnel of open-circuit type has a 4000-mm-long working section with an inlet area 527-mm-wide × 350 mm spanwise long. A test flat plate 2000 mm long made of polyvinyl chloride (PVC) is vertically set in the centerline of the test section in the front

Contributed by the Fluids Engineering Division of ASME for publication in the JOURNAL OF FLUIDS ENGINEERING. Manuscript received August 29, 2007; final manuscript received January 23, 2008; published online May 1, 2008. Assoc. Editor: James A. Liburdy. Paper presented at the 2007 ASME Fluids Engineering Division Summer Meeting and Exhibition (FEDSM2007), San Diego, CA, July 30–August 2, 2007.

  

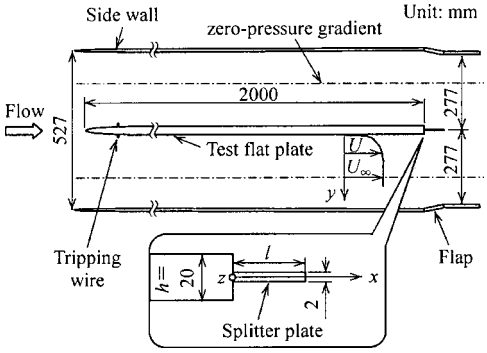


**Fig. 1 Configuration of flow field and coordinate system**

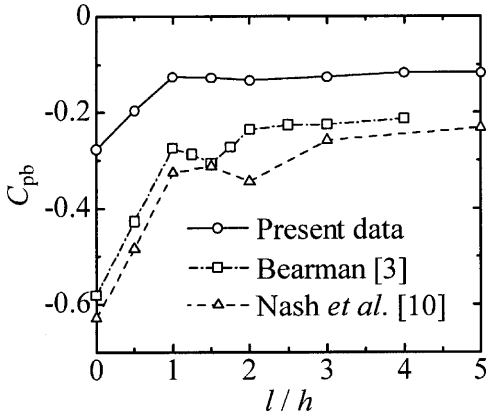


**Fig. 2 Base pressure coefficient. Uncertainty: less than 1% for base pressure ranging from about −40 Pa ($C_{pb}$∼−0.3) to −15 Pa($C_{pb}$∼−0.1).**

position. Figure 1 shows the schematic flow field ($xy$ plane), test flat plate, coordinate system, and nomenclature. The coordinates of $x$ and $y$ are determined as the streamwise distance from the trailing edge and the normal distance from the surface of the test flat plate, respectively. To establish a developed turbulent boundary layer, a trip wire 1 mm in diameter was placed at a downstream distance of 100 mm from the leading edge of the test flat plate. In order to maintain the constant freestream static pressure along the working section, the sidewalls and flaps of the test section were adjusted. Thus, the freestream zero-pressure gradient could be maintained for all experimental conditions. Measurement of the freestream static pressure was conducted with wall static pressure holes (40 holes each) at $y=140$ mm on the lower sidewall, as shown by the dash-dotted line in Fig. 1. At the spanwise center (cross section of $z=0$), experiments were made at unit Reynolds number $U_m/\nu$ of $9.93\times10^5$ m$^{-1}$ ($U_m \fallingdotseq 15$ m/s, $\nu$ as kinematic viscosity) based on the reference velocity, $U_m$. The Reynolds number based on the length of the test flat plate, $R_x = 2U_m/\nu$, is about $2\times10^6$. The turbulent intensity in the freestream is about 0.1%.

**2.2 Splitter Plate.** A splitter plate made of stainless steel is 2 mm thick × 350 mm spanwise long. It is vertically set in the centerline of the test section just behind the trailing edge of the test flat plate. The length of the splitter plate was adjusted $l = 10$ mm, 20 mm, 30 mm, 40 mm, 60 mm, 80 mm and 100 mm ($l/h=0.5-5$, seven types of $l$) in terms of the height of the test flat plate $h$. The base pressure was controlled by changing the length of the splitter plate.

**2.3 Measuring Techniques.** Measurement of the mean velocity was carried out with a single-hot wire probe (a tungsten filament 5 $\mu$m in diameter and 1 mm in sensor length) operated by a constant temperature anemometer. Instantaneous velocity signals were converted into digital data sets with a sampling frequency of 10 kHz for 10 s, and the time-averaged velocity profiles were calculated with a personal computer. Measurement of the static pressure distribution in the boundary layer was conducted with a Pitot static pressure tube 1.06 mm in diameter. Measurements of the velocity and the pressure distribution are executed on the six cross sections of $x/h=-20, -10, -5, -2.5, -0.5, 0$ (trailing edge). Measurement of the base pressure was conducted with a base pressure tube 1.06 mm in diameter with static pressure holes 0.3 mm in diameter made of stainless steel the same as the above mentioned Pitot tube. The base pressure tube was placed just behind the trailing edge of the test flat plate, and the center of the holes was located at a distance of 7 mm in the normal ($y$) direction from the centerline of the flat plate.

The uncertainty in the measurement of the mean velocity was less than 2% for velocities ranging from 4 m/s to 16 m/s and around 5% for lower velocities. The pressure uncertainty was estimated to be less than 1% for base pressure ranging from about −40 Pa to −15 Pa, and around 1% and 4% for boundary-layer pressures −8 Pa and −2 Pa, respectively.

## 3 Results and Discussion

**3.1 Variation in Base Pressure Coefficient.** Figure 2, which contains the data from Bearman [3] and Nash et al. [10], shows the effects of the length of the splitter plate $l/h$ on the base pressure coefficient $C_{pb}$. Without splitter plates ($l/h=0$), the value of $C_{pb}$ in the present data is about −0.28. This is about half of both the value of $C_{pb} \fallingdotseq -0.58$ obtained by Bearman [3] on a short flat plate consisting of a half-ellipse leading edge and the value of $C_{pb} \fallingdotseq -0.63$ obtained by Nash et al. [10] on a short flat plate at 0.4 in Mach number consisting of a single-wedge forebody. This difference in the value of $C_{pb}$ in the case without splitter plates for a long and a short flat plate is important. Furthermore, the value of $C_{pb}$ in the present study is considerably smaller than that of Roshko [6] in a circular cylinder of $C_{pb} \fallingdotseq -0.95$ and those of Apelt and West [4] both in a circular cylinder of $C_{pb} \fallingdotseq -1.2$ and in a normal flat plate of $C_{pb} \fallingdotseq -1.55$ (data not shown). Thus, the role in base pressure change for a long flat plate is different from that for a short flat plate, as mentioned in the Introduction.

$C_{pb}$ in the present study increases depending on the length of the splitter plates used. In particular, the value of $C_{pb}$ remains nearly constant at −0.13 with slight scatters for $1/h \geqq 1$, which achieves a pressure recovery of about 50% compared to that of the case without splitter plates. On the other hand, $C_{pb}$ monotonically increases (pressure recovery) with increasing $l/h$ within the range of $l/h<1$. The above mentioned approximate tendency of the present results can also be seen in the case for a short flat plate in Bearman [3] and Nash et al. [10] with slight scatters, as shown in Fig. 2. The difference in the effects of splitter plates for $l/h<1$ and $l/h \geqq 1$ suggests that the splitter plates differently influence the properties in the upstream boundary layer depending on $l/h$, if we assume that a value of base pressure is a scale that represents the strength of a separated vortex.

Next, we examine the normalized nondimensional base pressure coefficient $C$, and clarify the effects of the installation of splitter plates for a short and a long flat plate, where $C$ is defined by the following:

$$C = \{C_{pb} - (C_{pb})_{\text{without SP}}\}/(C_{pb})_{\text{without SP}} \quad (1)$$

In Eq. (1), the difference from the reference value of $C_{pb}$ in the case without splitter plates (indicated as "without SP") is regarded as the effect of the length of the splitter plate $l/h$.

Figure 3, shows the variation of $C$ along with $l/h$, which also shows the results from Bearman [3] and Nash et al. [10] for a

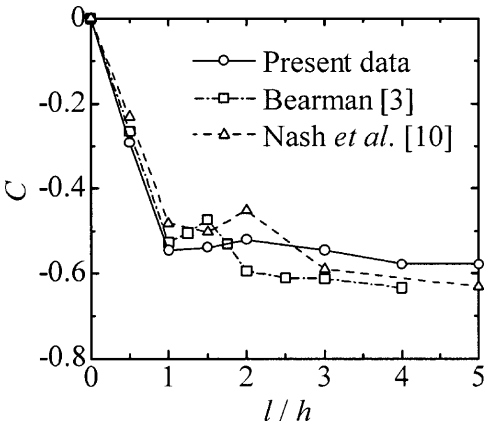


**Fig. 3 Normalized base pressure coefficient**

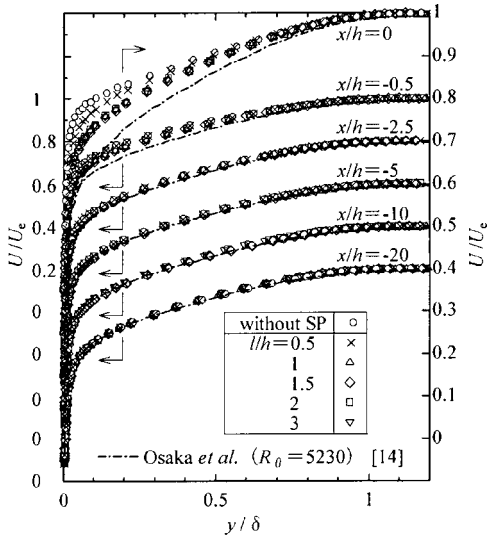


**Fig. 4 Mean velocity profiles. Uncertainty: less than 2% for velocities ranging from 4 m/s to 16 m/s ($U/U_e \fallingdotseq 0.25-1$) and around 5% for lower velocities.**

short flat plate. The results show that for $l/h=0$ (without SP) $C=0$, for $l/h<1$ $C$ rapidly decreases with increasing $l/h$ and for $l/h=1$ $C$ has a minimum value of −0.55. Thereafter, $C$ increases slightly with increasing $l/h$ to the maximum value of −0.52 at $l/h=2$ and beyond $l/h=2$ $C$ slightly decreases with increasing $l/h$ and consequently for $l/h \geqq 4$ $C$ remains constant at −0.58. Although the approximate tendency in $C$ of the present study is similar to that for the results in the short flat plate of Bearman [3] and Nash et al. [10], a detailed comparison shows some differences between them: e.g., $C$ is maximum at $l/h=1.5$ in a short flat plate of Bearman, while $C$ is minimum at $l/h=1.5$ and maximum at $l/h=2$ in the short flat plate of Nash et al. This detailed comparison shows a somewhat different tendency in their results and ours as well.

We will briefly examine why normalized nondimensional base pressure coefficient $C$ changes with $l/h$ and $C$ has a minimum value or a maximum value at certain values of $l/h$. First, as for why $C$ has a maximum value (base pressure coefficient $C_{pb}$ is minimum) in the case without splitter plates ($l/h=0$), we suppose that is due to the occurrence of minimum pressure in a separated bubble, in which the dividing streamline formed from a corner (separation point) of a trailing edge of a flat plate has a maximum curvature (e.g., Tani [11]). Second, as to the decreasing tendency of $C$ when a short splitter plate ($l/h<1$) is placed, we refer to the description by Tombazis and Bearman [12]: "The argument put forward as to why base drag is reduced is that if the vortex formation length can be increased slightly then the volume of fluid in the recirculation region increases and entrainment of a given amount of fluid out of the base into the forming vortices will be unable to sustain such a low pressure," and we consider that the vorticity weakens. Indeed, we confirmed the vortex strength expressed by the minimum pressure value on the wake centerline showed a tendency for vortex formation to be suppressed (minimum pressure is recovered and the position of the low pressure called trough (Nash et al. [10]) is moved downstream) with the splitter plate of $l/h \geqq 1$, and the vortex shedding is weakened with the splitter plate of $l/h>2$ obtained by the preliminary examination. Accordingly, the strength of circulation, i.e., the ratio of the velocity difference to the boundary-layer thickness in the upstream turbulent boundary layer, is considered to decrease compared to the case without splitter plates. This suggests that the increase in base pressure coefficient $C_{pb}$ (decreasing in $C$) is a result of the suppression of the acceleration tendency in the boundary layer, as mentioned later. Last, in the case of $l/h=1$, a position $x_{min}$ where pressure coefficient in a wake center (on the splitter plate surface) has a minimum value is located the most downstream. This implies that the length of the separated vortex increases with increasing $l/h$ below $l/h=1$. On the other hand, when a splitter plate longer than a certain length (e.g., $1/h \geqq 1.5$) is placed, we suppose that the separated vortex does not move much any longer with increasing $l/h$. This suggests the possibility that the variation in vorticity of the separated vortex is also small, and then $C_{pb}$ will be kept nearly constant. Indeed, in the case of $1/h \geqq 1.5$, $x_{min}/h$ was nearly constant at 1.05–1.1 obtained by the preliminary examination. Moreover, in the case of $l/h=2$, the rearmost position of the splitter plate is close to the reattachment point of the dividing streamline of the separated shear layer ($x_r/h=2.4$) obtained by the visualized experiment using a tuft method for the case of $l/h \geqq 3$. Therefore, it is clear that the separated vortex approaches the rearmost position of the splitter plate, as seen in the DNS result of Yao and Sandham [7], possibly by the Coanda effect (e.g., Ref. 13) and $C_{pb}$ slightly decreases ($C$ increases).

**3.2 Mean Velocity Profiles in Boundary Layer Near Trailing Edge of Flat Plate.** In the previous section, it was found that the base pressure coefficient changes depend on the value of $l/h$, and the variation is related to the properties of the upstream boundary layer. Therefore, in this section, we will investigate the characteristics of the mean velocity profiles in the boundary layer near the trailing edge of the flat plate. Figure 4 shows the mean velocity profiles in the boundary layer in the range of $x/h=-20$ to 0, and a comparison is made between the result in the case without splitter plates and that in the case of $l/h=0.5-3$. The mean velocity $U$ on the ordinate and normal distance from the flat plate surface $y$ on the abscissa are nondimensionalized with the local velocity at the boundary-layer edge $U_e$ and the boundary-layer thickness $\delta$, respectively. The results obtained at the trailing edge position of the flat plate are plotted in the double scale, as shown on the right-hand side on the ordinate. In the case without splitter plates, at $x/h=-20$ and −10, the mean velocity profiles are completely kept similar to that in the fully developed turbulent boundary layer on the smooth wall under the zero-pressure gradient in Osaka et al. [14], where the Reynolds number based on the momentum thickness $R_\theta$ for the present study is about 3400 in the velocity profiles at $x/h=-10$. At the downstream position, the velocity profiles in the inner layer (about the region of $y/\delta \leqq 0.2$) of the boundary layer begin to deviate from that of the fully developed turbulent boundary layer under the zero-pressure gradient or start to show a velocity excess (acceleration tendency). At the trailing edge, $x/h=0$, the velocity excess reaches maximum and

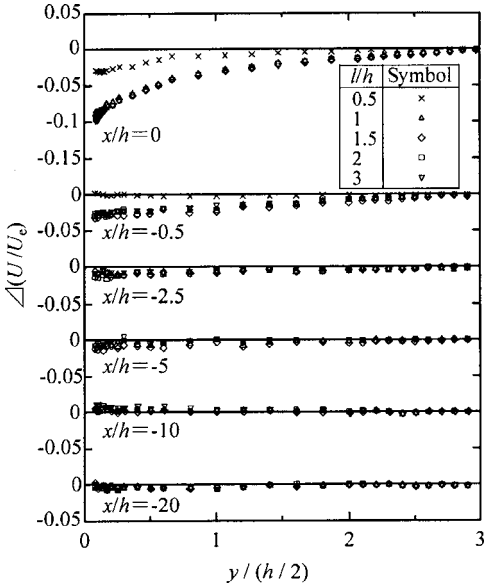


**Fig. 5 Mean velocity excess**

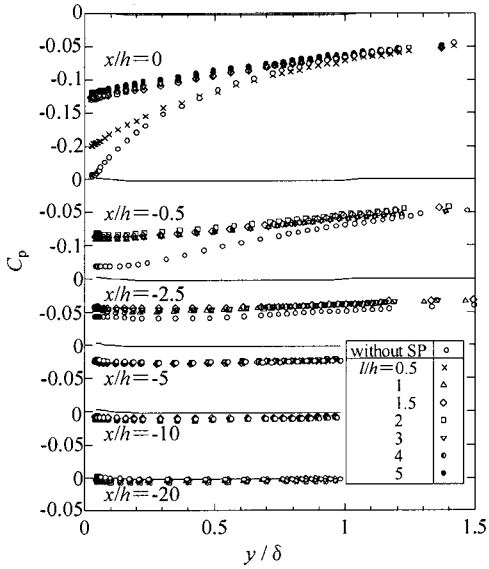


**Fig. 6 Static pressure coefficient. Uncertainty: around 1% and 4% for boundary-layer pressure −8 Pa ($C_p$∼−0.060) and −2 Pa ($C_p$∼−0.015), respectively.**

differences in $U/U_e$ greater than 20% from that in the turbulent boundary layer under the zero-pressure gradient are shown near the wall.

Next, in the case with splitter plates, the velocity profiles at $x/h=-5$ begin to slightly deviate from those in the case without splitter plates, provided the former velocity profiles are almost the same as those of Osaka et al. [14] under the zero-pressure gradient. At the downstream position, with increasing $x/h$ the velocity profiles still start to show the acceleration tendency, which is significant in the inner layer. However, the velocity excess from that under the zero-pressure gradient is smaller than in the case without splitter plates. At the trailing edge of the flat plate, although not readily observable, the greater the length of the splitter plate $l/h$, the smaller the velocity excess. Note the clear difference between the profile in the case of $l/h=0.5$ and that in the case of $l/h \geqq 1$.

Therefore, in order to investigate in detail the effect of the length of the splitter plate on acceleration tendency, the differences in the mean velocity profiles in the case with and without splitter plates $\Delta(U/U_e)$ are shown in Fig. 5, where $\Delta(U/U_e)$ is defined by the following:

$$\Delta(U/U_e) = (U/U_e)_{\text{with SP}} - (U/U_e)_{\text{without SP}} \tag{2}$$

In Eq. (2), $(U/U_e)_{\text{without SP}}$ is the reference value in the case without splitter plates (where condition with splitter plates is indicated as "with SP"). In addition, in order to investigate the normal effective length concerning the acceleration tendency, the abscissa shows as the ratio of the normal distance from the flat plate surface to the half of the height of the flat plate $y/(h/2)$, provided that the value of $l/h$ is in the range of 0.5–3. Since at $x/h=-20$ and −10, within the range of $y/(h/2)<3$, the value of $\Delta(U/U_e)$ is nearly zero, the effects of splitter plates cannot be seen at any distance from the wall. At $x/h=-5$, for $y/(h/2) \leqq 1$, $\Delta(U/U_e)$ has a small negative value, or the velocity is decreased by the installation of the splitter plates compared to the case without them. As $x/h$ increases further downstream, the absolute value of the negative $\Delta(U/U_e)$ increases (the velocity decreases compared to that in the case without splitter plates) and the effective distance from the wall $y/(h/2)$ increases. As for the approximate effect of the length of the splitter plate $l/h$, the greater the $l/h$ is, the greater is the absolute value of the negative $\Delta(U/U_e)$ and the longer the effective distance from the wall. At the trailing edge of the flat plate, $x/h=0$, the splitter plate has a strong effect on velocity profiles, and the velocity excess has negative values over the range beyond $y/(h/2)=2.5$. In addition, the effect of $l/h$ on the value of $\Delta(U/U_e)$ is roughly grouped into the cases of $l/h=0.5$ and $l/h \geqq 1$, and at the closest distance from the wall at the trailing edge of the flat plate for $l/h=0.5$, the value of $\Delta(U/U_e)$ is −0.03, while for $l/h \geqq 1$, the value of $\Delta(U/U_e)$ is −0.1. Moreover, at $x/h=-0.5$ for $l/h=0.5$, the value of $\Delta(U/U_e)$ is nearly zero. Thus, a shorter splitter plate has virtually no influence on the velocity profiles except in the trailing edge position. In this manner, the effect of $l/h$ on the mean velocity profiles is classified into two categories, for the cases of $l/h<1$ and $l/h \geqq 1$. The results agree with the effect of $l/h$ on the base pressure coefficient, as described in Sec. 3.1.

**3.3 Pressure Distribution in Boundary Layer Near Trailing Edge of Flat Plate.** As described in Sec. 3.2, since the installation of the splitter plate results in the suppression effect of the mean velocity excess in the boundary layer near the trailing edge of the flat plate, let us examine the variation of static pressure distribution in the boundary layer accompanied by the change in velocity. Figure 6 shows the variation of static pressure distribution $C_p$ along with the length of the splitter plate $l/h$ within the range of $x/h=-20$ to 0. The solid lines at each $x/h$ location in Fig. 6 indicate the pressure distributions at $x/h=-20$ in the case without splitter plates under the zero-pressure gradient. First, without splitter plates, at $x/h=-20$ over the whole region, both in and out of the boundary layer, $C_p$ is nearly zero and its gradient with respect to $y$ is also zero. Second, at $x/h=-10$ and −5, while keeping $\partial C_p/\partial y \fallingdotseq 0$, $C_p$ has a negative value. As $x/h$ increases further downstream, the value of $C_p$ begins to significantly decrease. At the same time, the tendency of $\partial C_p/\partial y>0$ starts to become stronger. At the trailing edge position of the flat plate, the range where $C_p$ takes a negative value increases to $y/\delta \geqq 1.5$.

With splitter plates, the distribution of $C_p$ is almost the same as that without them in the range between $x/h=-20$ and −5. As $x/h$ increases further downstream, despite the marked decrease in the negative value of $C_p$, the degree of decrease in $C_p$ is smaller than in the case without splitter plates (the static pressure recovers). From comparing the difference in the pressure distribution caused by the change in the length of the splitter plate at $x/h=0$, the effect of $l/h$ on $C_p$ can be roughly classified into two categories: $l/h=0.5$ and $l/h=1-5$. The decreasing $C_p$ in the latter case is

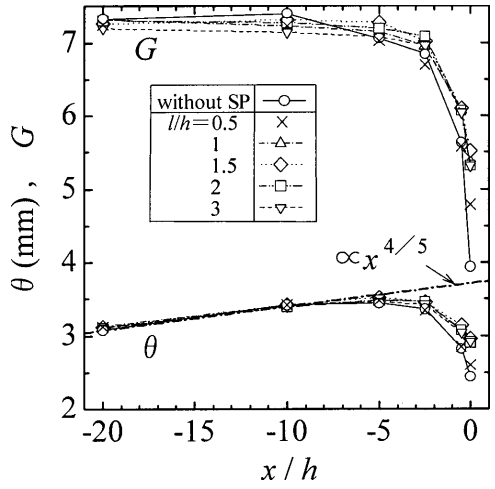


**Fig. 7 Momentum thickness and Clauser's shape parameter**

smaller than in the former case, and the gradient $\partial C_p/\partial y > 0$ is also smaller in the latter case. This corresponds to the findings on the velocity excess tendency in the mean velocity profiles affected by $l/h$.

Next, we investigate the streamwise variation in the value of $C_p$ both at the boundary-layer edge ($y/\delta=1$) and at the height of the inner layer ($y/\delta=0.2$). We then examine the acceleration tendency in the boundary layer. First, for $y/\delta=1$, the value of $C_p$ is negative and its absolute value independently increases downstream of the presence of splitter plates, that is, $\partial C_p/\partial(x/h) < 0$ (favorable pressure gradient), within the range of $x/h=-20$ to 0. Second, even in the height of the inner layer ($y/\delta=0.2$) in the boundary layer, the same tendency is also shown, but the degree of the pressure gradient (absolute value of $\partial C_p/\partial(x/h)$) is larger than in $y/\delta=1$. Accordingly, it is found that as $x/h$ increases further downstream from $x/h=-20$ to the trailing edge of the flat plate, the pressure distribution corresponding to the acceleration tendency is formed. Furthermore, the velocity excess tendency strongly appears in the inner layer.

**3.4 Variation of Properties in Boundary Layer Near Trailing Edge of Flat Plate.** Since the effect of the installation of the splitter plate on the mean velocity profiles was made clear in Sec. 3.2, let us examine the properties in the boundary layer in this section. Figure 7 shows the streamwise variation in momentum thickness $\theta$ and Clauser's shape parameter $G$. First, as for the momentum thickness in the case without splitter plates in the upstream range before $x/h=-10$, $\theta$ increases in proportion to $x^{4/5}$, which is similar to the development of the ordinary turbulent boundary layer (e.g., Osaka et al. [14]). On the other hand, in the downstream range after $x/h=-10$, the development of the boundary layer is suppressed and the rate of increase in $\theta$ decreases. Changes in $\theta$ switch to decrease in the downstream range after $x/h=-5$, after which $\theta$ rapidly decreases as $x/h$ increases toward the trailing edge ($x/h=0$) of the flat plate. In the case with splitter plates in the upstream range before $x/h=-10$, $\theta$ increases in proportion to $x^{4/5}$ just as with the development in the case without splitter plates. Thereafter, the increase of $\theta$ keeps appearing up to $x/h=-5$. Changes in $\theta$ switch to a decrease at $x/h=-2.5$, and the degree of decrease in $\theta$ is smaller than in the case without splitter plates. As $x/h$ increases further downstream to $x/h=0$, $\theta$ remarkably decreases, but the amount of decrease in $\theta$ is still small compared to that in the case without splitter plates. At the trailing edge of the flat plate ($x/h=0$), the amount of decrease in $\theta$ systematically decreases with increasing $l/h$ upon close comparison. In addition, the effect of $l/h$ on $\theta$ approximately falls into two

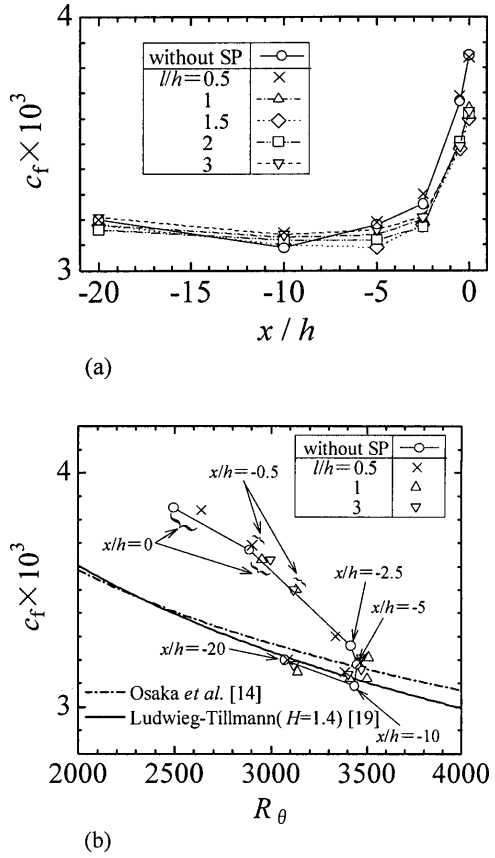


**Fig. 8 Local skin friction coefficient. (*a*) $c_f$ for $x/h$; (*b*) $c_f$ for $R_\theta$.**

categories: $l/h=0.5$ and $l/h \geqq 1$ at $x/h=0$.

Second, let us examine the streamwise variation in Clauser's shape parameter $G$. It was reported that the turbulent boundary layer under zero-pressure gradient takes about 6.8 as the value of $G$ by Clauser [15]. In the case without splitter plates, in the range up to $x/h=-10$, the value of $G$ is about 7.3, which is close to the value of that in the turbulent boundary layer under zero-pressure gradient. Thereafter, the change in $G$ switches to a decrease and at the downstream range after $x/h=-2.5$, it rapidly decreases. At the trailing edge of the flat plate ($x/h=0$), the value of $G$, about 4, indicates a very strong acceleration tendency. While in the case with splitter plates, at the downstream range after $x/h=-20$, the value of $G$ is slightly smaller than in the case without splitter plates and shows a weak decreasing tendency. In the vicinity of $x/h=-7.5$, however, the value of $G$ in the case with splitter plates is switched to have a larger value than in the case without splitter plates. At the further downstream position of $x/h=-2.5$, although the value of $G$ rapidly decreases, it is larger than in the case without splitter plates. Moreover, at the trailing edge of the flat plate ($x/h=0$), the value of $G$ differs depending on the value of $l/h$: the larger the $l/h$, the larger the $G$ by comparison. In addition, the effect of $l/h$ on $G$ approximately falls into two categories: $l/h=0.5$ and $l/h \geqq 1$ at $x/h=0$.

Third, let us examine the wall region near the trailing edge of the flat plate by the distribution of local skin friction coefficient $c_f$ to clarify the effects of splitter plates. Figure 8($a$) shows the streamwise variation in $c_f$. As described above, there exists a strong favorable pressure gradient in the boundary layer near the trailing edge (but not in freestream, $y/\delta \fallingdotseq 5$, as described in Sec. 2.1) of the flat plate in the flow field in the present study, which makes it difficult to obtain a precise $c_f$ value as seen in the report by Patel [16]. Hence, in the present study, the value of $c_f$ is obtained by the method using the Clauser chart [17] and a method

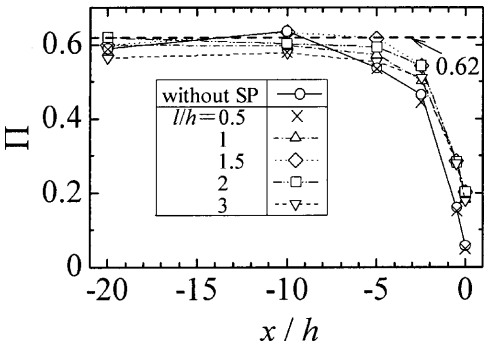


**Fig. 9 Wake parameter**

using the velocity gradient in the region near the wall (e.g., Ref. [18]). In the case without splitter plates, $c_f$ at $x/h=-20$ and $-10$ approximately take the same value as in the turbulent boundary layer under zero-pressure gradient according to Osaka et al. [14]. As $x/h$ increases further downstream, the local skin friction coefficient deviates upward from the distribution of Osaka et al. [14] with the velocity excess (acceleration tendency) in the inner layer gradually increasing. Approaching the trailing edge of the flat plate, the value of $c_f$ rapidly increases, thereafter increasing more than 25% from $c_f$ at $x/h=-10$ at the trailing edge. In the case with splitter plates, on the other hand, the value of $c_f$ is similar to that in the turbulent boundary layer under the zero-pressure gradient ($c_f$ continues to decrease) up to $x/h=-5$. In the vicinity of $x/h=-7.5$, however, the value of $c_f$ in the case with splitter plates switches to a smaller value than without splitter plates. Further downstream of $x/h=-5$, although the value of $c_f$ rapidly increases, the amount of increase in $c_f$ is smaller than in the case without splitter plates. At $x/h=0$, the effect of $l/h$ on $c_f$ may also be approximately classified into two categories: $l/h=0.5$ and $l/h \geqq 1$.

Figure 8($b$) shows the relation between $c_f$ and $R_\theta$. Variation of $c_f$ in the turbulent boundary layer under the zero-pressure gradient has been examined by many authors in detail, and reliable equations have been obtained. By comparing these equations and our results, it is possible to discuss in general the effect of the pressure gradient in the present study. The dash-dotted and solid lines in Fig. 8($b$) represent the equation from Osaka et al. [14] and the equation from Ludwieg and Tillmann [19] (at a constant shape factor of $H=1.4$), respectively, in the developed turbulent boundary layer. In the cases without splitter plates (until $x/h=-10$) and with splitter plates of $l/h \geqq 1$ (until $x/h=-5$), $c_f$ decreases as $R_\theta$ increases the same as in ordinary boundary-layer development. After that, changes in $c_f$ remarkably switched to increase with increasing $x/h$. As $x/h$ increases further downstream, $R_\theta$ decreases and $c_f$ conversely increases as a result of acceleration near the trailing edge. At that time, because the significant effect of the favorable pressure gradient, $c_f$ increases not along with the ordinary developed turbulent boundary-layer equations but deviates upward from that predicted by the equations.

Last, we investigate the wake parameter $\Pi$, which is closely associated with the variation of mean velocity profile in the outer layer. The value of $\Pi$ is a criterion that indicates the degree of mean velocity deviation from the log law formed in the inner layer caused by external force (e.g., pressure gradient) acting in the outer layer. Figure 9 shows streamwise variation in $\Pi$. In the case without splitter plates, at $x/h=-20$ and $-10$, the value of $\Pi$ is within the range of 0.6 and 0.62. This signifies the good two dimensionality of the present flow fields similar to the well-achieved turbulent boundary layer under zero-pressure gradient of Osaka et al. [14]. Further downstream of $x/h=-10$, approaching the trailing edge of the flat plate, the value of $\Pi$ remarkably decreases corresponding to the variation of $\theta$, $G$, and $c_f$. At the trailing edge of the flat plate ($x/h=0$), the value of $\Pi$ decreased to 0.05, indicating the pronounced acceleration tendency. However, in the case with splitter plates, the value of $\Pi$ remains nearly constant, which is similar to that in the turbulent boundary layer under zero-pressure gradient, with slight scatters for up to $x/h=-5$. At the downstream position, although the value of $\Pi$ decreases, the amount of decrease in $\Pi$ is smaller than in the case without splitter plates. At the trailing edge of the flat plate ($x/h=0$), the effect of $l/h$ on $\Pi$ is also classified into two groups: $l/h=0.5$ and $l/h \geqq 1$.

## 4 Conclusions

We studied the effects of splitter plates on a turbulent boundary layer near the trailing edge on a long flat plate. An experimental investigation was made under the freestream zero-pressure gradient. We conclude the following:

(1) Without the splitter plate ($l/h=0$), the absolute value of the base pressure coefficient of the long flat plate is considerably smaller than that of the short flat plate (bluff body).
(2) The presence of a short splitter plate with less than the flat plate thickness ($l/h<1$) shows a rapid pressure rise. A significant increase in the base pressure coefficient (about 50% the same as for short flat plate) is achieved with a long splitter plate ($l/h \geqq 1$) fitted to the long flat plate. A tendency for the base pressure to change with the length of the splitter plate is discussed in terms of the vortex structure expected behind the long flat plate.
(3) Within an inner layer ($y/\delta \leqq 0.2$) in the turbulent boundary layer within the range from the trailing edge ($x/h=0$) to the $x/h$ of about $-10$, the mean velocity increases more than in the upstream position in the case without the splitter plate. With the splitter plate, however, the base pressure rise makes the mean velocity distribution closer approach that of a fully developed turbulent boundary layer. In this case, the affected range of acceleration decreases from $10h$ upstream of the trailing edge without the splitter plate to $5h$ upstream. The effects of splitter plates on the mean velocity profiles are classified into two categories according to the length of the splitter plate: the velocity excess within an inner layer is slightly suppressed in the case of $l/h<1$, and the excess is appreciably suppressed in the case of $l/h \geqq 1$.
(4) The splitter plate of $l/h \geqq 1$ also has a strong effect on the values of the momentum thickness, Clauser's shape parameter, the local skin friction coefficient, and the wake parameter. Like the velocity excess range, the affected range in these properties in the turbulent boundary layer decreases to $5h$ upstream of the trailing edge with the splitter plate.

## Acknowledgment

The experiment of the present work was conducted at Takamatsu College of Technology, and the assistance provided by the students of the Department of Mechanical Engineering is gratefully acknowledged. The authors also appreciate the suggestions of Professor Shinsuke Mochizuki of the Department of Mechanical Engineering at Yamaguchi University.

## Nomenclature

$C_p$ = static pressure coefficient=$(p_s-p_0)/(\rho U_e^2/2)$
$C_{pb}$ = base pressure coefficient=$(p_b-p_0)/(\rho U_m^2/2)$
$c_f$ = local skin friction coefficient
$G$ = Clauser's shape parameter
$h$ = height of flat plate (=20 mm)
$l$ = length of splitter plate
$p_b$ = base pressure (=pressure behind flat plate)
$p_s$ = local static pressure in boundary layer
$p_0$ = atmospheric pressure

$U$ = local streamwise mean velocity
$U_e$ = local velocity at boundary-layer edge
$U_m$ = reference velocity (at $x=-1000$ mm, $y=140$ mm)
$x$ = streamwise distance from trailing edge
$y$ = normal distance from plate surface
$z$ = spanwise distance from plate center
$\delta$ = boundary-layer thickness (defined by $U/U_e=0.995$)
$\theta$ = momentum thickness
$\Pi$ = wake parameter
$\rho$ = air density

## References


[1] Tani, I., 1967, *Fluid Flows*, Iwanami, Tokyo, Chaps. 6 and 7.
[2] Bearman, P. W., and Trueman, D. M., 1972, "An Investigation of the Flow Around Rectangular Cylinders," Aeronaut. Q., **23**, pp. 229–237.
[3] Bearman, P. W., 1965, "Investigation of the Flow Behind a Two-Dimensional Model With a Blunt Trailing Edge and Fitted With Splitter Plates," J. Fluid Mech., **21**(2), pp. 241–255.
[4] Apelt, C. J., and West, G. S., 1975, "The Effects of Wake Splitter Plates on Bluff-Body Flow in the Range $10^4<R<5\times10^4$. Part, 2," J. Fluid Mech., **71**(1), pp. 145–160.
[5] Schlichting, H., 1979, *Boundary-Layer Theory*, McGraw-Hill, New York, Chaps. 23 and 25.
[6] Roshko, A., 1954, "On the Drag and Shedding Frequency of Two-Dimensional Bluff Bodies," NACA Technical Note 3169, pp. 1–29.
[7] Yao, Y. F., and Sandham, N. D., 2002, "Direct Numerical Simulation of Turbulent Trailing-Edge Flow With Base Flow Control," AIAA J., **40**(9), pp. 1708–1716.
[8] Eaton, J. K., and Johnston, J. P., 1981, "A Review of Research on Subsonic Turbulent Flow Reattachment," AIAA J., **19**(9), pp. 1093–1100.
[9] Bradshaw, P., and Wong, F. Y. F., 1972, "The Reattachment and Relaxation of a Turbulent Shear Layer," J. Fluid Mech., **52**(1), pp. 113–135.
[10] Nash, J. F., Quincey, V. G., and Callinan, J., 1963, "Experiments on Two-Dimensional Base Flow at Subsonic and Transonic Speeds," Aeronaut. Res. Council Reports and Memoranda (Great Britain), **3427**, pp. 1–61.
[11] 1984, *Progress in Fluid Mechanics Boundary-Layer*, I. Tani, ed., Maruzen, Tokyo, Chap. 4.
[12] Tombazis, N., and Bearman, P. W., 1997, "A Study of Three-Dimensional Aspects of Vortex Shedding From a Bluff-Body With a Mild Geometric Disturbance," J. Fluid Mech., **330**, pp. 85–112.
[13] Schlichting, H., 1979, *Boundary-Layer Theory*, McGraw-Hill, New York, Chap. 24.
[14] Osaka, H., Kameda, T., and Mochizuki, S., 1998, "Re-examination of the Reynolds-Number-Effect on the Mean Flow Quantities in a Smooth Wall Turbulent Boundary Layer," JSME Int. J., Ser. B, **41**(1), pp. 123–129.
[15] Clauser, F. H., 1956, "The Turbulent Boundary Layer," Adv. Appl. Mech., **4**, pp. 1–51.
[16] Patel, V. C., 1965, "Calibration of the Preston Tube and Limitations on its Use in Pressure Gradients," J. Fluid Mech., **23**(1), pp. 185–208.
[17] Clauser, F. H., 1954, "Turbulent Boundary Layers in Adverse Pressure Gradients," J. Aeronaut. Sci., **21**, pp. 91–108.
[18] 1986, *JSME Data Book: Flow Measurements*, The Japan Society of Mechanical Engineers ed., The Japan Society of Mechanical Engineers, Tokyo, Chap. 3.
[19] Ludwieg, H., and Tillmann, W., 1950, "Investigations of the Wall-Shearing Stress in Turbulent Boundary Layers," NACA TM 1285, pp. 1–25.

# Numerical Simulation for Vortex Structure in a Turbopump Inducer: Close Relationship With Appearance of Cavitation Instabilities

**Toshiya Kimura**
e-mail: kimura.toshiya@jaxa.jp

**Yoshiki Yoshida**
e-mail: yoshida.yoshiki@jaxa.jp

**Tomoyuki Hashimoto**
e-mail: hashimoto.tomoyuki@jaxa.jp

**Mitsuru Shimagaki**
e-mail: shimagaki.mitsuru@jaxa.jp

Japan Aerospace Exploration Agency,
Kakuda Space Center,
Kakuda,
Miyagi 981-1525, Japan

*Unsteady cavitation phenomena such as rotating cavitation and cavitation surge are often observed in a turbopump inducer of a rocket engine, sometimes causing undesirable oscillation of the system. Investigation of their mechanism and prediction of such unsteady phenomena are, therefore, crucial in the design of inducers. As many experiments have shown, the appearance of cavitation instability is highly related to the flow rate as well as to the inlet casing geometry. Experimental observations have shown that a very complex flow structure, including such phenomena as backflow and vortices, appears upstream of the inducer. In this work, therefore, we conducted 3D unsteady computational fluid dynamics simulations of noncavitating flow in a turbopump inducer, mainly focusing on the vortex structure, for three types of inlet casing geometry with various flow rates. Simulation results showed that the vortex structure for the geometry of the inlet casing and that for the flow rate differed. Especially, it was found that development of the tip leakage vortex was dependent on the inlet casing geometry and the flow rate. This tendency is analogous to that observed between the appearance of rotating cavitation and the casing geometry and flow rate in cavitation tunnel tests. This result strongly implies that the tip leakage vortex is responsible for the appearance of rotating cavitation. By adding a gutter to the inlet casing, it was found that backflow was completely confined to the gutter regardless of flow rates. This numerical result implies that the volume of cavity generated in the backflow region should be stable despite a change of the flow rate, resulting in the suppression of increase of the mass flow gain factor. This result also supports the experimental result that cavitation surge was effectively suppressed using such a casing with a gutter.* [DOI: 10.1115/1.2911678]

*Keywords: CFD, inducer, vortex structure, rotating cavitation, cavitation surge*

## Introduction

An inducer is a key component, which improves suction performance of rocket engine turbopumps. Turbopumps operate at high rotational speed to allow minimization of their size and weight and with low inlet pressure to realize reduction of the weight of a rocket. Hence, an inducer is operated under conditions susceptible to cavitation. Undesirable oscillations caused by unsteady cavitation phenomena are important problems faced in the design of turbopumps [1–3]. One of the major causes of shaft vibrations is a phenomenon known as "rotating cavitation," which generally occurs at cavitation numbers a few times larger than the breakdown value. During rotating cavitation, the cavity is unevenly (nonaxisymetrically) distributed on each blade and propagates blade to blade with a propagation speed slightly greater than that of the inducer [4,5]. It is sometimes called "supersynchronized rotating cavitation."

Kamijo et al. [6] showed that supersynchronous vibration, i.e., rotating cavitation, was almost completely extinguished by modifying the inducer casing just upstream of the inducer. In the modification, when the radius of the casing upstream of the inducer was enlarged so as to be lager than that of the inducer plus the tip clearance, rotating cavitation was effectively suppressed.

The effect of the casing geometry on cavitation instabilities has been extensively studied by Hashimoto et al. [7]. They conducted experiments using a cavitation tunnel, in which seven different types of inducer casing were tested for various flow rates, and examined the occurrence of cavitation instability for these casing geometries and flow rates. They found that cavitation instability could be more effectively suppressed for the casing with a larger step at the inlet, even though there was optimum step geometry, and for lower flow rates.

Shimagaki et al. [8] examined the effect of the inlet casing geometry on unsteady cavitation for two types of casing. They used transparent casings to visualize the flow pattern with a high-speed camera and the particle image velocimetry (PIV) method. They observed that the flow patterns were different for these casings and that supersynchronous rotating cavitation was suppressed using a casing with a step.

Another example in which the inducer casing geometry affects the occurrence of cavitation instability was presented in the report of Tomaru, et al. [9]. They showed experimentally that cavitation surge was effectively suppressed by making a small gutter at the inlet casing. They concluded that the volume change of the cavity in backflow vortices due to the change of flow rate was reduced by trapping of the backflow in the gutter, cavitation surge being suppressed as a result.

Upstream of the inducer, very complex flow structures are fre-

Contributed by the Fluids Engineering Division of ASME for publication in the JOURNAL OF FLUIDS ENGINEERING. Manuscript received December 18, 2006; final manuscript received December 17, 2007; published online May 5, 2008. Assoc. Editor: Steven Ceccio.

  

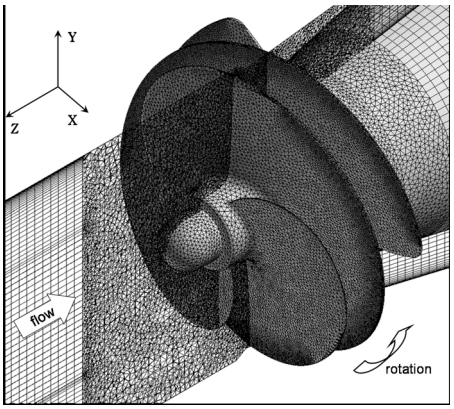


**Fig. 1 Computational grid around inducer**

quently observed. Since the fluid is pressurized by the inducer and a positive pressure gradient occurs at the inducer inlet, leakage flow occurs through the tip clearance between the tip end and the casing. This tip leakage flow results in generation of backflow along the casing, which then travels to the region upstream of the inducer. Typical vortex structures are sometimes observed to be associated with the backflow structure. One is a backflow vortex, which emerges in the shear region between the main flow and the backflow. It extends nearly parallel to the rotational axis of the inducer. The other is a tip leakage vortex, which is generated near the leading edge of the tip end of a blade and develops downstream along the blade. Interacting with cavitation, these complex flow structures are thought to trigger cavitation instabilities often observed in actual inducers.

Although it is difficult to observe these flow structures in detail in experiments, computational fluid dynamics (CFD) is one of the best tools to examine complex flow structure. In our previous study [10], CFD simulations were performed for a turbopump inducer to simulate experiments conducted at Kakuda Space Center of Japan Aerospace Exploration Agency (JAXA).

It was found that the flow structure, including vortices and backflow, was strongly affected by a slight modification of the inlet geometry of the casing and the flow rate [10]. That work was based on steady state simulations. However, the backflow and the vortex structures are essentially unsteady phenomena. In the present simulation, therefore, we performed unsteady simulations for casings with different types of geometry with several flow rates, corresponding to what had been done in the cavitation tunnel experiments [8,9].

In the present work, we focus mainly on the vortex structure and discuss the relation between the vortex and the appearance of cavitation instabilities. We will show that there is a clear relationship between development of vortices and appearance of cavitation instabilities. Especially, the tip leakage vortex is responsible to the occurrence of the rotating cavitation.

## Numerical Simulation

**Numerical Model.** The inducer modeled in the present simulation was designed for a liquid oxygen turbopump and used in the cavitation tunnel test at Kakuda Space Center of JAXA. The flow coefficient at the design point, the inlet incident angle, and the tip solidity are 0.0775, 3.3 deg, and 1.91, respectively (see also Ref. [11]). From the computer aided design (CAD) data of the inducer, a numerical grid was created. Figure 1 shows the grid structure around the inducer. The grid cells consist of tetrahedral and prismatic cells around the inducer and hexahedral cells in the upstream and downstream pipes. Calculations were performed with the number of cells being changed from about $1\times10^6$ to about $5\times10^6$, and the results were compared. With a larger number of cells, the flow structure became clearer and the computational cost

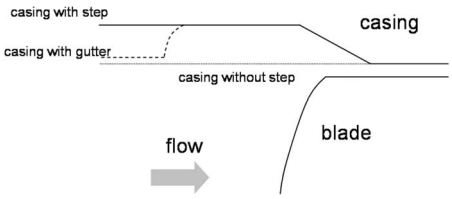


**Fig. 2 Three types of casing geometries: the casing with a step (solid line), the casing without a step (dotted line), and the casing with a gutter (dashed line)**

higher. However, since no distinct difference in the overall flow structure was found, a grid with $3.2\times10^6$ cells was used throughout the present simulations.

In the present simulations, three types of casing were used, namely, casings without a step, with a step, and with a gutter. Figure 2 shows a schematic diagram for these casing geometries in the axisymmetrical plane. The dotted line shows the outline of the casing without a step (straight casing) and the solid line represents the outline of the casing with a step. The height of the step is five times greater than the tip clearance. The dashed line shows the outline of the casing with a gutter.

The experiment was conducted in the cavitation tunnel using water and the rotation speed of the inducer was 6000 rpm. Hence, in the simulation, the same rotating speed was used and the fluid was assumed to be water. The Reynolds number of the typical case presented here is approximately $6\times10^6$.

**Numerical Method.** The simulation code used here is STAR-CD, a commercial code for thermofluid dynamic simulations, which has been developed and is produced by Computational Dynamics Ltd. [12]. The basic equations are the continuity equation of mass and the Navier–Stokes equation. The differential scheme is the second order monotone advection and reconstruction scheme (MARS), which is the original scheme of STAR-CD. In our previous simulations for this type of inducer, several types of *k-e* turbulence models with a wall function were used and compared. The overall flow structure with such phenomena as vortices and backflow was less affected. The development of the backflow region showed some difference according to the turbulence model. Hence, based on comparison with the water tunnel experiments on the development of backflow, we adopted the present type of turbulence model [13] and used it in our simulations.

At the inlet boundary, a uniform flow condition, constant pressure and flow rate were given. The flow rate was varied from 90% to 120% of the design flow rate. The zeroth order outflow condition was given at the outlet boundary. The inlet and the outlet boundaries were placed upstream and downstream nearly three times the diameter of the inducer. Calculation was performed in the rotating frame with an inducer rotation speed of 6000 rpm. Hence, the walls of the inducer and the hub were treated as stationary nonslip walls and the wall of the casing was treated as a moving wall rotating in the opposite direction.

We performed a steady state calculation for each case, and then an unsteady calculation was performed with the steady state flow field as an initial condition. The typical flow structure around an inducer is characterized by a backflow region and vortices. The backflow region is created by leakage flow from a tip clearance. The leakage flow swirls with the inducer with slower angular velocity. Since the main flow does not rotate, vortices are created in the interface region between the main flow and the backflow. Hence, such vortices, so-called backflow vortices, also rotate with the backflow region with slower rotating velocity than that of the inducer.

In steady state simulations, although the global flow structure was calculated, essentially unsteady phenomena such as backflow vortices were not necessarily reproduced. In the present work,

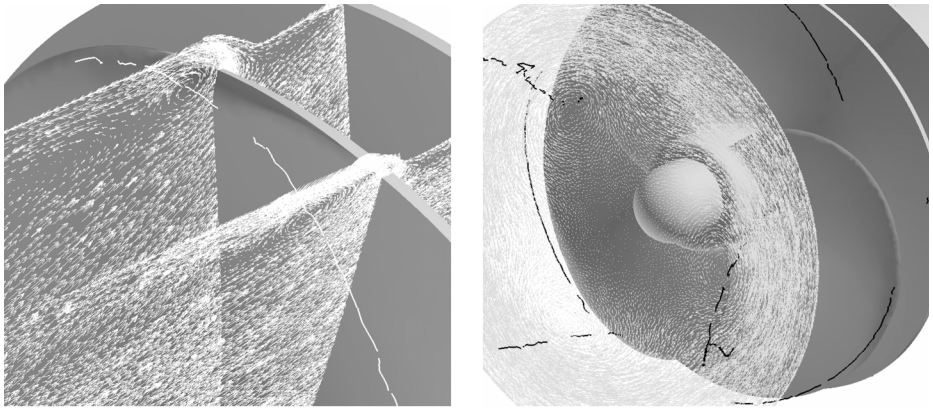

(*a*) (*b*)

**Fig. 3 Velocity distribution and vortex core lines. (*a*) shows the tip leakage vortex, which emerges near the tip end. White thick lines and arrows represent vortex core lines and velocity vectors, respectively. (*b*) shows backflow vortices (black thick lines) and velocity distribution (white arrows) on the plane normal to the rotational axis.**

therefore, unsteady simulations were performed for all cases, and the flow fields after a sufficient number of rotations were compared.

## Calculated Results

First, we conducted simulations for a casing with and one without a step at the inlet. The step geometry is the same one as used in a previous cavitation tunnel test conducted at Kakuda Space Center [8]. Second, calculations for the casing with a gutter were performed. A tunnel test with the same casing had previously been performed at IHI Corporation [9].

Tip leakage flow occurs due to the pressure gradient through the clearance, and then it rolls up just upstream of the tip, resulting in generation of a vortex, i.e., a tip leakage vortex, along the blade (Fig. 3(*a*)). The leakage flow develops a backflow region upstream along the casing. This leakage flow swirls due to the rotation of the inducer, but the main flow does not. Hence, in the shear region between the swirling backflow and the main flow, vortices, namely, backflow vortices, are generated and grow as the backflow region develops (Fig. 3(*b*)).

**Flow Field for the Casing With a Step.** Figure 4 shows the flow structure around the inducer for the casing with a step for different flow rates: Fig. 4(*a*) for $Q/Qd=0.9$, Fig. 4(*b*) for 1.0, Fig. 4(*c*) for 1.1, and Fig. 4(*d*) for 1.2, respectively. In the plane which includes the rotational axis of the inducer, the distribution of the velocity component in the direction of the rotational axis is shown. The positive direction corresponds to the upstream velocity component. The brightest region, therefore, represents the backflow region (i.e., positive axial velocity). The legend shown in the left-bottom corner in each figure shows the velocity scale (m) in the axis direction and the negative value means the main flow direction (left to right in the figure). Thick red lines plot the vortex cores, and thus these lines represent the distribution of vortices. These vortex lines were plotted using a commercial software for postprocessing of CFD data [14], which uses the eigenmode analysis to identify vortex cores [15]. Since the plane plotting the axial velocity distribution is transparent, vortex lines beyond the plane, which are slightly darkened, are also seen.

The backflow region becomes larger and thicker upstream of the inducer as the flow rate decreases. When the backflow region develops, the backflow vortex also develops. For higher flow rates, the backflow rapidly decreases. The backflow vortex also weakens, but the tip vortex develops.

For the case of the lowest flow rate (90% of nominal) in Fig. 4(*a*), the backflow region develops more than one radius, accompanied by long and distinct backflow vortices. There are actually three major backflow vortices, which rotate with slower rotational speed than that of the inducer. Tip vortices also develop, but they are short and end before reaching the next blade. Backflow vortices and tip vortices seem to interact with one another. The positions of tip vortices remain relatively unchanged during rotation of the inducer. However, their length varies with rotations of backflow vortices as if they are interacting with one another.

For a nominal flow rate (Fig. 4(*b*)), the backflow region still develops to nearly one radius upstream and backflow vortices emerge. Tip vortices are also observed but are as short as those in the case of lower flow rates. The evolution of backflow and tip vortices is almost the same as that observed in the case of a 90% flow rate, backflow vortices rotate at a slower rotation speed than that of the inducer, and the length of tip vortices changes at almost the same position.

With higher flow rates of 110% (Fig. 4(*c*)) and 120% (Fig. 4(*d*)), the backflow region further decreases and the large-scale backflow vortices almost disappear. On the other hand, the tip vortices show a remarkable development in Fig. 4(*c*), growing much longer than those in cases of lower flow rates. They grow and develop over the suction side of the next blade.

For the case of highest flow rate case (Fig. 4(*d*)), the tip vortices cannot extend in the upstream direction because backflow is strongly reduced. They extend into the interblade region and disappear near the throat.

**Flow Field for the Casing Without a Step.** Three cases with different flow rates for the straight casing (without a step) are shown in Fig. 5: $Q/Qd=0.9$ in Fig. 5(*a*), 1.0 in Fig. 5(*b*), and 1.1 in Fig. 5(*c*), respectively. The development of the backflow region strongly depends on the flow rate as observed in the cases of the casing with a step. The lower the flow rate is, the larger the backflow region becomes. However, the development of the backflow is much weaker than that in the casing with a step.

With the low flow rate of 90% (Fig. 5(*a*)), the backflow develops similarly to the case of a flow rate of 100% in the casing with a step (Fig. 4(*b*)) and backflow vortices are observed. However, these backflow vortices are much shorter than those seen in Fig. 4(*b*) and more vortices emerge. This difference seems to be due to the difference of structure of the backflow region.

In the casing of a step with 90% and 100% flow rates, the backflow shows a nonaxisymmetrical structure with nearly three periods in the circumferential direction and three major backflow vortices emerge as a result. In the straight casing (Fig. 5(*a*)), the length of the backflow region is similar to that seen in Fig. 4(*b*),

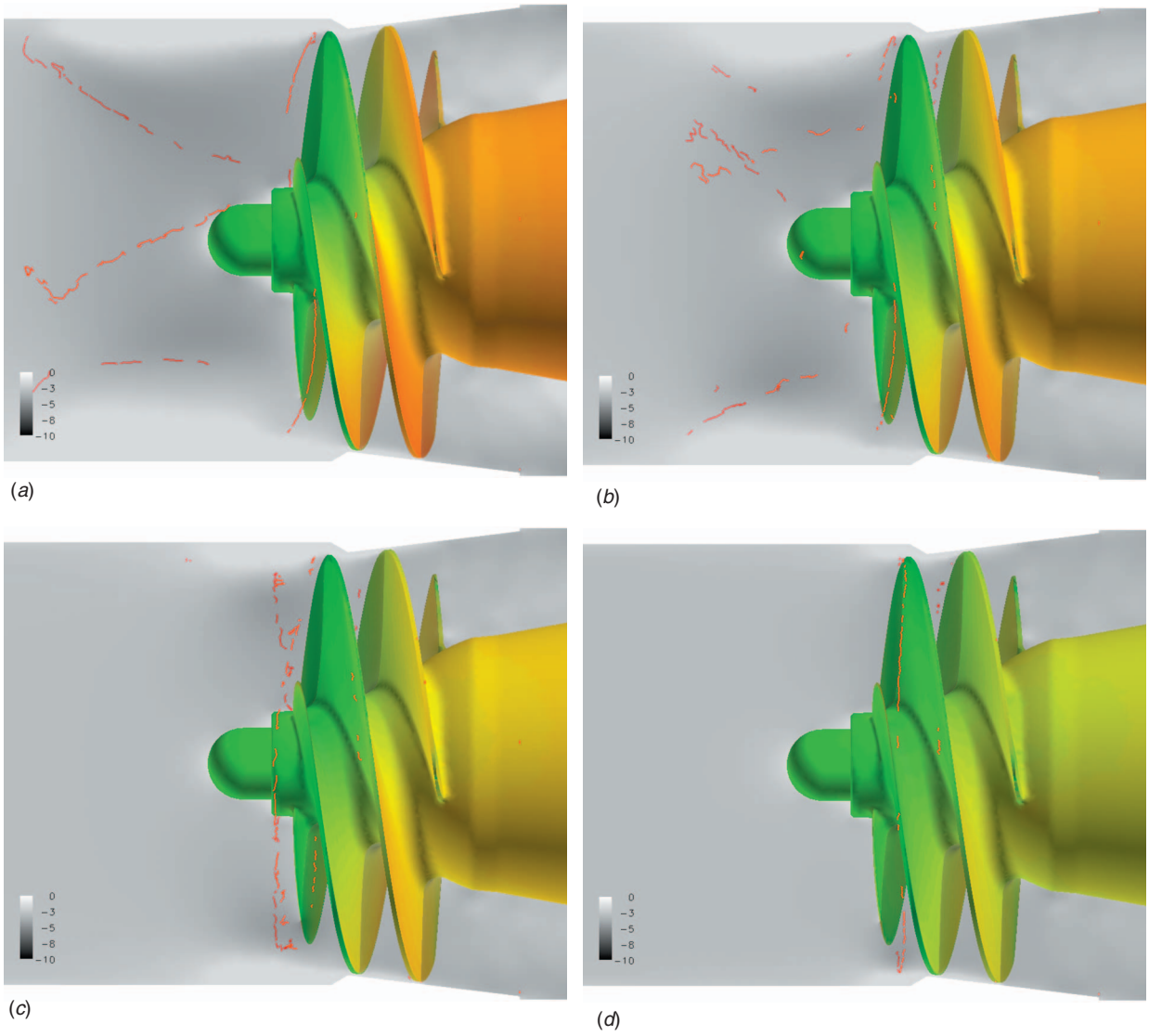


**Fig. 4 Distribution of the axial velocity component is plotted on the plane, which includes the rotation axis by a gray scale contour map. The brightest area represents the region with positive velocity, i.e., the backflow region. Thick red lines show vortex cores. The surface of the inducer is colored to show pressure. These figures show the results for the casing with a step with four different flow rates: (*a*) *Q*/*Qd*=0.9, (*b*) *Q*/*Qd*=1.0, (*c*) *Q*/*Qd*=1.1, and (*d*) *Q*/*Qd*=1.2.**

but the structure of the backflow is much smoother and axisymmetrical. Hence, at the interface region between the backflow and the main flow, many small-scale vortices appear.

Tip leakage vortices are also seen but are too short to reach the next blade. These tip vortices develop in almost the same position, and the fluctuation of their length with time is quite small compared with the cases for the casing with a step. This is also due to the axisymmetrical structure of the backflow region and axisymmetrical distribution of backflow vortices.

For higher flow rates (Figs. 5(*b*) and 5(*c*)), the backflow region becomes smaller and a tip leakage vortex develops. The tip leakage vortex in the case of a flow rate of 100% grows and reaches the next blade. For a higher flow rate of 110%, the tip leakage vortex develops and enters the throat region between the blades. Such vortices then seem to be dispersed there.

**Flow Field for the Casing With a Gutter.** By contracting the diameter of the casing, which was once enlarged by the step added at the inlet, a peripheral gutter is created on the inlet casing. A water tunnel test was performed for this type of casing, and its effect on the unsteady cavitation phenomenon was examined [9]. Several geometries for the gutter were examined and compared. In the present work, for the typical geometry of the gutter, simulations were conducted, for different flow rates (Fig. 6). The flow rates examined were $Q/Qd$=0.9 (Fig. 6(*a*)), 1.0 (Fig. 6(*b*)), and 1.1 (Fig. 6(*c*)), respectively.

A flow rate of 20% resulted in a large difference in the flow structure, especially backflow development, for the casing with and without a step as presented above. However, by adding a gutter to the casing, the backflow was completely trapped in the gutter and its structure was observed to be relatively insensitive to the change of the flow rate.

No typical backflow vortex or tip leakage vortex were observed as seen in the casing with and without a step. The leakage flow, which passed through the tip clearance, was forced to circulate within a gutter and formed a strong ringlike vortex over (upstream side) the inducer blades. Such a structure was also stable over time.

**Vortex Distribution.** To compare the relative location of the vortices, which appeared in three types of casing, vortex cores are plotted by expanding their coordinates on the $\theta$-$z$ plane in Fig. 7. The horizontal axis is the axial coordinate normalized by the axial

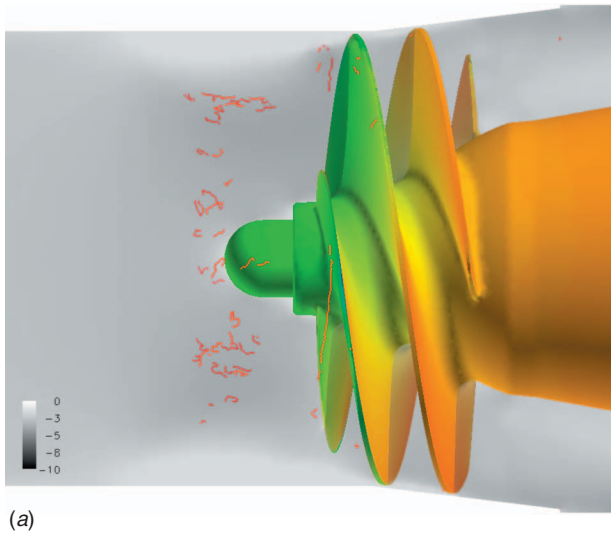


(*a*)

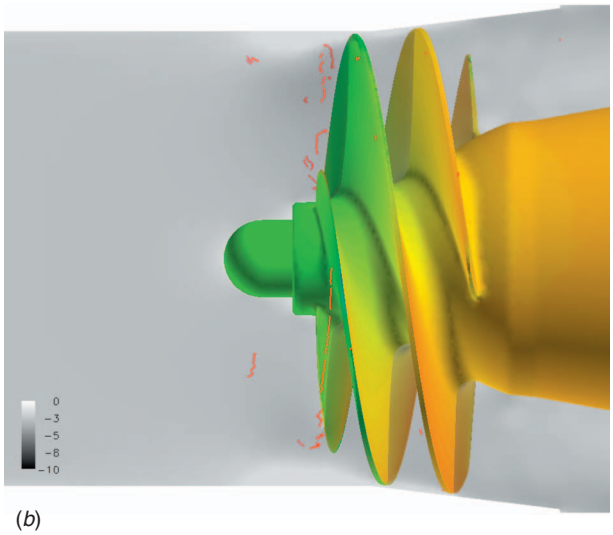


(*b*)

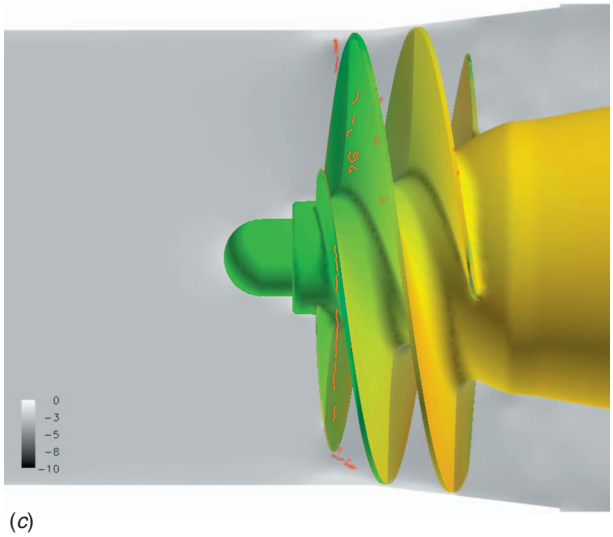


(*c*)

**Fig. 5 Distribution of axial velocity component and vortex cores for the casing without a step with three different flow rates: (*a*) *Q*/*Qd*=0.9, (*b*) *Q*/*Qd*=1.0, and (*c*) *Q*/*Qd*=1.1**

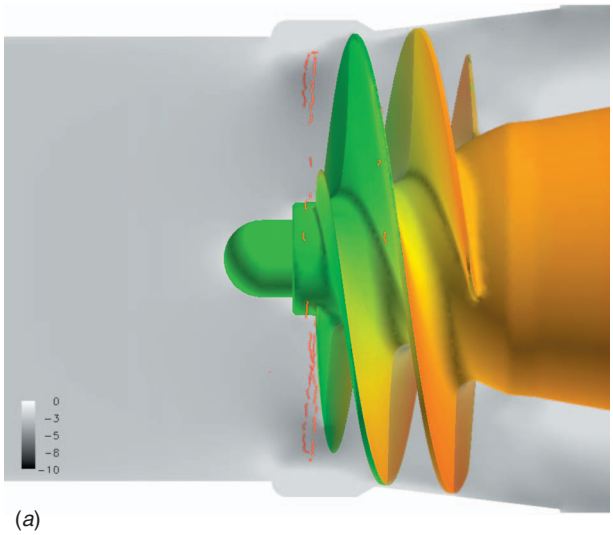


(*a*)

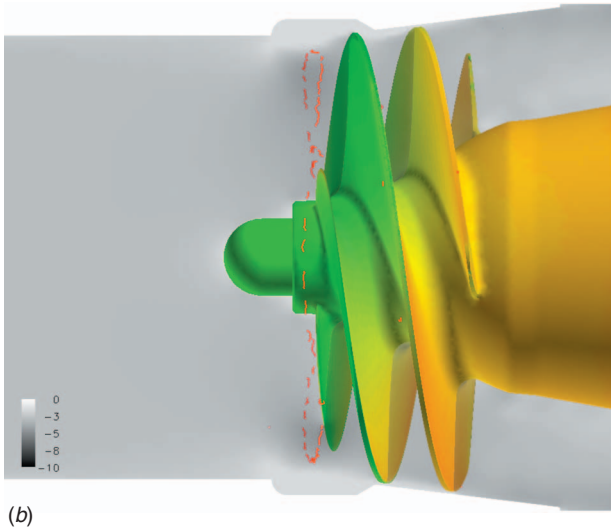


(*b*)

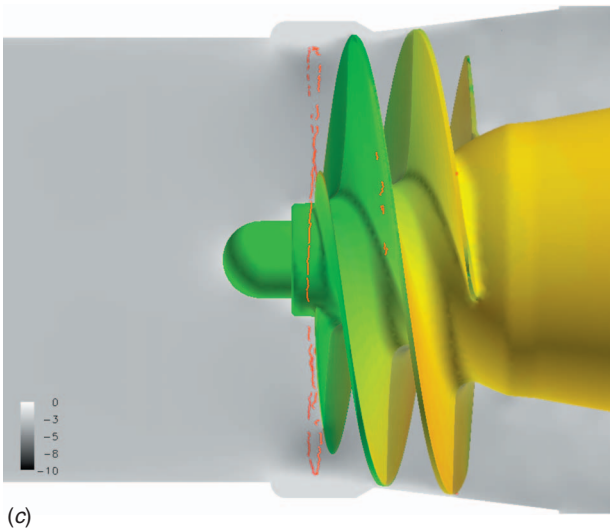


(*c*)

**Fig. 6 Distribution of axial velocity component and vortex cores for the casing with a gutter with three different flow rates: (*a*) *Q*/*Qd*=0.9, (*b*) *Q*/*Qd*=1.0, and (*c*) *Q*/*Qd*=1.1**

length, $L$, between the leading and the trailing edges of a blade. The vertical axis is the $\theta$-coordinate in the circumferential direction. $\theta$ is measured counterclockwise as viewed from upstream.

In Fig. 7, open and solid circles represent the position of the tip end of each blade. Open circles show that of the blades, the radius

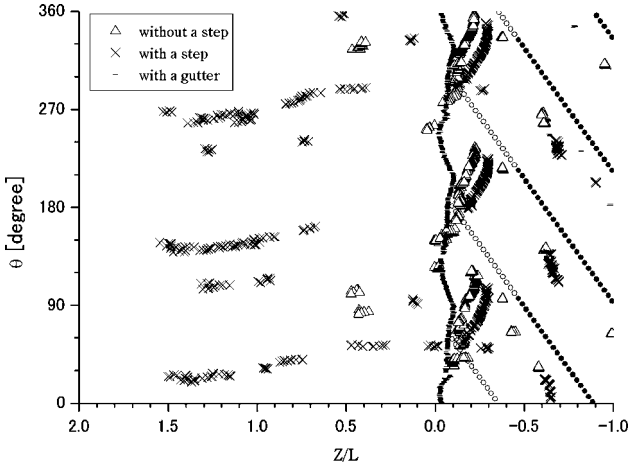


**Fig. 7 Distributions of vortex cores for three types of casing are plotted by three different kinds of symbols. Open and solid circles represent the tip end of each blade. Open circles show the tip end of the blade, whose radius is less than the maximum radius, i.e., swept back-region.**

of the tip being less than the maximum radius; i.e., a swept-back region along the leading edge. Other symbols show the location of vortex cores for three types of casing with a flow rate of 100%.

Dashes show vortex centers, which appeared in the casing with a gutter. It is clearly seen that they form a complete ringlike structure just upstream of the leading edge. Crosses and triangles represent vortex cores for the casing with and without a step, respectively. They are initiated in the swept-back part of the blade and develop downstream along the blades. The tip leakage vortices for the casing with and without a step show differences in generated position and length.

Tip leakage vortices for the casing without a step (shown by crosses) are longer than those for the casing with a step and are nearly the same length as the spacing between blades. On the other hand, in the casing with a step, tip leakage vortices are short, but three major backflow vortices are observed in the upstream region.

This figure also shows that the extension of each backflow vortex seems to reach the end of the tip leakage vortex. From the animation of the time variation of vortex structure created from time sequence data, we also observed that the extension of tip leakage vortices changed according to the phase of the backflow vortices, which rotated relative to the inducer. These findings suggest that the interaction between these vortices resulted in the shortness of the tip leakage vortices.

## Cavitation Tunnel Test

Experiments were performed using the cavitation tunnel test facility at Kakuda Space Center. The facility is a closed-loop cavitation tunnel that uses deaerated water as the working fluid. The test inducer is driven by a 185 kW direct current motor. The pressure adjustment system that pressurizes and depressurizes the test loop is located upstream of the inducer. A turbine flowmeter is used to measure the flow rate. A heat exchanger is installed in the loop and a constant temperature is maintained during the experiment. The inducer casings are made of transparent acrylic to allow observation of cavitation by using the PIV system and a high-speed video camera.

In order to confirm the occurrence of rotating cavitation or cavitation surge, pressure sensors are located around the inducer casing to measure pressure fluctuations, these fluctuations being analyzed by the fast Fourier transform (FFT) method. The spectrum of pressure fluctuation was plotted in the form of a water flow diagram for different flow rates.

Figures 8–11 show results of the analysis for two different casing geometries with flow rates ($Q/Qd$) ranging from 0.9 to 1.2. The axis labeled $f/f_0$ shows the frequency normalized by the rotating frequency of the inducer. The nonlabeled axis represents the time or the change of the cavitation number. During the experiment, the inlet pressure was gradually decreased to observe the change in the appearance of cavitation instability. The axis labeled $\Delta P$ shows the intensity of pressure fluctuation.

The typical features appearing in the spectrum of the pressure fluctuation are due to the passage of blades, rotating cavitation, and cavitation surge. In the present work, we focused on the appearance of supersynchronized rotating cavitation. There are several types of rotating cavitation: supersynchronized, subsynchronized, synchronized, and higher-order ones. Supersynchronized cavitation is the most typically observed and causes shaft vibration. This supersynchronized rotating cavitation (hereafter, RC) has a typical frequency of about $1.2f_0$, where $f_0$ is the frequency of the rotation of the inducer. Hence, we indicated RC in each figure.

In Fig. 8, with the lowest flow rate of $Q/Qd=0.9$, no RC was observed for both casing geometries. With nominal and 110% flow rates, RC was observed for the casing without a step (Figs. 9(*a*) and 10(*a*)), but not for that with a step (Figs. 9(*b*) and 10(*b*)). For the highest flow rate ($Q/Qd=1.2$, Fig. 11), RC was observed

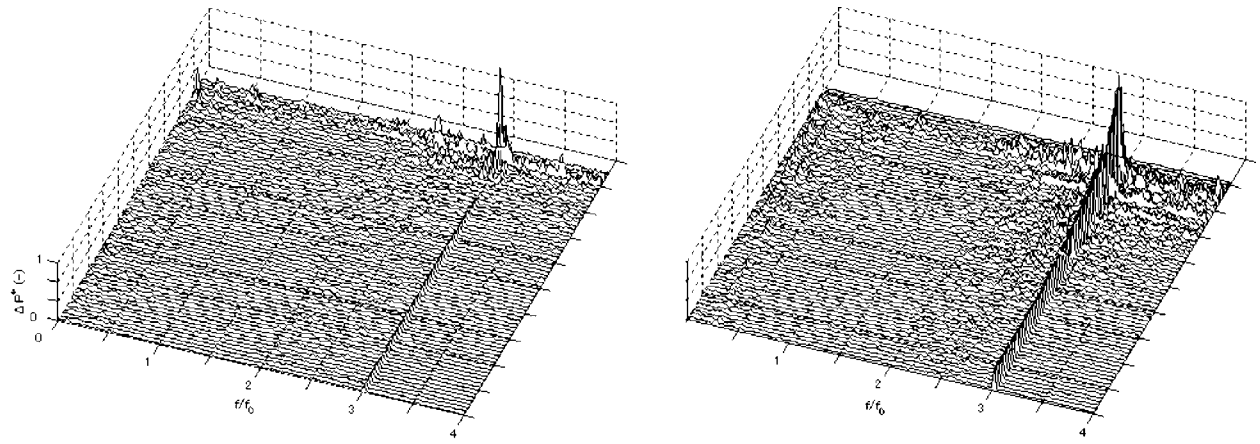


**Fig. 8 Water flow diagrams of pressure fluctuations for casings without a step (*a*) and with a step (*b*) with the flow rate $Q/Qd=0.9$. The axis labeled $f/f_0$ represents the frequency normalized by the rotation frequency. The nonlabeled axis shows the change of the cavitation number. The vertical axis labeled $\Delta P$ represents the intensity of pressure fluctuation.**

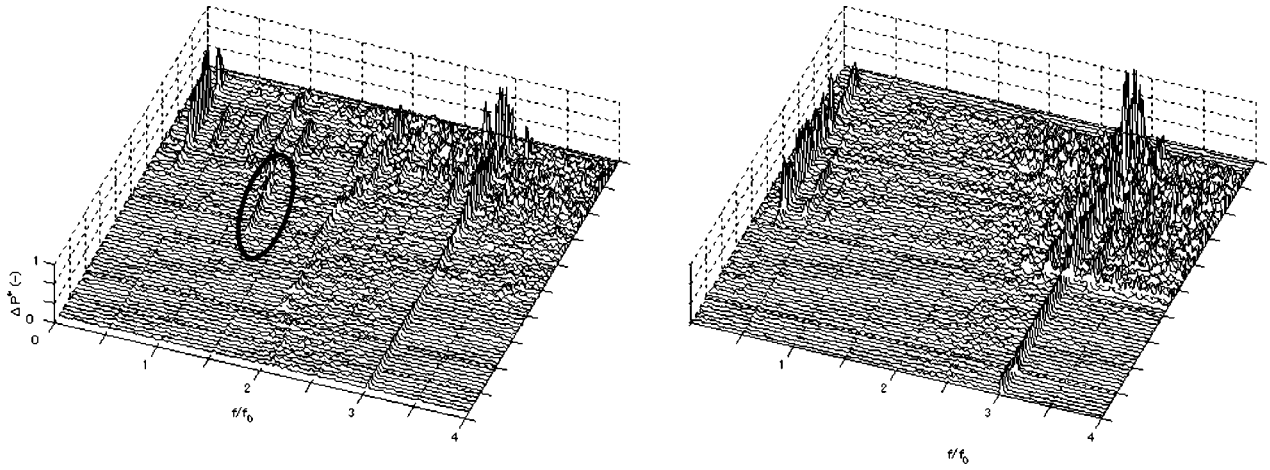


**Fig. 9 Water flow diagrams of pressure fluctuations for casings without a step (*a*) and with a step (*b*) with the flow rate *Q*/*Qd*=1.0. The fluctuation in the area marked by an oval is due to supersynchronized rotating cavitation.**

for both casing geometries, but was weaker in the casing with a step. The appearance of RC will be discussed in relation to the flow structure obtained in the present CFD in the following section.

## Discussion

The flow structure just upstream of the inducer was observed by using a PIV system. Small tracer particles were dissolved in water

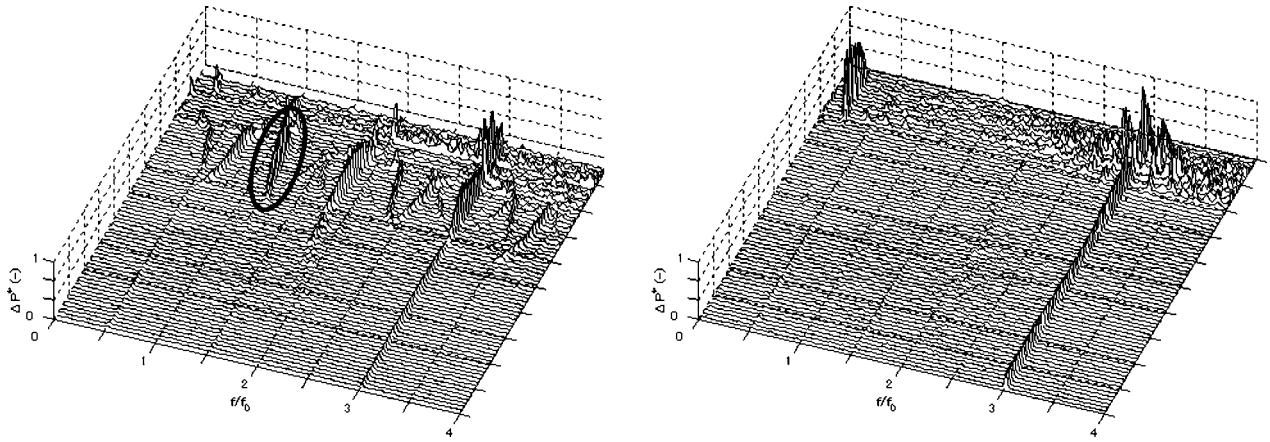


**Fig. 10 Water flow diagrams of pressure fluctuations for casings without a step (*a*) and with a step (*b*) with the flow rate *Q*/*Qd*=1.1. The fluctuation in the area marked by an oval is due to supersynchronized rotating cavitation.**

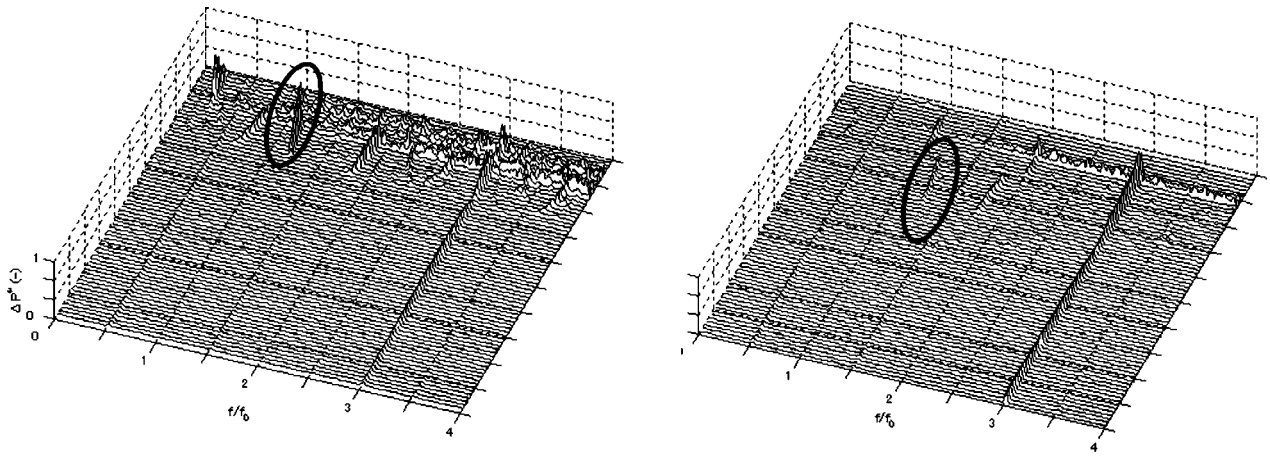


**Fig. 11 Water flow diagrams of pressure fluctuations for casings without a step (*a*) and with a step (*b*) with the flow rate *Q*/*Qd*=1.2. The fluctuation in the area marked by an oval is due to supersynchronized rotating cavitation.**

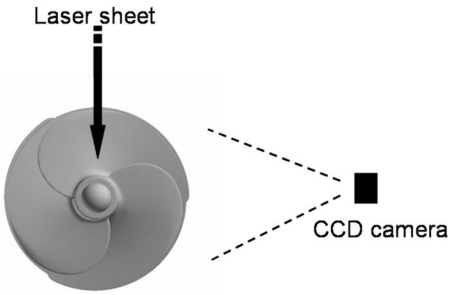


**Fig. 12 Schematic diagram of PIV system**

and sheetlike laser pulses were emitted at short intervals of 50 $\mu$s. A laser sheet was emitted parallel to the rotation axis of the inducer from above, and photographs were taken by a charge-coupled device (CCD) camera from the side position (see Fig. 12). From the pair of photographs taken at short intervals, the movements of tracers were detected and their velocities were calculated. These velocities were plotted and are overlaid on the photograph.

Figure 13 shows the velocity distribution on the plane including the rotational axis. The upper figures show the velocity map created from PIV visualization and the bottom ones are those from the CFD simulation. The figures on the left are for the casing with a step and those on the right are for the casing without a step. These figures show good agreement for backflow development between the PIV and CFD results for the two types of the casing, suggesting the validity of the present simulation.

Next, the relation between the flow structure and the appearance of unsteady cavitation phenomena will be discussed based on calculated and experimental results.

As mentioned above, cavitation tunnel experiments were conducted using transparent casings having different geometries, namely, with and without a step. The effect of the geometry of the casing on flow structure and cavitation instability was examined. The measurement of pressure fluctuation yields information on the occurrence of cavitation instabilities. We paid special attention to the occurrence of supersynchronized rotating cavitation for eight cases of two casing geometries and four flow rates. The results are presented in Figs. 8–11.

Table 1 presents an overview of the experimental results with regard to the occurrence of a rotating cavitation for the two casing types with four flow rates. Here, RC is forwardly rotating unsynchronized cavitation with a rotating frequency of about $1.2f_0$, in which $f_0$ is the rotating frequency of the inducer. In the table, "yes" and "no" mean that RC was "observed" and "not observed," respectively. "FL.R." and "geomtr" mean the flow rate and the geometry of the casing, respectively.

A clear tendency was found for the appearance of RC, the flow rate, and the casing geometry. RC is more likely to occur for higher flow rates and more effectively suppressed when a step is added to the casing. Such a tendency has also been confirmed also in previous experiments [7].

**Table 1 Occurrence of RC in experiment**

| Geomtr. \ FL.R | 0.9 | 1.0 | 1.1 | 1.2 |
|---|---|---|---|---|
| Step | No | No | No | Yes |
| No step | No | Yes | Yes | Yes |

In the present work, the same inducer and flow conditions as those used in the experiment were simulated. In the calculated results, as stated above, the flow structure changed sensitively in response to the casing geometry and the flow rate. Special attention was paid to the development of tip leakage vortices. The interaction was considered to occur between tip leakage vortices and blades when the tip leakage vortex extended nearly to the foreside of the next blade or entered the region between blades. Based on the present CFD results, the occurrences of the interaction for the two types of casing and flow rates are listed in Table 2.

In Table 2, yes means that interaction occurred between tip leakage vortices and blades, and no means that there was no interaction because the tip leakage vortices did not extend sufficiently or extended over the suction side of the next blade. No result is for the flow rate of 1.2 without a step because no calculation was made for this condition. However, the solution here is obviously, yes.

By comparing Tables 1 and 2, it can be seen that there is a clear correlation between the occurrence of RC and the interaction between a tip leakage vortex and a blade. Although the present results are based on noncavitating flow, cavitation occurs more easily in a vortex due to pressure being low inside a vortex than in the peripheral region. This correlation strongly suggests that the interaction between a tip leakage vortex and a blade plays an important role in triggering or causing RC.

Figure 14 presents photographs taken in the cavitation tunnel test at IHI Corporation [9] for the casing with a gutter (left figure) and for the casing with a step (right one). The pictures in the figure are reversed from their originals in the flow direction to facilitate comparison with the calculated results presented in the above figures. The cavitation number for these photographs is 0.055. Tap water was used as a working fluid but sufficiently degassed so that the dissolved oxygen was less than 2 mg/L.

The white-cloud-like structure is the cavitating region. Although the backflow region itself cannot be seen, based on cavity distribution, the backflow region apparently develops further upstream in the casing with a step than that in the casing with a

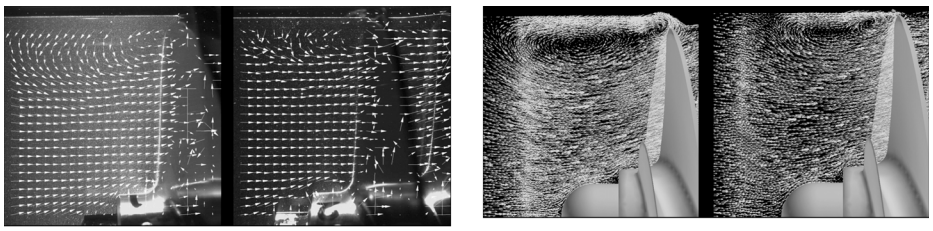

(*a*) (*b*)

**Fig. 13 Comparison between PIV visualization (*a*) and CFD velocity map (*b*) for the casings with a step (left) and without a step (right)**

Table 2 Interaction between tip leakage vortices and blades

| Geomtr. \ FL.R | 0.9 | 1.0 | 1.1 | 1.2 |
|---|---|---|---|---|
| Step | No | No | No | Yes |
| No step | No | Yes | Yes | — |

gutter. For the casing with a gutter, cavity distribution is confined to the gutter region just as the backflow region is confined to the gutter region shown in the simulation (Fig. 6).

In the tunnel test, the cavitation surge observed for the casing with a step was found to be effectively suppressed for the casing with a gutter. Measurement of the wall pressure fluctuation on the casing in the blade region showed the pressure fluctuation in the casing with a gutter to be much smaller than that in the casing with a step. From these results, it was concluded that the cavity volume generated by the backflow fluctuated much less in the casing with a gutter than that in the casing with a step.

Linear stability analysis [16] indicated that cavitation instabilities, including cavitation surge, likely occur when a mass flow gain factor, i.e., the index of the change in rate of cavity volume to the change of flow rate, is positive and large. Based on experimental results, the mass flow gain factor for the casing with a gutter was considered to be more reduced than that in the casing with a step, resulting in suppression of cavitation surge.

The flow structure observed for the casing with a gutter shown in the present CFD calculations supports the conclusion derived from the experiments. As shown in Fig. 6 and as stated above, by adding a gutter to the casing, the backflow was completely trapped in the gutter and a strong ringlike strong vortex was generated. Such structure showed little change with the change of flow rate and stable over time. The volume of the cavity generated in the backflow region, therefore, was stable despite a change of the flow rate, resulting in suppression of the increase of the mass flow gain factor.

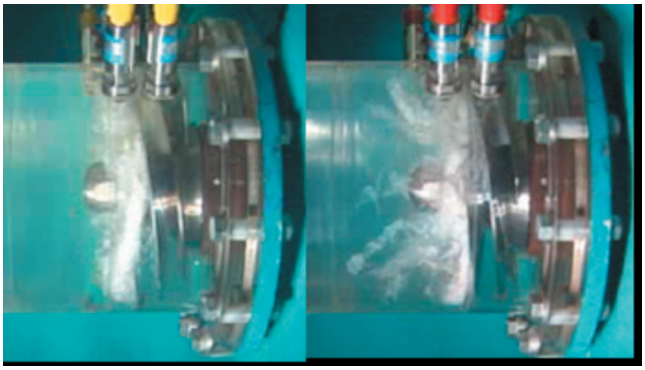

**Fig. 14 Photographs taken in tunnel tests for the casing with a gutter (left) and the casing with a step (right) (from Tomaru et al.)**

## Summary

Unsteady 3D CFD simulations were performed for noncavitating flows around a turbopump inducer. The main results are as follows.

- Slight modification of the casing geometry at the inlet and change of the flow rate strongly affect the flow around the inducer, especially the vortex structure.
- The interaction between a tip leakage vortex and the next blade seems to be strongly responsible for the appearance of rotating cavitation.
- A gutter added to the casing has a remarkable effect of confining backflow to the gutter region and results in effective suppression of cavitation surge.

## Acknowledgment

The authors would like to express their thanks to Mr. Y. Tomaru and Mr. M. Nakano, IHI Corporation, for providing photographs taken in tunnel test visualization for the casing with a gutter (Fig. 14). The authors also wish to express their appreciation to Dr. K. Sato for his help in conducting the simulations and processing the calculated data and to Mr. Yoshida for generating numerical grids.

## References

[1] Acosta, A. J., 1958, "An Experimental Study of Cavitating Inducers," *Proceedings of the Second Symposium on Naval Hydrodynamics*, pp. 533–557, Paper No. ONR/ACR-38.
[2] Ryan, R. S., Gross, L. A., Mills, D., and Michell, P., 1994, "The Space Shuttle Main Engine Liquid Oxygen Pump High-Synchronous Vibration Issue, the Problem, the Resolution Approach, the Solution," AIAA Paper No. 94-3153.
[3] Tsujimoto, Y., Yoshida, Y., Maekawa, S., Watanabe, M., and Hashimoto, T., 1997, "Observation of Oscillating Cavitation of an Inducer," J. Fluids Eng., **119**, pp. 775–781.
[4] Brennen, C. E., 1994, *Hydrodynamics of Pumps*, Concepts ETI Inc., Oxford University Press, Oxford.
[5] Kamijo, K., Shimura, T., and Watanabe, M., 1977, "An Experimental Investigation of Cavitating Inducer Instability," ASME Paper No. 77-WA/FW-14.
[6] Kamijo, K., Yoshida, M., and Tsujimoto, Y., 1993, "Hydraulic and Mechanical Performance of LE-7 LOX Pump Inducer," J. Propul. Power, **9**(6) pp. 819–826.
[7] Hashimoto, T., Hasegawa, S., Watanabe, M., Shimagaki, M., Nakamura, N., and Yoshida, Y., 2004, "Optimum Geometry of Inducer Liner for Suppression of Cavitation Fluctuations," Paper No. ISTS 2004-1-19.
[8] Shimagaki, M., Watanabe, M., Hashimoto, T., Hasegawa, S., Yoshida, Y., and Nakamura, N., 2006, "Effect of the Configurations on the Internal Flow in Rocket Pump Inducer," AIAA Paper No. 2006-5071.
[9] Tomaru, Y., Ugajin, H., Kawasaki, S., and Nakano, M., 2007, "Suppression of Cavitation Surge in Inducer by the Backflow Restriction Step," AIAA Paper No. 2007-5538.
[10] Kimura, T., Yoshida, Y., and Shimagaki, M., 2003, "Relation Between Geometries of Inducer Inlet and Backflow and Vortex Structures," AIAA Paper No. 2004-4022.
[11] Uchiumi, M., Kamijo, K., Sakazume, N., and Mihara, R., 2006, "Fatigue Strength of Rocket Pump Inducers," AIAA Paper No. 2006-5072.
[12] http://www.cd-adapco.com/.
[13] Yakhot, V., Orgszag, S. A., Thangam, S., Gatski, T. B., and Speziale, C. G., 1992, "Development of Turbulence Models for Shear Flow by a Double Expansion Technique," Phys. Fluids A, **4**(7), pp. 1510–1520.
[14] FIELD VIEW, Inteligent Light, URL: www.ilight.com.
[15] Haimes, R., and Kenwright, D., 1999, "On the Velocity Gradient Tensor and Fluid Feature Extraction," AIAA Paper Nos. 99-3288.
[16] Tsujimoto, Y., Kamijo, K., and Brennen, C. E., 2001, "Unified Treatment of Flow Instabilities of Turbomachines," J. Propul. Power, **17**, pp. 893–899.

**Oliver Reutter**

**Elena Smirnova**

**Jörg Sauerhering**

Institute of Technical Thermodynamics,
DLR,
Köln, Germany

**Stefanie Angel**
Department of Ferrous Metallurgy,
Aachen University,
52060 Aachen, Germany

**Thomas Fend**

**Robert Pitz-Paal**

Institute of Technical Thermodynamics,
DLR, Köln,
Germany

# Characterization of Air Flow Through Sintered Metal Foams

*This study investigates air flow in metallic foams, which are produced by the slip reaction foam sintering (SRFS) process. It was conducted as part of the collaborative research center (SFB) 561 "Thermally Highly Loaded, Porous and Cooled Multi-Layer Systems for Combined Cycle Power Plants." The flow through a porous medium is analyzed by Darcy's equation with the Dupuit/Forchheimer extension. All measurements can be described very well by this equation and permeability and inertial coefficients are obtained for a large quantity of samples with different base materials and different porosities. A threshold porosity of 70% is observed, above which the pressure loss significantly starts sinking with porosity. Additionally, it was found that the permeability was anisotropic. Permeability is lower in the direction of gravity during foaming. Scattering in the data of the permeability and inertial coefficients versus the porosity is observed and discussed.*
[DOI: 10.1115/1.2907419]

## 1 Introduction

The foams investigated in the present study are produced by the slip reaction foam sintering (SRFS) process. This is a promising method to produce open porous metallic foams. This process produces the porous cell structure by a chemical reaction process. In comparison to other production routes for metallic foams, the SRFS method provides several advantages as it allows working at room temperature and results in foams with a great variety of density pore size and pore shape. A wide range of base materials, such as iron, iron base, and nickel base alloys, can be supplied. As this foaming is a rather new method, there is not yet ready available data concerning the pore structure or the behavior to fluid flow. The foam structure is not similar to the foams made by casting using a polymer precursor as template or by metal deposition on cellular performs, such as polyurethane foams [1]. Therefore, it was necessary to conduct a series of extensive experiments in order to characterize the SRFS foams. A first introduction and first results have been published at the fourth International Conference on Nanochannels, Microchannels and Minichannels [2].

These foams promise a wide range of applications because there is a big choice of base materials and porosity. One promising application is the use of foam as an open wall element of combustion chambers. This topic is investigated within the collaborative research center (SFB) 561 "Thermally Highly Loaded, Porous and Cooled Multi-Layer Systems for Combined Cycle Power Plants." It aims at increasing the efficiency of the gas turbine by raising the gas temperature.

Within this research center, the present study was carried out. Increasing the temperature leads to the necessity of actively cooling the combustion chamber walls by effusion cooling, which means that cooling air is pressed through little holes into the chamber. The metallic foam is intended to be coated with a thermal barrier layer with laser drilled bore holes and used as a combustion chamber wall element [3,4]. The knowledge of the temperature distribution inside the wall element (foam+coating) is important to predict the lifetime of the materials employed. To predict the temperature, flow through the wall element has to be characterized. For this, experimental data on the heat transfer characteristics, the thermal conductivity, and the pressure drop characteristics are needed. The last property is subject of the present study.

## 2 Investigated Materials

The base of the technique is a metal suspension [5,6]. Fine metallic powders are mixed with a dispersant, solvent, and concentrated phosphoric acid as binder. The phosphoric acid forms a metal phosphate together with the metallic particles and hydrogen is set free by the reaction between the metallic particles and the acid. The metal phosphate freezes the hydrogen bubbles in the slip. After drying, the samples are sintered under defined, reducing conditions and as the solvent evaporates, an open porous structure with the porosity in the range of 62–87% is received. The process provides a wide range of process parameters, which allow adjusting the foam structure concerning density, pore size, and pore shape distribution to influence the mechanical and flow properties. Graded structures can be supplied. The scheme for obtaining such foams can be seen in Fig. 1.

The investigated samples for this study are made of Hastelloy B, Inconel 625, and NC-powder. The grain sizes range between 50 $\mu$m and 150 $\mu$m. The densities of the bulk material, the metal powder particles, and the apparent density are compiled in Table 1. The iron based samples (NC) were sintered at 1170°C for 60 min with a heating rate of 8 K/min, and the nickel based samples (Inconel 625 and Hastelloy B) at 1200°C for 60 min. Two intermediate temperature levels were set in the case of the nickel based samples during heating up, one at 150°C and the second at 350°C, to guarantee that the escaping water vapor will be moved out of the furnace. The heating rate was 3 K/min until 350°C and then 8 K/min. After evacuating the furnace one time before starting the sintering process, the samples were sintered under a reducing atmosphere of 100% $H_2$.

Contributed by the Fluids Engineering Division of ASME for publication in the JOURNAL OF FLUIDS ENGINEERING. Manuscript received December 18, 2006; final manuscript received March 6, 2008; published online April 25, 2008. Assoc. Editor: Timothy J. O'Hern.

  

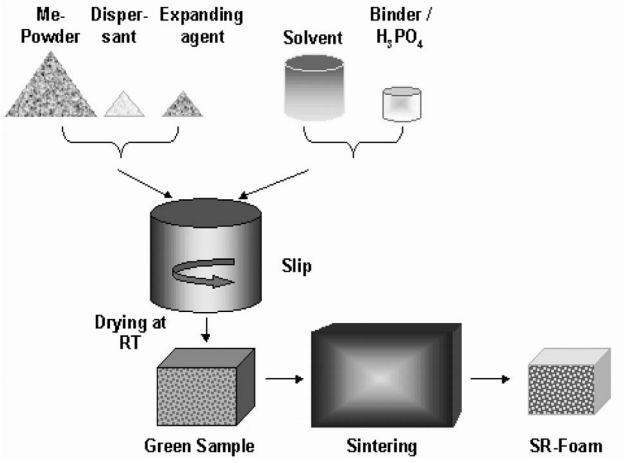


**Fig. 1 Scheme of the SRFS process**

Samples made only of the sintered slip without foaming show a porosity of about 50% (densities of 3.8–4.2 g/cm$^3$) and are called *sintered powder samples*. These samples are taken as representing the material of the pore walls in the foams. The foams have a total porosity between 62% and 87% (densities of 1.2–3.7 g/cm$^3$). The pores can be characterized as those that arise from the hydrogen foaming, called the primary pores, and those that are the spaces between adjacent grains of the sintered powder, called the secondary pores [7]. The secondary pores reach up to 0.3 mm diameter and the primary pores reach up to 3.5 mm.

All densities were determined as gravimetrical densities by weighing the foam samples, and dividing this weight by the total volume of the foam sample, which was calculated from measurements with a sliding caliper. The total porosity was determined by using the density of the bulk material as the reference.

The samples were produced at the Department of Ferrous Metallurgy at Aachen University. The samples are cylinders with diameters between 64 mm and 81 mm and the length was between 9 mm and 30 mm. The picture of a typical sample can be seen in Fig. 2 (left) together with an optical micrograph of the sample (right). For measurements of anisotropy effects, cubical samples were used with 45 mm side length.

**Table 1 Overview of the densities of the powder material**

| | Density of the bulk material (g/m$^3$) | Density of the powder particles | Apparent density of the powder |
|---|---|---|---|
| NC | 7.87 | 7.76 | 2.45 |
| Hastelloy B | 9.24 | Not determined | Not determined |
| Inconel 625 | 8.44 | 8.10 | 2.84 |

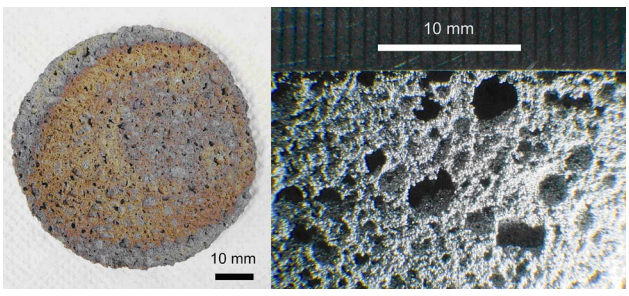


**Fig. 2 Picture of a sample of a Hastelloy B foam and a detailed view of the pore structure**

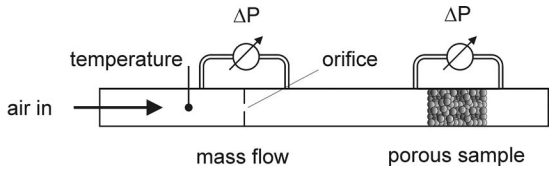


**Fig. 3 Experimental setup for measuring the pressure drop of the samples (schematic)**

## 3 Permeability and Experimental Setup

Referring to publications by Innocentini et al. [8], Boomsma et al. [9], Boomsma and Poulikakos [10], and Lage et al. [11,12], it is useful to describe the flow through a porous medium in terms of Darcy's equation with the Dupuit/Forchheimer extension (Eq. (1)) and not only by Darcy's equation. It is applicable, if the flow through a porous medium is not very low. As it fits the experimental data very well, only the extended equation was used in this study:

$$\frac{dP}{dx} = \frac{\eta_{\text{dyn}}}{K_1} v + \frac{\rho}{K_2} v^2 \tag{1}$$

Since the air flow velocity $v$ and the differential pressure loss $dP/dx$ are not constant along the path of the (compressible) fluid through the porous sample, an expression for $dP/dx$ at the outlet of the flow from the sample is needed, because at this location the air flow velocity $v=v_o$ is determined. For the determination of $v$, the mass flow $\dot{M}$ is needed, which is constant throughout the tubing and which is measured. Furthermore, the air density $\rho_o$ is needed, so the velocity may be calculated with the cross-sectional area $A$ according to

$$v_o = \frac{\dot{M}}{\rho_o A}$$

Air density data are taken from the tables using the temperature ($T_o$) and pressure data ($P_o$) at the outlet of the flow through the sample [13]. $v_o$ is understood as the velocity, which one would have in a 100% porous sample (superficial velocity).

The needed expression for the differential pressure loss $dP/dx$ is $P_i^2 - P_o^2/2P_oL$, so Eq. (1) may be rewritten for the case at the outlet location as

$$\frac{dP_o}{dx} = \frac{P_i^2 - P_o^2}{2P_oL} = \frac{\eta_{\text{dyn}}}{K_1} v_o + \frac{\rho_o}{K_2} v_o^2 \tag{2}$$

After plotting the data with different flow velocities and performing a second order polynomial fit, once more air density data are needed to extract $K_2$ from the coefficients of the fit. In this case, also $\rho_o$ is taken, which remains nearly constant for various $v_o$ throughout the duration of the test series, which usually takes an hour or shorter. Accordingly, $K_1$ is calculated with temperature dependent air viscosity data from Ref. [14]. In this way, $K_1$ and $K_2$ are acquired as material constants independent of the fluid, pressure, and temperature environment.

The experimental setup is shown in Fig. 3. A fan drives an air flow through a metal tube array. The mass flow rate was calculated from the pressure difference between two sensors before and behind a defined orifice, the absolute pressure, and the air temperature assuming a relative humidity of 50% at room temperature for the air density. The pressure drop across the sample was measured together with the air temperature close to the sample position. The orifice plate has been manufactured by Mangels (Wilhelmshafen, Germany) and the difference pressure sensors used were a DPI 260 by Druck (Germany) and a MaPress by Madur (Austria). The absolute pressure of the air in the laboratory was measured for each experiment and varied between 985 mbars and 1032 mbars depending on the weather. The experiment takes

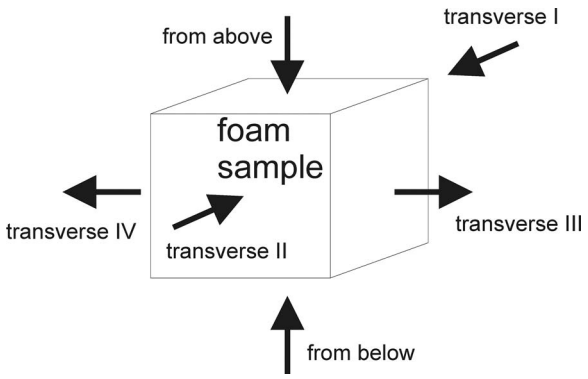


**Fig. 4 Sketch of the possible air flow directions in a cubic sample. Above and below can be distinguished in the sample, because of the direction of the gravity during the foaming and drying process.**

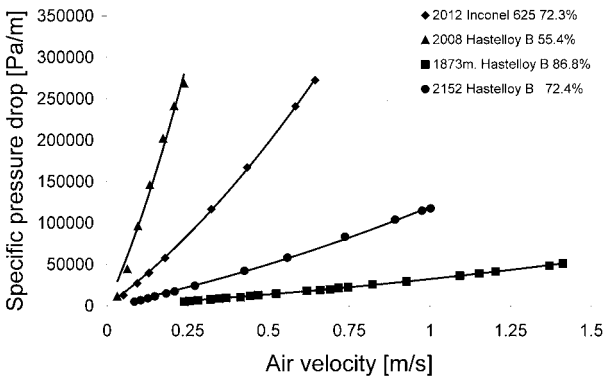


**Fig. 5 Pressure drop measurements of samples with different densities**

place at air temperatures slightly above room temperature caused by heat losses of the blower. Typical values for viscosity and air density are $1.82\ 10^{-5}$ Pa s and $1.21\ \mathrm{kg/m^3}$, respectively. The round sample was tightly inserted in a metal pipe with some layers of flexible foamed rubber around it. The air tightness of this sample holding was tested by inserting an impermeable block of steel with similar dimensions, as the samples in the sample holder and at maximum fan power only detecting a negligible mass flow. The area exposed to the flow varied between 32 $\mathrm{cm^2}$ and 52 $\mathrm{cm^2}$ for the cylindrical samples and 20 $\mathrm{cm^2}$ for the cubic samples.

The accuracy of the specific pressure drop measurements is dominated by the accuracy of the difference pressure measurements for low values of the specific pressure drop and by the accuracy of the measurement of the sample thickness for high values. So for measurements above 25,000 Pa/m, an error of about $\pm 5\%$ can be assumed, which rises for lower values and can reach values above 10%. For the velocity measurements, the error at low velocities is dominated by the accuracy of the difference pressure drop measurement over the orifice, while at high velocities, the geometric error of the superficial area dominates. The influence of the accuracy of the absolute pressure and temperature measurements is not very high. So above a velocity of 0.2 m/s, an uncertainty of approximately $\pm 5\%$ is realized, which significantly rises for lower velocities and can reach values above 40% for 0.05 m/s. As discussed by Innocentini et al. [15], the validity of the permeability coefficients is strictly restricted to the flow velocity regime occurring during measurement. Additionally, though the overall accuracy of pressure drop is comparably high for most samples (approximately $\pm 5\%$ along with $\pm 5\%$ uncertainty of the velocity) and the measurements can be very well fitted by a second order polynomial function, the uncertainty of the single coefficients $K_1$ and $K_2$ is higher, also because they are not independent of each other during fitting.

In order to investigate anisotropy effects, cubic samples have been manufactured. They are subjected to air flow in six different directions. During the process of foaming and drying, there is only one distinct direction, that of gravity. The samples were carefully prepared, so the direction during measurements was defined. For a sketch of the possible air flow directions, see Fig. 4.

## 4 Results

As examples, two plots of the pressure difference as a function of air velocity are presented in the Figs. 5 and 6. Figure 5 contains curves of foams with various densities. Figure 6 shows the results of the anisotropy investigations. The quadratic dependency of the pressure drop on flow velocity can be clearly seen. The second order polynomial function fits match the measured data very well, so the applicability of Eq. (1), from which the permeability coefficient $K_1$ and the inertial coefficient $K_2$ may be derived, is obvious. As the absolute pressure on the entrance of the tube array is limited by the experimental equipment, the velocity range of the measurements is limited, too. Consequently, the denser the sample, the smaller the velocity range of the measurement. The sintered powder samples, which have no primary porosity, were investigated at velocities of up to 0.2 m/s (left curve in Fig. 5).

In Fig. 5, we also see the dependency of the pressure drop on the velocity for the samples with different densities. As expected, the denser samples show higher pressure drops. The samples' density range varies from porous material, which was made out of only sintered powder metal (porosity $\varepsilon \approx 50\%$, density $\rho \approx 4\ \mathrm{g/cm^3}$) and foams, which were foamed ($\varepsilon \approx 87\%$, $\rho \approx 1.2\ \mathrm{g/cm^3}$). As base material, samples with Inconel 625, Hastelloy B and NC powder were used.

In Fig. 6, we see an example of an anisotropy measurement for an Inconel 625 sample. For this measurement, a cubic sample was used. Of the six possible directions of air flow in a cube, the result shows us groups of two different pressure drops. For the foaming direction, a higher pressure drop is observed compared to the transverse directions. A possible explanation of this is that there are more connections between the pores transverse to the foaming direction, and another one that the pores might be elongated transverse to the foaming direction. Most probably, it is a combination of both. At the moment, there are not yet enough optical investigations of the pore structure to decide this.

All investigated cubic samples showed the same behavior. For the further study of the pressure drop characteristics, round samples were used. All of these were subjected to an air flow in the foaming direction.

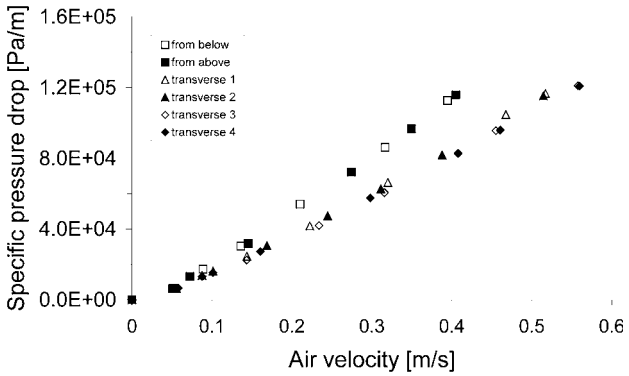


**Fig. 6 Pressure drop of a cubic Inconel 625 sample in six different directions**

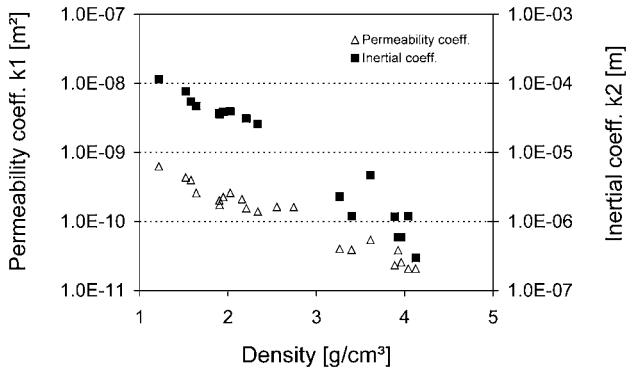


**Fig. 7 Dependency of the permeability and inertial coefficients on the density of the Hastelloy B foam samples**

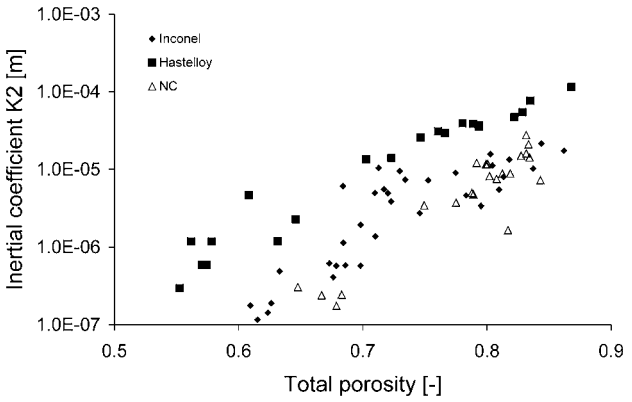


**Fig. 9 Comparison of the inertial coefficients sorted by matrix material**

Using the above described method for obtaining the permeability and the inertial coefficients, a large variety of samples has been measured. The results are presented for the three different material types (Inconel 625, Hastelloy B and iron (NC)).

Figure 7 shows the dependency of the permeability and inertial coefficients on the density for samples of Hastelloy B. The density of Hastelloy B as a dense material is 9.22 $g/cm^3$. As stated above, the densest samples were not foamed, but samples that were made by only sintering Hastelloy B powder without adding a foaming agent. A total number of five of these materials have been investigated. They have density values of approximately 4 $g/cm^3$. In this case, flow may be imagined as flow through a packed bed of sintered metal grains. As expected, a trend can be seen that samples with higher densities (lower porosity) show lower permeability and lower inertial coefficients. For the other materials, these dependencies are very similar; therefore we here only show the Hastelloy B results in such a diagram.

Comparisons of the obtained results for all materials are presented in the next two figures. In order to make the comparison possible, not the density (which is different for the base materials) but the total porosity is used. The data for inertial and permeability coefficients are separately presented. We see a dependency of pressure drop coefficients on total porosity in the figures. In all samples with all base materials, there is a trend to lower pressure drop at higher porosity but not a strict dependency. Samples with small difference in density can have a bigger difference in pressure drop than samples with a larger difference in density. For all materials, it is possible to find samples with about 8% difference in the total porosity and very similar permeability coefficients. It is not yet clear how to account for this effect. Possible explanations are the stochastic foaming effect, the manual laboratory scale production process, and the influence of the division of the total porosity into open, closed, and half-open porosities. The range of the iron and Inconel 625 samples pressure drop was similar. Hastelloy B sample pressure losses are smaller. This is probably an effect of the powder morphology and grain size distribution.

Furthermore, it can be seen from Fig. 8 that there is a minimum total porosity of about 70% above which permeability continuously increases. This may be explained by the primary pores forming a permeable network, whereas before primary pores are not connected by windows but only through the porous matrix walls.

Optical characterization (see Fig. 2) shows that the connections between primary pores (windows) are rather small and in the range of a few powder particle diameters, more like a small hole in a wall between pores. The walls of the primary pores are a porous sintered packed bed. This structure of the SRFS metal foam samples leads to lower permeability and inertial coefficients that one would expect from the primary pore dimensions and compared to foams on the basis of reticulated polyurethane foams with similar porosities (Fig. 9).

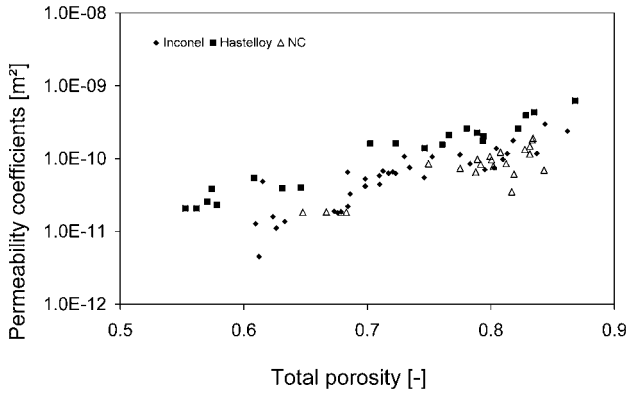


**Fig. 8 Comparison of the permeability coefficients sorted by matrix material**

## 5 Conclusions

There is a clear tendency that the higher the sample density, the lower the permeability. This corresponds to the known dependency of the permeability on porosity for other structures [3]. The results show that for the same porosity Hastelloy B samples significantly exhibit higher permeabilities than Inconel and NC samples. Anisotropy can be observed in the SRFS foams. In the direction of the foaming, the pressure drop is higher than in the transverse directions. For comparison of different densities, only data from the same flow direction were used. Above 70% total porosity, the primary pores seem to form a network. Above this porosity, there is a clear increase in permeability with increasing porosity. The data acquired on pressure drop characteristics of SRFS foams is an important tool for the manufacturer to create foams with the desired pressure drop characteristics. The design of functional elements, such as the porous combustion chamber wall of a gas turbine, may be improved.

## Acknowledgment

The support of the Deutsche Forschungsgemeinschaft (DFG) for the collaborative research center "Thermally Highly Loaded, Porous and Cooled Multi-Layer Systems for Combined Cycle Power Plants" (SFB 561) is thankfully acknowledged.

## Nomenclature

$P$ = absolute fluid pressure (Pa)

$\Delta P$ = pressure difference between inlet and outlet $P_i - P_0$ (Pa)

$L$ = length of the sample (m)
$\eta_{dyn}$ = dynamic viscosity of the fluid (Pa s)
$\nu$ = superficial velocity (m/s)
$\rho$ = density of the fluid ($kg/m^3$)
$\varepsilon$ = porosity (%)
$K_1$ = permeability coefficient ($m^2$)
$K_2$ = inertial coefficient (m)
$\dot{M}$ = mass flow rate (kg/s)
$A$ = cross section of the sample exposed to flow ($m^2$)

## References


[1] Ashby, M. F., Evans., A., Fleck, N. A., Gibson, L. J., Hutchinson, J. W., and Wadley, H. N. G., 2000, *Metal Foams: A Design Guide*, Butterworth-Heinemann, Boston.

[2] Reutter, O., Sauerhering, J., Smirnova, E., Fend, Th., Angel, St., and Pitz-Paal, R., 2006, "Experimental Investigation of Heat Transfer and Pressure Drop in Porous Metal Foams," *Proceedings of ASME ICNMM2006, Fouth International Conference on Nanochannels, Microchannels and Minichannels*, Limerick, Ireland, Jun. 9–21, Paper No. ICNMM2006-96135.

[3] Bohn, D., 2002, "New Materials and Cooling Systems for High Temperature, Highly Loaded Components in Advanced Combined Cycle Power Plants," *Seventh Liege Conference on "Materials for Advanced Power Engineering*, Liege, Belgium, Sept. 30–Oct. 02.

[4] Bohn, D., and Moritz, N., 2001, "Numerical Investigation on Flow Field and Heat Transfer Phenomena in Multi-Hole Cooling Configurations," *RTO-Symposium*, Loen, May.

[5] Scholz, P.-F., 1997, Patent DE 197, 16, 514, C, 1.

[6] Angel, S., Bleck, W., and Scholz, P.-F., 2005, "Adjusting the Pore Structure of Open Porous Metallic Foams Produced by the SlipReactionFoamSintering (SRFS)—Process," *Fourth International Conference MetFoam*, Kyoto, Japan, Sept. 21–23, Japan Institute of Metals.

[7] Angel, S., Bleck, W., Scholz, P.-F., and Fend, Th., 2004, "Influence of Powder Morphology and Chemical Composition on Metallic Foams Produced by Slip-ReactionFoamSintering (SRFS)—Process," Steel Res., **75**, pp. 483–488.

[8] de Mello Innocentini, M. D., Sepulveda, P., and dos Santos Ortega, F., "Permeability," *Cellular Ceramics*, M. Scheffler and P. Colombo, eds., Wiley-VCH, Weinheim, pp. 313–341.

[9] Boomsma, K., Poulikakos, D., and Ventikos, Y., 2003, "Simulation of Flow through Open Cell Metal Foams Using an Idealized Periodic Cell Structure," Int. J. Heat Fluid Flow, **24**, pp. 825–834.

[10] Boomsma, K., and Poulikakos, D., 2002, "The Effects of Compression and Pore Size Variations on the Liquid Flow Characteristics in Metal Foams," ASME J. Fluids Eng., **124**, pp. 263–272.

[11] Lage, J. L., and Antohe, B. V., 2000, "Darcy's Experiments and the Deviation to Nonlinear Flow Regime," ASME J. Fluids Eng., **122**, pp. 619–625.

[12] Lage, J. L. et al., 2005, "Protocol for Measuring Permeability and Form Coefficient of Porous Media," Phys. Fluids, **17**, 088101.

[13] 1991, VDI-Wärmeatlas, 6. Auflage, VDI-Verlag.

[14] Bohl, W., Technische Strömungslehre, 11 durchgesehene Auflage, Vogel Buchverlag, p. 268.

[15] Innocentini, M. D. M, Salvini, V. R., Pandolfelli, V. C., and Coury, J. R., Jr., 1999, "Assessment of Forchheimer's Equation to Predict the Permeability of Ceramic Foams," J. Am. Ceram. Soc., **82**(7), pp. 1945–1948.

**Hidesada Kanda**[1]
Professor
e-mail: kanda@u-aizu.ac.jp

**Takayuki Yanagiya**
Graduate student

Department of Computer Science and Engineering,
University of Aizu,
Aizu-Wakamatsu,
Fukushima 965-8580, Japan

# Hysteresis Curve in Reproduction of Reynolds' Color-Band Experiments

*This article describes the reproduction and extended analysis of Reynolds' color-band experiment. Reynolds found two critical Reynolds numbers ($R_c$) in pipe flows: $R_{c1}$ of 12,830 from laminar to turbulent flow and $R_{c2}$ of 2030 from turbulent to laminar flow. Since no clear relationship has been established between them, we studied how the entrance shape affects $R_c$. Thus, for the first time, a hysteresis graph can be drawn by connecting the two curves of $R_{c1}$ and $R_{c2}$ such that the two $R_c$ values lie on separate branches of the hysteresis plot.* [DOI: 10.1115/1.2903741]

## 1 Introduction

Laminar-turbulent transition in pipe flows is one of the fundamental problems of fluid dynamics and has been widely studied from experimental, numerical, and theoretical perspectives [1,2]. Among them, the findings of Reynolds [3] in 1883 still remain unexplained [4–6]. White [4] stated that "There is no theory of transition. After a century of research on the transition process, …, the mechanisms are still not completely understood…. A dramatic example of our limited knowledge is the fact that the original transition experiment (pipe flow) is still not well understood."

Reynolds observed that there were two critical Reynolds numbers ($R_c$) for the laminar-turbulent transition in pipe flows: $R_{c1}$ of 12,830, at which steady motion changes into eddies, as determined by the color-band method, and $R_{c2}$ of 2030, at which eddies change into steady motion, as found by the pressure-loss method.

In his color-band experiments, Reynolds discovered the law of similarity that now bears his name, the Reynolds number (Re), defined as $\mathrm{Re}=UD/\nu$, where $U$ is the mean axial velocity, $D$ the diameter of the pipe, and $\nu$ the kinematic viscosity of the fluid. For the upper $R_{c1}$ of 12,830, he obtained 29 values of (i) 11,830–13,600, (ii) 11,930–14,130, and (iii) 11,800–13,330 for three different pipes of diameters 2.68 cm, 1.527 cm, and 0.7886 cm, respectively. The observed values for the upper $R_{c1}$ thus slightly vary from 11,800 to 14,130.

Reynolds further observed the transition length, defined as the distance from the inlet to the point where the transition occurs: "Under no circumstances would the disturbance occur nearer to the trumpet than about 30 diameters in any of the pipes, and the flashes generally, but not always, commenced at about this distance." The dimensionless entrance length ($L_e/D$) is defined as the length required for the centerline velocity to reach 99% of its fully developed value. For Re above 500, $L_e/D \approx 0.056\mathrm{Re}$ [7]. The region beyond this entrance length is called the fully developed region. For the case of $R_c=12{,}830$, $L_e \approx 0.056 \times 2.68$ cm $\times 12{,}830 \approx 1930$ cm. Since Reynolds' pipes were all about 4 ft and 6 in. (138 cm) long, the transition necessarily occurred in the entrance region.

In his pressure-loss method, for two pipes of a quarter-inch (0.615 cm) and a half-inch (1.27 cm) diameter, he obtained two $R_c$ values of about 2030 and 2070, respectively. The pipe lengths were both 16 ft (488 cm). If tap water is in a disturbed state, some length of pipe is required before the disturbed state is smoothed out. Reynolds stated that "10 feet would be sufficient for the acquirement of a regular condition of flow." For the case of $R_c=2030$, $L_e \approx 0.056 \times 0.615$ cm $\times 2030 \approx 70$ cm. Since the measuring section was 11–16 ft (335–488 cm) downstream of the inlet, it is clear that transition was measured in the fully developed region.

Reynolds thus introduced the two transitions in the entrance region and in the fully developed region. Hereafter, we use the upper $R_{c1}$ of 12,830 and the lower $R_{c2}$ of 2030, which are typical of Reynolds' obtained values [8]. Here, a question arises: is it possible to find a factor that affects $R_c$ values of 2030 and 12,830 using the color-band method?

Concerning the upper $R_c$ of 12,830, however, discrepancies arose: using Reynolds' original apparatus, different $R_c$ values were obtained. Ekman [9] observed several different $R_c$ values ranging as high as 13,000, 21,000, 31,000, 42,000, and 51,000. Further, Van Dyke [10] observed that "modern traffic in the streets of Manchester made the critical Reynolds number lower than the value 13,000 found by Reynolds." It is generally believed that different disturbances in flow cause different $R_c$ values. On this point, Darbyshire and Mullin [11] found that a critical amplitude of disturbance is required to cause transition at a given Re and that this amplitude varies in a systematic way with Re.

In the color-band experiment, it is difficult to quantitatively control disturbances. Accordingly, we consider the contraction ratio, which apparently affects $R_c$. This objective might be rephrased as confirming another apparent cause of transition from disturbances. Prandtl and Tietjens [12] stated that "in order to obtain a high $R_c$, it is important to round off the entrance of the pipe."

Although the area contraction ratio is generally referenced, two contraction ratios are actually used: $C_b(=D_b/D)$ is the ratio of the bellmouth diameter ($D_b$) to pipe diameter, and $C_r(=r/D)$ is the ratio of the radius ($r$) of quadrant-arc rounds cut at the edge of the pipe to pipe diameter (see Fig. 3). In the ASHRAE Handbook of Fundamentals (ED1-3 Bellmouth, with Wall) [13–15], the entrance loss coefficient is described against the contraction ratio $C_r$, but no $R_c$ against $C_r$ relationship is described. Their relationship is supplemented by the significant results obtained in this study.

To this end, since March 2003, we have been conducting experiments similar to Reynolds' classical color-band experiment, and the number of experimental trials has exceeded 2300 (as of January, 2008). The principal objectives are (1) to investigate whether the contraction ratio apparently governs $R_c$, (2) to establish experimental procedures for the reproduction of Reynolds' obtained data, (3) to obtain $R_c$ values of 2030 and 12,830 under similar conditions, and (4) to discuss how Ekman could obtain high $R_{c1}$ values.

[1]Corresponding author.

Contributed by the Fluids Engineering Division of ASME for publication in the JOURNAL OF FLUIDS ENGINEERING. Manuscript received September 25, 2007; final manuscript received February 4, 2008; published online April 29, 2008. Assoc. Editor: Phillip M. Ligrani.

  

**Table 1 $R_c$ values obtained and experimental conditions adopted by previous researchers**

| Author | Year | $R_c$ | $R_c$ | Entrance | $C_b$ | Methods |
|---|---|---|---|---|---|---|
| Reynolds [3] | 1883 | 2030 | $R_{c2}$ | St | 1 | Pressure |
| Barnes and Coker [16] | 1905 | 1910–2040 | $R_{c1}$ | St | 1 | Temperature |
| Stanton and Pannell [17] | 1914 | 2500 | $R_{c2}$ | St | 1 | Pressure |
| Binnie [18] | 1945 | 1970 | $R_{c2}$ | St | 1 | Refraction |
| Senecal and Rothfus [19] | 1953 | 2100 | $R_{c2}$ | St | 1 | Pressure |
| Kanda and Oshima [20] | 1987 | 1930–2700 | $R_{c1}$ | St | 1 | Color band |
| Darbyshire and Mullin [11] | 1995 | 1760 | $R_{c2}$ | St | 1 | LDV |
| Reynolds [3] | 1883 | 11,830–13,600 | $R_{c1}$ | Be | 5.8 | Color band |
| Barnes and Coker [16] | 1905 | 4130–12,900 | $R_{c1}$ | Be | ? | Temperature |
| Ekman [9] | 1910 | 13,000–51,000 | $R_{c1}$ | Be | 5.8 | Color band |
| Stanton and Pannell [17] | 1914 | 16,000 | $R_{c1}$ | Be | ? | Pressure |
| Kanda and Oshima [20] | 1987 | 5790–6690 | $R_{c1}$ | Be | 2.9 | Color band |
| Tanekoda [21] | 1988 | 5535 | $R_{c1}$ | Be | ? | Tracer |
| Darbyshire and Mullin [11] | 1995 | 17,000 | $R_{c1}$ | Be | ? | LDV |

## 2 Background and Previous Investigations

Many researchers have tried to measure the limit of upper $R_c$ values using a variety of apparatuses—for example, a calming chamber, baffles, honeycomb, and screens. When considering Reynolds' problem, it is desirable to avoid geometric complication at the pipe inlet and, thus, to revert to bellmouth entrances. $R_c$ values obtained by previous researchers are summarized in Table 1, focusing on bellmouth entrances (Be, bottom half) and a straight pipe (St, top half). It is obvious from the table that $R_c$ takes a $R_{c,\min}$ value of about 2030 when using a straight pipe and that with bellmouth entrances, $R_c$ greatly increases from 2030 to two $R_c$ values, i.e., (a) 5500–6700, (b) 12,000, and higher.

We consider the entrance shapes of Reynolds' color-band experimental apparatus. Jackson of the University of Manchester kindly allowed the first author to photograph Reynolds' original bellmouths. The bellmouth diameter is about 15.5 cm for the pipe with a 2.68 cm diameter. Then, a question arose: is it true that if $R_{c,\min}$ of 2030 is multiplied by the contraction ratio $C_b$, then the value of $R_c=12{,}830$ is obtained? $R_c \approx 2030 \times 15.5/2.68 \approx 11{,}740$. This value is very close to 12,830. Moreover, we recall that Kanda and Oshima [20] performed similar color-band experiments with a bellmouth of $C_b=2.9$ and obtained $5790 < R_c < 6690$; $R_c \approx 2030 \times 2.9 \approx 5890$. Accordingly, it was conjectured on the basis of the above two examples that $R_c$ is approximately linearly proportional to $C_b$ in the presence of natural disturbances.

However, the above linear approximation was invalidated by preliminary experiments conducted in 2003, as shown in Fig. 1, where the flow state is plotted as a function of Re and $C_b$. In this plot, the experimental data are broadly scattered because there were no fixed experimental procedures (see Sec. 3.2 (ii)–(v)), and even at the same Re, a mixture of laminar, transition, and turbulent states is observed. The case of $C_b=6$ corresponds approximately to Reynolds' experiments with $R_c=12{,}830$, denoted by a solid circle (•) at the top right of the plot. Fortunately, we confirmed that $R_{c,\min} \approx 2030$ exists in the case of a straight pipe, denoted by a solid circle (•) at the bottom left of the plot, and that each entrance shape might have its respective minimum $R_c$.

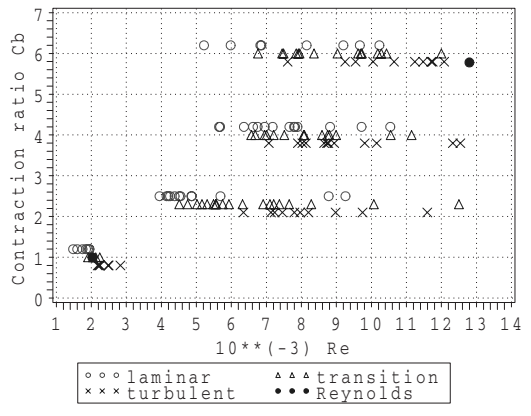


**Fig. 1 Flow state versus contraction ratio $C_b$ and Re**

## 3 Experiment

**3.1 Experimental Apparatus.** Reynolds' original tank was 46 cm wide, 180 cm long, and 40 cm high (water depth=38 cm), and his pipe was about 138 cm long, raised 20 cm from the bottom of the tank. Figure 2 is a schematic diagram of the apparatus of the present study. Our apparatus is slightly larger than Reynolds' original equipment. Experiments are conducted in a glazed tank 50 cm wide, 200 cm long, and 55 cm high. A pipe for overflow is installed at the side of the tank, and the water depth is 44 cm. A horizontal acrylic cylindrical pipe of 26 mm inner diameter, 40 mm outer diameter, and 150 cm length is placed 18.5 cm from the bottom of the tank and passes through the wall of the tank.

The flowmeter and two valves (valves 1 and 2) are installed outside the tank. The flowmeter is readable to two decimal places, and its accuracy is within 1%. The maximum flow rate is approximately 32 l/min, which corresponds to Re values of 23,000 at 15°C, 26,000 at 20°C, and 29,000 at 25°C. Therefore, water temperature was carefully measured twice.

The maximum flow flux considerably depends on the water level (WL), as the velocity of fluid in the pipe is determined by the vertical distance from WL to the exit position of the drain hose. In our case, the vertical distance from the pipe is limited to around 87 cm, while in Reynolds' case, it was 7 ft (214 cm), which was sufficient to yield Re values of over 50,000.

Ten exchangeable pipe entrances were prepared and used: namely, a straight pipe (St), five different quadrant-arc rounds (Qa1–Qa5), and four different bellmouth entrances (Be1–Be4), as shown in Fig. 3. The bellmouth shapes of Be1–Be4 are ASME standard 3:2 ellipses. The quadrant-arc round shapes of Qa1 ($r=1$ mm) through Qa5 ($r=5$ mm) were formed by cutting the edge of the pipe inlet. Although the shapes of the bellmouths and the quadrant-arc rounds are slightly different, they are considered to be equivalent. Thus, the contraction ratio $C_b$ ranges from 1 to 6; the Be4 bellmouth ($C_b=6$) corresponds to Reynolds' bellmouth attached to his 2.68 cm diameter pipe.

A color-dye container is installed at the top of the tank. The

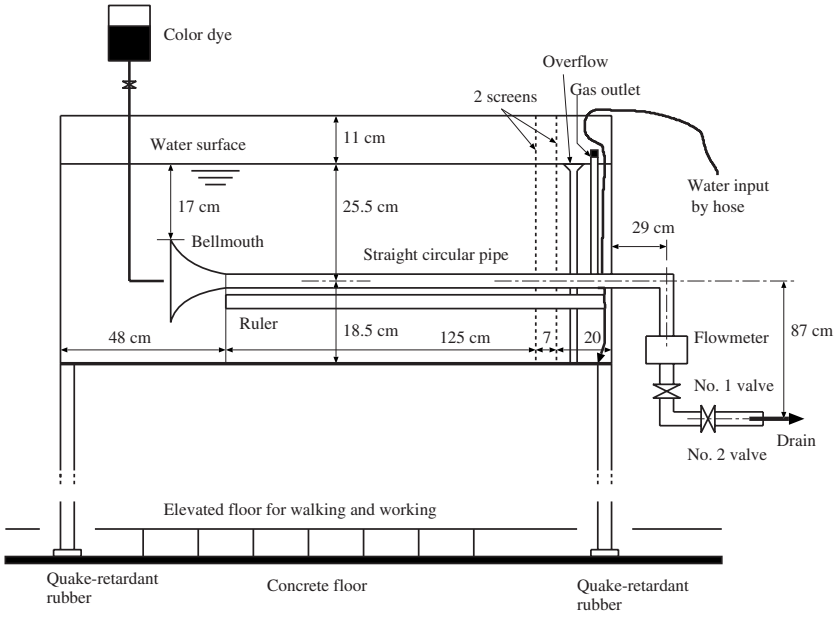


**Fig. 2 Schematic diagram of the experimental apparatus**

color dye consists of methylene blue solution and water in a volume ratio of 1:50, i.e., 20 ml of methylene blue in 1000 ml of water.

**3.2 Experimental Procedures.** To achieve high reproducibility of $R_c$, there were several issues that had to be resolved: (i) air bubbles on the pipe wall, (ii) disturbed water surface in the tank, (iii) distinction between $R_{c1}$ and $R_{c2}$, (iv) waiting time for water to become still in the tank, (v) varying Re due to the dropping of WL and initial laminar state, (vi) constant WL by supplying water at a high flow rate, (vii) and valve opening or closing operation. These are each considered.

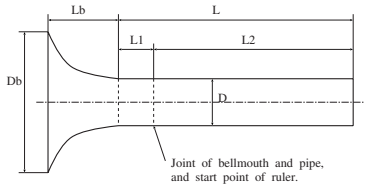


(a) Bellmouth entrance (Be1–Be4)

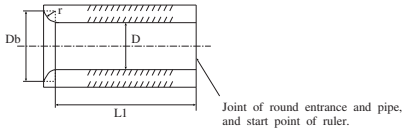


(b) Quadrant-arc round entrance (Qa1–Qa5)

| Entrance | $D_b$ | $r$ | $L_b$ | $C_b$ | $C_r$ | $L1$ | $L$ |
|---|---|---|---|---|---|---|---|
| St | 2.6 | 0.0 | - | 1 | 0.0 | 8 | 158 |
| Qa1 | 2.8 | 0.1 | 0.1 | 1.08 | 0.039 | 5.9 | 155.9 |
| Qa2 | 3.0 | 0.2 | 0.2 | 1.15 | 0.077 | 5.8 | 155.8 |
| Qa3 | 3.2 | 0.3 | 0.3 | 1.23 | 0.115 | 5.7 | 155.7 |
| Qa4 | 3.4 | 0.4 | 0.4 | 1.31 | 0.154 | 5.6 | 155.7 |
| Qa5 | 3.6 | 0.5 | 0.5 | 1.39 | 0.193 | 5.5 | 155.7 |
| Be1 | 4.0 | - | 1.05 | 1.54 | - | 5 | 156 |
| Be2 | 6.07 | - | 2.6 | 2.34 | - | 4 | 154 |
| Be3 | 10.4 | - | 5.85 | 4 | - | 4 | 154 |
| Be4 | 15.6 | - | 9.75 | 6 | - | 4 | 154 |

**Fig. 3 Sizes of ten pipe entrance shapes (unit: cm, $D$=2.6, $L2$=150)**

(i) Air solubility in water decreases as temperature rises. Since room temperature is usually higher than water temperature, if water is held for several hours in the tank, the temperature of the water rises and many small air bubbles adhere to the inside and outside of the pipe wall, presenting significant obstacles to pipe flow. Accordingly, the water was temporarily stored in a 500 l storage tank and heated with a 1 kW heater to approximately 15–20°C above its original temperature. Then, the heated water was moved to another tank and cooled to room temperature. Thus, the appearance of small air bubbles on the pipe wall was prevented.

(ii) The water surface in the tank is often slightly disturbed even if the air-conditioning system is turned off. We noted that when several plastic plates of 5 mm thickness were placed across the water surface, reproducibility was markedly improved. The plastic plates are connected merely by placing three long stainless-steel rulers across them. In this configuration, the plastic plates prevented disturbance from the top of the water surface and yielded a rigid boundary condition of velocities=0 at the water surface.

(iii) There are two different types of critical Reynolds numbers, i.e., $R_{c1}$ and $R_{c2}$. These different critical values must be distinguished.

(iv) A serious problem was determining how long the water should be held still in the tank after filling to reduce disturbance. This period is called the waiting time. Reynolds paid much attention to the stillness of the water, stating that "it was observed that the critical velocity was very sensitive to disturbance in the water before entering the tubes; and it was only by the greatest care as to the uniformity of the temperature of the tank and the stillness of the water that consistent results were obtained." Waiting times of 3 h for $R_{c1}$ and 20 min for $R_{c2}$ were used (see Sec. 4.1).

(v) Re varies slightly during measurements because of the loss of hydraulic height head. We measure WL from the top position of the water depth of 44 cm (WL=0 cm). An-

other serious problem was that the flow state changes from (a) laminar to laminar, (b) laminar to turbulent, or (c) laminar to turbulent and then back to laminar during measurements under fixed valve conditions. For bellmouths Be1–Be4, even at the maximum flow flux, the flow in the pipe begins in a laminar state, and this initial laminar state persists down to around a 5–7 cm drop of WL. This laminar state is called the initial laminar state. With decreasing WL, for example, Re is 24,700 at WL=2 cm (laminar), 24,000 at WL=7 cm (laminar), 23,200 at WL=10 cm (turbulent), and 22,700 at WL=14 cm (turbulent). If the measurements for WL drops of 2–7 cm were included, the laminar Re would be higher than the turbulent one. This confusing result must be avoided. The maximum measurable WL is 17 cm since the top of bellmouth Be4 is at WL=17 cm. Accordingly, the measurable WL is limited to 10–14 cm for $R_{c1}$. The relative difference in Re between WL=10 cm and 14 cm is $(23{,}200-22{,}700)/22{,}700=2.2\%$.

(vi) The WL is kept constant by supplying water at a high rate, but the water in the tank is somewhat disturbed by incoming water. Since the difference in $R_c$ by supplying water was larger than that described above (v), we followed Reynolds' no-supply procedure (see Sec. 4.4).

(vii) One opening or closing valve operation changed Re by 200–500, so that it is somewhat difficult to adjust Re to a target value with only one operation. Accordingly, it is desirable to first set the valves for a target value of Re and then to observe the flow state.

Therefore, Procedure 1 and Procedure 2 were devised for natural disturbance conditions.

*Procedure 1 for* $R_{c1}$. Water from the previous experiment remains above the top of the bellmouth in the tank. Water from the cooled storage tank is added to that from the previous experiment to the overflow level. The mixed water is slowly stirred several times with a wooden board to maintain the homogeneity of the temperature of the water. Then, the water is stilled by placing plastic plates on the water surface. Our standard waiting time is 3 h, and sometimes extends to over 16 h or 1 dy. Before starting the measurement, it is desirable to set the flow rate for a target value of Re by adjusting valve 1. Then, the measurement is started by quickly opening valve 2, and the WL, time, flow rate, and flow state for each 1 cm drop of WL are recorded. Such measurement continues until WL drops by 15 cm. The measured time is used to check the accuracy of the flowmeter. At the same time, the flow phenomenon is recorded with a digital video camera or a digital camera.

*Procedure 2 for* $R_{c2}$. The waiting time is 20 min. First, the experiment is started by abruptly and fully opening both valves 1 and 2 to their maximum flow rates. In the cases of St and Qa1–Qa5, the flow state is turbulent from the beginning of the experiment, whereas in the cases of Be1–Be4, the flow begins in a laminar state and becomes turbulent as WL drops by 3–7 cm. Next, after maintaining the turbulent state through an approximately 5 cm drop of WL, valve 1 is closed rapidly to achieve the target flow rate or Re. Valve 2 is used to adjust the flow rate more precisely. The period of closing the valves is from 40 s to 70 s, with an average time of about 60 s. The measurement continues until WL drops further by 2–5 cm after closing the valves. With decreasing Re, the recorded period becomes longer. Accordingly, WL, time, flow rate, and flow state for each 5 mm drop of WL are recorded.

In addition, let us consider the effects of continuously supplying water on $R_c$. To maintain constant WL=0, experiments were carried out with a flow rate of 10 l/min or 20 l/min using the Be4 bellmouth. Accordingly, Procedure 3 and Procedure 4 were devised.

*Procedure 3 for* $R_{c1}$ *by supplying water*. The waiting time is more than 3 h. The water is stilled by placing the plastic plates on the water surface at WL≈10 cm. If we start measurements at WL=0 cm, the initial laminar flow state continues for a few minutes. To obtain a nearly steady state, water is supplied at WL of about 10 cm. At the start, valve 1 is closed, while valve 2 is opened. While WL is raised from 10 cm to 2 cm, the supply flow rate is checked for 10 l/min or 20 l/min. When WL reaches the top level of WL=0 cm, we start measurements without stirring the mixed water. Then, by gradually opening valve 1, we observe $R_{c1}$ values until turbulent flow begins. Valve 2 is used to adjust the flow rate more precisely. The WL, time, flow rate, and flow state for each 30 s and 1 min are recorded. Such measurement continues for about 10 min. At the same time, the flow phenomenon is recorded with a digital camera.

*Procedure 4 for* $R_{c2}$ *by supplying water*. The procedure before measurements is the same as Procedure 3. When WL is raised to WL=0 cm, we start the experiment by abruptly and fully opening valves 1 and 2 to their maximum flow rates; this condition continues for 3 min. Then, by gradually closing valve 1, we observe $R_{c2}$ values until laminar flow begins. Valve 2 is used to adjust the flow rate more precisely. The WL, time, flow rate, and flow state for each 30 s and 1 min are recorded. Such measurement continues for about 3–4 min.

## 4 Results and Discussion

**4.1 Waiting Time and $R_c$ (Procedure 1).** In Reynolds' first experiment, the tank was filled from the water main through a hose and was allowed to stand for several hours, from 10 a.m. to 2 p.m. For his other experiments, the number of experiments varied from 1 to 7 per day.

To determine the waiting time, we carried out experiments by changing the waiting time from 5 min to longer than 15 h using the Be4 bellmouth at Re≈11,000, 12,000, and 13,000. The number of trials was five times for each waiting time. The average results for the initial laminar WL and probability of turbulence at WL=14 cm are listed in Table 2. The probability of turbulence for waiting times of longer than 1 h was 25% at Re≈11,000, 30% at Re≈12,000, and 90% at Re≈13,000, so that the $R_{c1}$ value was expected to range from 12,000 to 13,000.

For waiting times of shorter than 10 min, the initial flow state is greatly disturbed, so that uniform initial conditions cannot be obtained. For waiting times longer than 20 min, the initial laminar state appears. Waiting times of 1 h or longer are sufficient for experiments concerning $R_{c1}$. Following Reynolds, a waiting time of 3 h was used for $R_{c1}$.

The initial laminar state persists down to approximately a 6 cm drop of WL for waiting times longer than 30 min, but it persists down to around a 3 cm drop for the 20 min waiting time. Since the turbulent state of an approximately 5 cm drop of WL is required to achieve $R_{c2}$ disturbance conditions, a waiting time of 20 min was used for experiments concerning $R_{c2}$.

**4.2 Determination of Transition State (Procedures 1 and 2).** Tables 3 and 4 show examples of data log sheets for $R_{c1}$ and $R_{c2}$, respectively, where ○, △, and × denote the laminar, transition, and turbulent states. In the memo column, the change of the color band is recorded; the color band flows downstream, changing or shifting its figure as only straight, from straight to downward or upward, widened band, and wave of wavelength ≈40–100 cm.

It is easy to distinguish the laminar and turbulent states, but it is slightly difficult to determine the transition state, as there are many different patterns of transition, including puffs and slugs. First, we describe some difficulties in determining the flow state for $R_{c1}$. When Re approaches $R_c$, particularly for low values below around 4000, the transition state repeatedly disappears (relaminarization) and reappears (transition) during the 1 cm drop of WL. For example, a turbulent spot appears in the color band at

**Table 2 Waiting time versus initial laminar WL (cm) and probability (%) of turbulence at WL =14 cm (Procedure 1, the number of trials is five times for each waiting time and Re)**

| | Re≈11,000 | | Re≈12,000 | | Re≈13,000 | |
|---|---|---|---|---|---|---|
| Waiting time | Laminar WL | Turbulence | Laminar WL | Turbulence | Laminar WL | Turbulence |
| 5 min | 0.1 | 100 | 0.0 | 100 | 0.0 | 100 |
| 10 min | 1.0 | 80 | 0.1 | 60 | 0.5 | 100 |
| 15 min | 3.0 | 80 | 5.0 | 60 | 1.6 | 100 |
| 20 min | 2.7 | 40 | 3.5 | 80 | 3.5 | 100 |
| 30 min | 5.7 | 40 | 6.6 | 80 | 4.1 | 80 |
| 1 h | 11.8 | 40 | 9.6 | 40 | 9.2 | 80 |
| 2 h | 12.8 | 20 | 13.0 | 00 | 7.8 | 100 |
| 3 h | 13.0 | 20 | 11.4 | 40 | 8.4 | 80 |
| Above 15 h | 10.8 | 20 | 9.4 | 40 | 8.6 | 100 |
| Av.: above 1 h | 12.1 | 25 | 11.8 | 30 | 8.5 | 90 |

**Table 3 Example of data log sheet for $R_{c1}$ (Procedure 1) (Date (No.): March 24, Wed, 2006 (1), Time: 14:15 p.m., Entrance: Be4 Temperature (°C): room, 18.0; water, 18.8)**

| WL (cm) | Time | Flux (l/m) | State | $x_t$ (cm) | Re | Memo |
|---|---|---|---|---|---|---|
| 0 | ··· | ··· | ○ | ··· | ··· | ··· |
| 1 | 36 s | 16.71 | ○ | ··· | 13,190 | Straight |
| 2 | 1 min 13 s | 16.57 | ○ | ··· | 13,070 | Straight |
| 3 | 1 min 46 s | 16.48 | ○ | ··· | 13,010 | Straight |
| 4 | 2 min 23 s | 16.45 | ○ | ··· | 12,990 | Downward |
| 5 | 2 min 59 s | 16.31 | ○ | ··· | 12,875 | Straight |
| 6 | 3 min 37 s | 16.26 | ○ | ··· | 12,840 | Straight |
| 7 | 4 min 13 s | 16.20 | △ | ··· | 12,790 | Straight |
| 8 | 4 min 50 s | 16.11 | △ | ··· | 12,720 | Downward |
| 9 | 5 min 28 s | 15.96 | △ | 100–120 | 12,600 | |
| 10 | 6 min 05 s | 15.83 | △ | 105 | 12,500 | ··· |
| 11 | 6 min 43 s | 15.80 | ○ | ··· | 12,470 | Upward |
| 12 | 7 min 20 s | 15.73 | ○ | ··· | 12,420 | Upward |
| 13 | 7 min 58 s | 15.62 | △ | 120 | 12,330 | ··· |
| 14 | 8 min 36 s | 15.56 | △ | 120 | 12,280 | ··· |
| 15 | 9 min 15 s | 15.44 | △ | 120 | 12,190 | ··· |

**Table 4 Example of data log sheet for $R_{c2}$ (Procedure 2) (Date (No.): May 20, Wed, 2005 (1), Time: 17:27 p.m., Entrance: St Temperature (°C): room, 21.5; water, 20.4)**

| WL (cm) | Time | Flux (l/m) | State | $x_t$ (cm) | Re | Memo |
|---|---|---|---|---|---|---|
| 0 | ··· | ··· | × | ··· | ··· | ··· |
| 1 | ··· | 30.44 | △ | ··· | 24,990 | ··· |
| 2 | ··· | 30.34 | △ | ··· | 24,910 | ··· |
| — | — | — | × | — | — | — |
| 6 | ··· | 29.83 | △ | 3–6 | 24,490 | ··· |
| Closing time | ··· | | | | | |
| 7 | ··· | 2.53 | △ | ··· | ··· | ··· |
| 7.5 | 00 s | 2.55 | △ | 20–30 | 2090 | Upward |
| ··· | ··· | 2.51 | △ | ··· | 2060 | ··· |
| 8 | 1 min 59 s | 2.52 | △ | 20–30 | 2070 | ··· |
| ··· | ··· | 2.46 | ○ | ··· | 2020 | ··· |
| 8.5 | 4 min 00 s | 2.51 | ○ | ··· | 2060 | Band |
| ··· | ··· | 2.47 | ○ | ··· | 2030 | ··· |
| 9 | 6 min 00 s | 2.48 | ○ | ··· | 2040 | Band |
| ··· | ··· | 2.48 | ○ | ··· | 2040 | Upward |
| 9.5 | 8 min 04 s | 2.47 | ○ | ··· | 2030 | Upward |
| ··· | ··· | 2.44 | (△) | ··· | 2000 | ··· |
| 10 | 10 min 06 s | 2.48 | ○ | ··· | 2040 | Straight |
| ··· | ··· | 2.47 | (△) | ··· | 2030 | Band |

some distance from the inlet and travels downstream along the pipe; then, the next turbulent spot appears at almost the same distance from the inlet. The flow state between these two turbulent spots appears to be laminar, judging from the continuity of the color band. This phenomenon is called intermittency. With increasing Re, the length of the laminar color band becomes shorter, and the turbulent spots become more violent. Finally, the turbulent state begins. We used the criteria that in the transition state, at least one turbulent spot always exists in the color band. The turbulent state is clearly recognized because the color band abruptly and randomly disappears some distance downstream.

Next, concerning $R_{c2}$, relaminarization takes place during a 2–3 cm drop of WL and beyond. This means that the closing time of the valves may affect the flow state. Just after closing the valves, the following phenomena are observed: (a) The turbulent state immediately changes to the laminar state. (b) The turbulent state persists for a 5 mm drop of WL, then changes to a laminar one. (c) The turbulent state persists. Accordingly, the transition state for $R_{c2}$ is judged to be that when the transition or turbulent state continues for at least a 1 cm drop of WL.

Last, we consider how to determine the flow state since four combinations of transitions exist: (i) laminar to laminar, (ii) laminar to turbulent, (iii) turbulent to laminar, and (iv) turbulent to turbulent. For $R_{c1}$, it is assumed that case (i) is laminar, cases (ii) and (iv) are turbulent, and case (iii) is a mixture of turbulent and laminar due to laminarization. In case (ii), at a high Re, the initial state is laminar, but the state changes from laminar to turbulent as Re decreases; this laminar state is not regarded as laminar since it is generally believed that Re in a turbulent state is larger than that in a laminar state under similar conditions. For $R_{c2}$, case (i) is laminar and cases (ii)–(iv) are turbulent, although in case (iii) the state is often relaminarized during measurements.

**4.3 Critical Reynolds Numbers for $R_{c1}$ and $R_{c2}$ (Procedures 1 and 2).** Let us consider a determination method for $R_c$. Figure 4 shows the frequency of the flow state against Re in the vicinity of $R_c$, similar to a population pyramid in full detail, e.g., for the St and Be4 entrances, where the laminar and transition/turbulent flow states are separately grouped on the left and right sides. Each Re value was recorded by rounding to the nearest 50 or 100. From these figures, $R_c$ is determined under the condition that the frequency of the transition/turbulent state is greater than that of the laminar state above the value of $R_c$; for other entrances, the above population pyramid method was used. A summary of frequencies of experimental values is shown in Table 5, where Re denotes the range of trial Re, ○ and × are the frequencies of laminar and transition/turbulent states, respectively, and (*) denotes $R_c$. $R_c$ values are shown in Fig. 5 and listed in Tables 5 and 6.

The main features of our experimental results are as follows.

(1) In Fig. 5, values of $R_{c1}$ and $R_{c2}$ are plotted against the contraction ratio $C_b$. When connecting the two lines of $R_{c1}$ and $R_{c2}$, a hysteresis curve could be drawn. For example, at $C_b=6$, $R_{c1}$ and $R_{c2}$ can be connected when disturbances are given by changing the waiting time or supply water rate (see Tables 2 and 7).

(2) The lower $R_{c2}$ value of 2050 was obtained for the straight circular pipe as

$$R_{c,\min} = \lim_{C_b \to 1} R_{c2} = R_{c2}(\mathrm{St}) \approx 2050 \qquad (1)$$

This result agrees well with previous researchers' results for a straight pipe entrance, as listed in Table 1.

(3) The value of $R_{c1}$ steadily and smoothly increases as the contraction ratio $C_b$ increases from $C_b=1$ (St) through $C_b=1.08$ (Qa1)–1.31 (Qa4), to $C_b=1.39$ (Qa5). Then, $R_{c1}$ reaches a constant value of 12,200–12,500 for the entrance shapes of $C_b=1.39$ (Qa5) through $C_b=6$ (Be4). In this way, it is possible to reproduce the upper $R_{c1}$ value of around 12,830 for $C_b \geqq \sim 1.4$

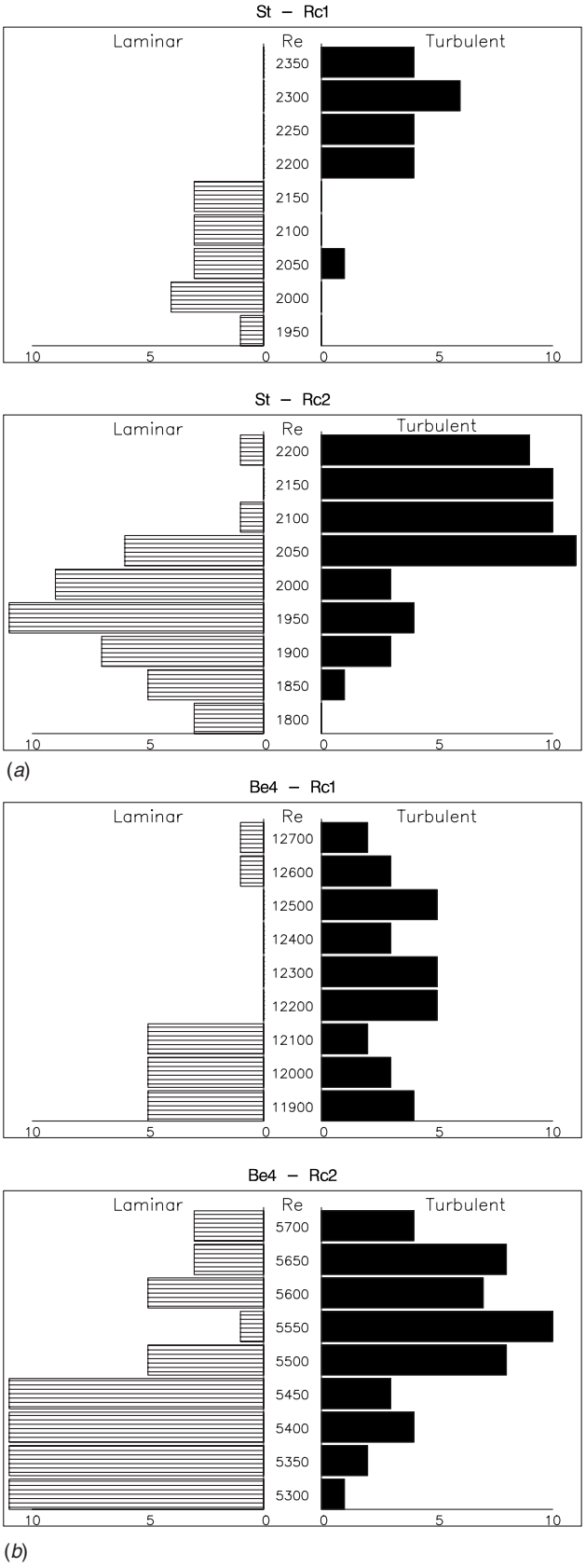


**Fig. 4 Frequency of flow states against Re in the vicinity of $R_c$ for St and Be4 (Procedures 1 and 2); (*a*) Straight pipe (St), (*b*) bellmouth (Be4)**

**Table 5 Frequency of flow states against Re in the vicinity of $R_c$ (Procedures 1 and 2, ○ denotes laminar, × is transition/turbulent, and * is $R_c$)**

| | $R_{c1}$ | | | $R_{c2}$ | | |
|---|---|---|---|---|---|---|
| Entrance | Re | ○ | × | Re | ○ | × |
| St | 2000–2150 | 13 | 1 | 1850–2000 | 32 | 11 |
| | 2200*–2350 | 0 | 18 | 2050*–2200 | 8 | 40 |
| Qa1 | 3450–3550 | 10 | 1 | 2950–3100 | 15 | 6 |
| | 3600*–3750 | 2 | 17 | 3150*–3250 | 3 | 13 |
| Qa2 | 4800–4950 | 17 | 9 | 3900–4050 | 9 | 4 |
| | 5000*–5150 | 13 | 21 | 4100*–4250 | 9 | 19 |
| Qa3 | 6500–6650 | 17 | 6 | 4450–4600 | 17 | 1 |
| | 6700*–6850 | 3 | 21 | 4650*–4800 | 8 | 18 |
| Qa4 | 8550–8700 | 17 | 8 | 4650–4800 | 25 | 7 |
| | 8750*–8900 | 3 | 22 | 4850*–5000 | 10 | 24 |
| Qa5 | 11,800–12,100 | 16 | 3 | 5050–5150 | 7 | 0 |
| | 12,200*–12,500 | 9 | 16 | 5200*–5350 | 10 | 20 |
| Be1 | 12,300–12,400 | 10 | 1 | 5000–5150 | 23 | 12 |
| | 12,500*–12,800 | 4 | 10 | 5200*–5350 | 6 | 16 |
| Be2 | 11,900–12,100 | 7 | 3 | 5300–5400 | 22 | 4 |
| | 12,200*–12,400 | 10 | 23 | 5450*–5650 | 28 | 26 |
| Be3 | 12,300–12,400 | 13 | 6 | 5300–5450 | 30 | 7 |
| | 12,500*–12,800 | 5 | 16 | 5500*–5650 | 22 | 24 |
| Be4 | 11,900–12,100 | 15 | 9 | 5300–5450 | 44 | 10 |
| | 12,200*–12,700 | 0 | 18 | 5500*–5650 | 14 | 33 |

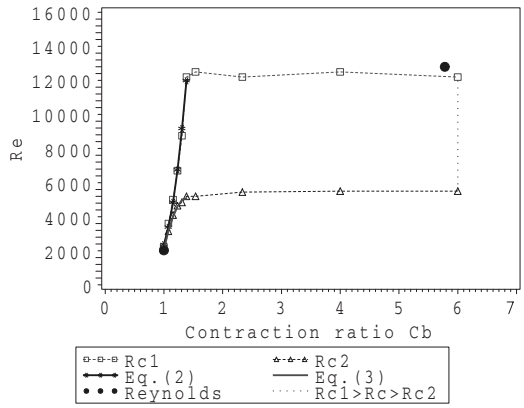


**Fig. 5 Hysteresis curve drawn by connecting two lines of $R_{c1}$ and $R_{c2}$ against contraction ratio $C_b$**

and to verify Reynolds' classic result.

Similarly, the value of $R_{c2}$ steadily and smoothly increases from $C_b=1$ to 1.39 and continues to slightly increase to $C_b=2.34$ (Be2). Then, the value of $R_{c2}$ reaches another constant value of 5450–5500 for $C_b \geqslant \sim 2.3$. Note that $R_{c2}$ reaches 5200 at $C_b=1.39$ (Qa5) and that both $R_{c1}$ and $R_{c2}$ are almost completely determined by the small quadrant-arc rounds ($r=1-5$ mm) shaped at the pipe inlet ($D=2.6$ cm).

(4) What factor primarily affects $R_c$ in the Reynolds' color-band experiment among $C_b$, separation of $R_{c1}$ and $R_{c2}$, waiting time, and supply water rate? Let us compare the magnitude of factors by considering the ratio of an upper $R_c$ to a lower $R_c$ under the same conditions. The first key factor should be $C_b$ or $C_r$ since the ratio is 12,200/2200=5.5 for $R_{c1}$ and 5500/2050=2.7 for $R_{c2}$. The second factor is the ratio of $R_{c1}$ to $R_{c2}$: the ratio is

**Table 6 Experimental values of $R_{c1}$ and $R_{c2}$ versus contraction ratio (Procedures 1 and 2)**

| | | | $R_{c1}$ | | | $R_{c2}$ | | |
|---|---|---|---|---|---|---|---|---|
| Entrance | $C_b$ | $C_r$ | Expt. | Eq. (2) | Error (%) | Expt. | Eq. (3) | Error (%) |
| St | 1 | 0 | 2200 | 2370 | 7.7 | 2050 | 2060 | 0.5 |
| Qa1 | 1.08 | 0.039 | 3600 | 3390 | −5.8 | 3150 | 3170 | 0.6 |
| Qa2 | 1.15 | 0.077 | 5000 | 4850 | −3.0 | 4100 | 4000 | −2.4 |
| Qa3 | 1.23 | 0.115 | 6700 | 6750 | 0.7 | 4650 | 4600 | −1.0 |
| Qa4 | 1.31 | 0.154 | 8750 | 9170 | 4.8 | 4850 | 4980 | 2.7 |
| Qa5 | 1.39 | 0.192 | 12,200 | 11980 | −1.8 | 5200 | 5100 | −1.9 |
| Be1 | 1.54 | ⋯ | 12,500 | ⋯ | ⋯ | 5200 | ⋯ | ⋯ |
| Be2 | 2.34 | ⋯ | 12,200 | ⋯ | ⋯ | 5450 | ⋯ | ⋯ |
| Be3 | 4 | ⋯ | 12,500 | ⋯ | ⋯ | 5500 | ⋯ | ⋯ |
| Be4 | 6 | ⋯ | 12,200 | ⋯ | ⋯ | 5500 | ⋯ | ⋯ |

**Table 7 Effects of supplying water on $R_c$ (Procedures 3 and 4)**

| $R_{c1}$ (10 l/m) | | | $R_{c1}$ (20 l/m) | | | $R_{c2}$ (10 l/m) | | | $R_{c2}$ (20 l/m) | | |
|---|---|---|---|---|---|---|---|---|---|---|---|
| No. | Re (×) | Re (○) | No. | Re (×) | Re (○) | No. | Re (×) | Re (○) | No. | Re (×) | Re (○) |
| 1 | 8050 | 7200 | 6 | 7500 | 6950 | 11 | 6450 | 6200 | 16 | 6250 | 5350 |
| 2 | 7500 | 7200 | 7 | 6000 | 5450 | 12 | 7000 | 6950 | 17 | 6500 | 5500 |
| 3 | 10050 | 9250 | 8 | 7200 | 6600 | 13 | 7700 | 7100 | 18 | 6350 | 5650 |
| 4 | 9150 | 8450 | 9 | 6750 | 6300 | 14 | 7900 | 7500 | 19 | 7000 | 6100 |
| 5 | 11650 | 11600 | 10 | 6900 | 6750 | 15 | 7900 | 7100 | 20 | 6650 | 6450 |
| Av. | 9300 | 8750 | — | 6850 | 6400 | — | 7400 | 6950 | — | 6550 | 5800 |
| $R_c$ | 9000 | | — | 6650 | | — | 7200 | | — | 6200 | |

12,200/5500=2.2 at $C_b$=6. The ratio when varying the waiting time is approximately 13,000/11,000=1.2 at $C_b$=6 (see Table 2). For varying rates of supplying water, the ratios are 9000/6650 =1.4 for $R_{c1}$ and 7200/6200=1.2 for $R_{c2}$ (see Table 7). Therefore, it is clear that $C_b$ or $C_r$ primarily affects both $R_{c1}$ and $R_{c2}$ and that the separation of $R_{c1}$ and $R_{c2}$ considerably affects $R_c$. In comparison with these main factors, the effects of the waiting time and the supply of water on $R_c$ are found to be relatively small.

(5) Consider whether or not the sharp edge is a singular point for $R_c$. It is generally believed that "If the inlet has sharp corners, flow separation occurs at the corners, and a vena contracta is formed. The fluid must accelerate locally to pass through the reduced flow area at the vena contracta [22]." Here, the singular point is defined as whether or not $R_c$ can be a smooth continuous function of $C_b$ or $C_r$ at $C_b$=1.

First, to evaluate the smoothness of experimental data, the method of least squares for a polynomial of degree of 2 against $C_r$ was adopted since the relative errors of a linear polynomial are considerably larger than that of a quadratic. From the data presented in Table 6, the value of $R_{c1}$ can be approximated as

$$R_{c1}(C_r) \approx 2370[65.7(C_r)^2 + 8.5(C_r) + 1], \quad 0 \leqslant C_r \leqslant 0.192 \tag{2}$$

Similarly, for the value of $R_{c2}$, we obtain the approximation

$$R_{c2}(C_r) \approx 2060[-39.6(C_r)^2 + 15.3(C_r) + 1], \quad 0 \leqslant C_r \leqslant 0.192 \tag{3}$$

The relative errors between such calculated values and empirical data are listed in Table 6. To compare Eqs. (2) and (3) with the experimental data, the calculated results are plotted together with the data in Fig. 5. The maximum absolute relative error of $R_{c1}$ is 7.7% at $C_r$=0 (St) and no greater than 5.8% for others. The errors of 7.7% and 5.8% for St and Qa1, respectively, may be caused by the difficulty of observations owing to intermittent turbulence. In contrast, the maximum absolute relative error of $R_{c2}$ is 2.7% at $C_r$=0.154 (Qa4) and no greater than 2.4% for others.

If the manufacturing error of the radius is 0.1 mm, then the absolute errors of $R_{c1}$ and $R_{c2}$ are estimated as

$$R_{c1}\left(\frac{0.01}{2.6}\right) \approx 80 \quad \text{and } R_{c2}\left(\frac{0.01}{2.6}\right) \approx 120 \tag{4}$$

Thus, the quadrant-arc rounds should be precisely manufactured. The precision of the quadrant-arc rounds was checked using a radius gauge that can measure radii from 1.0 mm to 7.0 mm in 17 levels.

Next, the transition length for the straight pipe flow was approximately 6–13 diameters at Re≈2000 but 4–7 diameters at Re≈13,000. (The transition length for bellmouth entrances elongates up to 20–50 diameters with increasing $C_b$, as Reynolds observed.) Therefore, it may be concluded that the sharp edge is not a singular point for transition phenomena at Re≈2000 because of the smoothness of Eqs. (2) and (3) near the inlet and the laminar-state region 6–13 diameters from the inlet.

(6) Under the condition of no plastic plates on the water surface and a waiting time of 10 min, the value of $R_{c2}$(St) was around 1750 rather than 2050 [23]. However, it was then difficult to sustain the transition state for more than a 1–2 cm drop of WL. For simplicity, replication of the same experimental conditions is desirable, so the case of no plates was omitted from this study.

**4.4 Effects of Supplying Water on $R_c$ (Procedures 3 and 4).** The maximum pump flux is 20 l/min. The measurement period is restricted by the volume of the 500 l storage tank. Thus, the water supply rate was determined to be 10 l/min and 20 l/min. The constant surface level of WL=0 was almost maintained for $R_{c1}$ as the flow flux was 6.98 l/min, 9.77 l/min, and 12.56 l/min at 15°C for Re=5000, 7000, and 9000, respectively. In the case of $R_{c2}$, however, the maximum flow flux was approximately 32 l/min, which is higher than 10 l/min or 20 l/min, so that WL fell from 0 cm to 6.6 cm or 3.6 cm in the first 3 min, respectively. At the drop of around 7 cm, Re changed slightly from 23,670 (32.36 l/min) to 22,490 (30.74 l/min) at 15.8°C.

The number of trials was five times for each case. Table 7 shows the experimental results. Re(○) and Re(×) stand for Re in a laminar and a turbulent state, respectively. $R_c$ values were roughly estimated as the average of Re(○) and Re(×) values since it is somewhat difficult to obtain a precise $R_c$ value because of the difficulty of a precise valve operation. The main features of our experimental results are as follows.

(1) It is clear that $R_{c1}$ and $R_{c2}$ decrease as the supply rate increases.
(2) Four $R_c$ values of 9000, 6650, 7200, and 6200 fall between $R_{c1}$ of 12,200 and $R_{c2}$ of 5500 at $C_b$=6, which were obtained under the no-supply condition.
(3) $R_{c1}$ of 6650 with a supply of 20 l/min is smaller than $R_{c2}$ of 7200 with 10 l/min. This indicates that the measuring period of 3–4 min causes the relaminarization from a turbulent state. Therefore, it is desirable to avoid gradual valve operation and to immediately set the valves to a target value of Re and observe the flow state.

**4.5 Discussion.** Let us discuss (i) transition in the fully developed region and (ii) the high value of $R_{c1}$=51,000 obtained by Ekman.

(i) Reynolds observed a transition in the fully developed region in his pressure-loss experiments. The transition occurs after the parabolic velocity profile becomes artificially distorted [6,24,25]. Then, puffs and slugs generated by the disturbances in the fully developed region were identical to the structures observed when the flow in the inlet region underwent transition. Transition was also observed in the fully developed region under natural disturbance conditions [26]. Here, a question arises: Where do the transitions take place under natural disturbance condi-

tions? Granger [14] and Tanekoda [21] stressed that the transition from laminar to turbulent flow occurs necessarily in the entrance region. Measurements of the transition length will be required in future research since it is one of the physical properties of transition as well as the intermittent turbulence [4].

(ii) Ekman obtained high $R_{c1}$ values of 13,000–51,000 using Reynolds' original apparatus. Our concern is Ekman's experimental procedure. Ekman accelerated the flow of water by adjusting the levered drain valve. The maximum WL in Reynolds' tank is 10 cm ($38-20-15.5/2=10$; see Sec. 3.1), so that the measurable WL would be 0–8 cm. For $R_c=51{,}000$, the velocity was 230 cm/s and the pipe diameter was 2.6 cm. If the flow rate were constant, the measurement period would be 47.2 s: (180 cm long $\times$40 cm wide$\times$8 cm WL)/($\pi/4\times2.6^2\times230$)=47.2 s. This period appears to be too short to control the flow rate.

Our starting from WL=6 cm corresponds to Reynolds' and Ekman's starting from WL=0 cm, where the initial water depth was 44 cm in this study and 38 cm for Reynolds' apparatus. On the basis of Ekman's WL, our results were as follows. (i) At the maximum Re$\approx$30,000, the initial laminar state persisted to WL =5 cm, and then the state became turbulent; (ii) when Re was approximately 10,000 for WL=0–3 cm and then increased to 30,000, the flow state was laminar for WL=0–7cm but became turbulent at WL=8cm.

Even under natural disturbance conditions, the flow phenomena or disturbances in the tank change with Re and WL; the flow phenomena change depending on experimental procedures. Therefore, the difference in experimental procedures might be the cause of Ekman's high $R_c$ values.

## 5 Conclusions

Re primarily and generally affects $R_c$ for a laminar-turbulent transition. For pipe flows, we experimentally studied what factor, besides Re, mainly affects $R_c$. For the first time, we observed that an apparent cause of the transition is the contraction ratio of pipe entrances, particularly that of the small quadrant-arc rounds cut at the pipe inlet.

In the entrance region of pipe flow, there are two critical values for the laminar-turbulent transition depending on the magnitude of disturbances: $R_{c1}$ from laminar to turbulent flow and $R_{c2}$ from turbulent to laminar flow. We devised Procedure 1 for $R_{c1}$ and Procedure 2 for $R_{c2}$, and a good reproduction of Reynolds' color-band experiments was achieved. Each entrance shape has a specific $R_{c1}$ and $R_{c2}$. The value of $R_{c1}$ continuously increased and reached a constant value of $R_{c1}\approx12{,}200-12{,}500$ for $C_b\geqq\sim1.4$, where Reynolds' value of 12,830 could be reproduced. Similarly, the value of $R_{c2}$ continuously increased and reached a constant value of $R_{c2}\approx5450-5500$ at $C_b\geqq\sim2.3$. Reynolds' value of 2030 could be reproduced by a method similar to Reynolds' color-band method when using a straight pipe.

If we assume a hysteresis curve that connects the two branches of $R_{c1}$ and $R_{c2}$, then each line appears to have the property of continuity even at a sharp-edge corner of the pipe. Accordingly, it may be deduced that the sharp-edge corner is not a singular point for transition phenomena at Re$\approx$2030.

Finally, future research will be focused on the analysis of the theoretical relationship between entrance shapes and $R_c$ [27].


## Acknowledgment

We wish to express our sincere appreciation to Emeritus Professor T. L. Kunii, Emeritus Professor T. Ikegami, and Professor M. Cohen of the University of Aizu for encouraging us. We would also like to sincerely thank Emeritus Professor J. D. Jackson of the University of Manchester, Emeritus Professor F. Stenger of the University of Utah, and Professor Y. Tsujimoto of Osaka University for their valuable advice and comments and the Information Synergy Center, Tohoku University for its outstanding computational services.


## Nomenclature

$C_b$ = contraction ratio ($D_b/D$)
$C_r$ = contraction ratio ($r/D$)
$D$ = pipe diameter
$D_b$ = bellmouth diameter
$r$ = radius of quadrant-arc round cut at the pipe inlet
$R_c$ = critical Re for the laminar-turbulent transition
$R_{c1}$ = $R_c$ from laminar to turbulent flow
$R_{c2}$ = $R_c$ from turbulent to laminar flow
$R_{c,\min}$ = minimum $R_c$
Re = Reynolds number based on diameter and mean velocity
WL = water level from the top water surface (WL =0 cm)

## References


[1] Kerswell, R. R., 2005, "Recent Progress in Understanding the Transition to Turbulence in a Pipe," Nonlinearity, **18**, pp. R17–R44.
[2] Eckhardt, B., Schneider, T. M., Hof, B., and Westerweel, J., 2007, "Turbulence Transition in Pipe Flow," Annu. Rev. Fluid Mech., **39**, pp. 447–468.
[3] Reynolds, O., 1883, "An Experimental Investigation of the Circumstances Which Determine Whether the Motion of Water Shall be Direct or Sinuous, and of the Law of Resistance in Parallel Channels," Philos. Trans. R. Soc. London, **174**, pp. 935–982.
[4] White, F. M., 1991, *Viscous Fluid Flow*, 2nd ed., McGraw-Hill, New York, pp. 369–370.
[5] Drazin, P. G., 2002, *Introduction to Hydrodynamic Stability*, Cambridge University Press, Cambridge, England, p. 5.
[6] Eliahou, S., Tumin, A., and Wygnanski, A., 1998, "Laminar-Turbulent Transition in Poiseuille Pipe Flow Subjected to Periodic Perturbation Emanating From the Wall," J. Fluid Mech., **361**, pp. 333–349.
[7] Chen, R.-Y., 1973, "Flow in the Entrance Region at Low Reynolds Numbers," ASME J. Fluids Eng., **95**, pp. 153–158.
[8] Lamb, H., 1975, *Hydrodynamics*, 6th ed., Cambridge University Press, London, p. 664.
[9] Ekman, V. W., 1910, "On the Change From Steady to Turbulent Motion of Liquids," Ark. Mat., Astron. Fys., **6**(12), pp. 1–16.
[10] Van Dyke, M., 1982, *An Album of Fluid Motion*, Parabolic, Stanford, p. 61.
[11] Darbyshire, A. G., and Mullin, T., 1995, "Transition to Turbulence in Constant-Mass-Flux Pipe Flow," J. Fluid Mech., **289**, pp. 83–114.
[12] Prandtl, L., and Tietjens, O. G., 1957, *Applied Hydro- and Aeromechanics*, Dover, New York, p. 35.
[13] ASHRAE Handbook Committee, 1997, *ASHRAE Handbook of Fundamentals*, ASHRAE, Atlanta, p. 32.32.
[14] Granger, R. A., 1995, *Fluid Mechanics*, Dover, New York, pp. 484 and 511–512.
[15] White, F. M., 1999, *Fluid Mechanics*, 4th ed., McGraw-Hill, New York, p. 372.
[16] Barnes, H. T., and Coker, E. G., 1904, "The Flow of Water Through Pipes: Experiments on Stream-Line Motion and the Measurement of Critical Velocity," Proc. R. Soc. London, Ser. A, **74**, pp. 341–356.
[17] Stanton, T. E., and Pannell, J. R., 1914, "Similarity of Motion in Relation to the Surface Friction of Fluids," Philos. Trans. R. Soc. London, Ser. A, **214**, pp. 199–224.
[18] Binnie, A. M., 1945, "A Double-Refraction Method of Detecting Turbulence in Liquids," Proc. Phys. Soc. London, **57**, pp. 390–402.
[19] Senecal, V. E., and Rothfus, R. R., 1953, "Transition Flow of Fluids in Smooth Tubes," Chem. Eng. Prog., **49**(10), pp. 533–538.
[20] Kanda, H., and Oshima, K., 1987, "Numerical Study of the Entrance Flow and Its Transition in a Circular Pipe (2)," *Proceedings of the Symposium on the Mechanics for Space Flight 1986*, Report No. SP5, Instiution of Space and Astronautical Science, Tokyo, pp. 47–76.
[21] Tanekoda, S., 1988, *Fluid Dynamics by Learning From Flow Images*, Asakura, Tokyo, p. 165, in Japanese.
[22] Fox, R. W., and McDonald, A. T., 1994, *Introduction to Fluid Mechanics*, Wiley, New York, pp. 336–337.

[23] Kanda, H., and Yanagiya, T., 2005, "Experimental Conditions for Minimum Critical Reynolds Number in Pipe Flow," *Proceedings of the ASME International Mechanical Engineering Congress and Exposition*, Orlando, Paper No. IMECE2005-80637.
[24] Leite, R. J., 1959, "An Experimental Investigation of the Stability of Poiseuille Flow," J. Fluid Mech., **5**, pp. 81–96.
[25] Rubin, Y., Wygnanski, I. J., and Haritonidis, J. H., 1979, "Further Observations on Transition in a Pipe," *Proceedings of the IUTAM Symposium on Laminar-Turbulent Transition*, Stuttgart, pp. 17–26.
[26] Reshotko, E., 1958, "Experimental Study of the Stability of Pipe Flow. I. Establishment of an Axially Symmetric Poiseuille Flow," Jet Propulsion Laboratory, Pasadena, Progress Report No. 20-364.
[27] Kanda, H., "Calculation of Minimum Critical Reynolds Number in Pipe Flows," *Proceedings of the 21th CFD Symposium*, JSFM, Paper No. D3-2.

# Acoustic Power Calculation in Deep Cavity Flows: A Semiempirical Approach

**P. Oshkai**[1]
e-mail: poshkai@me.uvic.ca

**T. Yan**

**A. Velikorodny**

**S. VanCaeseele**

Department of Mechanical Engineering,
University of Victoria,
P.O. Box 3055 STN CSC,
Victoria, BC, Canada, V8W 3P6

*Acoustic power generated by turbulent flow over a coaxial side branch (deep cavity) resonator mounted in a rectangular duct is calculated using a semiempirical approach. Instantaneous flow velocity is decomposed into an irrotational acoustic component and vorticity-bearing hydrodynamic field. The total velocity at several phases of the acoustic oscillation cycle is measured using digital particle image velocimetry. The acoustic velocity field is numerically calculated. The emphasis is on the effect of the accurate geometry representation for the acoustic field modeling on the calculated acoustic power. Despite the generally low levels of acoustic radiation from the coaxial side branches, when the main duct is incorporated into the model for calculation of the acoustic velocity, the acoustic velocity exhibits substantial horizontal (streamwise) components in the vicinity of the cavity corners. This streamwise acoustic velocity correlates with hydrodynamic horizontal velocity fluctuations, thus contributing to the calculated acoustic power. Spatial structure and strength of the acoustic source change as the distance between the side branches varies. Global quantitative imaging approach is used to characterize the transformation of the acoustic source structure in terms of patterns of instantaneous and phase-averaged flow velocity, vorticity, and streamline topology as well as time-averaged acoustic power.* [DOI: 10.1115/1.2907413]

*Keywords: flow-acoustic coupling, side branch resonators, PIV*

## Introduction

Internal flow past a deep cavity (side branch) mounted in a duct is often characterized by the coupling between the self-sustained oscillations of the separated shear layer that forms across the mouth of the cavity and the resonant acoustic modes of the side branch. This resonant phenomenon, which occurs in many industrial processes involving transport of a fluid through a pipeline and has been reported by several authors including Chen and Sturchler [1] and Baldwin and Simmons [2], involves high-amplitude pressure pulsations and flow oscillations.

Flow tone generation past multiple side branches has been a subject of many investigations, as summarized by Ziada and Bühlmann [3]. Classification of side branch resonances as fluid-resonant oscillators was performed by Rockwell and Naudascher [4]. Keller and Escudier [5] investigated flow-acoustic resonances in covered cavities and discussed the transfer of energy from the mean flow to the acoustic wave field. It was shown that in the case of high Mach number flow over a covered cavity, the excitation mechanism is gas dynamic in nature. In contrast to this regime is the edge-tone generation mechanism (i.e., impingement of vortical structures on a solid boundary), which is predominant in the case of low Mach number flows that are subject of the present study. When a turbulent flow passes over a deep cavity (side branch) mounted in a duct, a shear layer is created between the moving fluid in the main duct and the stationary fluid in the side branch. Flow-acoustic coupling occurs when the frequency of the hydrodynamic shear layer instability matches the resonant acoustic mode of the side branch. The resonant acoustic waves interact with small-scale vortical structures in the shear layer. This interaction results in formation of large-scale vortices that are convected downstream and eventually release part of their energy to the acoustic field. This energy contributes to the increase of the amplitude of the acoustic waves and, in turn, to the radiated noise.

Characterization of the acoustic noise source in terms of its shape and the contribution of individual vortices to the generated acoustic power continue to present significant challenges despite the considerable insight provided by recent investigations. Hourigan et al. [6] and Stoneman et al. [7] characterized acoustically coupled shear layer oscillations in terms of the number of vortices formed in the shear layer during a typical oscillation cycle. The theoretical background for these experimental and numerical studies was provided by the aerodynamic sound theory outlined by Howe [8]. In addition, Dequand et al. [9,10] studied the behavior of acoustically coupled flows over deep cavity resonator. The authors identified the characteristic flow regimes and provided the numerical and analytical models of the flow. More recently, investigations of flow-acoustic coupling mechanisms related to cavity flows were conducted by Amandolèse et al. [11], Oshkai et al. [12], and Arthurs et al. [13].

The foregoing investigations have provided considerable insight into the physics of flow-acoustic coupling. The present study aims to address a number of issues that remain unresolved. The results presented herein correspond to a low Mach number turbulent flow past a coaxial side branch resonator. In contrast to the earlier work, the present study represents the first application of vortex sound theory in conjunction with global quantitative flow imaging and numerical simulation of the two-dimensional acoustic wave field. Implementation of this semiempirical approach allows identification of regions where the energy exchange between the acoustic and vorticity-bearing fields takes place.

The present study focuses on a coaxial side branch system, which involves two side branches mounted on the opposite sides of a rectangular duct and inline with each other. A schematic of the experimental arrangement is shown in Fig. 1. Global, quantitative images of the flow were obtained using digital particle image velocimetry (DPIV). These images, obtained in conjunction with measurements of acoustic pressure, provide insight into the

[1]Corresponding author.

Contributed by the Fluids Engineering Division of ASME for publication in the JOURNAL OF FLUIDS ENGINEERING. Manuscript received July 12, 2007; final manuscript received February 8, 2008; published online May 1, 2008. Assoc. Editor: Juergen Kompenhans. Paper presented at the 2007 ASME Pressure Vessels and Piping Conference (PVP2007), San Antonio, TX, July 22–26, 2007.

  

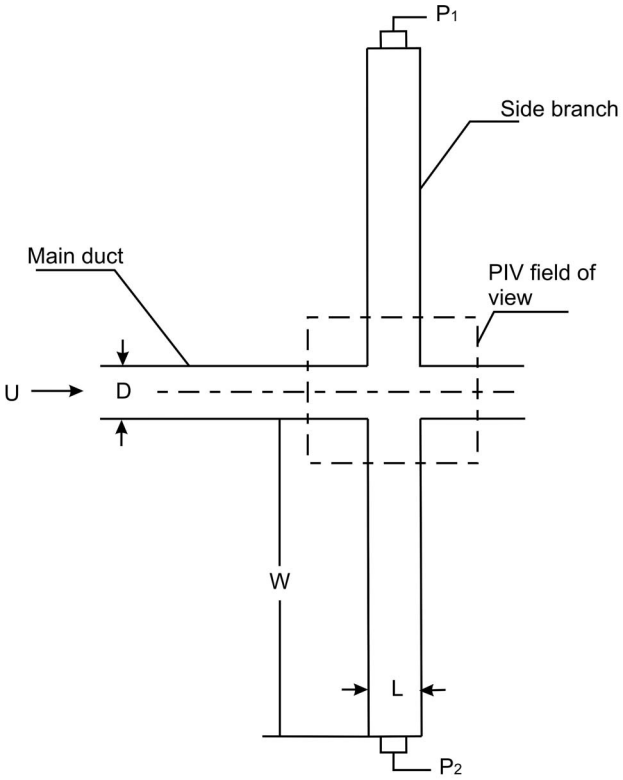


**Fig. 1 Schematic of the coaxial side branch resonator**

spatial structure of the acoustic source corresponding to two distinct hydrodynamic modes of shear layer oscillation for two values of the main duct width. In order to provide additional details of the acoustic source structure, the acoustic mode shapes encountered during the generation of flow tones were numerically simulated. The acoustic velocity was deduced from these numerical calculations.

## Experimental System and Techniques

Complete details of the experimental system are described by Oshkai et al. [12]. Only the essential features are described herein.

Air was supplied by a compressor located in a separate room and isolated from the experimental apparatus. An inlet plenum served as a settling chamber upstream of the coaxial side branch system, which is schematically shown in Fig. 1.

The duct had a streamwise length of 492 mm and a height (the out-of-page dimension) of 25.4 mm. Two coaxial side branches were mounted on the opposite sides of the main duct, 454 mm downstream of the duct inlet. The side branches had a square cross section, and were constructed of a 3.2-mm-thick aluminum. The main duct extended for additional 12.6 mm downstream of the side branch arrangement.

In the present investigation, the flow features are compared for the two cases corresponding to a relatively large value of the main duct width ($D=13$ mm) and a smaller value of $D=6.5$ mm. Dimensions of the individual side branches ($L=25.4$ mm, $W=483$ mm) were chosen to provide an opportunity for observation of at least two distinct hydrodynamic modes of the shear layer oscillation for both values of the main duct width.

Measurements of unsteady pressure were performed using piezoelectric microphone pressure transducers, indicated as $P_1$ and $P_2$ in Fig. 1. The pressure transducers had a nominal sensitivity of 10340 V/Pa and were deployed at the dead ends of side branch resonator. The pressure signals were converted to a digital form at the time of acquisition.

DPIV was employed for the purposes of global, quantitative flow visualization. Oil droplets with the typical diameter of approximately 1 $\mu$m were used as tracer particles. Images of the tracers, which were illuminated by a laser, were captured by a high-resolution digital camera and processed to yield the global instantaneous flow velocity measurements. Depending on the flow velocity and the factor of magnification of the camera lens, the delay of the two pulses was chosen such that adequate displacements of the particle images on the charge coupled device (CCD) are obtained.

For the present study, a lens with a focal length of 60 mm was used in conjunction with a $1376\times1040$ pixel CCD. Each particle image was divided into interrogation windows that corresponded to individual vectors in the velocity field. A multipass interrogation process with a final interrogation window size of $32\times32$ pixels and 50% overlap between the windows was employed to provide a physical resolution of 73 pixels/mm, which corresponds to the velocity vector field resolution of $0.22\times0.22$ mm$^2$. The system provided 4.9 cross-correlated images per second. The velocity data contained approximately 2% bias uncertainty due to the erroneous vectors that were replaced by interpolation during postprocessing stage. In addition, errors associated with location of the particle displacement correlation peak (precision errors) accounted for uncertainty of approximately 2%.

The trigger signal to the laser was recorded together with the acoustic pressure signals. This provided the information regarding the phase of acquisition of each velocity field with respect to a typical acoustic cycle.

Since the temporal resolution of the DPIV system was limited to 4.9 Hz (in terms of cross-correlated image pairs), while the range of the acoustic frequencies in the present study was between 172 Hz and 883 Hz, a phase-locking technique was employed in the present study, which enabled acquisition of 100 cross-correlated pairs of flow images at each predetermined phase of the acoustic oscillation cycle using the real-time acoustic pressure signal as a reference. The acoustic pressure signal was acquired using an analog-to-digital data acquisition board (National Instruments PXI-4472). A computer code was developed to control the data acquisition board and to determine the point of the occurrence of zero amplitude with a rising edge in the real-time pressure signal. At the corresponding time instant, single pulse transistor-transistor logic (TTL) signal was sent to trigger the camera for image capture.

The acoustic pressure signal was essentially sinusoidal, and the dominant frequency was well separated from other components. Therefore, the acoustic pressure signal was not filtered, and the ambiguity of the phase calculation was estimated based on the predominant frequency of the shear layer oscillation mode and the data acquisition frequency. The period of the pressure data acquisition (0.00002 s) corresponds to approximately 4 deg of the complete oscillation period, which results in the ambiguity of $\pm4$ deg in the phase calculation.

One hundred pairs of images at each predetermined phase of the acoustic oscillation cycle were acquired. Ensemble averaging of the PIV images corresponding to the same phase was performed to produce a single global quantitative representation of the flow at that phase.

## Numerical Simulation of Acoustic Field

Acoustic mode shapes encountered during the experiments were numerically modeled. Solution of a modified two-dimensional Helmholtz equation was obtained using COMSOL 3.2 software. The boundary conditions at the open ends of the duct were set to zero acoustic pressure. All other surfaces were modeled as solid boundaries. Figure 2 shows the computational domain and boundary conditions for the case of the wide main duct ($D/L=0.5$). A nonuniform computational mesh with a total of 33,920 triangular elements was employed to provide adequate resolution in these regions. A close-up of the refined mesh in the

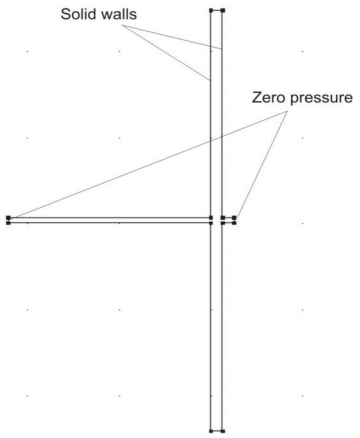


**Fig. 2 Computational domain and boundary conditions**

cross-junction region is shown in Fig. 3. The acoustic field defined as the unsteady potential flow component of the velocity field has singularities at the sharp corners of the cross junction. In order to numerically resolve these singularities, the cross-junction corners were represented by curved elements with a radius of 0.1 mm. The radius of curvature was chosen to be substantially smaller than the resolution of the experimentally obtained velocity field while ensuring numerical convergence upon grid refinement. All mathematically possible eigenvalues for the frequency range of interest were simulated. The corresponding pressure distributions were used to calculate the values of acoustic velocity during the generation of resonant tones.

It should be pointed out that an alternative approach to simulating the acoustic field could involve using low-frequency Green's function, as proposed by Howe [8]. The correct singular behavior of Green's function at the sharp corners can be obtained by matching the acoustic velocity in the region represented by plane wave propagation to an incompressible potential flow representation.

The simulated frequencies are compared to the measured values in the subsequent sections. Moreover, these results are compared to the frequency values predicted by a simple theoretical resonator model that is commonly employed to represent deep open-closed coaxial side branches.

While the numerical simulation yields all mathematically possible eigenvalues, only the modes that correspond to low radiation losses into the main duct can be excited in the physical system. The acoustic modes corresponding to the in-phase oscillation of the pressure in the side branches are strongly damped by radiation along the main pipe and, consequently, are not excited in the experimental apparatus. In the vicinity of the corners of the cross junction, nonzero values of acoustic velocity are also observed during excitation of the resonant modes, as it is discussed in the Acoustic Power section. While affecting the spatial structure of the acoustic noise source, this nonzero acoustic velocity corresponds to relatively low values of acoustic flux into the main duct and therefore to negligible acoustic radiation.

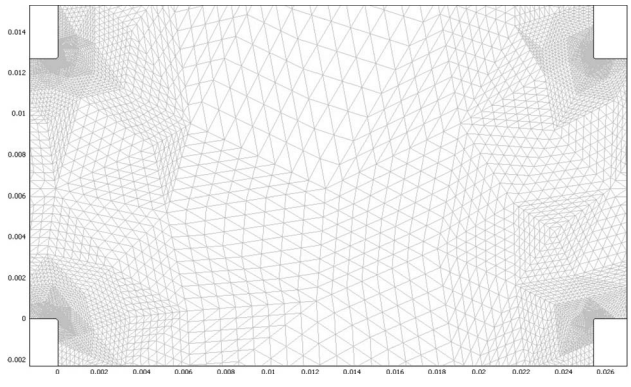

**Fig. 3 Close-up of the computational mesh in the cross-junction region**

**Table 1 Simulated, theoretical, and measured resonant frequencies for the case of the wide main duct ($D/L=0.5$)**

| $f_{simulated}$, Hz | $f_{theoretical}$, Hz | $f_{measured}$, Hz |
|---|---|---|
| $f_1=143$ | | |
| $f_2=175$ | $f_1=175$ | $f_1=172$ |
| $f_3=356$ | | |
| $f_4=459$ | | |
| $f_5=527$ | $f_3=526$ | $f_3=521$ |
| $f_6=711$ | | |
| $f_7=810$ | | |
| $f_8=879$ | $f_5=877$ | $f_5=878$ |
| $f_9=1064$ | | |
| $f_{10}=1177$ | | |
| $f_{11}=1230$ | $f_7=1228$ | |

It has also been demonstrated (e.g., by Ziada et al. [14]) that for long side branches ($W/D \gg 1$), the resonant frequencies of a coaxial side branch resonator can be predicted using the following theoretical expression:

$$f = \frac{(2n-1)c_0}{2(2W+D)}, \quad n = 1,2,3,\ldots \tag{1}$$

where $m=2n-1$ is the acoustic resonant mode number and $c_0 = 343$ m/s is the speed of sound.

Tables 1 and 2 compare the simulated frequencies to those observed in the experiments as well as to the values predicted by Eq. (1) for the two values of the main duct width ($D/L=0.5$ and 0.25), respectively. Here, $f_m$ refers to the $m$th oscillation mode. It should be noted that both the theoretical and the numerical predictions of the resonant frequencies are within $\pm 3\%$ of the measured frequencies of the acoustic modes, which are described in detail in the following section.

Based on the frequency results alone, it can be concluded that the coaxial side branches strongly exhibit coupled acoustic behavior for both values of the main duct width. These observations are in general agreement with the results of Arthurs et al. [13] However, as it is demonstrated in subsequent sections, when the width of the main duct is decreased, increased hydrodynamic interaction between the separated shear layers results in substantial changes in the structure of the acoustic source.

**Table 2 Simulated, theoretical, and measured resonant frequencies for the case of the narrow main duct ($D/L=0.25$)**

| $f_{simulated}$, Hz | $f_{theoretical}$, Hz | $f_{measured}$, Hz |
|---|---|---|
| $f_1=143$ | | |
| $f_2=175$ | $f_1=177$ | $f_1=172$ |
| $f_3=358$ | | |
| $f_4=432$ | | |
| $f_5=526$ | $f_3=530$ | $f_3=524$ |
| $f_6=710$ | | |
| $f_7=793$ | | |
| $f_8=877$ | $f_5=883$ | $f_5=883$ |
| $f_9=1061$ | | |
| $f_{10}=1168$ | | |
| $f_{11}=1228$ | $f_7=1236$ | |

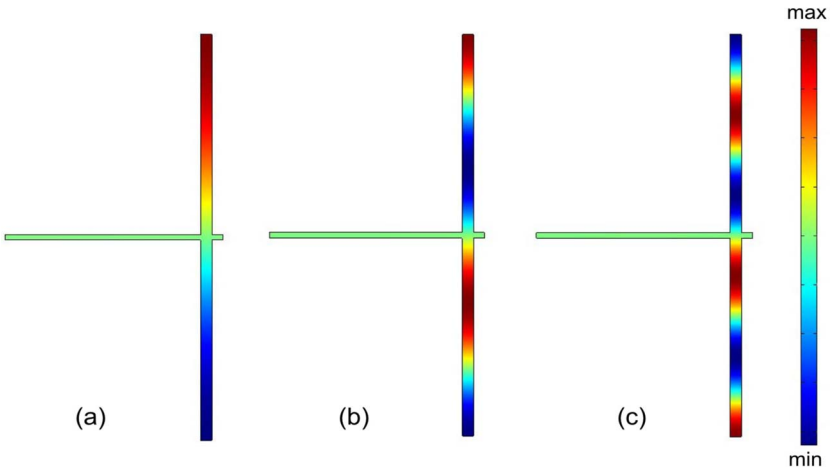


**Fig. 4 Resonant acoustic mode shapes: (*a*) first mode (*f*=175 Hz); (*b*) third mode (*f*=527 Hz); (*c*) fifth mode (*f*=879 Hz)**

Mode shapes corresponding to the first three resonant acoustic modes ($m=1$, 3, and 5) are shown in Fig. 4. For low Mach number flows, the total flow velocity can be represented by a linear combination of an incompressible vorticity-bearing velocity and an irrotational acoustic velocity [8]. The acoustic velocity is defined as the unsteady component of the irrotational part of the total flow velocity. Thus, the predicted mode shapes were used to calculate patterns of acoustic velocity at several phases of a typical acoustic oscillation cycle during excitation of the coaxial side branch resonator by a fully turbulent inflow. The acoustic velocity was determined from the values of the local acceleration due to fluctuations of acoustic pressure (Eq. (3)), as it is described in the Acoustic Power section. The incompressible vorticity-bearing (hydrodynamic) velocity field was calculated by subtracting the acoustic velocity from the total phase-averaged flow velocity that was experimentally measured using the DPIV technique, as described in the previous section.

## Overview of Acoustic Response

The three-dimensional plots of Fig. 5 show the magnitude of the measured acoustic pressure peaks on a plane of frequency versus the mean flow velocity magnitude in the main duct.

The spectra of Fig. 5(*a*) correspond to the wide main duct ($D/L=0.5$). The plot shows that the first acoustic mode ($f=172$ Hz) is excited first as the velocity increases. The second mode to be excited is the fifth acoustic mode ($f=878$ Hz). The highest peak corresponds to the third acoustic mode ($f=521$ Hz). The measured frequencies are within $\pm 3\%$ of the theoretical resonance frequencies, which confirms that the model described by Eq. (1) provides a good prediction of resonant acoustic modes. Figure 5(*a*) also indicates that the amplitude of acoustic oscillation is increased as the mean flow velocity increases.

The corresponding plot for the narrow main duct ($D/L=0.25$) is shown in Fig. 5(*b*). Similar to the wide duct case, the first, fifth, and third acoustic modes are sequentially excited as the flow velocity increases. In contrast to the previous case, however, the frequency of the dominant resonant mode switches from the fifth to the seventh acoustic mode as the flow velocity $U$ reaches approximately 43 m/s. Significant pressure peaks also exist at the first acoustic mode for the range of flow velocities between $U=43$ m/s and 48 m/s. It is suggested that this quasi-locked-on response of the resonator occurs due to increased interaction between the separated shear layers with the decrease of the main duct width. As the velocity is further increased, the predominant pressure peak switches back to the third acoustic mode at $U=48$ m/s.

## Overview of Flow Patterns

Instantaneous images of flow velocity $\underline{V}$ and out-of-plane vorticity $\omega_z$ corresponding to the locked-on flow tone for the case of the wide duct ($D/L=0.5$) are shown in Fig. 6. The images corre-

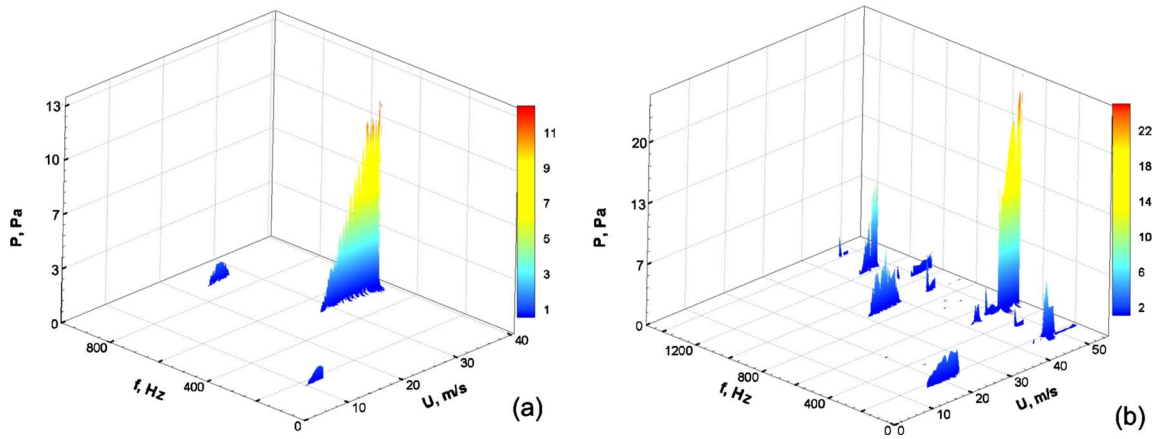


**Fig. 5 Three-dimensional representation of pressure amplitude as a function of frequency and flow velocity: (*a*) *D*/*L*=0.5; (*b*) *D*/*L*=0.25**

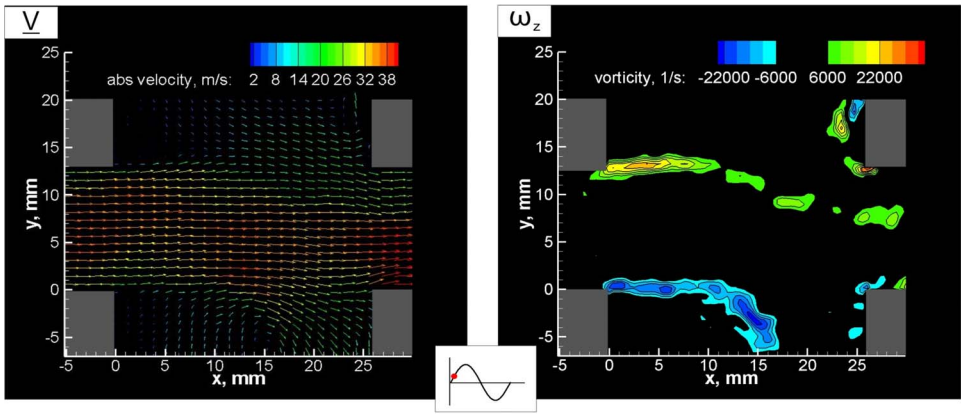


**Fig. 6 Instantaneous flow patterns corresponding to the first hydrodynamic oscillation mode ($D/L=0.5$, Sr=0.34, $U_{ac}/U=0.0005$)**

spond to a phase in the acoustic oscillation cycle, which is indicated by a circle in the inset schematic. The mean flow velocity is 38 m/s and the acoustic frequency $f=521$ Hz, which yields a Strouhal number of $\mathrm{Sr}=fL/U=0.34$. The observed value of the dimensionless acoustic velocity $U_{ac}/U$ for this case is equal to 0.0005. Assuming planar acoustic wave propagation inside the side branches, the acoustic velocity amplitude $U_{ac}$ can be determined from the acoustic pressure amplitude $P$: $U_{ac}=P/\rho_0 c_0$, where $\rho_0$ is the mean fluid density and $c_0$ is the speed of sound.

The vorticity plot illustrates how coupling of the shear layer instability with the acoustic waves results in rollup of the shear layer into larger-scale vortical structures as they are convected downstream along the mouth of the side branch. These large-scale vortices generally have lower peak vorticity than the small-scale vortices located immediately downstream of the separation corner of the cavity, but possess larger circulation values and increased convective speed. Images presented herein correspond to the first hydrodynamic mode of the shear layer oscillation, when one large-scale vortex forms in the shear layer during a typical oscillation cycle.

Figure 6 illustrates a flow regime during which the two shear layers that form across the top and bottom side branches impinge upon the downstream corners of the corresponding side branches. The vorticity of the opposite sign that is induced in the vicinity of the downstream corners of the side branches due to the interaction of the separated shear layer with the solid boundary.

The flow regime corresponding to the increased shear layer interaction that occurs at the lower value of the main duct width ($D/L=0.25$) shown in Fig. 7, where the Strouhal number Sr $=0.28$ and the dimensionless acoustic velocity $U_{ac}/U=0.001$. In this regime, the transverse oscillations of the shear layers result in their impingement on the downstream corners of the opposing side branches. This interaction suggests that the structure of the acoustic power source will significantly change as the main duct width is decreased.

In addition to instantaneous flow measurements, implementation of real-time analysis of measured acoustic pressure in conjunction with DPIV imaging resulted in a series of global quantitative images of the acoustically coupled flow that show formation and propagation of large-scale vortices during a typical acoustic cycle. Figure 8 shows the phase averaged flow patterns for the two values of the main duct width $D$ at the same phase of the acoustic cycle ($\varphi=10$ deg of a sinusoidal pressure fluctuation). These flow patterns were obtained by ensemble averaging 100 DPIV measurements that were acquired at the same phase of the acoustic pressure oscillation cycle. The left and right columns of Fig. 8 correspond to the values of $D/L$ of 0.5 and 0.25, respectively. The images show plots of phase-averaged flow velocity $\langle \underline{V} \rangle_p$, vorticity $\langle \omega_z \rangle_p$, and streamline patterns (from top to bottom). At this phase, the acoustic velocity is directed into the upper side branch, and a new vortex is formed at the upstream edge of upper side branch (indicated in the vorticity plot). The vortex in the lower shear layer has been fully developed and convected downstream. The patterns of the streamline topology correspond to the reference frame moving from left to right with the speed of $0.5U$, which

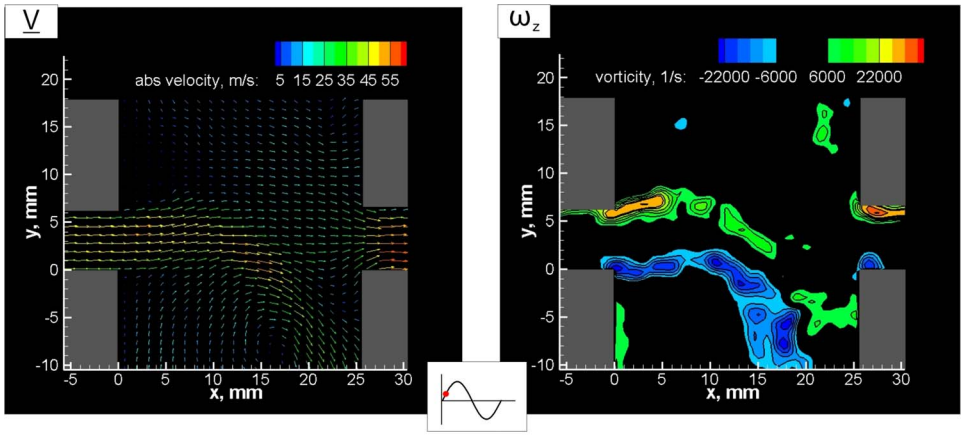


**Fig. 7 Instantaneous flow patterns corresponding to the first hydrodynamic oscillation mode ($D/L=0.25$, Sr=0.28, $U_{ac}/U=0.001$)**

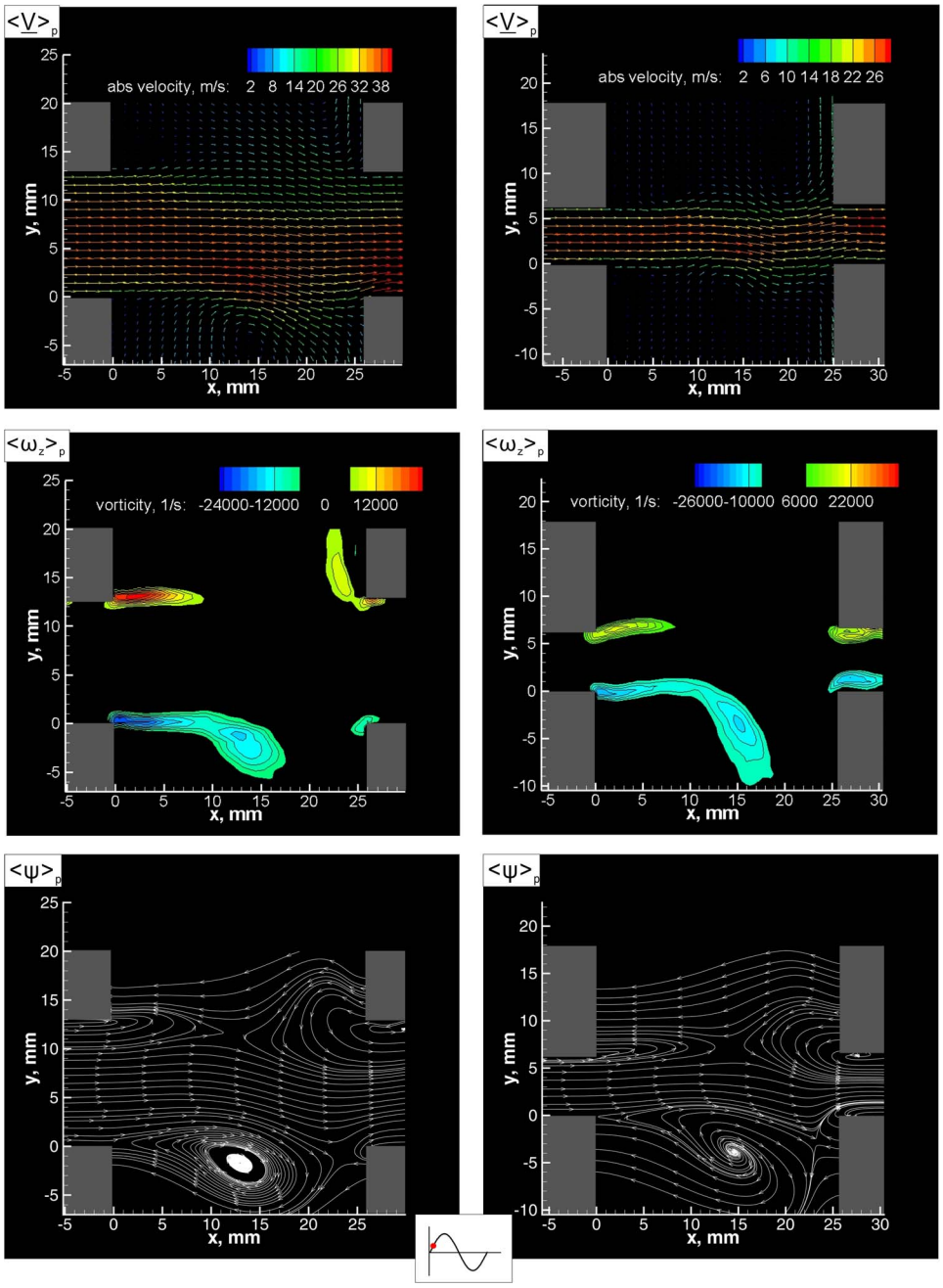


**Fig. 8 Phase-averaged flow patterns corresponding to the first hydrodynamic oscillation mode at $\varphi$=10 deg**

approximates the average convective speed of the large-scale vortices in the shear layers. The plots show higher levels of circulation of the large-scale vortices in the case of the narrower main duct. In addition, the interaction between the vortical structures in the top and bottom shear layers is increased as the main duct becomes narrower.

## Acoustic Power

The acoustic energy produced by the vortex shedding can accumulate due to the presence of the acoustic resonating modes with a high quality factor. The instantaneous acoustic power $P_w$ generated by vorticity $\underline{\omega}$, within a volume $V$, can be obtained from

$$P_w = \int\int\int_V -\rho_0(\underline{\omega} \times \underline{V}) \cdot \underline{u_{ac}} dV \tag{2}$$

where $\rho_0$ is the fluid density, $\underline{V}$ is the fluid velocity, and $u_{ac}$ is the acoustic particle velocity. The theoretical framework for this approach to acoustic power calculation has been developed by Howe [8]. It should be noted that while the conditions for its applicability are satisfied in the present investigation, the case of the narrow main duct can be represented by a jet-drive model outlined by Dequand [9,10].

The hydrodynamic contribution to the acoustic power integral, $(\underline{\omega} \times \underline{V})$, was calculated based on the global phase-averaged flow measurements presented in the Experimental System and Tech-

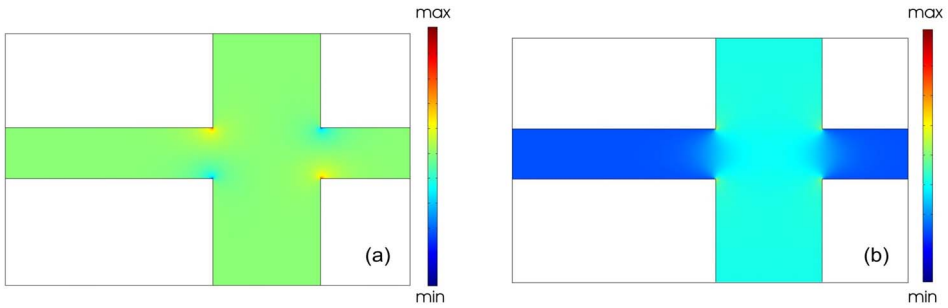


**Fig. 9 Amplitude of the horizontal and the vertical components of acoustic velocity ($D/L=0.5$): (*a*) $(U_{ac})_x$; (*b*) $(U_{ac})_y$**

niques section. The amplitudes of the horizontal and vertical components of the acoustic particle velocity $\underline{u}_{ac}$ were determined from the values of the local acceleration due to fluctuations of acoustic pressure $p$:

$$(U_{ac})_i = -\frac{1}{2\pi f \rho_0}\frac{\partial p}{\partial x_i} \tag{3}$$

where $f$ is the resonant frequency. The numerically simulated pressure mode shapes that are shown in Figs. 4 and 5 were used to calculate the magnitudes of the acoustic velocity corresponding to the first and the third resonant acoustic modes. The acoustic velocity fluctuations were assumed to be $\pi/2$ radians out of phase with the fluctuations of the acoustic pressure.

Distributions of the amplitude of the horizontal and vertical components of the acoustic particle velocity $\underline{u}_{ac}$ in the cross-junction region are shown in Fig. 9.

The acoustic wave is largely two dimensional, with a primary direction of propagation inline with the coaxial branches ($y$-direction). Low values of the horizontal component of the acoustic velocity $(U_{ac})_x$ are observed in the side branches and in the main duct. This effect corresponds to the low values of acoustic losses into the main duct that were reported for similar configurations by Arthurs et al. [13] and Ziada et al. [14], among others. However, elevated values of the horizontal acoustic velocity $(U_{ac})_x$ are observed in the vicinity of the corners of the side branches. The pattern of the vertical component of the acoustic velocity $(U_{ac})_y$ shown in Fig. 9(*b*) also exhibits deviations from the one-dimensional wave propagation pattern in the vicinity of the leading and trailing corners of the cross junction. Previously developed semiempirical approaches for acoustic power calculation (Oshkai et al. [12]) employed a one-dimensional acoustic model, which did not account for variations of the acoustic velocity in the vicinity of the corners. The present experimental setup has been optimized to provide effective seeding of the flow and to allow optical access to the regions immediately close to the solid boundaries.

Pattern of the time-averaged acoustic power generated during the first hydrodynamic oscillation mode in the case of the wide duct ($D/L=0.5$) is shown in Fig. 10(*a*). The structure of the acoustic power producing region exhibits two distinct source-sink pairs. The sinks correspond to the regions where the acoustic energy is absorbed by the flow field. The sources correspond to the large-scale vortical structures. In addition, a region of negative acoustic power is located along the centerline of the main duct and close to the downstream end of the cross junction. These negative values are due to the correlation between the low values of acoustic flux into the main duct, which was observed in Fig. 9(*a*) and the distributed vorticity that exists in this region.

The decrease of the main duct width to $D/L=0.25$ corresponds to increased interaction between the shear layers, which results in formation of a single acoustic power source region close to the centerline of the main duct, as shown in Fig. 10(*b*). The source is accompanied by two sinks that correspond to the regions in the shear layers where vortex development takes place. It should be noted that the source region extends across almost the entire opening of the coaxial side branch resonator. The peak values of the generated acoustic power correspond to large-scale vortices, which extend far into the side branches during the transverse oscillations of the separated shear layers. Moreover, separated flow regions immediately downstream of the impingement corners of the side branches result in the formation of two additional sources of acoustic power.

Pattern of the time-averaged acoustic power generated during the second hydrodynamic oscillation mode in the case of the wide

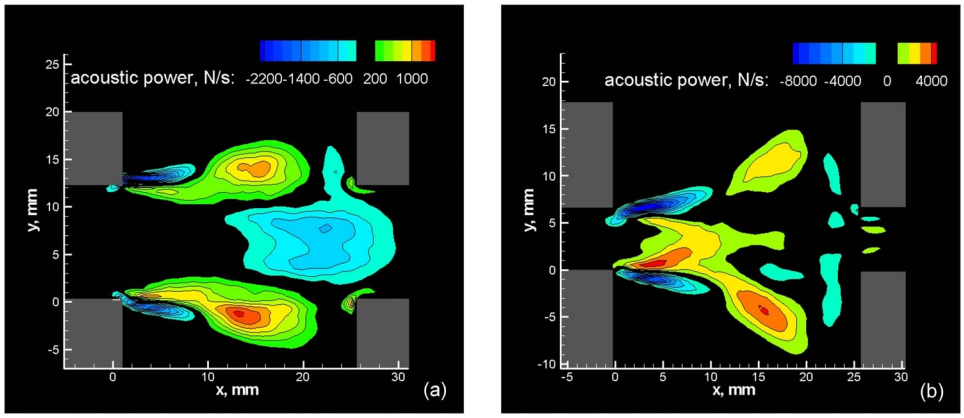


**Fig. 10 Patterns of time-averaged acoustic power corresponding to the first hydrodynamic oscillation mode: (*a*) $D/L=0.5$; (*b*) $D/L=0.25$**

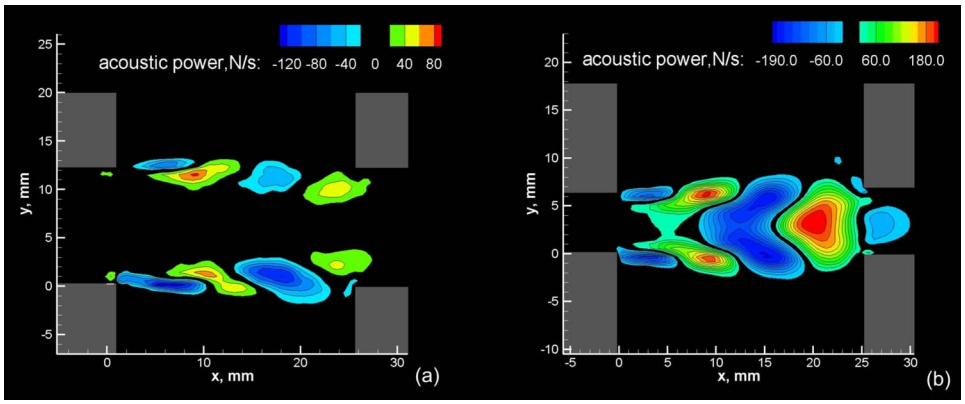


**Fig. 11 Patterns of time-averaged acoustic power corresponding to the second hydrodynamic oscillation mode. (*a*) $D/L=0.5$; (*b*) $D/L=0.25$**

duct ($D/L=0.5$) is shown in Fig. 11(*a*). A more complex acoustic power source structure is observed in comparison to that of the first hydrodynamic mode. The peak amplitude of acoustic power is significantly lower than the values observed in Fig. 10(*a*). In this flow regime, two vortices traverse the mouth of the side branch during a typical period of acoustic velocity oscillation. As they are convected across the cavity opening, each vortex provides a positive and a negative contribution to the acoustic power budget. Since there is no significant interaction between the upper and lower shear layers, four discrete pairs of sink and source regions exist over the junction area.

The spatial distribution of the generated acoustic power is substantially different in the case of the narrow main duct, $D/L=0.25$ (shown in Fig. 11(*b*)). Immediately after the separation, the amplitude of the transverse oscillations of the shear layers is limited, and two discrete source-sink pairs exist in the vicinity of the upstream corner of the junction. The two sink regions with peak amplitudes of 190 N/s are located at $x=4$ mm. Farther downstream, the transverse shear layer undulations increase in amplitude, and a large single sink of acoustic power is present. This sink region exhibits high levels of negative acoustic power due to the increasing circulation of the large-scale vortices. Prior to impingement on the downstream side branch corner, the two interacting shear layers produce a single large-scale source region. Flow separation from the downstream corners of the side branches correlates with the acoustic flux into the main duct and results in negative contribution to the acoustic power budget.

## Conclusions

Acoustic response of a coaxial side branch resonator was investigated using a combination of DPIV imaging with the measurements of unsteady acoustic pressure. Resonant flow tones corresponding to the two hydrodynamic modes of shear layer oscillation are characterized in terms of acoustic pressure amplitude and frequency of the dominant pressure peak.

As the flow velocity in the main duct is increased, the available resonant acoustic modes of the coaxial side branches are excited in the same order for the wide and narrow main ducts. However, for the narrow value of the duct, the predominant pressure peak exhibited a shift to a lower acoustic mode. It is suggested that this shift is due to the increased level of interaction between the separated shear layers.

Frequencies of the resonant acoustic modes and corresponding mode shapes were also numerically simulated. The calculated frequencies were in good agreement with the measured values, as well as with the frequencies predicted by a theoretical model for long coaxial side branches.

In addition, the decrease of the main duct width has a pronounced effect on the acoustic power source structure due to the increased interaction between the unsteady shear layers that form across the side branches. The spatial structure of the acoustic power producing region changes from two independent sources to a single source as the main duct width decreases. Moreover, acoustic flux into the main duct in conjunction with flow separation at the downstream corners of the side branches results in formation of additional sources of acoustic power.

It should be noted that viscothermal damping along the pipe walls has significant effect on acoustic response of systems with long side branches at atmospheric pressure, similar to the experimental system presented herein [15]. The amplitude of the pulsations and, consequently, the time dependence of the vorticity distribution in the source region are influenced by damping in the side branches. These effects are less pronounced in high-pressure industrial pipe systems, which limits the range of applicability of the present results.

Plans for future research activities in this area include investigation of the effect of degree of hydrodynamic interaction between the shear layers while maintaining their coupling through the acoustic field. Various levels of vortex interaction will be obtained by introducing modifications of the cross-junction geometry.

## Acknowledgment

The authors would like to acknowledge financial support by Natural Sciences and Engineering Research Council of Canada (NSERC) under a Discovery grant.

## References

[1] Chen, Y. N., and Sturchler, R., 1977, "Flow-Induced Vibrations and Noise in a Pipe System With Blind Branches Due to Coupling of Vortex Shedding," *Internoise 77*, Zurich.
[2] Baldwin, R. M., and Simmons, H. R., 1986, "Flow-Induced Vibration in Safety Relief Valves," ASME J. Pressure Vessel Technol., **108**(3), pp. 267–272.
[3] Ziada, S., and Bühlmann, E. T., 1992, "Self-Excited Resonances of Two Side-Branches in Close Proximity," J. Fluids Struct., **6**, 583–601.
[4] Rockwell, D., and Naudascher, E., 1978, "Review of Self-Sustaining Oscillations of Flow Past Cavities," ASME Trans. J. Fluids Eng., **100**, 152–165.
[5] Keller, J. J., and Escudier, M. P., 1983, "Flow-Excited Resonances in Covered Cavities," J. Sound Vib., **86**(2), pp. 199–226.
[6] Hourigan, K., Stokes, A. N., and Welsh, M. C., 1986, "Flow-Induced Acoustic Resonance for a Bluff Body in A Duct: A Numerical study," *Ninth Australian Fluid Mechanics Conference*, Auckland.
[7] Stoneman, S. A. T., Hourigan, K., Stokes, A. N., and Welsh, M. C., 1988, "Resonant Sound Caused by Flow Past Two Plates in Tandem in a Duct," J. Fluid Mech., **192**, pp. 455–484.
[8] Howe, M. S., 1975, "Contributions to the Theory of Aerodynamic Sound, With Applications to Excess Jet Noise and the Theory of the Flute," J. Fluid Mech., **71**, pp. 625–673.
[9] Dequand, S., Hulshoff, S. J., and Hirschberg, A., 2003, "Self-Sustained Oscillations in a Closed Side Branch System," J. Sound Vib., **263**, pp. 359–386.
[10] Dequand, S., Willems, J. F. H., Leroux, M., Vullings, R., van Weert, M., Thieulot, C., and Hirschberg, A., 2003, "Simplified models of Flue Instru-

ments: Influence of Mouth Geometry on the Sound Source," J. Acoust. Soc. Am., **113**, pp. 1724–1735.
[11] Amandolese, X., Hemon, P., and Regardin, C., 2004, "An Experimental Study of the Acoustic Oscillations by Flows Over Cavities," ASME J. Vibr. Acoust., **126**, pp. 190–195.
[12] Oshkai, P., and Yan, T., 2006, "Experimental Investigation of Coaxial Side Branch Resonators," *ASME Pressure Vessels and Piping Division Conference*, Vancouver.
[13] Arthurs, D., Ziada, S., and Bravo, R., 2006, "Flow Induced Acoustic Resonances of an Annular Duct with Co-Axial Side Branches," *ASME Pressure Vessels and Piping Division Conference*, Vancoucer, BC, Canada.
[14] Ziada, S., and Shine, S., 1999, "Strouhal Numbers of Fow-Excited Acoustic Resonance of Closed Sede Branches," J. Fluids Struct., **13**, pp. 127–142.
[15] Kriesels, P. C., Peters, M. C. A. M., Hirschberg, A., Wijnands, P. J., Iafrati, A., Riccardi, G., Piva, R., and Bruggeman, J. C., 1995, "High-Amplitude Vortex-Induced Pulsations in a Gas Transport System," J. Sound Vib., **184**, pp. 343–368.

**T. A. Jankowski**[1]
e-mail: jankowski@lanl.gov

**E. N. Schmierer**

**F. C. Prenger**

Mechanical and Thermal Engineering Group
(AET-1),
Los Alamos National Laboratory,
MS J580,
Los Alamos, NM 87545

**S. P. Ashworth**
Superconductivity Technology Center
(MPA-STC),
Los Alamos National Laboratory,
MS T004,
Los Alamos, NM 87545

# A Series Pressure Drop Representation for Flow Through Orifice Tubes

*A simple model is developed here to predict the pressure drop and discharge coefficient for incompressible flow through orifices with length-to-diameter ratio greater than zero (orifice tubes) over wide ranges of Reynolds number. The pressure drop for flow through orifice tubes is represented as two pressure drops in series; namely, a pressure drop for flow through a sharp-edged orifice in series with a pressure drop for developing flow in a straight length of tube. Both of these pressure drop terms are represented in the model using generally accepted correlations and experimental data for developing flows and sharp-edged orifice flow. We show agreement between this simple model and our numerical analysis of laminar orifice flow with length-to-diameter ratio up to 15 and for Reynolds number up to 150. Agreement is also shown between the series pressure drop representation and experimental data over wider ranges of Reynolds number. Not only is the present work useful as a design correlation for equipment relying on flow through orifice tubes but it helps to explain some of the difficulties that previous authors have encountered when comparing experimental observation and available theories.*
[DOI: 10.1115/1.2907408]

## 1 Introduction

Understanding and predicting the relationship between pressure drop and flow rate through orifices is essential for the design and evaluation of fluid power and flow control devices [1,2]. Although this relationship is well understood for sharp-edged orifices at high Reynolds number, many recent studies have attempted to characterize and explain the observed pressure drop for flow through micro-orifices (tens to hundreds of microns in diameter) with large length-to-diameter ratio. Even with low viscosity liquids, Reynolds numbers in these micro-orifices approach the creeping flow regime because of the small size scales involved. Small orifice configurations can be found widely in use in microscale thermal and mechanical systems [3–5], and are important in understanding the behavior of a number of biofluid systems involving the drainage of fluids through capillaries [6]. Additionally, flow through periodically arranged microscale orifice tubes has been suggested as a model for flow through porous media [7].

As we show in the following brief literature survey, although a number of numerical and experimental studies of low Reynolds number flow through orifice tubes have been performed, no wide ranging correlations or simple theories are available to predict and understand the flow through these devices.

**1.1 Nomenclature for Flow Through Orifices.** A typical orifice flow configuration is shown in Fig. 1. The fluid flows through the entrance region, a tube of diameter $D$, with an average velocity $V$, and we consider only incompressible flows here with constant density $\rho$ and viscosity $\mu$. The orifice diameter is given by $d$, and the length of the orifice in the flow direction is $L$. The diameter ratio is expressed as $\beta=d/D$. The average velocity of the fluid in the orifice is represented by $v_0$, and by continuity $V=\beta^2 v_0$. Orifices are classified according to the length-to-diameter ratio $L/d$. A sharp-edged or squared-edged orifice has $L/d<0.125$, $0.125<L/d<2$ for a thick-walled orifice, and for a short-tube orifice $L/d>2$ [5]. Throughout the paper we use the term sharp-edged orifice to refer to orifices with $L/d\leq 0.125$ and the term orifice tube to refer to both thick-walled and short-tube orifices with $L/d>0.125$.

The relationship between pressure drop and flow rate through orifices and tubes is normally presented in one of the three ways, using the flow coefficient $K$, the Darcy friction factor $f$, or the discharge coefficient $C_d$. For incompressible flow, the equations relating pressure drop to velocity are given by

$$\Delta P=\frac{1}{2}K\rho v_0^2,\quad \Delta P=\frac{1}{2}\left(f\frac{L}{D}\right)\rho v_0^2,\quad \text{and}\quad v_0=C_d\sqrt{\frac{2\Delta P}{\rho(1-\beta^4)}} \tag{1}$$

where $\Delta P$ is the pressure drop. Equation (1) shows that

$$K=f\frac{L}{D}=\frac{(1-\beta^4)}{C_d^2} \tag{2}$$

In most studies, the discharge coefficient $C_d$ is used to relate the pressure drop to the flow rate through an orifice. The discharge coefficient is the ratio of the actual rate of flow to an ideal flow rate and accounts for frictional losses and flow constriction. As such, the discharge coefficient is always less than 1. The discharge coefficient in circular orifices is generally a function of the orifice Reynolds number $\mathrm{Re}=\rho v_0 d/\mu$, the diameter ratio $\beta$, and the length-to-diameter ratio $L/d$.

**1.2 Flow Through Sharp-Edged Orifices ($L/d<0.125$).** For sharp-edged orifices with Reynolds numbers greater than $3\times10^5$, standard texts and handbooks report that the discharge coefficient is independent of Reynolds number. With $\beta<0.25$, the discharge coefficient for these high Reynolds number flows is approximately $C_d\simeq 0.6$, with the discharge coefficient approaching $C_d=1$ as the diameter ratio approaches $\beta=1$ [8,9]. For small orifice Reynolds numbers, however, the discharge coefficient in a sharp-edged orifice is affected by both the Reynolds number and the diameter ratio. In experiments by Johansen, the discharge coefficients for sharp-edged orifices with diameter ratios ranging from $\beta=0.209$ to $\beta=0.794$ were measured for Reynolds numbers $0<\mathrm{Re}<2.5\times10^5$ [10]. The general trends of the data collected by Johansen

[1]Corresponding author.

Contributed by the Fluids Engineering Division of ASME for publication in the JOURNAL OF FLUIDS ENGINEERING. Manuscript received July 23, 2007; final manuscript received February 27, 2008; published online May 5, 2008. Assoc. Editor: Timothy J. O'Hern.

  

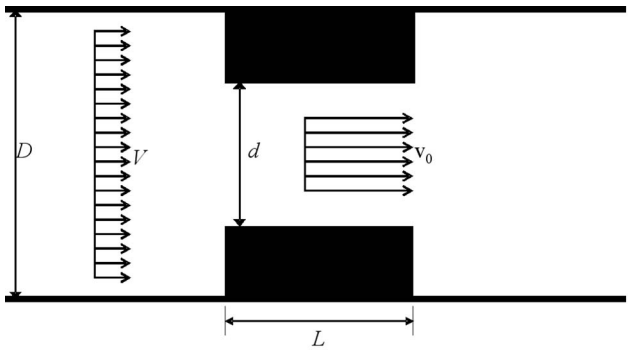


**Fig. 1 A typical orifice flow configuration**

are reproduced here in Fig. 2. The data show a linear relationship between discharge coefficient and square root of Reynolds number for $Re < 10$. Beyond $Re = 10$, the discharge coefficient increases to a maximum value, then decreases to the expected high Reynolds number limit of $C_d = 0.6$. Tuve and Sprenkle, as cited by Perry and Green [8], later confirmed the trends observed in Fig. 2 for sharp-edged orifices. In flow visualization studies by Johansen with a sharp-edged orifice configuration with $\beta = 0.5$, "a slight degree of vorticity in the form of ripples" [10] is observed between the boundary of the jet issuing downstream of the orifice and the recirculation zone behind the orifice plate for Reynolds numbers between $Re = 150$ and $Re = 250$. These disturbances of the downstream jet occur at a Reynolds number corresponding to the maximum observed discharge coefficient. Increasing the orifice Reynolds number beyond this critical value ($Re = 150$) was shown to decrease the reattachment length downstream of the orifice, increasing the flow losses, and leading to the observed reduction in discharge coefficient shown in Fig. 2.

A number of analytical and numerical studies have been performed for sharp-edged orifices in the low Reynolds number regime. For creeping flow through an infinitesimally thin orifice in a plane wall ($\beta = 0$), Sampson found that the discharge coefficient is expressed as [11,12]

$$C_d = \sqrt{\mathrm{Re}/(12\pi)} \tag{3}$$

which agrees well with the experimental results of Johansen for $Re < 10$ and for small diameter ratios. Finally, Mills [13] and Keith and John [14] provided accurate numerical solutions to the two-dimensional axisymmetric Navier–Stokes equations using the vorticity-stream function formulation. The numerical solutions

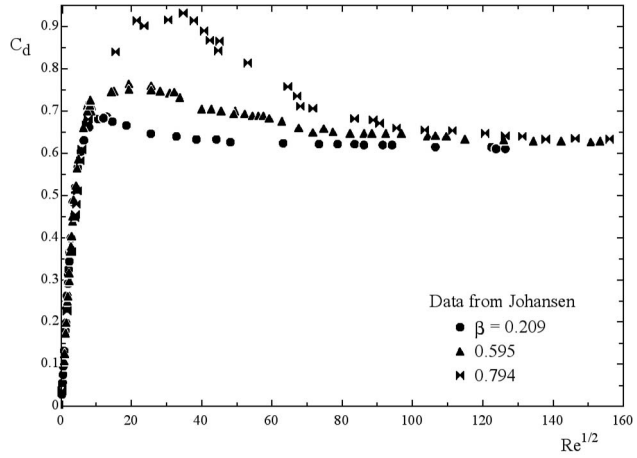


**Fig. 2 Data collected by Johansen [10] for sharp-edged orifices over a wide range of Reynolds number and diameter ratio**

were calculated with $Re < 100$ for flow through sharp-edged orifices with diameter ratios from $\beta = 0.3$ to $\beta = 0.7$. Discharge coefficients calculated with the numerical analyses also agreed with the experimental results of Johansen and Tuve and Sprenkle for Reynolds numbers up to $Re = 100$.

Rather than using tabulated or graphical data as shown in Fig. 2 to predict the discharge coefficient for flow through orifices, a number of authors have attempted to curve fit the data for sharp-edged orifices over a wide range of Reynolds number to provide a design correlation. Borutzky et al. [2] present a two parameter curve fit to the experimental data which captures the behavior of the discharge coefficient for the limits as $Re \to 0$ and as $Re \to \infty$ (that is, the slope at $Re = 0$ and the constant value as $Re \to \infty$). A correlation with two free parameters, however, fails to capture the overshoot near $Re = 150$. For this reason, a four parameter empirical correlation was developed by Wu et al. [1]. The general form of the correlation is given by

$$C_d = C_{d,\infty}\left[1 + a_1 \exp\left(-a_2 \frac{\sqrt{\mathrm{Re}}}{C_{d,\infty}}\right) + a_3 \exp\left(-a_4 \frac{\sqrt{\mathrm{Re}}}{C_{d,\infty}}\right)\right] \tag{4}$$

where $C_{d,\infty} = C_d(\mathrm{Re} \to \infty)$, and for flow through sharp-edged orifices, the coefficients $a_1$, $a_2$, $a_3$, and $a_4$ are determined from the conditions

$$C_d(\sqrt{\mathrm{Re}} = 0) = 0, \quad C_d(\sqrt{\mathrm{Re}} = \sqrt{\mathrm{Re}}_{\max}) = C_{d,\max},$$

$$\left.\frac{dC_d}{d\sqrt{\mathrm{Re}}}\right|_{\sqrt{\mathrm{Re}} \to 0} = \frac{1}{\sqrt{12\pi}}$$

and

$$\left.\frac{dC_d}{d\sqrt{\mathrm{Re}}}\right|_{\sqrt{\mathrm{Re}} \to \sqrt{\mathrm{Re}}_{\max}} = 0 \tag{5}$$

The conditions in Eq. (5) specify the value of the discharge coefficient and its slope at the origin and at the maximum value of each curve in Fig. 2.

**1.3 Flow Through Orifice Tubes ($L/d > 0.125$).** A number of experimental studies have also been performed with orifice tubes at low Reynolds number. In the experiments performed by Kiljanski [15], Hasegawa et al. [16], and Phares et al. [6], the discharge coefficient decreased from the expected sharp-edged orifice discharge coefficient as the length-to-diameter ratio of the orifice was increased. The observed reduction in the discharge coefficient for orifice tubes was attributed to friction along the walls of the finite-length orifices.

Hasegawa et al. [16] and Kusmanto et al. [17] used commercially available software packages employing the finite element method to model the flow through orifice tubes. The results obtained by Kusmanto et al. confirm that, as expected, increasing the length-to-diameter ratio decreases the discharge coefficient because of friction in the finite-thickness orifices. Kusmanto et al. show that their numerical data compare well, qualitatively, to the experimental data of Hasegawa et al., and the numerical data appear to match the asymptotic limit predicted by Dagan et al. [18] as the Reynolds number approaches zero. The numerical simulations, under the assumptions of laminar flow, are carried out for Reynolds numbers up to 316. However, considering the work of Johansen discussed earlier [10], and the appearance of time-dependent disturbances downstream of the orifice for $Re > 150$, the numerical results of Kusmanto et al. for Reynolds number larger than 150 should be viewed with some skepticism.

A number of design correlations are available for predicting the discharge coefficient as a function of Reynolds number and length-to-diameter ratio in orifice tubes. For creeping motion ($Re \to 0$) in an orifice in a plane wall ($\beta = 0$), Dagan et al. [18] developed exact solutions to the governing equations and developed an approximate correlation for the discharge coefficient, which is expressed as

$$C_d = \sqrt{\frac{\mathrm{Re}}{64L/d + 12\pi}} \tag{6}$$

Comparing Eq. (6) to the expression for the discharge coefficient through an infinitesimally thin orifice given in Eq. (3), and considering Eqs. (1) and (2), one finds that the pressure drop through an orifice tube in creeping flow can be represented as two pressure drops in series; the pressure drop caused by flow through a sharp-edged orifice in series with a pressure drop through a tube with fully developed flow for which $f=64/\mathrm{Re}$. Phares et al. [6] confirmed that, for small Reynolds number and large length-to-diameter ratio (i.e., when the first term in the denominator of Eq. (6) dominates), the pressure drop for flow through orifice tubes can be accurately predicted by assuming Hagen–Poiseuille flow in a tube of length $L$ and diameter $d$.

Over larger ranges of the Reynolds number, where the creeping flow assumption may no longer hold and flow within the orifice may not be fully developed, Liu et al. [7] suggest the use of an empirical relation. The relation given by Liu et al. is expressed in terms of the friction factor as

$$f\frac{L}{d} = \frac{64}{\mathrm{Re}}\frac{L}{d} + \frac{36}{\mathrm{Re}} + 1.8\frac{\mathrm{Re}}{256 + \mathrm{Re}^2}(\mathrm{Re} - 8) \tag{7}$$

The coefficients appearing in the third term of Eq. (7) were determined through regression analysis to fit the experimental data of Kiljanski [15] as well as experimental data collected by Liu et al. The data of Kiljanski, however, were collected for flow through orifices discharging free liquid jets into air rather than for pure orifice flows discharging into liquid. Because of this, the applicability of Eq. (7) to flows through orifice tubes at high Reynolds number has been questioned [17]. Indeed, evaluating the limit of Eq. (7) as $\mathrm{Re}\to\infty$ gives $fL/d=1.8$, which by Eq. (2) for $\beta=0$ gives $C_d=0.75$. This value is 23% higher than the accepted value of $C_d=0.6$.

A simple pressure drop model that can be used to accurately predict the discharge coefficient in orifices over a large range of Reynolds number for any length-to-diameter ratio is developed here. The model is developed in Sec. 2. In Sec. 3, a numerical analysis of flow through orifice tubes is outlined, and calculated discharge coefficients from the numerical analysis and experimental data are compared to the model developed in Sec. 2. Finally, conclusions are given in Sec. 4.

## 2 Discharge Coefficient Model

A semiempirical model for the discharge coefficient for flow through orifices of arbitrary length-to-diameter ratio is developed by treating the total pressure drop through the orifice as a pressure drop through a sharp-edged orifice in series with a pressure drop for developing flow along the walls of the finite-length orifice. Although this series representation has been shown to be valid for low Reynolds number creeping flow with fully developed flow in the orifice tube [18], it has not been confirmed over a wide range of Reynolds number with developing flow in the orifice tube. A series pressure drop discharge coefficient model developed here will be compared to experimental data and numerical results for orifices installed with small diameter ratios, $\beta \le 0.25$.

The portion of the pressure drop produced by a sharp-edged orifice is represented in the model using a modified form of the four parameter curve fit developed by Wu et al. [1]. We express the discharge coefficient for the sharp-edged orifice $C_{d,s}$ as

$$C_{d,s} = 0.6\left[1 + \exp\left(-a_1\frac{\sqrt{\mathrm{Re}}}{0.6}\right) - a_2\exp\left(-a_3\frac{\sqrt{\mathrm{Re}}}{0.6}\right) + a_4\left(1 - \frac{\sqrt{\mathrm{Re}}}{1+\sqrt{\mathrm{Re}}}\right)\right] \tag{8}$$

and use the data from Johansen [10] with $\beta=0.209$ to evaluate the conditions in Eq. (5) as

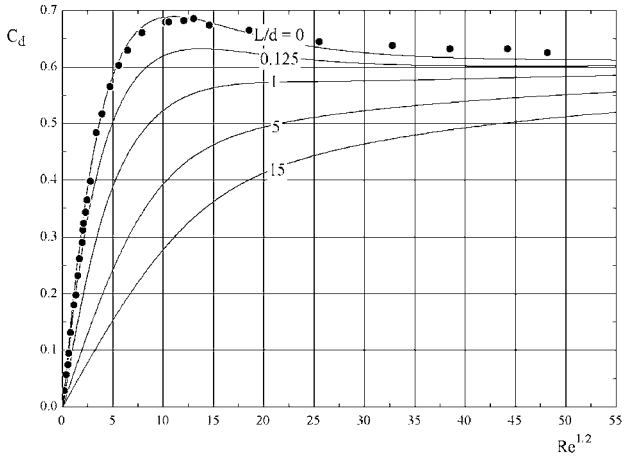


**Fig. 3 Discharge coefficient predicted by Eq. (12) for sharp-edged orifices and orifice tubes with $\beta \le 0.25$; the data points are from Johansen [10] for a sharp-edged ($L/d=0$) orifice with $\beta=0.209$**

$$C_{d,s}(\sqrt{\mathrm{Re}}=0) = 0, \quad C_{d,s}(\sqrt{\mathrm{Re}}=11) = 0.69,$$

$$\left.\frac{dC_{d,s}}{d\sqrt{\mathrm{Re}}}\right|_{\sqrt{\mathrm{Re}}\to 0} = \frac{1}{\sqrt{12\pi}}$$

and

$$\left.\frac{dC_{d,s}}{d\sqrt{\mathrm{Re}}}\right|_{\sqrt{\mathrm{Re}}\to 11} = 0 \tag{9}$$

The conditions in Eq. (9) are applied to Eq. (8) to determine the constants $a_1$, $a_2$, $a_3$, and $a_4$. These conditions allow the sharp-edged discharge coefficient to be determined from

$$C_{d,s} = 0.6\left[1 + \exp(-0.12\sqrt{\mathrm{Re}}) - 2.16\exp(-0.26\sqrt{\mathrm{Re}}) + 0.16\left(1 - \frac{\sqrt{\mathrm{Re}}}{1+\sqrt{\mathrm{Re}}}\right)\right] \tag{10}$$

By using the conditions in Eq. (9), which were determined from experimental data with $\beta=0.209$, the expression in Eq. (10) is valid for sharp-edged orifice flow in a configuration with small diameter ratio ($\beta \le 0.25$).

The pressure drop within the orifice tube is treated as a laminar developing flow, for which the friction factor is expressed as [19]

$$f\frac{L}{d} = \frac{4}{\mathrm{Re}}\frac{L}{d}\left(\frac{3.44}{\sqrt{\xi}} + \frac{16 + 0.3125/\xi - 3.44/\sqrt{\xi}}{1 + 2.12\times 10^{-4}\xi^{-2}}\right) \tag{11}$$

where $\xi = L/(d\mathrm{Re})$.

Treating the total pressure drop as two pressure drops in series, and using Eq. (1), the overall discharge coefficient for flow through orifice tubes is determined from

$$C_d = \left(\frac{1}{C_{d,s}^2} + f\frac{L}{d}\right)^{-1/2} \tag{12}$$

where for small diameter ratios $1-\beta^4 \simeq 1$, and $C_{d,s}$ and $fL/d$ are evaluated from Eqs. (10) and (11), respectively. Although Eqs. (10)–(12) are developed for the case of small diameter ratio ($\beta \le 0.25$), equivalent expressions could be developed for configurations with larger diameter ratio by modifying the conditions in Eq. (9) and reevaluating the coefficients used in Eq. (10).

Predicted discharge coefficients for orifices with Reynolds numbers from 0 to 3000 and with length-to-diameter ratios from 0 to 15 are presented in Fig. 3. The model presented in Eq. (12)

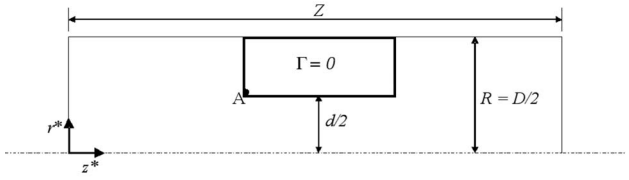


**Fig. 4 The computational domain used in the numerical simulation of flow through orifice tubes**

requires empirical data for the evaluation of the sharp-edged orifice ($L/d<0.125$) term $C_{d,s}$. Experimental data for a sharp-edged orifice with $\beta=0.209$ from Johansen [10] are also shown in the figure. The results indicate that the curve fit in Eq. (10) represents the experimental data for the $L/d=0$ case to within 2%. Additionally, as expected, the discharge coefficient decreases as the length-to-diameter ratio is increased.

Figure 3 and the development of Eq. (12) indicate that, unlike previous models and correlations suggested for predicting the discharge coefficient for orifice tubes (for example, Eqs. (6) and (7)), the series pressure drop model developed here does apply over a wide range of Reynolds number and does properly predict the behavior of the discharge coefficient for sharp-edged orifices for both creeping flow and high Reynolds number flow. Additionally, by using the expression in Eq. (11) for laminar developing flow, the series pressure drop model will reduce to laminar flow in a tube in the limiting case of an orifice tube with a large length-to-diameter ratio (the second term in Eq. (12) dominates for large $L/d$).

Having shown that the series pressure drop model presented in Eq. (12) does properly predict the discharge coefficient for these limiting cases (small and large Re and large $L/d$), we next compare the model developed here with numerical and experimental data for flow through orifice tubes over wide ranges of Reynolds number and length-to-diameter ratio.

## 3 Discharge Coefficient Model Validation

**3.1 Numerical Analysis of Flow Through Orifice Tubes.** Numerical simulations of laminar incompressible flow through orifice tubes were performed. A computational fluid dynamics (CFD) code has been developed for the flow configuration shown in Fig. 4. Flow through the orifice tubes is represented as two-dimensional flow with symmetry about the longitudinal axis ($r^*=0$). Dimensionless variables are defined as

$$r=r^*/R, \quad z=z^*/R, \quad \mathbf{u}=\mathbf{v}/V, \quad \Pi=p/(\rho V^2), \quad \text{and} \quad \Gamma=\frac{\rho VR}{\mu} \tag{13}$$

where $R=D/2$ is the radius of the entrance region and $V$ is the average velocity in the entrance region. Defining variables in this way, the dimensionless governing equations are

$$\frac{1}{r}\frac{\partial}{\partial r}(ru_r)+\frac{\partial u_z}{\partial z}=0 \tag{14}$$

$$u_r\frac{\partial u_r}{\partial r}+u_z\frac{\partial u_r}{\partial z}=-\frac{\partial \Pi}{\partial r}-\left[\frac{1}{r}\frac{\partial}{\partial r}(r\tau_{rr})+\frac{\partial \tau_{rz}}{\partial z}\right] \tag{15}$$

$$u_r\frac{\partial u_z}{\partial r}+u_z\frac{\partial u_z}{\partial z}=-\frac{\partial \Pi}{\partial z}-\left[\frac{1}{r}\frac{\partial}{\partial r}(r\tau_{rz})+\frac{\partial \tau_{zz}}{\partial z}\right] \tag{16}$$

with

$$\tau_{rr}=-\frac{2}{\Gamma}\frac{\partial u_r}{\partial r}, \quad \tau_{rz}=-\frac{1}{\Gamma}\left(\frac{\partial u_r}{\partial z}+\frac{\partial u_z}{\partial r}\right), \quad \text{and} \quad \tau_{zz}=-\frac{2}{\Gamma}\frac{\partial u_z}{\partial z} \tag{17}$$

The boundary conditions used throughout the orifice flow simulations are fully developed flow at the inlet and outlet of the solution domain, symmetry conditions at the symmetry axis ($r=0$), and no-slip conditions at the solid wall ($r=1$). Referring to Fig. 4, the boundary conditions are

$$u_r=u_z=0 \quad \text{at} \quad r=1 \tag{18}$$

$$u_r=\partial u_z/\partial r=0 \quad \text{at} \quad r=0 \tag{19}$$

and

$$u_r=0 \quad \text{and} \quad u_z=2(1-r^2) \quad \text{at} \quad z=0 \quad \text{at} \quad z=Z/R \tag{20}$$

The CFD code was developed for pure tube flow. No boundary conditions are explicitly specified at the boundary of the orifice. The presence of the orifice in the solution domain is specified by setting the diffusion coefficient $\Gamma=0$ for nodes that lie in the solid region representing the orifice plate. Equation (13) shows that setting $\Gamma=0$ is equivalent to having an infinite viscosity (solid) at these nodes, forcing the code to calculate zero velocity.

The equations and boundary conditions in Eqs. (14)–(20) are discretized using the control volume method on a structured, staggered grid, with uniform step sizes in the $r$- and $z$-directions. Second-order centered differences are used to approximate the diffusion terms and the QUICK [20] method is used for the convective terms in the governing equations. The derivative boundary condition at the symmetry axis is represented by a second-order centered-difference formula. The discretized continuity and momentum equations are solved using the SIMPLER method [21]. Iterations of the SIMPLER method were continued until the residuals of each equation were reduced at least three orders of magnitude from the initial guessed (zero-velocity) solution.

The performance of the code developed here was evaluated using the grid convergence index (GCI) [22]. The GCI is used to measure the error in a numerical solution. In the GCI method, a parameter of interest is calculated using grids of various sizes. The GCI, which represents an error band that can be applied to these calculated values, is then evaluated. Throughout the grid convergence studies, the apparent order of the numerical method $\gamma$ is evaluated, and a safety factor of 1.25 is applied to the GCI. Roache suggests that evaluating the GCI in this way gives 95% certainty that the GCI will be larger than the actual relative error [23].

Flow through an orifice with $\beta=0.25$ and $L/d=1$ is used as a reference calculation for the GCI method. Calculations were performed for orifice flows with Reynolds numbers from 6.25 to 150. For the lowest Reynolds number, Re=6.25, the inlet of the solution domain is positioned 4 orifice diameters upstream of the orifice, and the outlet of the solution domain is 15 orifice diameters downstream of the orifice. For the highest Reynolds number, Re =150, the inlet and outlet were positioned 15 and 48 orifice diameters upstream and downstream, respectively. Through some parametric studies, we found that these geometries were sufficient to ensure that the upstream and downstream fully developed boundary conditions did not influence the flow near the orifice.

For each Reynolds number, calculations were performed on three grids with different ($r\times z$) resolutions. The GCI is evaluated using the total pressure drop from the inlet to the outlet of the solution domain as a parameter of interest. Results are shown in Table 1. In each case, as expected, the code converges as a second-order ($\gamma=2$) method. The calculated GCI indicates that less than 7% error in the evaluation of pressure drop can be expected using the ($128\times1024$) grid.

**Table 1 Grid convergence studies based on the total pressure drop for the $L/d=1$ orifice**

| GCI based on total pressure drop $\Delta\Pi$ from inlet to outlet of the domain with the L/d=1 short tube orifice | | | | | | |
|---|---|---|---|---|---|---|
| Grid (r x z) | $\Delta\Pi$ | Re | $L_{up}$ | $L_{down}$ | GCI | $\gamma$ |
| 128 x 1024 | 2396 | 6.25 | 4d | 15d | 4.0% | 1.5 |
| 64 x 512 | 2541 | 6.25 | 4d | 15d | 10.9% | |
| 32 x 256 | 2961 | 6.25 | 4d | 15d | | |
| 128 x 1024 | 756 | 25 | 4d | 15d | 4.1% | 1.8 |
| 96 x 748 | 773 | 25 | 4d | 15d | 6.7% | |
| 64 x 512 | 814 | 25 | 4d | 15d | | |
| 128 x 1024 | 486 | 56.25 | 9d | 30d | 3.9% | 2.1 |
| 96 x 748 | 499 | 56.25 | 9d | 30d | 7.0% | |
| 64 x 512 | 534 | 56.25 | 9d | 30d | | |
| 128 x 1024 | 374 | 100 | 9d | 30d | 6.7% | 1.6 |
| 96 x 748 | 386 | 100 | 9d | 30d | 10.4% | |
| 64 x 512 | 413 | 100 | 9d | 30d | | |
| 128 x 1024 | 329 | 150 | 15d | 48d | 5.1% | 1.9 |
| 96 x 768 | 339 | 150 | 15d | 48d | 8.6% | |
| 64 x 512 | 367 | 150 | 15d | 48d | | |

**3.2 Comparing Numerical Results to the Series Pressure Drop Model.** In Fig. 5, results from the pressure drop model presented in Eq. (12) are compared to results from the numerical simulations for Reynolds number up to 150, with $0.125 \leq L/d \leq 15$, and for $\beta=0.25$. The numerical results are calculated with the $(128\times1024)$ grid. Throughout, the discharge coefficient is calculated using corner pressure taps (i.e., evaluating the pressure difference using locations immediately upstream and downstream of the orifice). The upstream and downstream lengths in the solution domain are the same as those used in Sec. 3.1 and shown in Table 1 to ensure that solutions are independent of the boundary conditions.

The error bars for the discharge coefficients calculated with the finite-difference method are set to $\pm3.4\%$. The GCI calculated in the previous section indicates that a maximum of 6.7% error in the calculation of pressure drop can be expected for the data from the numerical simulations. Assuming propagation of this error to the calculation of the discharge coefficient, and using the Kline–McClintock second power law [24], Eq. (1) shows that the error associated with the discharge coefficient is half as large as the error associated with the pressure drop.

The results in Fig. 5 show that the simple series representation of pressure drop through orifice tubes is able to accurately predict the discharge coefficient for orifice Reynolds numbers up to 150. The maximum error between the series pressure drop representation and the CFD calculations is 9% for the $L/d=1$, $\mathrm{Re}=150$ data point.

The numerical simulations were only performed for Reynolds numbers up to 150. For higher Reynolds numbers, experimental data are compared to the series pressure drop model developed in Sec. 2.

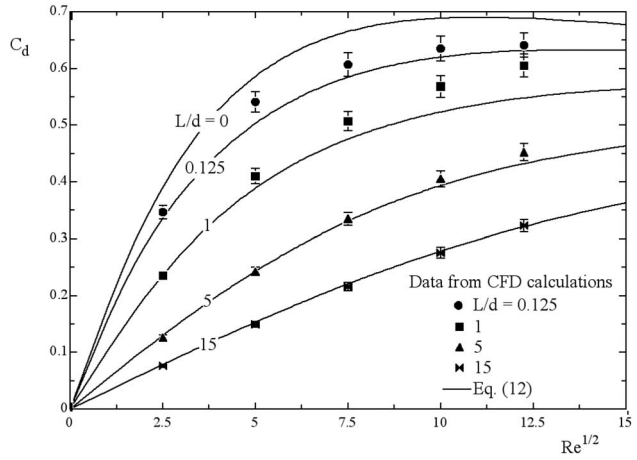


**Fig. 5 Data from the numerical simulations with $\beta=0.25$ compared to Eq. (12)**

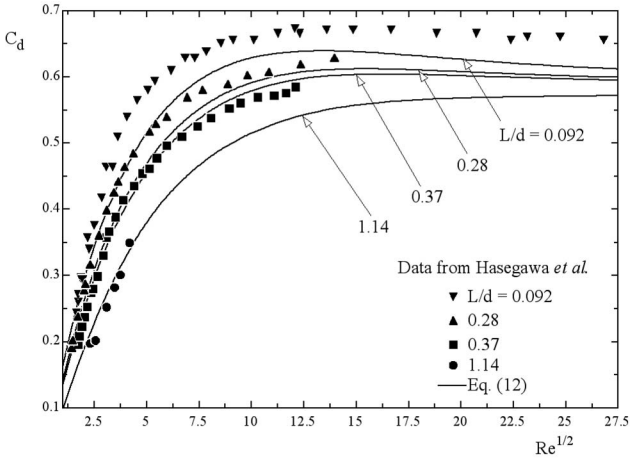


**Fig. 6 Experimental data from Hasegawa et al. [16] compared to Eq. (12); Hasegawa et al. do not report the value of $\beta$, which is presumably small $\beta<0.25$**

**3.3 Comparing Experimental Data to the Series Pressure Drop Representation.** Results predicted by the series pressure drop model, developed here in Eq. (12), are compared to experimental data collected by Hasegawa et al. [16] in Fig. 6. Four of the data sets presented by Hasegawa et al. for the flow of water through micro-orifices with diameters ranging from 109 $\mu$m to 8.8 $\mu$m and with length-to-diameter ratios from 0.092 to 1.14 are compared to the series pressure drop representation for $0<\mathrm{Re}\leq700$. Figure 6 shows that Eq. (12) predicts the discharge coefficient to within 9%. Additionally, both the slope of the data as $\sqrt{\mathrm{Re}}\to0$ and the $L/d$ dependence of the data are captured by the simple series pressure drop representation for flow in the orifice tubes.

In Fig. 7, the series pressure drop model developed here is compared to the experimental data of Phares et al. [6]. The pressure drops through orifices of 80–150 $\mu$m diameter with aspect ratios from $L/d=2$ to $L/d=5$ were measured with water and a 50/50 vol. % glycerol/water solution. Equation (12) consistently underpredicts the experimental data. For example, with the $L/d$

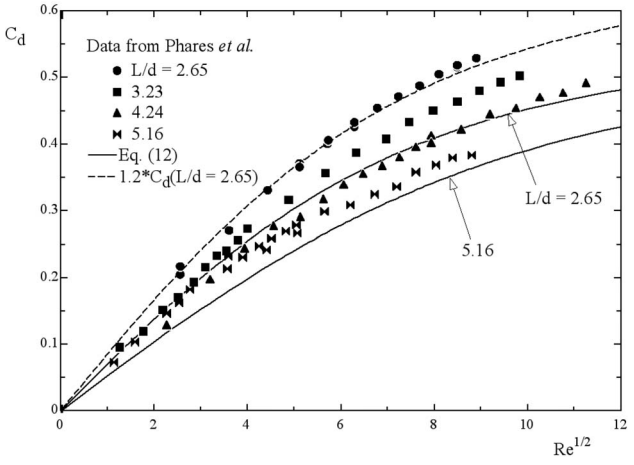


**Fig. 7 Experimental data of Phares et al. [6] compared to the series pressure drop representation developed here; for the data of Phares et al. $\beta$, ranges from 0.008 to 0.016**

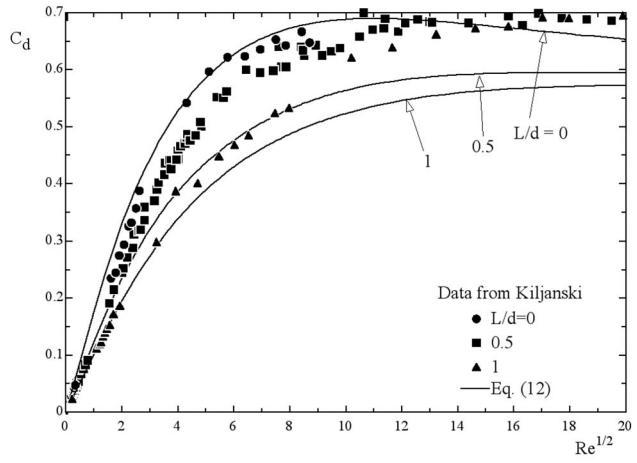


**Fig. 8 Equation (12) compared to the experimental data collected by Kiljanski [15]; in the experiments by Kiljanski, $\beta$ ranges from 0.05 to 0.13**

=2.65 orifice, the series pressure drop representation developed here predicts discharge coefficients 20% lower than observed in the experiments over the entire range of Reynolds number presented.

These consistently low predictions may be caused by the assumption of a sharp upstream orifice edge (see Point A in Fig. 4) in the development of the model in Eq. (12). Representing the edge radius at Point A in Fig. 4 as $\eta$, the sharp-edged orifice configuration used here to develop the model would represent $\eta=0$. Hobbs and Humphreys [25] indicate that the discharge coefficient is considerably increased by even small upstream edge radii. The data reviewed by Hobbs and Humphreys for sharp-edged orifices fit the equation

$$C_d = C_{d,s}\left(1 + 5.5\frac{\eta}{d}\right) \tag{21}$$

where $C_{d,s}$ is the sharp-edged discharge coefficient with $\eta=0$. This correlation indicates that a 20% increase in the discharge coefficient will be produced if the upstream edge radius is 4% of the orifice diameter. Although Phares et al. did not explicitly measure the upstream edge radius, the manufacturer of their orifices did indicate that the upstream and downstream edge radii are on the order of a micron. Considering the $L/d=2.65$ orifice tested by Phares et al. with a diameter of $d=150$ $\mu$m, an upstream edge radius of only 6 $\mu$m could increase the discharge coefficient by 20%. This edge radius certainly seems plausible considering the manufacturer's reported estimates.

Finally, for illustrative purposes, Eq. (12) is compared to the experimental data of Kiljanski [15] in Fig. 8 for orifice tubes with $L/d$ ratios of 0, 0.5, and 1, with Reynolds numbers from 0 to 400. The orifices used by Kiljanski are 2 mm, 3 mm, and 5 mm in diameter and, as discussed earlier, the orifices discharge a free jet of liquid (potato syrup, glycerin, and glycol) into air. For very low Reynolds numbers, $Re<10$, the series pressure drop model, once again, properly predicts the slope of the data near the origin and the $L/d$ dependence of the data. For higher Reynolds numbers, however, the series pressure drop representation significantly underpredicts the discharge coefficient. Higher discharge coefficients than predicted by Eq. (12) are expected for the experiments performed by Kiljanski since the orifices discharge into air rather than liquid, which eliminates the interaction of the jet and the recirculation zone behind the orifice, decreasing the downstream flow losses.

## 4 Conclusions

Numerical and experimental data for the discharge coefficient for flow through orifice tubes have been correlated to a simple pressure drop model developed here. Flow through orifice tubes can be represented as a pressure drop through a sharp-edged orifice in series with developing flow in a tube. This simple model has been validated with numerical and experimental data for Reynolds numbers up to 3000 and with length-to-diameter ratios up to 15. This general model could easily be extended to consider a number of geometric effects such as noncircular orifices and nonzero inlet edge radii.

## Acknowledgment

Los Alamos National Laboratory is an equal opportunity employer operated by Los Alamos National Security LLC for the Department of Energy. Funding for this work was provided by the Superconductivity Technology Center at the Los Alamos National Laboratory.

The authors would like to thank the two JOURNAL OF FLUIDS ENGINEERING reviewers for their in-depth reviews and for their suggestions and comments.

## Nomenclature

**English**

- $a$ = coefficients determined in the curve fit of experimental orifice flow data
- $C_d$ = discharge coefficient
- $d$ = orifice diameter
- $D$ = diameter of entrance and exit regions
- $f$ = Darcy friction factor
- $K$ = flow coefficient
- $L$ = orifice length in the flow direction
- $L_{\text{down}}$ = length of the exit region downstream of the orifice tube
- $L_{\text{up}}$ = length of the entrance region upstream of the orifice tube
- $p$ = pressure
- $r$ = radial direction
- $R$ = radius of entrance and exit regions
- Re = Reynolds number based on orifice diameter and velocity
- $\mathbf{u}$ = dimensionless velocity vector
- $\mathbf{v}$ = dimensional velocity vector
- $v_0$ = average velocity in the orifice tube
- $V$ = average velocity in the entrance region
- $z$ = axial direction
- $Z$ = length in the axial direction

**Greek**

- $\beta$ = diameter ratio, $d/D$
- $\gamma$ = order of the numerical method
- $\Gamma$ = diffusion coefficient
- $\Delta P$ = pressure drop through the orifice
- $\eta$ = upstream edge radius
- $\mu$ = viscosity
- $\xi$ = dimensionless parameter, $L/(d\text{Re})$
- $\Pi$ = dimensionless pressure
- $\rho$ = density
- $\tau$ = component of the stress tensor

**Subscripts**

- max = maximum value
- $r$ = in the $r$-direction
- $s$ = sharp edged
- $z$ = in the $z$-direction
- $\infty$ = evaluated as $\text{Re}\rightarrow\infty$

### Superscripts

$*$ = dimensional variable

## References


[1] Wu, D., Burton, R., Schoenau, G., and Bitner, D., 2003, "Modelling of Orifice Flow Rate at Very Small Openings," Int. J. Fluid Power, **4**, pp. 31–39.

[2] Borutzky, W., Barnard, B., and Thoma, J., 2002, "An Orifice Flow Model for Laminar and Turbulent Conditions," Simulation Modelling Practice and Theory, **10**, pp. 141–152.

[3] Mishra, C., and Peles, Y., 2005, "Flow Visualization of Cavitating Flows Through a Rectangular Slot Micro-Orifice Ingrained in a Microchannel," Phys. Fluids, **17**, p. 113602.

[4] Mishra, C., and Peles, Y., 2005, "Size Scale Effects on Cavitating Flows Through Microorifices Entrenched in Rectangular Microchannels," J. Microelectromech. Syst., **14**, pp. 987–999.

[5] Tu, X., Hrnjak, P. S., and Bullard, C. W., 2006, "Refrigerant 134a Liquid Flow Through Micro-Scale Short Tube Orifices With/Without Phase Change," Exp. Therm. Fluid Sci., **30**, pp. 253–262.

[6] Phares, D. J., Smedley, G. T., and Zhou, J., 2005, "Laminar Flow Resistance in Short Microtubes," Int. J. Heat Fluid Flow, **26**, pp. 506–512.

[7] Liu, S., Afacan, A., and Masliyah, J. H., 2001, "A New Pressure Drop Model for Flow-Through Orifice Plates," Can. J. Chem. Eng., **79**, pp. 100–106.

[8] Perry, R. H., and Green, D., 1984, *Perry's Chemical Engineering Handbook*, 6th ed., McGraw-Hill, New York.

[9] Fox, R. W., and McDonald, A. T., 1992, *Introduction to Fluid Mechanics*, 4th ed., Wiley, New York.

[10] Johansen, F. C., 1930, "Flow Through Pipe Orifices at Low Reynolds Numbers," Proc. R. Soc. London, Ser. A, **126**, pp. 231–245.

[11] Sampson, R. A., 1891, "On Stokes's Current Function," Philos. Trans. R. Soc. London, Ser. A, **182**, pp. 449–518.

[12] Jeong, J. T., and Choi, S. R., 2005, "Axisymmetric Stokes Flow Through a Circular Orifice in a Tube," Phys. Fluids, **17**, p. 053602.

[13] Mills, R. D., 1968, "Numerical Solutions of Viscous Flow Through a Pipe Orifice at Low Reynolds Numbers," J. Mech. Eng. Sci., **10**, pp. 133–140.

[14] Keith, T. G., and John, J. E. A., 1977, "Calculated Orifice Plate Discharge Coefficients at Low Reynolds Number," ASME J. Fluids Eng., **99**, pp. 424–425.

[15] Kiljanski, T., 1993, "Discharge Coefficient for Free Jets from Orifices at Low Reynolds Number," ASME J. Fluids Eng., **115**, pp. 778–781.

[16] Hasegawa, T., Suganuma, M., and Wantanabe, H., 1997, "Anomaly of Excess Pressure Drops of the Flow Through Very Small Orifices," Phys. Fluids, **9**, pp. 1–3.

[17] Kusmanto, F., Jacobsen, E. L., and Finlayson, B. A., 2004, "Applicability of Continuum Mechanics to Pressure Drop in Small Orifices," Phys. Fluids, **16**, pp. 4129–4134.

[18] Dagan, Z., Weinbaum, S., and Pfeffer, R., 1982, "An Infinite-Series Solution for the Creeping Motion Through an Orifice of Finite Length," J. Fluid Mech., **115**, pp. 505–523.

[19] Shah, R. K., 1978, "A Correlation for Laminar Hydrodynamic Entry Length Solutions for Circular and Noncircular Ducts," ASME J. Fluids Eng., **100**, pp. 177–179.

[20] Leonard, B. P., 1979, "A Stable and Accurate Convective Modelling Procedure Based on Quadratic Upstream Interpolation," Comput. Methods Appl. Mech. Eng., **19**, pp. 59–98.

[21] Patankar, S. V., 1980, *Numerical Heat Transfer and Fluid Flow*, 1st ed., Hemisphere, Washington, DC.

[22] Roache, P. J., 1998, *Verification and Validation in Computational Science and Engineering*, 1st ed., Hermosa, Albuquerque, NM.

[23] Roache, P. J., 2003, "Conservatism of the Grid Convergence Index in Finite Volume Computations on Steady-State Fluid Flow and Heat Transfer," ASME J. Fluids Eng., **125**, pp. 731–732.

[24] Figliola, R. S., and Beasley, D. E., 1995, *Theory and Design for Mechanical Measurements*, 2nd ed., Wiley, New York.

[25] Hobbs, J. M., and Humphreys, J. S., 1990, "The Effect of Orifice Plate Geometry Upon Discharge Coefficient," Flow Meas. Instrum., **1**, pp. 133–140.

# Turbulent Boundary Layer With Negligible Wall Stress

**Noor Afzal**
Faculty of Engineering & Technology,
Aligarh Muslim University,
Aligarh 202002, India

*The turbulent boundary layer subjected to strong adverse pressure gradient near the separation region has been analyzed at large Reynolds numbers by the method of matched asymptotic expansions. The two regions consisting of outer nonlinear wake layer and inner wall layer are analyzed in terms of pressure scaling velocities* $U_p=(\nu p'/\rho)^{1/3}$ *in the wall region and* $U_\delta=(\delta p'/\rho)^{1/2}$ *in the outer wake region, where* $p'$ *is the streamwise pressure gradient and* $\rho$ *is the fluid density. In this work, the variables* $\delta$*, the outer boundary layer thickness, and* $U_\delta$*, the outer velocity scale, are independent of* $\nu$*, the molecular kinematic viscosity, which is a better model of fully developed mean turbulent flow. The asymptotic expansions have been matched by Izakson–Millikan–Kolmogorov hypothesis leading to open functional equations. The solution for the velocity distribution gives new composite log-half-power laws, based on the pressure scales, providing a better model of the flow, where the outer composite log-half-power law does not depend on the molecular kinematic viscosity. These new composite laws are better and one may be benefited from their limiting relations that for weak pressure gradient yield the traditional logarithmic laws and for strong adverse pressure gradient yield the half-power laws. During matching of the nonlinear outer layer two cases arise: One where* $U_\delta/U_e$ *is small and second where* $U_\delta/U_e$ *of order unity (where* $U_e$ *is the velocity at the edge of the boundary layer). In the first case, the lowest order nonlinear outer flow under certain conditions shows equilibrium. The outer flow subjected to the constant eddy viscosity closure model is governed by the Falkner–Skan equation subjected to the matching condition of finite slip velocity on the surface. The jet- and wakelike solutions are presented, where the zero velocity slip implying the point of separation, which compares well with Coles traditional wake function. In the second case, higher order terms in the asymptotic solutions for nearly separating flow have been estimated. The proposed composite log-half-power law solution and the limiting half-power law have been well supported by extensive experimental and direct numerical simulation data. For moderate values of the pressure gradient the data show that the proposed composite log-half-power laws are a better model of the flow.* [DOI: 10.1115/1.2903754]

## 1 Introduction

The turbulent boundary layer with negligible wall shear stress, in the neighborhood of separation, was considered by Stratford [1]. Using dimensional arguments for large adverse pressure gradient, the half-power law for velocity distribution was proposed by Stratford, and the self-preserving nonlinear outer flow was patched with by Townsend [2] and the outer non-linear wake layer expansion was asymptotically matched with the inner wall layer expansion in Stratford's variables by Afzal [3]. For strong adverse pressure gradient, the dimensional analysis of the outer flow as a shallow wake layer and inner layer was matched by Kader and Yaglom [4] to obtain the half-power laws, supported by experimental data. For the shallow outer wake layer, Mellor and Gibson [5] employed the eddy viscosity closure model and carried out an equilibrium analysis leading to half-power law velocity profile.

An alternate velocity defect $(U_e-u)/U_{S1}$ versus $y/B_1$, giving half-power law, was proposed by Perry and Schofield [6] and Schofield [7]. Simpson [8] showed that Perry and Schofield scaling is supported upstream of separation. Dengel and Fernholz [9] while comparing their measurements proposed that Schofield profile is valid only at one point in the adverse pressure gradient region on its way to the point of separation and is not a good approximation for other profiles. The scaling velocity $U_{S1}$ was related to the maximum shear stress, but this is not supported by the data. Dengel and Fernholz [9] for an asymptotic separation profile assumed seventh order polynomial in $y/B_1$, which fits well to the data. In their work, the slip velocity $U_{S1}$ was related to the backflow coefficient $\chi_w$, defined as the fraction of the total time that the flow spends in the upstream direction in the vicinity of the wall. The proposed linear relationships are $U_{S1}/U_e=1.01+0.485\chi_w$ for the velocity scale and $H=2.205+1.385\chi_w$ for the shape factor in the domain $\chi_w\leqslant 70$. By using Perry–Schofield coordinates as modified by Dengel and Fernholz [9], the curves were reported to collapse [10]. Angele and Klingmann [11] applied [9] separation bubble between separation and reattachment. Skote and co-worker [12,13] have observed that the procedure of determining the velocity scales a posteriori from the collapsed velocity profile makes the analysis less valuable. Alving and Fernholz [10] data of the velocity profile showed considerable departure from the law of the wall valid for zero pressure gradient flow. Furthermore, the data shown in the conventional outer layer variables $u/U_e$ versus $\sqrt{Y}$ in Fig. 11 [10] have substantive half-power regions (for at least six velocity profiles) where pressure gradients are large, but the half-power law was not perused further for these regions.

The strong adverse pressure gradient data of Skare and Krogstad [14] deals with the equilibrium aspects in terms of traditional logarithmic law $u_+=2.44\ln y_+ +5.2$ and wake is very dominant part of this flow where the freestream velocity varies as $U_e=U_r(x-x_0)^{-m}$, giving $m=0.22$ and $U_r=23.6$ m/s. When the pressure gradient was increased, the level of logarithmic law was found to shift downward and an apparent value of Karman constant decreased, but Skare and Krogstad [14] have pointed out that it may be due to Reynolds number effect. Elsberry et al. [15]

Contributed by the Fluids Engineering Division of ASME for publication in the JOURNAL OF FLUIDS ENGINEERING. Manuscript received May 5, 2006; final manuscript received August 18, 2007; published online May 7, 2008. Assoc. Editor: James A. Liburdy.

  

proposed that their entire velocity profile data could be adequately represented by Coles [16,17] composite wall-wake law, and Coles parameter $\Pi$ is a linear function of $C_f^{-1/2}$, where $C_f$ is the skin friction coefficient. The freestream velocity varies as $U_e=U_r(x-x_0)^{-m}$, giving $m=0.21$ and $U_r=17.8$ m/s for Case A and $m=0.18$ and $U_r=16.7$ m/s for Case B considered. The three layer theory near the separation region has been advocated in a turbulent boundary layer by Melnik [18] and Durbin and Belcher [19]. In Ref. [19], the overlap, in the inner and intermediate layers provides logarithmic laws, and the intermediate and outer layers provide the Stratford half-power laws for velocity distribution. It has been shown by Simpson [8], Dengel and Fernholz [9], and Angele and Klingmann [11] that the logarithmic region gradually disappears under strong adverse pressure in the gradient turbulent boundary layer develops toward separation. Moreover, Skote [12] and Skote and Henningson [13] from direct numerical simulation (DNS) data have shown that the half-power law compares much better than the logarithmic law proposed by Chawla and Tennekes [20] and Tennekes and Lumely [21].

The aim of the present work is to formulate a general outer layer governed by equations of a nonlinear wake, where the lowest order outer nonlinear flow does not depend on the molecular kinematic viscosity $\nu$. The matching of the nonlinear outer layer with the wall layer leads to more general results. It may be pointed out first that the works of Kader and Yaglom [4] and Mellor and Gibson [5] have linearized the outer flow about $U_c$ (the velocity at the edge of the boundary layer) and considered the velocity defect relation $(U_c-u)/u_\delta=g(y/\delta)$ along with the wall layer and proposes the half-power law near separation. Second, in several other works [19–24], the lowest order outer layer was dependent on $\nu$, the molecular kinematic viscosity. Chawla and Tennekes [20], Tennekes and Lumely [21], and Shih et al. [22] adopted the outer velocity scale $U_p=(\nu p'/\rho)^{1/3}$ and boundary layer thickness $\delta=\delta(U_p/U_e)$ and whose matching with the inner layer yields an outer velocity defect logarithmic law, in which outer layer scales $U_p$ and $\delta$ depend on the molecular kinematic viscosity. Indinger et al. [23] for the outer velocity defect $(U_e-u)/u_\tau$ proposed a logarithmic law, whose additive constant depends on the nondimensional pressure gradient $K_+=\nu p'/\rho u_\tau^3$, involving the molecular kinematic viscosity. In the work of Durbin and Belcher [19], the leading order outer boundary layer depends on $U_p/U_e$, i.e., the molecular kinematic viscosity $\nu$. From the dimensional analysis in the turbulent boundary layer with strong adverse pressure gradient, Vieth et al. [24] proposed a composite law where Karman constant $k=k(K_+)$ is not appropriate, due to Karman constant dependence on the molecular kinematic viscosity. In the strong adverse pressure gradient, if the outer layer depends on the molecular kinematic viscosity $\nu$, then the outer wake layer may not be fully developed turbulent flow, and reverse transition would be expected [25]. There is no evidence of reverse transition under strong adverse pressure gradient flows from the extensive experimental data reported in the literature [17–25].

The present work deals with the two layer theory for the turbulent boundary layer subjected to the strong adverse pressure gradient with negligible wall stress in the neighborhood of the separation region, for large Reynolds number by the method of matched asymptotic expansions. The lowest order outer layer does not depend on the molecular kinematic viscosity, which is a better model of fully developed mean turbulent flow. The open boundary layer equations of mean turbulent motion have been analyzed in the two regions of the outer nonlinear wake layer (and shallow wake in Appendix A) and the inner wall layer have been matched in the overlap region by Izakson–Millikan–Kolmogorov argument, leading to new composite log-half-power laws, which is a better model of the flow. These new composite laws, described in Appendix B, are better and one may be benefited from their limiting relations that for weak pressure gradient yield the traditional logarithmic laws and for strong adverse pressure gradient yield the half-power laws. For moderate values of the pressure gradient, the data show that the proposed composite log-half-power laws are a better model of the flow in the overlap region. The separating and reattaching flow under strong adverse pressure gradient with negative velocity gradient is described in Appendix C.

## 2 Boundary Layer Under Strong Adverse Pressure Gradient

The boundary layer equations for two-dimensional incompressible mean turbulent flow subject to pressure gradient, in standard notations, are

$$\frac{\partial u}{\partial x}+\frac{\partial v}{\partial y}=0 \tag{1}$$

$$u\frac{\partial u}{\partial x}+v\frac{\partial u}{\partial y}=-\frac{1}{\rho}p'(x)+\nu\frac{\partial^2 u}{\partial y^2}+\frac{\partial \tau}{\rho\partial y}+\frac{\partial \mathcal{T}}{\rho\partial x} \tag{2}$$

Here, $\tau=-\rho\langle u'v'\rangle$ is the Reynolds shear stress and $\mathcal{T}=-\rho\langle u'^2-v'^2\rangle$ is the effective normal stress. Furthermore, $u$ and $v$ are the velocity components in $x$ streamwise and $y$ normal coordinates, $p'(x)=-\rho U_e dU_e/dx$ is the pressure gradient, $U_e$ is the velocity at the edge of the boundary layer of thickness $\delta$, $\tau_w$ is the wall shear stress, $\rho$ is the fluid density, and $\nu$ is the molecular kinematic viscosity. The boundary conditions at the wall and edge of the turbulent boundary layer are $y=0$, $u=v=\tau=\mathcal{T}=0$ and $y/\delta\to\infty$, $u\to U_e(x)$, $\tau\to 0$ and $\mathcal{T}\to 0$.

The inner velocity scale $U_p=(\nu p'/\rho)^{1/3}$ is based on the pressure gradient $p'$ and molecular kinematic viscosity $\nu$ and the outer velocity scale $U_\delta=(\delta p'/\rho)^{1/2}$ on the pressure gradient $p'$ and boundary layer thickness $\delta$. Furthermore, where $L=-U_e/(dU_e/dx)$ is the scale of streamwise flow variations, $\Lambda=\tau_w/\delta p'$ and $R_p=U_p\delta/\nu$ are the parameters of the flow.

*Inner Wall Layer*. In the strong adverse pressure gradient flow near separation, inner variables are $y_p=yU_p/\nu$, $u_\times=u/U_p$, and $\tau_\times=\tau/\rho U_p^2$. The boundary layer equation (2) in terms of inner wall variables yields

$$\frac{\partial u_\times}{\partial y_p}+\tau_\times=\Lambda R_p+y_p+O\left(\frac{u_p L}{\nu}\right)^{-1} \tag{3}$$

In the viscous sublayer near the wall, the Reynolds shear stress $\tau_\times$ may be neglected and an integral of relation (3) gives the velocity distribution

$$u_\times=\frac{1}{2}y_p^2+\Lambda R_p y_p \tag{4}$$

*Outer Wake Layer*. The outer layer variables are $Y=y/\delta$, $u/U_e=F'(x,Y)$, $T=\tau/\rho U_\delta^2$, and $\Gamma=\mathcal{T}/\rho U_\delta^2$. The boundary layer equations ((1) and (2)) in terms of outer variables yield

$$\begin{aligned}\frac{\partial T}{\partial Y}-\left(1+\frac{1}{m}\right)F\frac{\partial^2 F}{\partial Y^2}+\left(\frac{\partial F}{\partial Y}\right)^2-1&=\frac{x}{m}\left(\frac{\partial F}{\partial x}\frac{\partial^2 F}{\partial Y^2}-\frac{\partial F}{\partial Y}\frac{\partial^2 F}{\partial x\partial Y}\right)\\&+w^2\left[\frac{x}{m}\frac{\partial \Gamma}{\partial x}+2\left(1+\frac{x}{m}\frac{dw}{dx}\right)\Gamma\right]+O\left(\frac{\nu}{w^2U_e\delta}\right)\end{aligned} \tag{5}$$

Here, $w=U_\delta/U_e$ is the perturbation parameter and $m=(\delta/U_e)\times(dU_e/d\delta)$ and $\beta=m/(1+m)$ are the pressure gradient parameters. The outer expansions are

$$\frac{u}{U_e}=U_0(x,Y)-wU_1(x,Y)+o(w) \tag{6}$$

$$T=\frac{\tau}{\rho U_\delta^2}=T_0(x,Y)+wT_1(x,Y)+o(w) \tag{7}$$

$$\Gamma = \frac{\mathcal{T}}{\rho U_\delta^2} = \Gamma_0(x,Y) + w\Gamma_1(x,Y) + o(w) \tag{8}$$

which gives the first and second order outer equations stated below.

In the first order wake equations $U_0(x,Y)=F_0'(x,Y)$,

$$\beta T_0' - F_0 F_0'' - \beta(1 - F_0'^2) = x(1-\beta)(F_0'' F_{0x} - F_0' F_{0x}') \tag{9}$$

In the second order outer equations $U_1(x,Y)=F_1'(x,Y)$,

$$\beta T_1' - F_0 F_1'' + \beta\left[2 - (1-\beta)\frac{x w_x}{w}\right] F_0' F_1' - \left[1 - (1-\beta)\frac{x w_x}{L w}\right] F_0'' F_1 = x(1-\beta)(F_1'' F_{0x} - F_1' F_{0x}' + F_0'' F_{1x} - F_0' F_{1x}') \tag{10}$$

The boundary conditions at the edge of the boundary layer $Y \to \infty$ are $F_0'(X,\infty) - 1 = T_0(X,\infty) = F_1'(X,\infty) = T_1(X,\infty) = 0$.

*Matching With Pressure Gradient.* The matching of velocity $u$ and Reynolds shear stress $\tau$ demands $u_{i,o} = u_{o,i}$ and $\tau_{i,o} = \tau_{o,i}$, where superscript $(i,o)$ denotes the outer limit of the inner solution and superscript $(o,i)$ denotes the inner limit of the outer solution. The matching of the nondimensional mixing length parameter

$$\left(\frac{y}{\sqrt{\tau}}\frac{\partial u}{\partial y}\right)_{i,o} = \left(\frac{y}{\sqrt{\tau}}\frac{\partial u}{\partial y}\right)_{o,i} \tag{11}$$

is also of significance. These relations provide the matching functional equations, as we are dealing with open equations of the mean turbulent shear flow without any closure [26–28].

*Izakson–Millikan–Kolmogorov (IMK) Hypothesis.* Between the viscous and the energetic scales in any turbulent flow exists an overlap domain over which the solutions characterizing the flow in the two corresponding limits must match as the Reynolds number approaches infinity.

The resemblance of the IMK hypothesis to conventional matching associated with closed equations seems peculiar to turbulence theory. For sufficiently large Reynolds numbers, there exists an overlap domain where the inner and outer layer solutions must match (the inner limit ($y_p$ fixed, $R_p \to \infty$) of outer expansions in the outer limit ($Y$ fixed, $R_p \to \infty$) of the inner expansion). The matching condition (20), expressed in terms of the appropriate outer expansion (6) and and inner variables (Eq. (8)), yields

$$\frac{y_p}{\sqrt{\tau_\times}}\frac{\partial u_\times}{\partial y_p} = \frac{U_e}{U_\delta}\frac{Y}{\sqrt{T}}\frac{\partial U_0}{\partial Y} - \frac{Y}{\sqrt{T}}\frac{\partial U_1}{\partial Y} \tag{12}$$

as $y_p \to \infty$ and $Y \to 0$ for $R_p \to \infty$. The inner equation (3) for large $y_p$ yields the Reynolds shear stress $\tau_\times$, which matches with the outer Reynolds shear stress $T$ given by Eq. (7) to yield

$$\tau_\times = y_p + \Lambda R_p \tag{13a}$$

$$T = Y + \Lambda \tag{13b}$$

Two situations have been analyzed where $U_e/U_\delta$ is large and $U_e/U_\delta$ is of order unity.

**2.1 $U_e/U_\delta$ is Large.** The first term on the right hand side of (12) approaches infinity for $U_e/U_\delta \gg 1$ and the matching demands that

$$\frac{Y}{\sqrt{Y+\Lambda}}\frac{\partial U_0}{\partial Y} \to 0 \quad \text{as } Y \to 0 \tag{14}$$

which admits a simple solution of the outer layer $\partial U_0/\partial Y \neq 0$ at $Y=0$, predicting the outer layer slip velocity on the wall $b_S \equiv U_S(x)/U_e(x) = U_0(x,0) = F_0'(x,0)$. The matching relation (12) in the light of Reynolds shear stress (13*a*) and (13*b*) yields

$$\frac{y_p}{\sqrt{y_p + \Lambda R_p}}\frac{\partial u_\times}{\partial y_p} = -\frac{Y}{\sqrt{Y+\Lambda}}\frac{\partial U_1}{\partial Y} = A \tag{15}$$

where $A$ is a constant, independent of $y_p$ and $Y$ as $R_p \to \infty$. The integrations give the following relations.

The composite log-half-power law of the wall is

$$\frac{u}{U_p} = A\sqrt{y_p + \Lambda R_p} + \frac{A}{2}\sqrt{\Lambda R_p}\left[\ln y_p - 2\ln\left(\sqrt{y_p + \Lambda R_p} + \sqrt{\Lambda R_p}\right)\right] + C \tag{16}$$

The composite log-half-power non-linear wake law is

$$\frac{U_S - u}{U_\delta} = -A\sqrt{Y+\Lambda} + \frac{A}{2}\sqrt{\Lambda}\left[-\ln Y + 2\ln\left(\sqrt{Y+\Lambda} + \sqrt{\Lambda}\right)\right] + E \tag{17}$$

The matching velocity profiles ((16) and (17)) in the overlap region give

$$U_S(x) = U_p C + U_\delta E \tag{18}$$

The constants $C$ and $E$ for consistency of the matching [28] require

$$C = \frac{A}{2}\sqrt{\Lambda R_p}\left[\ln(\Lambda R_p)^{3/2} + C_1\right], \quad E = \frac{A}{2}\sqrt{\Lambda}\left[-\ln\Lambda - E_1\right] \tag{19}$$

$$C_1 = 2\ln 2 - 2 + \frac{2B}{A}, \quad E_1 = 2\ln 2 - 2 + \frac{2D}{A} \tag{20}$$

where $B$ and $D$ are also constants. Relation (18), based on Eqs. (19) and (20), gives the skin friction logarithmic law

$$\frac{U_S}{u_\tau} = \frac{A}{2}\ln R_\tau + B + D, \quad R_\tau = \frac{u_\tau \delta}{\nu} \tag{21}$$

and satisfies the condition that the outer slip velocity $U_S = 0$ at the point of separation $\Lambda = 0$. The uniformly valid velocity profile from the union of inner and outer solutions after subtraction of the common part, above the sublayer, becomes

$$\frac{u}{U_e} = f'(Y) + \frac{u_\delta}{U_e}\left[A\left(\sqrt{Y+\Lambda} - \sqrt{1+\Lambda}\right) - \frac{A}{2}\sqrt{\Lambda}Z_1(Y) + \Pi(W(X,Y) - 1)\right] \tag{22}$$

$$Z_1(Y) = -\ln Y + 2\ln\left(\frac{\sqrt{Y+\Lambda} + \sqrt{\Lambda}}{\sqrt{1+\Lambda} + \sqrt{\Lambda}}\right) \tag{23}$$

Here, $W(X,Y)$ is the wake function subjected to the boundary conditions $W(X,0)=0$ and $W(X,1)=1$, and $\Pi$ is the wake parameter given below.

$$W(X,Y) = \frac{1}{\Pi}\left[U_1(X,Y) + A\sqrt{Y+\Lambda} - \frac{A}{2}\sqrt{\Lambda}\left(\ln Y - 2\ln\left(\sqrt{Y+\Lambda} + \sqrt{\Lambda}\right)\right) - E\right] \tag{24}$$

$$\Pi = -A\sqrt{1+\Lambda} + A\sqrt{\Lambda}\ln\left(\sqrt{1+\Lambda} + \sqrt{\Lambda}\right) + E \tag{25}$$

Furthermore, the flow approaching the separation ($\Lambda \to 0$) and the matching relations (16) and (17) become

$$\text{inner layer:} \quad \frac{u}{U_p} = A\sqrt{y_p} + C, \quad y_p \to \infty \tag{26}$$

$$\text{wake layer:} \quad \frac{U_S - u}{U_\delta} = -A\sqrt{Y} + E, \quad Y \to 0 \tag{27}$$

In the neighborhood of point of separation $\Lambda \to 0$, Eq. (19) yields $E \to 0$, and with $\Pi = -A + E$, the uniformly valid solution (22) becomes

$$\frac{u}{U_e} = f'(Y) + \frac{U_\delta}{U_e} A[\sqrt{Y} - W(Y)] \tag{28}$$

The above analysis corresponds to the forward attached flow where $\partial u/\partial y$ is positive and the case of the separated and reattached flow where $\partial u/\partial y$ is negative is descried in Appendix C.

**2.2 $U_e/U_\delta$ is of Order Unity.** In this case, matching condition (12) becomes

$$\frac{y_p}{\sqrt{\tau_\times}} \frac{\partial u_\times}{\partial y_p} = \frac{U_e}{U_\delta} \frac{Y}{\sqrt{T_0}} \frac{\partial U_0}{\partial Y} = A \tag{29}$$

as $y_p \to \infty$ and $Y \to 0$ for $R_p \to \infty$. Based on Reynolds shear matching relations (13*a*) and (13*b*), the velocity from relations (39*a*) and (39*b*) yields $u_\times(y_p) = A\sqrt{y_p}$, $u/U_\delta = (U_e/U_\delta)U_0(Y) = A\sqrt{Y}$. In the overlap region, (29) may also be expressed as

$$\tau_\times = \left( A y_p \frac{\partial u_\times}{2 \partial y_p} \right)^2 \tag{30a}$$

$$T_0 = \left( A \frac{U_\delta}{2U_e} Y \frac{\partial U_0}{\partial Y} \right)^2 \tag{30b}$$

*Outer wake layer in the inner overlap region.* Under the transformation $\eta = \gamma Y$, $f_0(x,\eta) = \gamma F_0(x,Y)$, $G_0(x,\eta) = \gamma T_0(x,Y)$, and $\gamma = (AU_\delta/2U_e)^2$, the outer layer equation (9) subjected to the matching conditions (30*b*) yields

$$\beta G_0' = f_0 f_0'' + \beta(1 - f_0'^2) \tag{31a}$$

$$G_0 = (\eta f_0'')^2 \tag{31b}$$

$\eta \to 0$, $f_0 \to 0$, $f_0' \to 2\sqrt{\eta}$, $G_0 \to \eta$ and $\eta \to \infty$, $f_0' \to 1$, $G_0 \to 0$. The asymptotic power series solutions for $\eta \to 0$ are

$$f_0(\eta) = \sum_{n=0} C_n \eta^{n+3/2} \tag{32a}$$

$$G_0(\eta) = \sum_{n=0} A_n \eta^{n+1} \tag{32b}$$

and the rapidly decreasing coefficients $C_n$ are $A_n$, with increasing $n$ given by

$$C_0 = 4/3, \quad C_1 = 4(d-3)/45, \quad C_2 = 2(d-3)(9d+5)/4725 \tag{33}$$

$$A_0 = 1, \quad A_1 = 2(d-3)/3, \quad A_2 = 8(d-3)(3d-5)/135 \tag{34}$$

where $d = 1/\beta$. The recurrence relations for $C_n$ and $A_n$ are

$$8(n+1)(2n+1)(2n+3)C_n = 4\sum_{p=0}^{n-1} (2n-2p-1)[(2n-2p+1)d - (2p+3)]C_p C_{n-p-1} - \sum_{p=0}^{n-1} (2p+1)(2p+3)(2n-2p+1)^2(2n-2p+3)C_p C_{n-p} \tag{35}$$

$$16A_n = \sum_{p=0}^{n} (2p+1)(2p+3)(2n-2p+1)(2n-2p+3)C_p C_{n-p} \tag{36}$$

The first three terms of the velocity profile and Reynolds shear stress in the overlap region become

$$u/U_e = \eta^{1/2}[2 + 2(d-3)\eta/9 + (d-3)(9d+5)\eta^2/675 + \cdots] \tag{37}$$

$$\tau/\rho U_e^2 = \eta + 2(d-3)\eta^2/3 + 8(d-3)(3d-5)\eta^3/135 + \cdots] \tag{38}$$

and higher order terms may be estimated from these recurrence relations.

*Inner wall layer in the outer overlap region.* The inner equation (9) becomes

$$\frac{\partial u_\times}{\partial y_p} + \tau_\times = \Lambda R_p + y_p \tag{39a}$$

$$\tau_\times = \left( \frac{1}{k} y_p \frac{\partial u_\times}{\partial y_p} \right)^2 \tag{39b}$$

and matching conditions are $y_p \to \infty$, $u_\times \to A\sqrt{y_p}$, $\tau_\times \to \Lambda R_p + y_p$. The solution of Eqs. (39*a*) and (39*b*) for large $\zeta$ gives the velocity and Reynolds shear stress

$$\frac{u}{U_p} = 2\zeta^{1/2} - \phi_1 \zeta^{-1/2} - \frac{A^4}{32}\zeta^{-1} + \phi_1^2 \zeta^{-3/2} + \phi_1 \frac{A^4}{32}\zeta^{-2} + \cdots \tag{40}$$

$$\frac{\tau A^2}{4\rho U_p^2} = \phi_1 + \zeta - \frac{A^4}{32}\zeta^{-1/2} - \phi_1 \frac{A^4}{64}\zeta^{-3/2} - \frac{A^8}{128}\zeta^{-2} + \cdots \tag{41}$$

where $\zeta = y_p A^2/4$ and $\phi_1 = \Lambda R_p A^2/4$.

## 3 Outer Nonlinear Wake Layer Closure

The integration of the mean momentum boundary layer equation (2) subjected to the boundary conditions gives

$$\frac{d\theta}{dx} + (2+H)\frac{1}{U_e}\frac{dU_e}{dx} = \frac{\tau_w}{\rho U_c^2} \tag{42}$$

where normal Reynolds stress term $\mathcal{T}$ has been neglected. Here, $H = \delta^*/\theta$ is the shape factor, $\theta$ is the momentum thickness, and $\delta^*$ is the displacement thickness. In terms of the outer variables, the mean momentum integral (42) gives the value of $m$, the pressure gradient parameter,

$$m = -\frac{1 + \left( \dfrac{xd\delta_2}{\delta_2 dx} \Big/ \dfrac{xd\delta}{\delta dx} \right)}{2 + H(1+\Lambda^*)} \tag{43}$$

where $\Lambda^* = (\delta^*/\delta)\Lambda = \tau_w/(\delta^* p') = \Lambda/\delta_1$, $\delta_1 = \delta^*/\delta = \int_0^1 (1-F')dY$, and $\delta_2 = \theta/\delta = \int_0^1 F'(1-F')dY$. The velocity profile is under equilibrium $F(x,Y) = f(Y)$ provided $(x/\delta_2)(d\delta_2/dx) = 0$ and pressure gradient parameter $m$ becomes

$$m = -\frac{1}{2 + H(1+\Lambda^*)} \tag{44}$$

The first order outer nonlinear wake layer Eq. (9) has been analyzed (when $U_e/U_\delta$ large as described in Sec. 2.1) subjected to the boundary conditions of outer oncoming velocity and Reynolds stresses for $Y \to \infty$, $u \to U_e(x)$ and $\tau \to 0$, along with the matching condition (14) with the inner wall layer. The matching relation (14) admits a simple solution of the outer layer near the wall having $\partial U_0/\partial Y \neq 0$ at $Y = 0$, which predicts a finite outer layer slip velocity $b_S = U_0(x,0) = U_S(x)/U_e(x)$ at the wall, which would be used in the friction factor matching relations (18), (21), and (68). Adopting constant eddy viscosity closure model,

$$\tau = \rho \nu_\tau \frac{du}{dy} \tag{45}$$

where $\nu_\tau = \alpha_C U_e \delta^*$, $\delta = \alpha_C a_1 (x - x_o)$, $(1+m)a_1 = \delta^*/\delta$, and $\alpha_C$ is the Clauser [29,30] universal constant. In the outer wake layer variables, the closure hypothesis (45) yields $T_0(x,Y) = -\beta^{-1} F_0''(x,Y)$. The outer momentum equation (9) becomes

$$F_0''' + F_0 F_0'' + \beta(1 - F_0'^2) = x(1-\beta)(F_0' F_{0x}' - F_0'' F_{0x}) \quad (46)$$

subjected to the matching conditions $F_0(x,0)=0$ and $F_0''(x,0)=-\beta\Lambda$ and the boundary condition $F_0'(x,\infty)=1$. For $U_e$ proportional to $\delta^m$, the outer layer is under equilibrium $F_0(X,Y)=f(Y)$, where the outer equations reduce to the self-similar equations

$$f''' + ff'' + \beta(1 - f'^2) = 0 \quad (47)$$

$$f(0) = 0 \quad (48a)$$

$$f''(0) = -\beta\Lambda \quad (48b)$$

$$f'(\infty) = 1 \quad (48c)$$

where

$$-\beta\Lambda = \frac{C_f/\alpha_C}{2\int_0^\infty (1-f')dY} \quad (49)$$

Here, Eq. (47) is the nonlinear Falkner–Skan equation subjected to the boundary conditions (48*a*)–(48*c*) for the freestream velocity and prescribed wall shear stress on an impermeable wall. The solution predicts the outer layer velocity $U_S/U_e \equiv b_S = f'(0)$. The integral of the outer wake layer (65) yields $m=-(1-q)/(2+H-q)$, and $q=f''(0)/\delta_1 = C_f/(2\alpha_C\delta_1\delta_2)$, from which the near separation region $C_f \to 0$ yields $m=-(2+H)^{-1}$ which was first proposed in the Appendix of the paper by Afzal [3].

For $\Lambda=0$, Eqs. (47) and (48*a*)–(48*c*) closely resemble with the Falkner–Skan equations for self-preserving flow in a laminar wake, whose solution is given in Ref. [31]. We describe below the wake and jet flows where $f''(0)=0$ for $f'(0)\neq 0$, the point of separation $f''(0)=f'(0)=0$, and wall shear stress effects $f''(0)\neq 0$ for $f'(0)\neq 0$.

(i) $f''(0)=0$, $f'(0)\neq 0$. The solution of Falkner–Skan equation (65) and boundary condition (66) for $f''(0)=0$ demands $\Lambda=0$, which gives the wakelike solution for $-1/3<m\leqslant m_0$ $(-0.5<\beta\leqslant\beta_0)$ and jetlike solution $-1/2\leqslant m<-1/3 (-1\leqslant\beta<-0.5)$, where $m_0=-0.165858$ $(\beta_0=-0.198838)$. An approximate wake-/jetlike solution gave

$$f'(Y) = 1 - [1 - f'(0)]\exp(-d_0 Y^2) \quad (50)$$

$$f'(0) = -2\frac{m-m_0}{1+2m} \quad (51a)$$

$$d_0 = -\frac{1}{2}\frac{m}{1+m}\frac{1-2m_0}{1+2m} \quad (51b)$$

The outer layer slip velocity $f'(0)=0$ at $m=m_0$ has certain implications on flow separation, and solutions (50), (51*a*), and (51*b*) become

$$\frac{u}{U_e} = f'(Y) = 1 - \exp(-0.09942Y^2) \quad (52)$$

The reverse flow solutions also exist for wakelike flows for $m_0<m<0$ $(\beta_0<\beta<0)$ and jetlike flows for $-\infty\leqslant m\leqslant -1/2 (1<\beta<-1)$ are also not considered here. In $-1/2\leqslant m\leqslant m_0$, Fig. 9 shows wakelike and jetlike flows of the nonlinear outer layer flow equations. Furthermore, the jetlike solution would be useful for wall jetlike flow, not further considered here.

(ii) $f''(0)=0$, $f'(0)=0$. The solution of Falkner–Skan equation (47) under boundary conditions $f(0)=f'(0)=f''(0)=f'(\infty)-1=0$ predicts that $m=m_0=-0.168585$. The numerical velocity profile solution $f'(Y)$ is normalized $\zeta_e^{-1}\int_0^{\delta_e} f'(Y)dY=1$, where $\delta_e$ is the boundary layer thickness at $f'(Y=\delta_e)=0.99$. The normalized solution at the point of separation (shown later in Fig. 10) compares well to Coles wake function

$$f'(Y/\delta_e) = W(Y) \quad (53)$$

The log-wake law of Coles [16,17] is

$$\frac{U_e - u}{u_\tau} = -\frac{1}{k}\ln Y + \frac{\Pi_e}{k}[W_C(1) - W_C(Y)] \quad (54)$$

Here, $W_C(Y)$ is the Coles wake function, with boundary conditions $W_C(0)=0$ and $W_C(1)=1$ and satisfies the normalizing condition $\int_0^1 W_C(Y)dY=1/2$. When separation is approached, the parameter $\Pi_C/k$ tends to infinity, and we get $\Pi_C=k(C_f/2)^{-1/2}$. The Coles parameter $\Pi_C$ that is a linear function of $C_f^{-1/2}$ was also proposed by Elsberry et al. [15]. The relation $\Pi_C$ becomes unbounded in the neighborhood of separation domain, but the velocity profile (54) at the point of separation (or reattachment) becomes

$$\frac{u}{U_e} = W_C(Y) \quad (55)$$

which may be compared to our relation (53).

(iii) $f''(0)\neq 0$, $f'(0)=b_S$. The numerical solution of the Falkner–Skan equation (47) subjected to boundary conditions (48*a*)–(48*c*) for various values of $\beta$ is shown in Fig. 12 for friction factor $C_f/\alpha_C$ against the slip velocity parameter $b_S$. For the estimation of $C_f$, the Clauser [29,30] universal constant $\alpha_C=0.018$ may be adopted. Earlier, Clauser [30], in his Fig. 8, p. 47, presented velocity profiles, for various values of $\beta$, from the solution of Eq. (47), and boundary conditions (48*a*) and (48*c*) for various values of the slip velocity are in the range $0\leqslant f'(0)=u(0)/U_e\leqslant 0.8$. This solution was transformed by Clauser [30] into velocity defect coordinates $(U_e-u)/u_\tau$ versus $Y$, and its comparison with the experimental data predicted $\alpha_C\simeq 0.018$, a universal constant. This overconstrainment led Clauser [29,30] to the definition of the equilibrium turbulent boundary layers where $\Lambda^*=(\delta^* p'/\tau_w=\text{const}$ and $1/\Lambda^*$ is the Rotta–Clauser parameter. Coles [16] carried out this approach of shallow wake one step further by Eq. (54) by introducing a wake function $W_C(Y)$ and parameter $\Pi_C$ to account for the outer part of the boundary layer. Thus, the present work on the outer layer, which does not depend on the molecular kinematic viscosity, under constant eddy viscosity hypothesis yields the Falkner–Skan equation for a turbulent wake subjected to the finite velocity slip on the wall. This is basically significant as it describes a new and better model for the strong adverse pressure gradient flow in the neighborhood of the separation domain.

## 4 Results and Discussion

The solution for the velocity distribution gives new composite log-half-power laws, based on the pressure scales, providing a better model of the flow, where the outer composite log-half-power law does not depend on the molecular kinematic viscosity. The composite law (Eq. (16)) in inner variables $(u_\times=u/U_p, y_p)$ and composite law (Eq. (17)) in outer variables $[(U_S-u)/U_\delta, Y]$ for weak pressure gradient yield to the logarithmic laws and for strong adverse pressure gradient yield to the half-power laws (26) and (27) in the neighborhood of separation. The velocity profiles in inner variables $(u_\times, \sqrt{y_p})$ from the data of Skare and Krogstad [14] are shown in Fig. 1(*a*). The substantial square region may be seen for each of the data. Furthermore, on pressure based velocity scales, the velocity data are nearly in equilibrium, showing very little change of constants $A$ and $C$ in half-power law (Eq. (26))

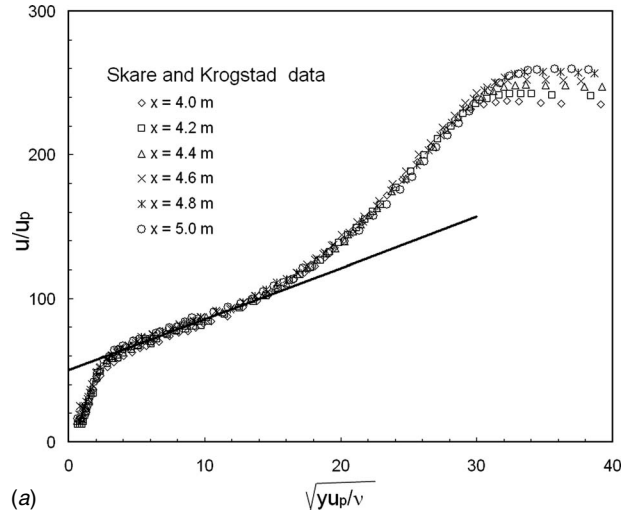


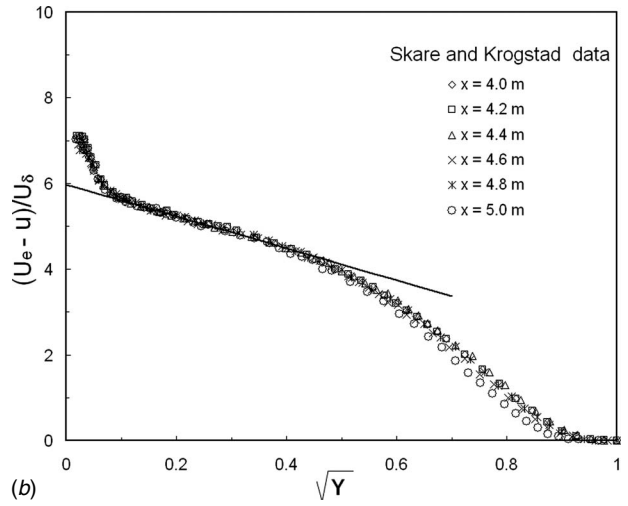


**Fig. 1 Velocity profile data of Skare and Krogstad [14] for adverse pressure gradient in terms of pressure velocity scaling and comparison with half-power law: (*a*) inner wall layer variables and (*b*) outer layer variables**

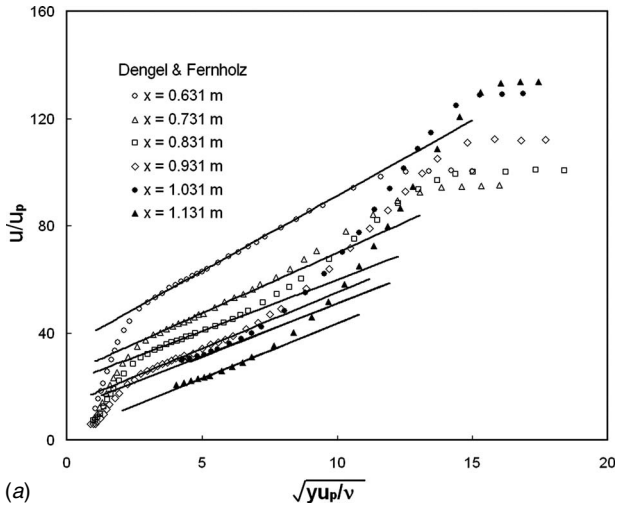


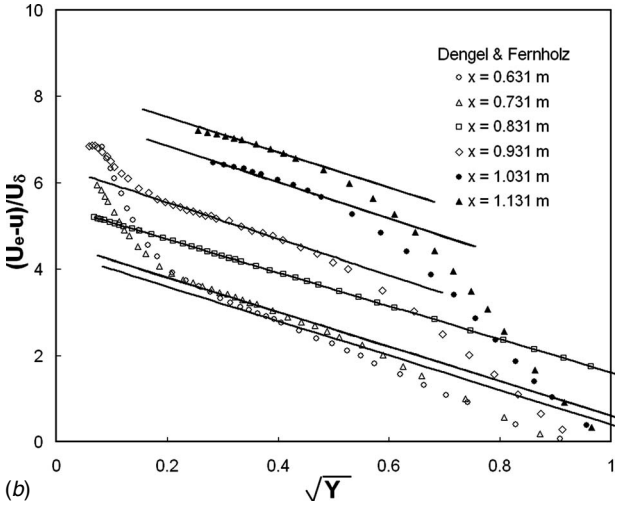


**Fig. 2 Velocity profile data of Dengel and Fernholz [9] for adverse pressure gradient in terms of pressure velocity scaling and comparison with half-power law: (*a*) inner wall layer variables and (*b*) outer layer variables**

domain. The data of Dengel and Fernholz [9] and Angele and Klingmann [11] in inner variables $(u_\times, \sqrt{y_p})$ are shown in Figs. 2(*a*) and 3(*a*) where the effect of the pressure gradient shifts each of the velocity profile data. The line marked for half-power law behavior of the data is fitted by Eq. (26), leading to estimation of constants $A$ and $C$ for that pressure gradient.

Skote [12] and Skote and Henningson [13] considered the DNS data of Na and Moin [33] in the neighborhood of separation for four velocity profiles at $X=150$, 155, 157, and 158 (where the separation occurs at $X=158$) which is shown in Fig. 4 along with the proposed half-power law. The limiting relation (26), corresponding to Stratford half-power law, is also shown in the same figure. The DNS data of Skote [12] and Skote and Henningson [32] for two velocity profiles at $X=412$ and 500 shown in Fig. 5 are also compared with the half-power law (26). It is also shown by Skote [12] and Skote and Henningson [13,32] that in the inner region, the half-power law compares much better than the logarithmic law proposed by Chawla and Tennekes [20] and Tennekes and Lumely [21]. Moreover, Simpson [8], Dengel and Fernholz [9], and Angele and Klingmann [11] have pointed out that the logarithmic region gradually disappears under the strong adverse pressure gradient in the turbulent boundary layer developing toward separation.

DNS velocity profile in inner variables $(u_\times, y_p)$ from the data of Skote [12] and Skote and Henningson [32] for strong adverse pressure gradient but away from separation is shown in Fig. 6(*a*) on the logarithmic scale and Fig. 6(*b*) on the half-power scale. The composite velocity profile (Eq. (16)) against the axial variable on the logarithmic scale and half-power scale is also shown, respectively, in these figures, which are supported well by the DNS data. The data for moderate values of the pressure gradient show that the proposed composite log-half-power laws are a better model of the flow in the overlap region.

The velocity profile data of Skare and Krogstad [14], Dengel and Fernholz [9], and Angele and Klingmann [11] are shown in Figs. 1(*b*), 2(*b*), and 3(*b*) in terms of shallow wake layer variables $[(U_e-u)/U_\delta, \sqrt{Y}]$ consisting of Eq. (A17), and the intercept $E_k$ has been estimated from the fit of each data. In the proposed outer nonlinear wake layer relation (17) in the variables $[(U_S-u)/U_\delta, \sqrt{Y}]$ the outer layer slip velocity ratio $b_S=U_S/U_e$ have been estimated from the lowest order outer nonlinear wake layer. The Falkner-Skan equations (47) subjected to the boundary conditions (48*a*)–(48*c*). The experimental data in outer wake layer variables is not displayed here and would be presented in a later publication. The nonlinear wake layer intercept $E$ from relations (17) and (A17) yield

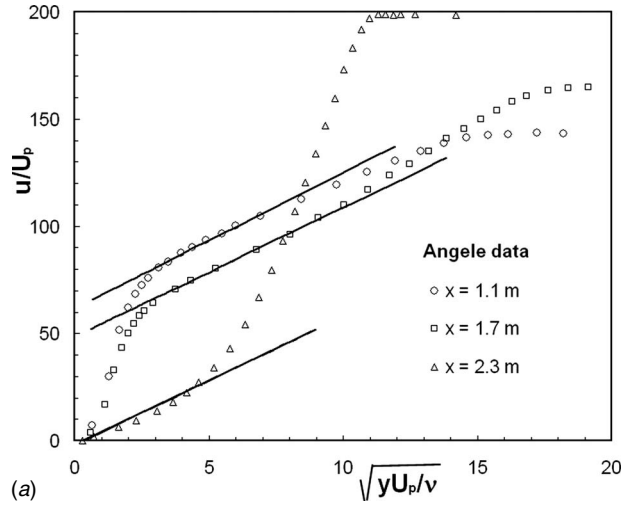


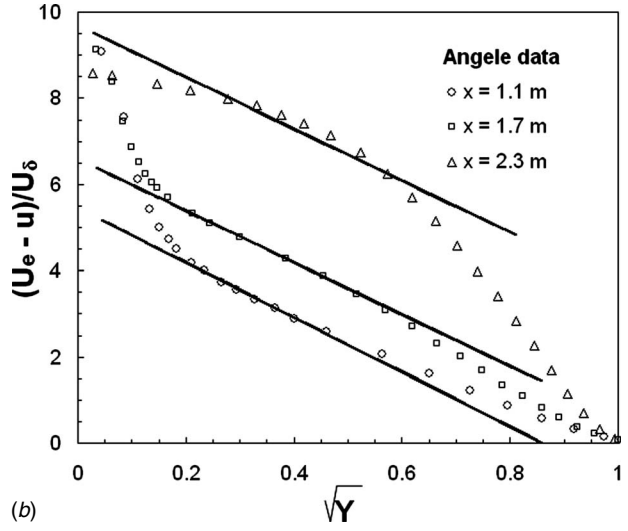


**Fig. 3 Velocity profile data of Angele and Klingmann [11] for adverse pressure gradient in terms of pressure velocity scaling and comparison with half-power law: (*a*) inner wall layer variables and (*b*) outer layer variables**

$$E = E_k + \frac{U_S - U_e}{U_\delta} = E_k + (b_S - 1)\frac{U_e}{U_\delta} \tag{56}$$

where the slip velocity $b_S = f'(0)$ is prediction from Eq. (51*a*) based on closure model solution of the Falkner-Skan equation for the non-linear wakes. The comparison of velocity profiles is shown in Fig. 4 for $X=412$ and $X=500$ from the DNS data of Skote and Henningson [32]. In these works [12,13,32,33], all the

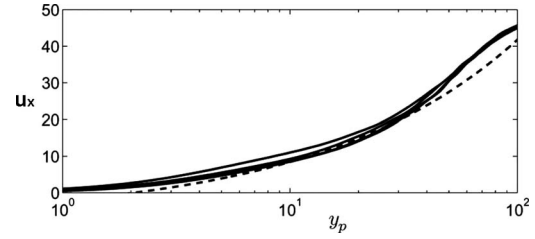


**Fig. 4 Comparison of the velocity profile from the DNS data of Na and Moin [33] under strong adverse pressure gradient at $X=150, 155, 157, 158$; --- half-power law (26); — DNS data (after Skote and Henningson [13]); here, $X = x/\delta_0^*$**

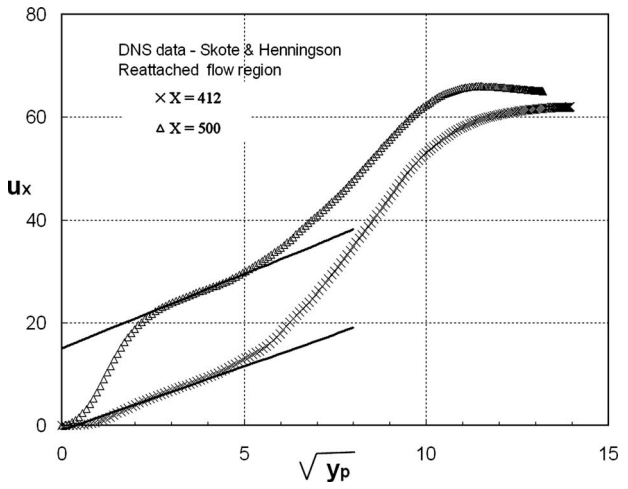


**Fig. 5 Comparison of the velocity profile in the flow reattachment region, $X=412$ and $X=500$, from the DNS data of Skote and Henningson [32] under adverse pressure gradient with the half-power law (26)**

quantities are nondimensionalized by the freestream velocity and the displacement thickness at the starting position of the simulation ($x=0$) where the flow is laminar. A line drawn from the half-power law (Eq. (26)) shows a substantial linear region for each of the data and the constants $A$ and $C$ have been estimated.

An extensive comparison of the present theory with all available two-dimensional measurement of Bell, Clauser, Ludwig and Tillmann, Newman, Perry, Schubauer and Klebanoff, Schubauer and Spangenberg, and Stratford (from Coles and Hirst [17]), Dengel and Fernholz [9], Alving and Fernholz [10], Angele and Klingmann [11], Skare and Krogstad [14], and Samuel and Joubert [34] has been estimated. The various proposals for half-power law slope $A$ are given below:

In Perry et al. [6,7],

$$A = 0.236\left[\frac{\delta}{\delta^*}\left(\frac{U_{S1}}{U_e}\right)^3\left(\frac{U_e}{U_\delta}\right)^2\right]^{1/2} \tag{57}$$

In Kader and Yaglom [4],

$$A = (20 + 200\Lambda)^{1/2} \tag{58}$$

In Afzal [3],

$$A = 3.5 + 19.7\Lambda \tag{59}$$

In Vieth et al. [24],

$$A = 2[0.41 + 0.18\exp\{-0.0045(\Lambda R_p)^2\}]^{-1} \tag{60}$$

Equation (60) by Vieth et al. [24] contains an additional parameter, the Reynolds number $R_p$ involving molecular kinematic viscosity $\nu$, in contrast to Eq. (58) by Kader and Yaglom [4] and Eq. (59) by Afzal [3] (see also Ref. [35]). Equation (57) from Perry and Schofield [6] and Schofield [7] is complex in nature, involving three parameters, $\delta^*/\delta$, $U_\delta/U_e$, and $U_{S1}/U_e$. The extensive data for the prefactor of half-power law $A$ are shown in Fig. 7 against $\Lambda$, under strong adverse pressure gradient near separation. Equation (58) by Kader and Yaglom [4] and Eq. (59) by Afzal [3] are also shown in the same figure. Furthermore, if $A=2/k$, then $k=2/(20+200\Lambda)^{1/2}$ from Kader and Yaglom [4], $k=2/(3.5+19.7\Lambda)$ from Afzal [3], and $k=0.41+0.18\exp\{-0.0045(\Lambda R_p)^2\}$ from Vieth et al. [24]. An inspection of Fig. 7, for half-power law slope $A=2/k$ [33] for $k=0.41$, would not be inconsistent with the data for $0.01<\Lambda<0.15$ for strong adverse pressure gradient.

In the strong adverse pressure gradient flow near separation, the intercept $C$ of the inner half-power law is stated below.

In Kader and Yaglom [4],

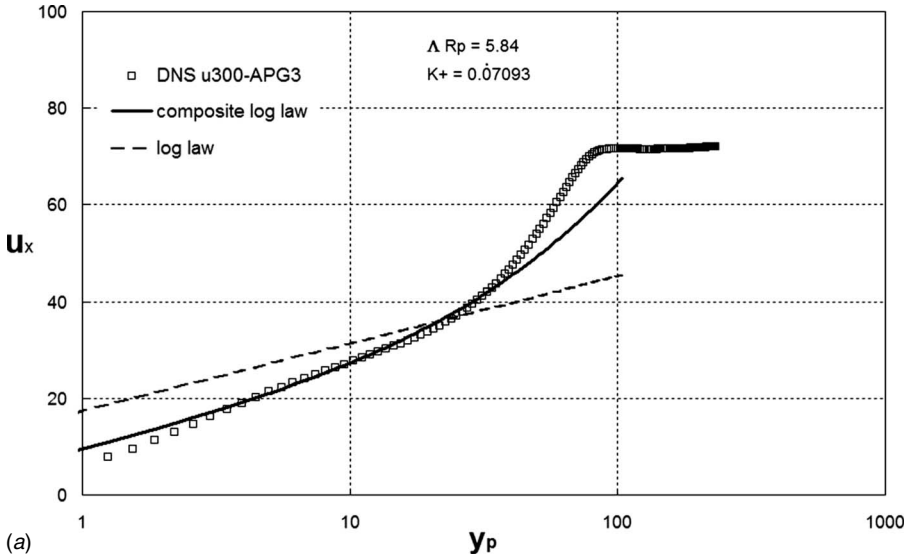


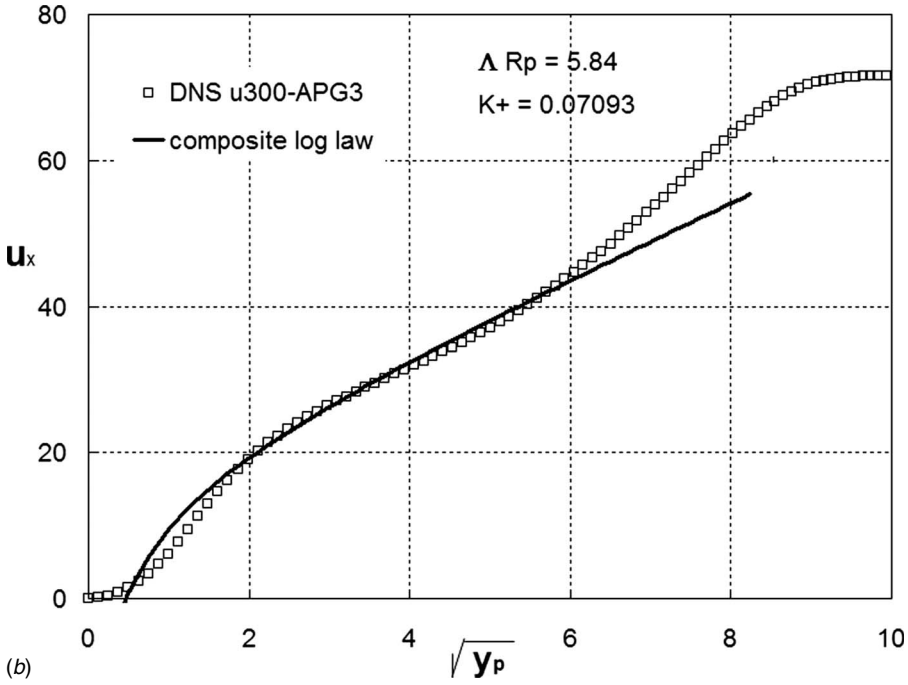


**Fig. 6 Comparison of the velocity profile at $X=300$ from the APG3 DNS data of Skote and Henningson [30] under adverse pressure gradient with the present composite laws based on pressure the velocity scaling with axial coordinate $y_p$ in terms of (*a*) logarithmic scale and (*b*) half-power scale**

$$C = \sqrt{\Lambda R_p}\left[2.44 \ln \Gamma - \frac{15}{\sqrt{\Gamma}} - \frac{6}{\Gamma}\right], \quad \Gamma = \frac{(\Lambda R_p)^{3/2}}{5 + 50\Lambda} \tag{61}$$

In Afzal [3],

$$C = 2.25\Lambda R_p - 0.012(\Lambda R_p)^2 \tag{62}$$

In Vieth et al. [24],

$$C = 5 - [1.695 \ln(\Lambda R_p)^{3/2} + 3.96]\exp(-50\Lambda R_p) \tag{63}$$

In the present work,

$$C = \frac{A}{2}\sqrt{\Lambda R_p}[\ln(\Lambda R_p)^{3/2} + C_1] \tag{64}$$

The inner layer intercept $C$ from the present work is given by Eq. (64) with $C_1=0$, which has been compared to the extensive data in Fig. 8. The leading term in Eq. (62) describes data very well for $\Lambda R_p < 60$. The relation shows that $C$ is negative for $0 < \Lambda R_p < 1$. The minimum value is $C=-2.692$ at $\Lambda R_p=0.135$. For $\Lambda R_p \to 0$, Eq. (61) shows $C \to -\infty$ and Eq. (63) shows $C \to +\infty$, whereas Eq. (64) shows $C \to 0$.

The outer layer constant $E$ proposed by Afzal [3] is

$$E = 6.5(\beta_o - \beta), \quad \beta_0 = -0.198838 \tag{65}$$

which shows $E=0$ at the point of separation $\beta=\beta_0$. In the present work, outer constant $F$ is given below,

$$E = \frac{A}{2}\sqrt{\Lambda}[-\ln \Lambda - E_1] \tag{66}$$

The outer constant $E$ may be estimated from local velocity defect outer wake law (17) or else from relation (56), as described ear-

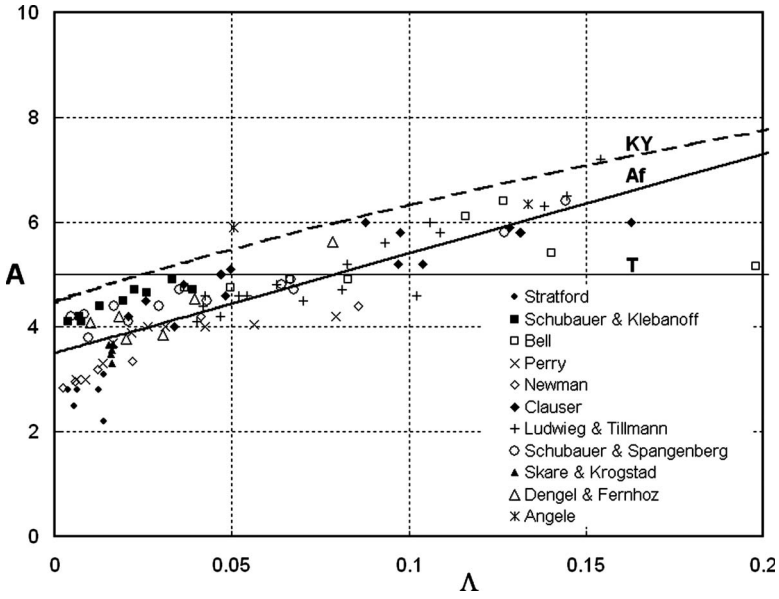


**Fig. 7 Slope of half-power law under adverse pressure gradient data: KY: Kader and Yaglom [4], Af: Afzal [3], and *T*: $A=2/k$, $k=0.41$**

lier. In the present work, the wake layer constant $E$ for each data point is estimated from matching relation (18), in which nondimensional velocity slip $b$ is adopted from relation (70) and $C$ is taken from the data shown in Fig. 8. The outer wake layer constant $E$ is shown in Fig. 9 along with our prediction (66) for $E_1=1.5$. As $\Lambda\to 0$ near separation, the constant $E\to 0$ and Eq. (66), is supported by the data shown in the same figure. Furthermore, the slip velocity $b_S$ is connected to matching (Eq. (18)) that may be expressed as

$$E = b_S\frac{U_e}{U_\delta} - CR_p^{-1/2} \tag{67}$$

where as $R_p\to\infty$, $E\to b_S U_e/U_\delta$. The skin friction (Eq. (21)) in terms of the slip velocity $b_S$ becomes

$$b_S\sqrt{\frac{2}{C_f}} = \frac{A}{2}\ln\left(R_\delta\sqrt{\frac{C_f}{2}}\right) + B + D, \quad R_\delta = \frac{U_e\delta}{\nu} \tag{68}$$

In the neighborhood of the separation point, the slip velocity parameter $b_S=0$ and the flow domain correspond to $0\leqslant b_S\leqslant 1$. When $U_S\equiv U_e$ and $b_S\equiv 1$, the outer flow is a shallow wake, and relation (67) for traditional skin friction logarithmic law is recovered [16]. Kader and Yaglom [4] under strong adverse pressure gradient considered the shallow outer wake layer ($U_S\equiv U_e$) in terms of variables $(U_e-u)/U_\delta$ versus $\sqrt{Y}$. Consequently, the half-power law and skin friction law of Kader and Yaglom [4] given by Eqs. (A14) and (A5) in Appendix A are not valid in the neighborhood of the separation region.

The outer layer is governed by the nonlinear wake equation and

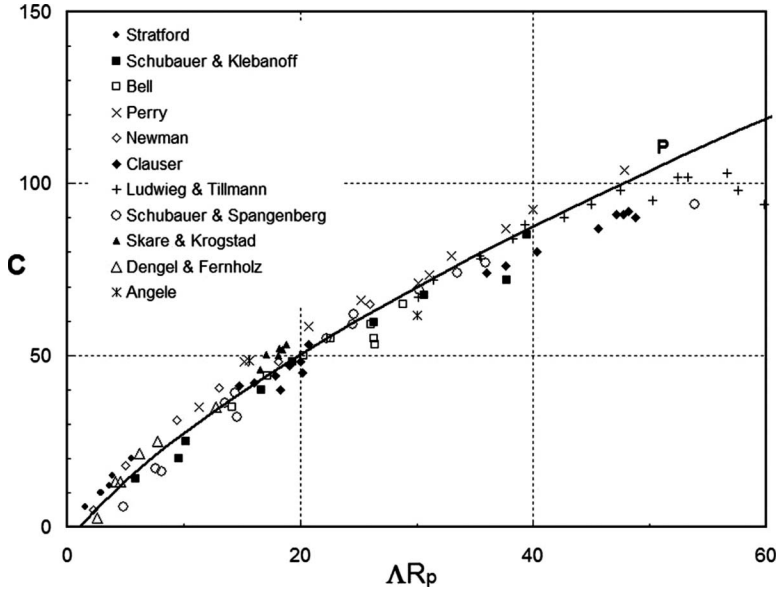


**Fig. 8 Wall layer intercept of half-power law under adverse pressure gradient; — present proposal: $kC=\sqrt{\Lambda R_p}[\ln(\Lambda R_p)^{3/2}-C_1]$ for $C_1=0$**

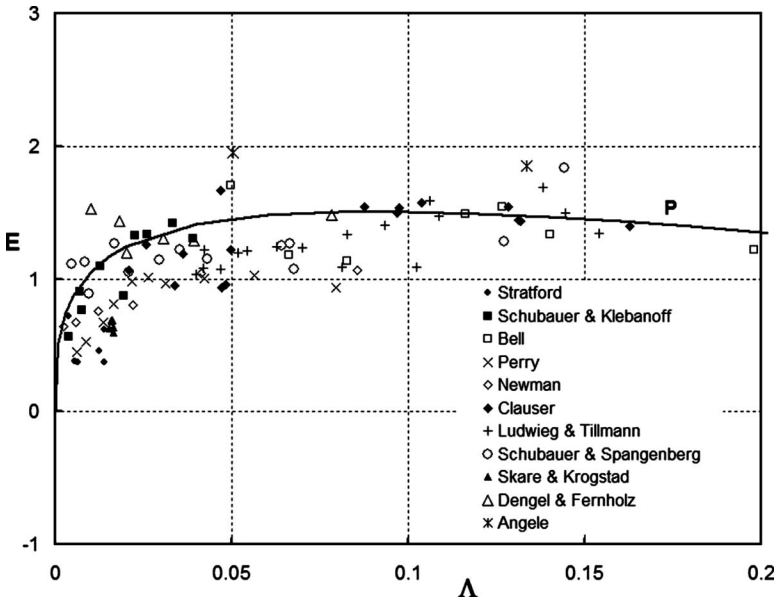


**Fig. 9 Outer wake layer intercept of half-power law under adverse pressure gradient; — present proposal: $kE=\sqrt{\Lambda}[-\ln\Lambda-E_1]$ for $E_1=1.5$**

**Table 1 Values of *m* from experiments near separation**

| Proposals | *m* |
|---|---|
| Ludwieg and Tillmann [37] | −0.23 |
| Newman [39] | −0.228 |
| Schubauer and Klebanoff [38] | −0.257 |
| Stratford [1] | −0.25 |
| Townsend [2] | −0.234 |
| Simpson [8] | −0.251 |
| Simpson [8] | −0.222 |
| Skare and Krogstad [14] | −0.22 |
| Alving and Fernholz [10] | −0.226 |
| Castillo et al. [40] | −0.21 |
| Elsberry et al. [15] Case A | −0.21 |
| Elsberry et al. [15] Case B | −0.18 |
| Present work and Afzal [3] | −0.165858 |

is under equilibrium provided that velocity $U_e \propto \delta^m$ for constant value $m$, which from Eq. (44) near domain of separation $\Lambda \approx 0$, gives

$$m = -(2+H)^{-1} \tag{69}$$

The pressure gradient parameter $m$ in the turbulent boundary layer from the extensive experimental data for the strong adverse pressure gradient near the verge of separation is given in Table 1. The neighborhood of the separation domain $-0.25 < m \leqslant m_0$ $(-1/4 < \beta \leqslant \beta_0)$, where $m_0 = -0.165858$ $(\beta_0 = -0.1988838)$ at the point of separation is of particular interest. Addendum A1 in the data of Elsberry et al. [15] shown in their Fig. (28b) is in good agreement with Eq. (69).

The lowest outer nonlinear equations are in equilibrium for constant values of $m$. By subjecting the constant eddy viscosity closure model, the outer flow is governed by Falkner–Skan equation (47) with boundary conditions (48*a*)–(48*c*). The Falkner–

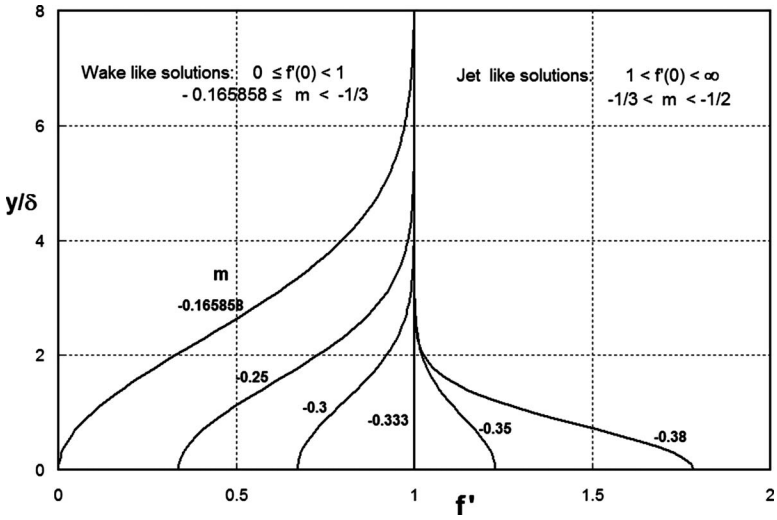


**Fig. 10 Wake- and jetlike velocity profile solutions from the lowest order outer nonlinear wake layer with Clauser eddy viscosity model from Falkner–Skan equations (47) and (48*a*)–(48*c*)**

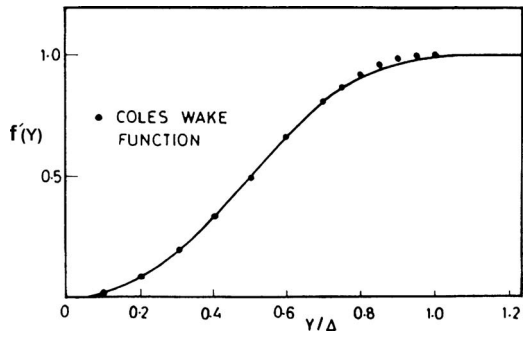


**Fig. 11 Comparison of Coles wake function with the solution of the velocity profile from the lowest order outer nonlinear wake layer equations with constant eddy viscosity model for zero velocity the slip $C_f = b_S = 0$, predicting $m = -0.165858$**

Skan equation (47) and boundary condition (48*b*) for $f''(0)=0$ (demand $\Lambda=0$), give the wakelike solution for $-1/3 < m \leq m_0$ ($-0.5 < \beta \leq \beta_0$) and the jetlike solution $-1/2 \leq m < -1/3$ ($-1 \leq \beta < -0.5$), where $m_0=-0.165858$ ($\beta_0=-0.198838$). The reverse flow solutions also exist for wakelike flows for $m_0 < m < 0$ ($\beta_0 < \beta < 0$) and jetlike flows for $-\infty \leq m \leq -1/2$ ($1 < \beta < -1$) are also not considered here. The wake- and jetlike solutions for $-1/2 \leq m \leq m_0$ are shown in Fig. 10, implying the nonlinearity of the lowest order outer flow. The wake- and jetlike closed form approximate solution (51*b*) is given below,

$$b_S = 2\frac{m_0 - m}{1 + 2m} \tag{70}$$

where $m_0=-0.165858$. The solution to Falkner–Skan equation (47) under boundary conditions $f(0)=f'(0)=f''(0)=f'(\infty)-1=0$ that yields $m=m_0$ correspond to the zero slip velocity, implying the point of flow separation. Furthermore, the normalized velocity profile (Eq. (53)) shown in Fig. 11 compares well to Coles [16] wake function. For $\Lambda \neq 0$, the solution of Falkner–Skan equation (47) with boundary conditions (48*a*)–(48*c*) shown in Fig. 12 predicts the skin friction parameter $C_f/\alpha_C$ against the nondimensional slip velocity $b_S = U_S/U_e$. The skin friction coefficient $C_f$ may be estimated from thenumerical value $\alpha_C \approx 0.018$ of Clauser's universal constant [30].

## 5 Conclusions

The turbulent boundary layer equations subjected to strong adverse pressure gradient with negligible wall stress have been analyzed in terms of pressure based velocity scales $U_p$ in the inner layer and $U_\delta$ in the outer layer. The outer layer is governed by the equations of a nonlinear wake and the lowest order outer flow does not depend on the molecular kinematic viscosity, which is a better model for fully developed mean turbulent flow. Whereas in the earlier work [19,24], the lowest order outer flow is taken to be dependent on the molecular kinematic viscosity.

The asymptotic expansions in the inner and the outer regions have been matched by IMK hypothesis leading to open functional equations. The velocity distribution in the overlap region gives new composite laws based on pressure scalings and provides a better model of the flow. The solutions for new composite log-half-power laws provide a better model of the flow, where the outer composite log-half-power law does not depend on the molecular kinematic viscosity. Furthermore, these new composite laws are better and one may be benefited from their limiting relations that for weak pressure gradient yield the traditional logarithmic laws and for strong, adverse pressure gradient yield the half-power laws. The proposed limiting half-power law has been supported by extensive experimental and DNS data. For moderate values of the pressure gradient, the data show that the proposed

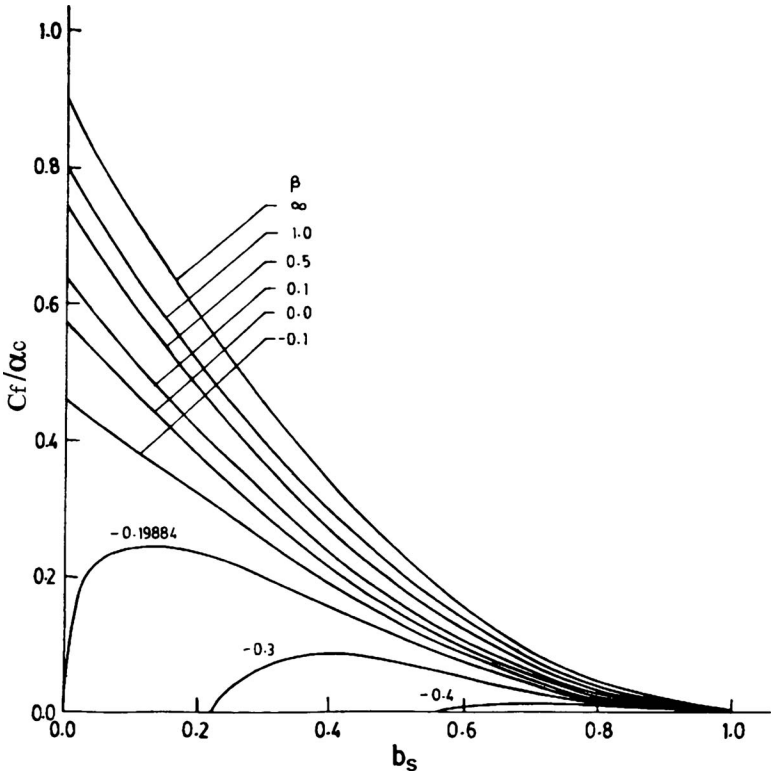


**Fig. 12 The skin friction parameter $C_f/\alpha_C$ and wall slip velocity parameter $b_S = U_S/U_e$ from the solution of the lowest order outer nonlinear wake layer equations from the constant eddy viscosity model**

composite log-half-power laws are a better model of the flow in the overlap region, where the outer composite log-half-power law does not depend on the molecular kinematic viscosity.

The constants $A$, $C$, and $E$ in the matching relations would have to be determined by appealing to experiments, as the matching will not give them. The constants estimated from the extensive experimental data show that constant $A$ depends on $\Lambda$, $C$ depends on $\Lambda R_p$, and $E$ depends on $\Lambda$. For $A=2/k$, the constant $k$ depends on the pressure gradient parameter $\Lambda$, but data would not be inconsistent with $k=0.41$. The present predictions (Eq. (65)) for the inner layer and Eq. (57) for the outer layer compare well with to data.

The lowest order outer flow is described by the inviscid nonlinear turbulent wake layer equations, which are under equilibrium for a constant value of $m$, where $U_e \propto (x-x_0)^m$. In the neighborhood of separation, the constant $m$ proposed in Table 1 from various works show appreciable difference when compared to the present prediction $m_0=-0.165858$ ($\beta_0=-0.198838$). This is basically significant as it describes a new and better model for the strong adverse pressure gradient flow in the neighborhood of the separation domain.

The lowest order outer nonlinear flow region under constant eddy viscosity hypothesis yields the Falkner–Skan equation with pressure gradient parameter $\beta=m/(1+m)$ subjected to the boundary conditions of finite slip velocity $b_S$ on the wall and oncoming strewn velocity $U_e$. It admits the wakelike solution for $-1/3<m\leqslant m_0$ and jetlike solution $-1/2\leqslant m<-1/3$, where $m_0=-0.165858$ corresponds to the zero slip velocity, implying the point of separation. The solution at $m=m_0$ with zero slip upon normalization compares well to the Coles [16] wake function. Thus, the present work on the outer layer, which does not depend on the molecular kinematic viscosity, under constant eddy viscosity hypothesis yields the Falkner–Skan equation for a turbulent wake subjected to the finite velocity slip on the wall.

Kader and Yaglom [4] and Mellor and Gibson [5] considered the outer layer as the linearized shallow wake with velocity defect $(U_e-u)/U_\delta$ whose matching with the wall layer gives the half-power law (Eq. (A4)). The outer layer in the present work is a nonlinear outer wake layer, where the matching provides the local velocity defect law $(U_S-u)/U_\delta$ and the composite law (Eq. (27)), which near separation yields the half-power law (Eq. (33)). For a linearized shallow outer flow $U_S \equiv U_e$, Eq. (33) yields Eq. (A4). Clearly, the work of Kader and Yaglom [4] and Mellor and Gibson [5] for the outer layer as the linearized shallow wake is not valid in the neighborhood of the separation region. For transitional rough surface, the matching of the inner wall layer and outer wake layer under to strong adverse pressure gradient near separation has been described in the Appendix of the paper by Afzal [42].

## Acknowledgment

The author is grateful for the support of All India Council of Technical Education, New Delhi.

## Nomenclature

$A$ = a constant in the matching relations (16) and (17)
$A_n$ = Coefficients in series expansion (32$b$)
$b_S$ = outer layer slip velocity on the surface, $U_S/U_e = F_0'(x,o)$
$B$ = a constant in skin friction relation (21)
$B_1$ = a constant
$C$ = a constant in the inner matching relation (16)
$C_1$ = a constant in Eq. (20)
$C_f$ = skin friction coefficients
$C_n$ = coefficients in series expansion (32$a$)
$d$ = $1/\beta=(1+m)/m$
$d_0$ = a constant in Eq. (50)
$D$ = a constant in skin friction relation (21)
$E$ = a constant in the outer matching relation (17)
$E_k$ = the value of $E$ in a shallow wake flow
$E_1$ = a constant in Eq. (20)
$f'(Y)$ = nondimensional lowest order self-similar velocity profile, $F_0'(x,Y)$
$f_0'(x,\eta)$ = velocity profile (A1) in Eqs. (31$a$) and (32$a$)
$F'(x,Y)$ = nondimensional velocity profile, $u/U_e$
$F_0'(x,Y)$ = lowest order outer velocity profile
$h'o(x,Y)$ = non-dimensional velocity defect for a shallow outer wake layer defined by Eq. (A1)
$H$ = the shape factor, $\delta^*/\theta=\delta_1/\delta_2$
$k$ = the Karman constant
$K_+$ = nondimensional pressure gradient, $\nu p'/\rho u_\tau^3$
$L$ = length scale from streamwise pressure gradient, $-U_e/(dU_e/dx)$
$m$ = pressure gradient parameter, $(\delta/U_e)(dU_e/d\delta)$
$p$ = static pressure
$p'$ = streamwise pressure gradient
$R_p$ = Reynolds number based on pressure scale velocity, $U_p\delta/\nu$
$R_\tau$ = friction Reynolds number, $u_\tau\delta/\nu$
$T(x,Y)$ = nondimensional outer Reynolds shear stress, $\tau/\rho U_\delta^2$.
$T_0(x,Y)$ = lowest order outer Reynolds shear stress
$u'$ = velocity fluctuation over the mean velocity $u$
$u(x,y)$ = streamwise mean velocity at a point
$u_\times$ = inner velocity profile, $u/U_p$
$u_\tau$ = the friction velocity, $\sqrt{\tau_w/\rho}$
$U_e$ = velocity at the edge of the boundary layer
$U_S$ = outer layer slip velocity on the surface
$U_p$ = inner velocity scale, $(\nu p'/\rho)^{1/3}$
$U_\delta$ = outer velocity scale, $(\delta p'/\rho)^{1/2}$
$v(x,y)$ = normal mean velocity at a point
$v'$ = velocity fluctuations over mean velocity $v$
$w$ = outer perturbation parameter, $U_\delta/U_e$
$W(x,Y)$ = wake function
$W_C(Y)$ = Coles wake function
$x$ = the coordinate in the streamwise direction
$x$ = in Figs. 4–6 is $x/\delta_0^*$
$x_0$ = the reference coordinate in the streamwise direction
$X$ = nondimensional stream coordinate in DNS solutions, $x/\delta_0^*$
$y_+$ = traditional wall variable, $yu_\tau/\nu$
$y$ = the coordinate in the normal direction
$y_p$ = nondimensional inner variable
$Y$ = nondimensional outer variable, $y/\delta$
$Z_1(Y)$ = a function defined by Eq. (23)

### Greek Symbols

$\alpha_C$ = Clauser universal constant
$\beta$ = pressure gradient parameter, $m/(1+m)$
$\gamma$ = $(AU_\delta/2U_e)^2$
$\delta$ = boundary layer thickness
$\delta_0^*$ = displacement thickness at origin in DNS solutions
$\delta_1$ = $\delta^*/\delta$
$\delta_2$ = $\theta/\delta$
$\delta^*$ = displacement thickness
$\lambda$ = $\delta p'/\tau_w=\Lambda^{-1}$
$\Delta$ = shallow wake scale (A3), $\delta/w=\gamma x$
$\zeta$ = inner variable, $y_pA^2/4$

$\eta$ = outer variable, $\gamma Y$
$\theta$ = momentum thickness
$\Lambda$ = nondimensional wall stress parameter, $\tau_w/\delta p'$
$\Lambda^*$ = alternate nondimensional wall stress parameter, $\Lambda\delta^*/\delta$
$\nu$ = molecular kinematic viscosity
$\nu_\tau$ = eddy kinematic viscosity
$\rho$ = density of fluid
$\tau$ = Reynolds shear stress, $-\rho\langle u'v'\rangle$
$\tau_\times(x,y_p)$ = nondimensional inner Reynolds shear stress, $\tau/\rho U_p^2$
$\tau_w$ = shear stress on the surface

**Calligraphic Symbol**

$\mathcal{T}$ = effective normal Reynolds stress, $-\rho\langle u'^2 - v^2\rangle$

## Appendix A: Outer Layer as a Shallow Wake

The flow in the shallow outer wake layer $F_0(X,Y)=Y$ and $U_S=U_e$ was analyzed by Mellor and Gibson [5] and Kader and Yaglom [4]. The lowest order equations (Eqs. (21) and (22)) yield $T_0'(Y)=0$, or $T_0(Y)=$const that fails to satisfy the two boundary conditions on the Reynolds shear stress, and a revision for the shallow outer layer with small velocity defect is needed.

The outer expansions (Eqs. (6)–(8) for a shallow outer wake layer become

$$\frac{u}{U_e} = F' = 1 - wh_0'(x,Y) + O(w^2) \tag{A1}$$

$$\frac{\tau}{\rho U_e^2 w^2} = T = t_0(x,Y) + O(w) \tag{A2a}$$

$$\frac{\mathcal{T}}{\rho U_e^2 w^2} = \Gamma = \chi_0(x,Y) + O(w) \tag{A2b}$$

where $Y=y/\delta$, $\delta=w\Delta$, and $w=U_\delta/U_e$. The matching of outer layer (Eq. (A1)) with the inner layer (Eq. (3)) by IMK hypothesis gives the following.

Inner wall layer:

$$\frac{u}{U_p} = A\sqrt{y_p} + C \tag{A3}$$

Outer velocity:

$$\frac{U_e - u}{U_\delta} = -A\sqrt{Y} + E_k \tag{A4}$$

The relation:

$$U_e = CU_p + E_k U_\delta \tag{A5}$$

Here, the inner law (Eq. (A3)) is of the same form as Eq. (26) but the defect layer (Eq. (A4)) and matching (Eq. (A5)) for the shallow outer wake layer are different from the nonlinear wake (Eqs. (27) and (18), respectively).

The first order outer momentum equation and boundary conditions are

$$t_0' - \frac{(\Delta w U_e)_x}{wU_e} Y h_0'' + 2\Delta U_{ex} h_0' + \Delta h_{0x}' = 0 \tag{A6}$$

$$Y \to \infty, \quad h_0' \to 0 \quad \text{and } t_0 \to 0 \tag{A7}$$

The integration of outer equations (A6) with respect to $Y$ gives

$$t_0 - \frac{(\Delta U_e)_x}{U_e} Y h_0' + \frac{(\Delta U_e^3 h_0)_x}{U_e^3} = 0 \tag{A8}$$

where $\delta=w\Delta$, $\Delta=\gamma x$ and terms of order $w_x/w$ have been neglected. For $U_e=c\Delta^m$, the outer equation (A8) subjected to boundary and matching conditions becomes

$$t_0/\gamma - (1+m)Yh_0' + (1+3m)h_0 = 0 \tag{A9}$$

$$h_0(0) = t_0(0) = 0 \quad \text{and } h_0'(Y) = -A\sqrt{Y} + E_k \quad \text{as } Y \to 0 \tag{A10}$$

$$h_0'(\infty) = t_0(\infty) = 0 \tag{A11}$$

Mellor and Gibson [5] for the specific eddy viscosity closure model ($t_0=e_1 h_0''$), based on $\delta^*$ rather than $\delta$, provided that the numerical solution $m=-0.23$, proposed that

$$\frac{U_e - u}{U_\delta} = 10.27\sqrt{\frac{\delta^*}{\delta}} - 15.6\sqrt{\lambda_m Y} \tag{A12}$$

$$\lambda_m^2 = \frac{\delta^*}{\delta}\left(\frac{U_\delta}{U_e}\right)^2 = -0.00948 \tag{A13}$$

Kader and Yaglom [4] adopted the outer layer as a shallow wake and from the extensive experimental data proposed that

$$\frac{U_e - u}{U_\delta} = E_k - (20 + 200\Lambda)^{1/2}\sqrt{Y} \tag{A14}$$

where $E_k=10(3\Lambda^2+0.16)^{1/4}$ and the skin friction law is

$$\frac{U_e}{u_\tau} = 2.44\ln\Gamma - \frac{15}{\sqrt{\Gamma}} - \frac{6}{\Gamma} + 10\left[3 + \frac{0.16}{\Lambda^2}\right]^{1/4} \tag{A15a}$$

$$\Gamma = \frac{(\Lambda R_p)^{3/2}}{5 + 50\Lambda} \tag{A15b}$$

In the work of Kader and Yaglom [4], the skin friction (Eq. (A15)) and outer velocity defect law (A14) and in Mellor and Gibson [5] the outer velocity defect law (A12) are based on the assumption that the outer layer as the shallow wake which is not valid in the neighborhood of the separation point.

The matching of the outer shallow outer wake layer relation (A1) with inner wall layer (3) based on matching relation (11) yields the following relations.

Composite log-half power wall law:

$$\frac{u}{U_p} = A\sqrt{y_p + \Lambda R_p} + \frac{A}{2}\sqrt{\Lambda R_p}[\ln y_p - 2\ln(\sqrt{y_p + \Lambda R_p} + \sqrt{\Lambda R_p})] + C \tag{A16}$$

Composite log-half power velocity defect law:

$$\frac{U_e - u}{U_\delta} = A\sqrt{Y + \Lambda} + \frac{A}{2}\sqrt{\Lambda}[-\ln Y + 2\ln(\sqrt{Y + \Lambda} + \sqrt{\Lambda}] + E_k \tag{A17}$$

The matching of inner and outer relations (A16) and (A17) in the overlap region yields the relation (A5). The outer velocity defect law (A17) represents a shallow wake. The matching relation (A5) becomes singular at the point of separation and becomes unbounded in the neighborhood of the separation. In fact, in the neighborhood of the separation point, the outer wake layer is nonlinear as described by the outer wake layer law (17) along with the matching condition (18).

## Appendix B: Asymtptotic Relations for Weak and Strong Adverse Presure Gradiants When Outer Layer is a Non-Linear Wake

In the case of strong adverse presure gradiant near separation, as $\Lambda \to 0$, the matching relation (16) in inner variables becomes

$$\frac{u}{U_p} = A(y_p)^{1/2} + C + \frac{A}{2}(\Lambda R_p)^{1/2}\left[ -\left(\frac{\Lambda R_p}{y_p}\right)^{1/2} + \frac{1}{12}\left(\frac{\Lambda R_p}{y_p}\right)^{3/2} - \frac{1}{40}\left(\frac{\Lambda R_p}{y_p}\right)^{5/2} + \cdots \right] \tag{B1}$$

and the matching relation (17) in outer variables becomes

$$\frac{U_S - u}{U_\delta} = -A(Y)^{1/2} + E + \frac{A}{2}\Lambda^{1/2}\left[ \left(\frac{\Lambda}{Y}\right)^{1/2} - \frac{1}{12}\left(\frac{\Lambda}{Y}\right)^{3/2} + \frac{1}{40}\left(\frac{\Lambda}{Y}\right)^{5/2} + \cdots \right] \tag{B2}$$

For the weak presure gradiant, away separation as $\Lambda \to \infty$, the matching relation (16) and (17) in inner and outer variables become

$$\frac{u}{U_p} = \frac{A}{2}(\Lambda R_p)^{1/2}\left[ \ln y_p + \frac{2B}{A} + \ln(\Lambda R_p)^{1/2} + \frac{1}{2}\frac{y_p}{\Lambda R_p} - \frac{1}{16}\left(\frac{y_p}{\Lambda R_p}\right)^2 + \frac{1}{48}\left(\frac{y_p}{\Lambda R_p}\right)^3 + \cdots \right] \tag{B3}$$

$$\frac{U_S - u}{U_\delta} = \frac{A}{2}(\Lambda)^{1/2}\left[ -\ln Y + \frac{2D}{A} - \frac{1}{2}\frac{Y}{\Lambda} - \frac{1}{16}\left(\frac{Y}{\Lambda}\right)^2 + \frac{1}{48}\left(\frac{Y}{\Lambda}\right)^3 + \cdots \right] \tag{B4}$$

In the traditional variables,

$$y_+ = \frac{y u_\tau}{\nu}, \quad K_+ = \frac{\nu p'}{\rho u_\tau^3}, \quad \lambda = \frac{\delta p'}{\rho \tau_w}, \quad k = \frac{2}{A} \tag{B5}$$

the strong adverse presure gradiant near separation ($\Lambda \to 0$) and the relations (B1) and (B2) become

$$\frac{u}{U_\tau} = A(K_+ y_+)^{1/2} + (K_+)^{1/3} C + \frac{A}{2}\left[ -(K_+ y_+)^{-1/2} + \frac{1}{12}(K_+ y_+)^{-3/2} - \frac{1}{40}(K_+ y_+)^{-5/2} + \cdots \right] \tag{B6}$$

$$\frac{U_S - u}{U_\tau} = -A(\lambda Y)^{1/2} + (\lambda)^{1/2} E + \frac{A}{2}\left[ (\lambda Y)^{-1/2} - \frac{1}{12}(\lambda Y)^{-3/2} + \frac{1}{40}(\Lambda Y)^{-5/2} + \cdots \right] \tag{B7}$$

For weak presure gradiants flow ($\Lambda \to \infty$) and the relations (B3) and (B4) become

$$\frac{u}{U_\tau} = \frac{A}{2}\left[ \ln y_+ + \frac{2B}{A} + \frac{1}{2}K_+ y_+ - \frac{1}{16}(K_+ y_+)^2 + \frac{1}{48}(K_+ y_+)^3 + \cdots \right] \tag{B8}$$

$$\frac{U_S - u}{U_\tau} = \frac{A}{2}\left[ -\ln Y + \frac{2D}{A} - \frac{1}{2}\lambda Y + \frac{1}{16}(\lambda Y)^2 - \frac{1}{48}(\lambda Y)^3 + \cdots \right] \tag{B9}$$

The matching relations in the overlap regin give

$$U_S(x) = U_p C + U_\delta E. \tag{B10}$$

$$\frac{U_S}{u_\tau} = \frac{A}{2}\ln R_\tau + B + D, \quad R_\tau = \frac{u_\tau \delta}{\nu} \tag{B11}$$

These relations satisfies the condition that outer slip velocity $U_S = 0$ at the point of separation $\Lambda = 0$ and $U_S \to U_e(x)$ as far away from separation point $\Lambda \to \infty$, and outer velocity profile may be obtained from the solution of outer wake layer Eqs. (47) and (48*a*)–(48*c*). For a transitional rough surface, the extension of the above matching relations between outer non-linear-wake layer and inner wall layer have been described in the Appendix of paper by Afzal [42].

## Appendix C: Separating and ReattachingFlow

In general, the friction velocity $u_\tau$ may be defined as

$$u_\tau = \sqrt{j\nu\left(\frac{\partial u}{\partial y}\right)_{y=0}}, \quad j = 1 \quad \text{or } j = -1 \tag{C1}$$

for the flow before or after the point of separation (as well as the separating to reattaching flows under strong adverse pressure gradients for appropriate values of $j$). Furthermore, $j=1$ corresponds to the forward attached flow where $\partial u/\partial y$ is positive and $j=-1$ to the separated flow where $\partial u/\partial y$ is negative. Equations (13*a*) and (13*b*) for Reynolds shear stress that match with outer the layer Reynolds shear stress $T$ become

$$\tau_\times = y_p + j\Lambda R_p \tag{C2a}$$

$$T = Y + j\Lambda \tag{C2b}$$

In the viscous sublayer near the wall, the Reynolds shear stress $t_\times$ may be neglected, and an integral of relation (4) that gives the velocity distribution for separate flow ($j=-1$) is

$$u_\times = \frac{1}{2}y_p^2 - \Lambda R_p y_p \tag{C3}$$

where the velocity gradient near the wall is negative.

In the separated flow $j=-1$, the velocity gradient near the wall is negative, and the matching relation (15) becomes

$$\frac{y_p}{\sqrt{y_p - \Lambda R_p}}\frac{\partial u_\times}{\partial y_p} = -\frac{U_e}{u_\delta}\frac{Y}{\sqrt{Y - \Lambda}}\frac{\partial U_1}{\partial Y} \tag{C4}$$

The integrations of the expressions from relations (C4) give the following results.

The composite law of the wall is

$$\frac{u}{u_p} = \frac{1}{k}\left[ 2\sqrt{y_p - \Lambda R_p} - 2\sqrt{\Lambda R_p}\arctan\left(\sqrt{\frac{y_p}{\Lambda R_p} - 1}\right)\right] + C^1 \tag{C5}$$

The composite non-linear wake wall is

$$\frac{U_S - u}{u_\delta} = \frac{1}{k}\left[ -2\sqrt{Y - \Lambda} + 2\sqrt{\Lambda}\arctan\left(\sqrt{\frac{Y}{\Lambda} - 1}\right)\right] + E^1 \tag{C6}$$

Based on results (C5) and (C6), the skin friction law is

$$U_S(x) = C^1 u_p + u_\delta E^1 \tag{C7}$$

The results (C5) and (C6) may also be expressed in terms of friction velocity as the following. In the composite wall law,

$$\frac{u}{u_\tau} = \frac{1}{k}[2\sqrt{K_+ y_+ - 1} - 2\arctan(\sqrt{K_+ y_+ - 1})] + B^1 \tag{C8}$$

In the composite wake law,

$$\frac{U_S - u}{u_\tau} = \frac{1}{k}[-2\sqrt{\lambda Y - 1} + 2\arctan(\sqrt{\lambda Y - 1})] + D^1 \tag{C9}$$

where $B_1$ and $D_1$ are given as

$$B^1 = C^1 \frac{u_p}{u_\tau}, \quad D^1 = E^1 \frac{u_\delta}{u_\tau} \tag{C10}$$

and matching of (C8) and (C9) leads to relation (C7). The logarithmic dependence has been replaced by the arctan function. However, the asymptotic relations (26) and (27) are recovered from the proposed Eqs. (C5) and (C6) in the neighborhood of the separation point. Relation (C8) was obtained by McDonald [36] from the Townsend [41] extended wall law in which the streamwise pressure gradient was replaced by shear stress gradient. Relation (C5) was proposed from relation (C8) by Skote [12] and Skote and Henningson [32].

## References


[1] Stratford, B. S., 1959, "The Prediction of Separation of the Turbulent Boundary Layers," J. Fluid Mech., **5**, pp. 1–35.

[2] Townsend, A. A., 1960, "The Development of Turbulent Boundary Layers With Negligible Wall Stress," J. Fluid Mech., **8**, pp. 143–155.

[3] Afzal, N., 1983, "Analysis of a Turbulent Boundary Layer Subjected to a Strong Adverse Pressure Gradient," Int. J. Eng. Sci., **21**, pp. 563–576.

[4] Kader, B. A., and Yaglom, A. M., 1978, "Similarity Treatment of Moving Equilibrium Turbulent Boundary Layers in Adverse Pressure Gradients," J. Fluid Mech., **89**, pp. 305–342.

[5] Mellor, G. I., and Gibson, D. M., 1966, "Equilibrium Turbulent Boundary Layers," J. Fluid Mech., **24**, pp. 225–253.

[6] Perry, A. E., and Schofield, W. H., 1973, "Mean Velocity and Shear Stress Distribution in Turbulent Boundary Layers," Phys. Fluids, **16**, pp. 2068–2074.

[7] Schofield, W. H., 1986, "Two Dimensional Separating Turbulent Boundary Layer," AIAA J., **24**, pp. 1611–1620.

[8] Simpson, R. L., 1996, "Aspects of the Turbulent Boundary Layer Separation," Prog. Aerosp. Sci., **32**, pp. 457–521.

[9] Dengel, P., and Fernholz, H. H., 1990, "An Experimental Investigation of an Incompressible Turbulent Boundary Layer in the Vicinity of Separation," J. Fluid Mech., **212**, pp. 615–636.

[10] Alving, A., and Fernholz, H. H., 1995, "Mean Velocity Scaling in and Around a Mild Turbulent Separation Bubble," Phys. Fluids, **7**(8), pp. 1956–1969.

[11] Angele, K. P., and Klingmann, M. B., 2006, "SPIV Measurements in a Weakly Separating and Reattaching Turbulent Boundary Layer," Eur. J. Mech. B/Fluids, **25**(2), pp. 209–222.

[12] Skote, M., 2001, "Studies of Turbulent Boundary Layer Flow Through Direct Numerical Simulation," Ph.D. thesis, KTH-Stockholm, Sweden.

[13] Skote, M., and Henningson, D. S., 1999, "Analysis of the Data Base From a DNS of a Separating Turbulent Boundary Layer," Center for Turbulence Research ARB, Stanford, pp. 225–237.

[14] Skare, P. E., and Krogstad, P. A., 1994, "A Turbulent Equilibrium Boundary Layer Near Separation," J. Fluid Mech., **272**, pp. 319–348.

[15] Elsberry, K., Loefffler, J., Zhou, M. D., and Wygnanssi, I., 2000, "Experimental Study of a Boundary Layer That is Maintained on the Verge of Separation," J. Fluid Mech., **423**, pp. 227–281.

[16] Coles, D., 1956, "The Law of the Wake in the Turbulent Boundary Layer," J. Fluid Mech., **1**, pp. 191–226.

[17] Coles, D., and Hirst, E. A., 1969, "Computations of Turbulent Boundary Layer," *1968 AFOSR-IFP-Stanford Conference*, Vol. 2, pp. 1–504.

[18] Melnik, R. E., 1989, "An Asymptotic Theory of Turbulent Separation," Comput. Fluids, **17**, pp. 165–184.

[19] Durbin, P. A., and Belcher, S. E., 1992, "Scaling of Adverse Pressure Gradient Turbulent Boundary Layers," J. Fluid Mech., **238**, pp. 699–722.

[20] Chawla, T. C., and Tennekes, H., 1973, "Turbulent Boundary Layers with Negligible Wall Shear: A Singular Perturbation Theory," Int. J. Eng. Sci., **11**, pp. 45–64.

[21] Tennekes, H., and Lumely, J. L., 1972, *A First Course in Turbulence*, The MIT Press, Cambridge.

[22] Shih, T. H., Povinelli, L. A., and Liu, N. S., 2003, "Application of Generalized Wall Function for Complex Turbulent Flows," J. Turbul., **4**, 15 pp., http://jot.iop.org/.

[23] Indinger, T., Buschmann, M. H., and Gad-el-Hak, M., 2006, "Mean Velocity Profile of Turbulent Boundary Layers Approaching Separation," AIAA J., **44**(11), pp. 2465–2474.

[24] Vieth, D., Kiel, R., and Gersten, K., 1998, "Two Dimensional Turbulent Boundary Layer With Separation and Reattachment Including Heat Transfer," *Monogaphien der Forscherguppe Wirbel und Warmeubertragung* (Notes on Numerical Fluid Mechanics, M. Fiebig, ed., Vieweg-Verlag, Wiesbaden.

[25] Narasimha, R., and Sreenivasan, K. R., 1979, "Relaminarization of Fluid Flow," Adv. Appl. Mech., **19**, pp. 221–309.

[26] Afzal, N., 1976, "Millikan's Argument at Moderately Large Reynolds Numbers," Phys. Fluids, **19**, pp. 600–602.

[27] Afzal, N., and Narasimha, R., 1976, "Axisymmetric Turbulent Boundary Layers Along a Circular Cylinder With Constant Pressure," J. Fluid Mech., **74**, pp. 113–129.

[28] Afzal, N., 1996, "Wake Layer in Turbulent Boundary Layer with Pressure Gradient: A New Approach," invited lecture in *Asymptotic Methods for Turbulent Shear Flows at High Reynolds Numbers*, K. Gersten, ed., Kluwer Academic, Dordrecht, pp. 95–118.

[29] Clauser, F. H., 1954, "Turbulent Boundary Layers in Adverse Pressure Gradients," J. Aeronaut. Sci., **21**, p. 91–108.

[30] Clauser, F. H., 1956, *The Turbulent Boundary Layers* (Advances in Applied Mechanics Vol. 4), Academic, New York, pp. 2–51.

[31] Berger, S. A., 1971, *Laminar Wakes*, Elsevier, New York, pp. 69–76.

[32] Skote, M., and Henningson, D. S., 2002, "Direct Numerical Simulation of a Separating Turbulent Boundary Layer," J. Fluid Mech., **471**, pp. 107–136.

[33] Na, Y., and Moin, P., 1998, "Direct Numerical Simulation of a Separated Turbulent Boundary Layer," J. Fluid Mech., **374**, pp. 379–405.

[34] Samuel, A. E., and Joubert, P. N., 1974, "A Boundary Layer Developing in an Increasingly Adverse Pressure Gradient," J. Fluid Mech., **66**, pp. 481–505.

[35] Spangenberg, W. G., Rowland, W. K., and Mease, N. E., 1967, "Measurements in a Turbulent Boundary Layer Maintained in a Nearly Separating Conditions," in *Fluid Mechanics of Internal Flows*, G. Sovron, ed., Elsevier, Netherlands, pp. 110–151.

[36] McDonald, H., 1969, "The Effects of Pressure Gradient on the Law of the Wall in Turbulent Flows," J. Fluid Mech., **35**, pp. 311–336.

[37] Ludweig, H., and Tillmann, W., 1950, "Investigation of the Wall Shearing Stress in Separation of Turbulent Boundary Layer," NACA TM 1265.

[38] Schubauer, G. B., and Klebanoff, P. S., 1951, "Investigation of Separation of Turbulent Boundary Layer," NACA Report No. 1030.

[39] Newman, B. G., 1951, "Some Contribution to the Study of Turbulent Boundary Layer Separation," Australian Department of Supply Report No. ACA-53.

[40] Castillo, L., Xia, W., and George, W., 2004, "Separation Criterion for Turbulent Boundary Layer via Similarity Analysis," ASME J. Fluids Eng., **126**, pp.297–304.

[41] Townsend, A. A., 1976, *The Structure of Turbulent Shear Flows*, Cambridge University Press, New York.

[42] Afzal, N., 2008, "Alternate Scales for Turbulent Boundary Layers on Traditional Rough Walls: Universal Log Laws," ASME J. Fluids Eng., **130**, p. 041202.

# A Separation Criterion With Experimental Validation for Shear-Driven Films in Separated Flows

**M. A. Friedrich**

**H. Lan**

**J. L. Wegener**

**J. A. Drallmeier**[1]
e-mail: drallmei@mst.edu

**B. F. Armaly**

Department of Mechanical and Aerospace Engineering,
Missouri University of Science and Technology,
400 West 13th Street,
Rolla, MO 65409-0050

*The behavior of a shear-driven thin liquid film at a sharp expanding corner is of interest in many engineering applications. However, details of the interaction between inertial, surface tension, and gravitational forces at the corner that result in partial or complete separation of the film from the surface are not clear. A criterion is proposed to predict the onset of shear-driven film separation from the surface at an expanding corner. The criterion is validated with experimental measurements of the percent of film mass separated as well as comparisons to other observations from the literature. The results show that the proposed force ratio correlates well to the onset of film separation over a wide range of experimental test conditions. The correlation suggests that the gas phase impacts the separation process only through its effect on the liquid film momentum.*
[DOI: 10.1115/1.2907405]

## 1 Introduction

The dynamics of thin liquid films that develop on a solid surface and are driven by an adjacent gas flow have applications in many engineering problems, and as such have been extensively studied. The dynamics of the separation of such films from the solid surface due to a sudden expansion in geometry and its atomization by the separated/reattached gas shear layer (see Fig. 1), however, have received little attention. The films that are considered in this study can be classified as thin ($\sim 100\ \mu$m), shear driven, and interacting with the adjacent separated gas flow. Such complex interaction between the liquid film and the gas in separated flow is encountered in fuel and air mixture preparation for spark ignition engines, as well as in atomizer design, refrigerant flows in evaporators, and wave plate mist eliminators.

For example, in a port-fuel-injection engine, the liquid fuel will normally accumulate as a film on the surfaces of intake valves and port walls during the cold-start period and enter into the cylinder by the shearing force of the intake air flow. It has been shown in many works (such as Felton et al. [1] and Dawson and Hochgreb [2]) that the liquid fuel usually deposits as thin films on the intake valve and port surfaces during the engine cold-start period, and these films are seen to atomize to varying degrees with the inflowing air and enter the cylinder as droplets and ligaments. The presence of these films has been correlated to uHC emissions (Landsberg et al. [3] and Stanglmaier et al. [4] among others). Knowledge of the fuel film separation at sharp valve and port edges is essential to accurately predict the fuel/air mixture preparation for improved fuel efficiency and reduced emissions. To model these processes, a clearer understanding must be developed of the dynamics between the coupled gas phase (separated/reattached flow) and liquid phase, along with the details of the dominant interfacial instabilities. Of particular interest in this study is the prediction of film separation from the solid surface as a function of gas phase velocity, liquid film flow rate, and wall angle.

## 2 Background

Gas-liquid flows have application in a multitude of engineering problems and as a result have been studied for many years. An attempt is made here to classify the problem at hand, given this large body of research that is found in many fields.

A significant amount of work can be found in the literature dealing with gas-liquid flows in pipes. An often stated objective in this body of work is the prediction of transitions between the many propagation modes including stratified flow, annular flow, slug flows, and plug flows [5]. Of these flow regimes, the films considered in this problem would be most similar to the annular flow condition, but with small film thickness scales.

Another related field is referred to as viscous thin film flow. Here, the force that drives the film determines the problem classification. For example, driving forces could include gravity [6] and moving pressure disturbances [7]. Given that the typical film thickness in the posed problem is on the order of 100 $\mu$m, it would fit into this body of work. However, the driving force for this study is the shear force imparted by the adjacent gas flow phase.

Once the film reaches the end of the supporting substrate, breakup often occurs. A recent review of the literature concerning breakup processes of wall-bounded films, in comparison to jets and sheets, is given by Lightfoot [8]. Some of the most comprehensive work done in shear-driven thin liquid films for atomization is that by Wittig and co-workers [9–11], where their work focused on prefilming atomizers for gas turbine engine applications. In fact, some aspects of the liquid film transport model used here are derived from the fine work of this group. Several important differences exist, however, between the geometry of a prefilming atomizer and the geometry considered here. For the prefilming atomizer, the shearing air is encountered on both sides of the thin liquid sheet once it departs from the atomizer. The solid substrate is effectively a splitter plate between the two air flows, coming to a sharp edge at the exit leaving no expanding wall corner to negotiate. Finally, gas phase velocities in a prefilming atomizer are on the order of 50 m/s (or much greater) to ensure significant atomization. As a result, the development of criteria to predict when the film separates is not applicable.

Two general theories have been proposed in the literature to predict film separation. The first, put forth by O'Rourke and Amsden [12], considers a balance between the inertia of the liquid film

[1]Corresponding author.

Contributed by the Fluids Engineering Division of ASME for publication in the JOURNAL OF FLUIDS ENGINEERING. Manuscript received July 31, 2007; final manuscript received February 4, 2008; published online April 25, 2008. Assoc. Editor: Theodore Heindel.

  

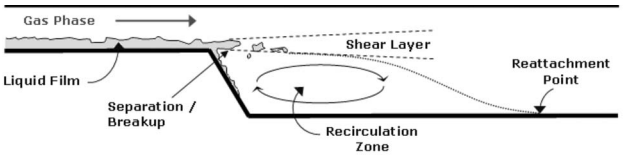


**Fig. 1 Schematic of shear-driven film interaction with separated gas phase flow resulting in partial film separation from the substrate at the corner**

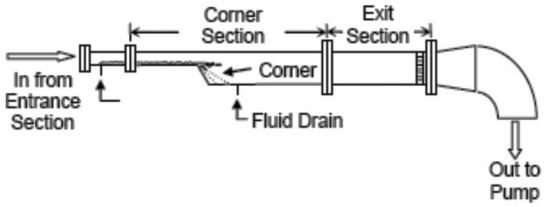


**Fig. 2 Schematic of test section**

at a sharp corner in the wall and the pressure difference between the gas phase and the film at the wall. No experimental validation of this model was done. The second approach is that of Maroteaux et al. [13,14] who argued the separation at a corner to be analogous to a Rayleigh–Taylor instability. In this approach, instabilities in the liquid film are amplified by a body force (i.e., normal acceleration) developed as the film rotates around the corner. Calibration of the model was done using a limited number of experiments. However, Gubaidullin [15] points out several inconsistencies with the approach of Maroteaux et al. [13] including differences in the definition of the acceleration of the film at the corner. In addition, recent work by Steinhaus et al. [16] suggests that the analysis of Maroteaux et al. [13] shows different trends than what is experimentally observed.

Neither the approach of O'Rourke and Amsden [12] nor Maroteaux et al. [13,14] have been rigorously compared to experiment and both use rather ambiguous constants to fit the results to limited observations, which at times seem to be in conflict with the experimental observations of others. Our hypothesis considers the role of film inertia to overcome surface tension and gravitational effects at the corner.

## 3 Scope

The key objective of this study is the analytical development and experimental validation of a comprehensive separation criterion for predicting the film behavior at the corner. The criterion must be able to capture whether the film will separate from the corner to break up into droplets or negotiate the corner and stay attached. To this end, the development of a test facility to create, control, and observe a shear-driven liquid film up to a sudden expansion (corner) is discussed. The criterion was formulated and developed to be a submodel of a larger numerical model used to predict film propagation along a surface. Hence, quantitative estimates of the film thickness and average film velocity just before separation are required as inputs to the separation criteria. For this study, these are obtained using a simple two-dimensional shear-driven film simulation model, based on the work of Wittig and co-workers [9–11]. This film simulation model was chosen based on its extensive use and validation presented in the literature. Clearly, other simulation approaches could be used for this (e.g., a volume of fluid (VOF)-type model as presented by Thiruvengadam et al. [17]). The focus of this study, then, is not the film propagation before the corner but the development of a force balance model to predict the onset of film separation at the corner given these inputs of film thickness and average film velocity. Observations using high speed imaging of the film separation phenomena as well as quantitative measures of liquid film mass attached to the wall after the corner are used to discuss the effectiveness of the developed force balance model.

## 4 Experimental Facility

**4.1 Shear-Driven Film Test Section.** The flow facility consists of a four part test section mounted to an optics table platform. Flow is pulled through the test section using a large liquid ring vacuum pump. Flow rates through the test section are determined using a laminar flow element. Corrections are made for local temperatures and pressures resulting in uncertainties of less than 3% in the flow rate.

A schematic of the test section is shown in Fig. 2. A 1.43 m long entrance region (not shown) provides for two-dimensional flow spanwise across the test section at the point of film introduction. The dimensions of the test section at the point of film introduction and up to the corner are 2 cm tall $\times 10$ cm wide, giving an aspect ratio of 5. The liquid is introduced through a porous brass plug on the bottom wall in the film introduction section. Simulations indicate that with the entrance region previously specified, flow should be two-dimensional with this aspect ratio (i.e., limited wall effects) for the center 7.5 cm of the test section. It is over this center 7.5 cm width of the test section that the film is introduced. The liquid flow into the test section is quantified on a volumetric flow basis and measured using a rotometer with an uncertainty of 2.5%. For the results presented here, the liquid was water with the addition of a surfactant (Surfynol 465) at 0.1% and 1.0% by mass, which results in surface tensions $\sigma$ of 0.042 N/m and 0.026 N/m, respectively. The surfactant had minimal effect on the fluid viscosity, which was measured to be $0.983 \times 10^{-3}$ N s/m$^2$ for the 0.1% solution and was $1.027 \times 10^{-3}$ N s/m$^2$ for the 1.0% solution, effectively the same as water at ambient conditions.

The corner section is removable from the configuration such that the angle of the corner in the bottom wall may be changed. Currently, a 60 deg angle, measured from the horizontal, is being used. The length of the duct from the point of film introduction to the corner is 23 cm. After the corner, the duct has an aspect ratio of 1.429 wherein an exit section provides for a transition from the test section to the 10.2 cm diameter piping, which runs to the liquid ring pump. Great care is taken to ensure that the test section is horizontal to prevent biasing of the film flow.

Significant effort was expended in developing a test section, which resulted in uniform gas phase velocities spanwise across the test section near the corner. Although the film is uniformly introduced over the center 7.5 cm width of the test section, the film width changes as it reaches the corner due to surface tension. Figure 3 shows the typical variation in the width of the film, 5 mm from the corner, as a function of gas phase velocity for a surface tension of 0.042 N/m. The film width is measured based on imaging through a window in the top of the test section with an uncertainty of 3% determined by parallax and scale resolution. Clearly, increased gas velocity, and hence shear force, keeps the film spread over the test section lower wall, counteracting the surface tension forces. These same surface tension forces impact the film separation at the corner and will be discussed in the development of the separation criterion.

The liquid film flow condition is characterized by the use of a film Reynolds number $\mathrm{Re}_f$ based on the volumetric flow introduced to develop the film $\dot{\forall}_f$ and the measured film width $w_f$ at each flow condition:

$$\mathrm{Re}_f = \frac{\dot{\forall}_f \rho_f}{w_f \mu_f} \tag{1}$$

Each flow condition can then be characterized by a gas phase velocity $U_g$ and the film Reynolds number $\mathrm{Re}_f$. A range of experimental gas and liquid phase flow conditions was considered. Gas

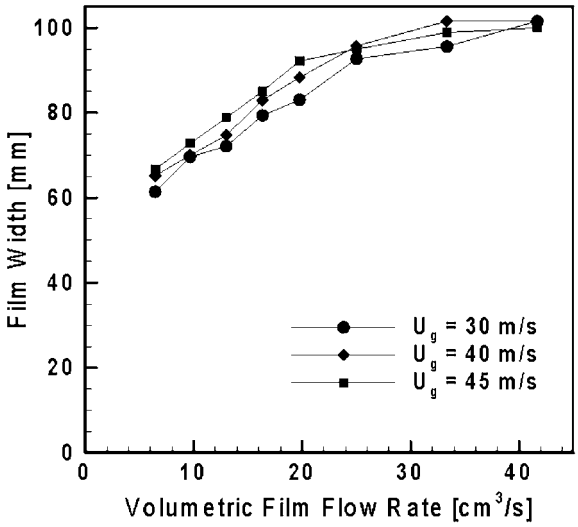


**Fig. 3 Film width near the test section corner as a function of film flow rate and gas phase velocity**

phase velocities ranged from 20 m/s to 45 m/s and liquid flow rates varied from 6.5 $cm^3/s$ to 41.5 $cm^3/s$. This results in a variation of film $Re_f$ from approximately 100–400.

**4.2 High Speed Imaging System.** The general characteristics of the liquid film, including the surface instabilities and interaction of the film with the separated gas phase at the corner, were characterized using high speed imaging. A Photron 1280 PCI high speed camera, with close-up lenses totaling +7 diopter, was used to capture 2000 frames per second at $640 \times 256$ resolution. A typical image from this system is shown in Fig. 4. The spatial resolution of these results is determined by the pixel resolution of the camera. At the current magnification, the spatial resolution shown in Fig. 4 is approximately 100 $\mu$m.

**4.3 Film Separation Measurement.** Measurement of the degree to which the liquid film is separated from the corner is made by pulling off the liquid that stays attached to the downward sloping wall after the corner. A porous brass plug was placed downstream of the test section corner on the downward slope of the lower wall as a means to extract the mass of the liquid film that stays attached to the wall. As shown in Fig. 5, the porous plug (6 mm wide) extends across the span of the test section and is flushed with the sloping wall to prevent any disturbance of the flow. The brass plug is located 6 mm from the corner, which was determined by flow visualization to be far enough from the corner as to not impact the film separation process and yet not low enough to capture liquid that may be pulled up the sloping wall by the recirculation flow region behind the step. Suction is applied below the porous plug to draw the liquid from the wall, which is then captured and the mass measured. Sufficient suction is applied

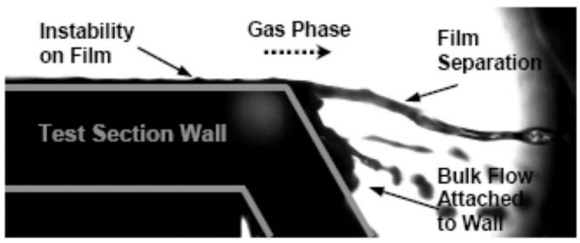


**Fig. 4 High speed imaging (2000 frames per second) of the film interaction with the separated gas flow at the test section corner**

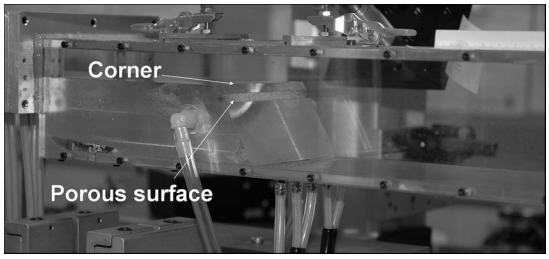


**Fig. 5 Picture of the test section showing the porous surface where the film that remains attached after the corner is removed**

behind the porous plug, adjusted at each flow condition, for complete removal of the liquid from the wall without pulling the gas through the porous surface. Imaging is used at each set point to ensure that the liquid film was removed.

Film suction collection times were on the order of 1 min in duration with an uncertainty of 1%. The captured volume is weighed to establish a mass flow of liquid attached to the wall, which, along with the measured liquid flow into the test section, provides the mass flow of liquid separated at the corner. Combined uncertainty in this measurement is 5%.

## 5 Shear-Driven Film, Rough Wall Model

A computational fluid dynamics (CFD) model is used to study the shear-driven liquid film propagation along the bottom wall of the test section. The focus of the current work is the development of a separation model for use in the context of a comprehensive numerical film model; hence, the film propagation model, chosen from the literature, is used to predict film thickness and film velocity at the wall corner, before the point of separation. A brief description of the chosen model is given, followed by a few predictions of film characteristics.

The two-dimensional rough wall model proposed by Sattelmayer and Wittig [9] for simulating shear-driven liquid film flow is used. This model has been shown to provide good agreement with measured values for the average film thickness [10,11]. The model treats the liquid film as an equivalent rough wall interacting with the turbulent gas flow, with the wall roughness being a function of the interfacial shear stress and the average film thickness. The interfacial shear stress provides the coupling between the liquid and the gas flows, and an iterative procedure is developed to arrive at a converged solution. This scheme was implemented in a computational code to numerically simulate the development of the shear-driven liquid film in the turbulent gas flow inside the experimental duct geometry.

**5.1 Gas Flow Model.** The two-dimensional incompressible Reynolds-averaged Navier–Stokes equations, along with the continuity equation, were used to simulate the gas flow. The $k$-$\varepsilon$, turbulence model was utilized with wall functions (high-Reynolds-number model) applied to the rough wall (the film boundary) and low-Reynolds-number model applied to the other smooth wall of the duct. The general form for the governing equations can be represented by

$$\frac{\partial u}{\partial x} + \frac{\partial v}{\partial y} = 0 \tag{2}$$

$$\nabla \cdot (\rho \phi \mathbf{V}) = \nabla(\Gamma_\phi \nabla \phi) + S_\phi \tag{3}$$

where $\Gamma_\phi$ is an effective diffusion coefficient and $S_\phi$ denotes the source term [18]. The governing equations for the two velocity components ($u$ and $v$), the turbulent kinetic energy ($k$), and its dissipation ($\varepsilon$) can be represented by Eq. (3), where $\phi$ is the corresponding variable and $\mathbf{V}$ is the velocity vector. These equations were discretized using a finite volume method in a staggered

grid system, with the SIMPLE algorithm used to deal with the coupling between flow and pressure grids. The discretized equations were solved by a line by line tridiagonal matrix algorithm method (TDMA). Several grid densities and distributions (nonuniform) were considered to ensure a grid independent solution, and a grid of 120($X$) and 66($Y$) was selected for generating the final results. The use of higher grid densities (i.e., 1.5 and 2 times greater than the one cited above) had minimal effect on the final results. The approximate relative error in film thickness is 1.9% and in film velocity is 2.2% when the grid is doubled. At least five grid points were set inside the laminar sublayer near the smooth wall where the low-Reynolds-number turbulence model was used; on the other hand, the first grid point for the gas flow near the rough wall (liquid film) is placed outside of the viscous sublayer where $11.3 \leq y_p^+ \leq 40$ is satisfied. The grid for simulating the turbulent gas flow is distributed between the first grid point $p$ near the rough wall and the smooth wall.

The wall roughness (or liquid film) effect $k_s$ is incorporated into the logarithmic law of the rough wall through the following relations:

$$u_p^+ = \frac{1}{\kappa'} \ln y_p^+ + C(\mathrm{Re}_{ks}) \tag{4}$$

where

$$u_p^+ = \frac{u_p (c_\mu^{1/4} k_p^{1/2})}{\tau_p/\rho}, \quad y_p^+ = \frac{y_P (c_\mu^{1/4} k_p^{1/2})}{\nu}$$

and $C(\mathrm{Re}_{ks})$ is a function that is dependent on the roughness Reynolds number $\mathrm{Re}_{ks} = (c_\mu^{1/4} k^{1/2}) k_s/\nu$. The functional relation for $C(\mathrm{Re}_{ks})$ can be found in the literature [10]. The term $y_p$ is the distance of the first grid point in the computational domain for the gas flow from the rough wall. The shear stress $\tau_p$ is given by [18]

$$\tau_p = \frac{\rho c_\mu k_p^2 u_p}{y_p \varepsilon_p} \tag{5}$$

To start the gas flow simulations, initial values for all of the dependent variables need to be assumed as $u = \bar{u}_{\mathrm{in}}$, $v = 0$, $k = 0.005 \bar{u}_{\mathrm{in}}^2$, and $\varepsilon = 0.1 k^2$. In addition, for a given liquid film volume flow rate ($\dot{V}_f/w_f$), the average film thickness ($h_f$) needs to be assumed at the start of the simulation. This provides a means for calculating the average film velocity and the wall shear stress from the following relations:

$$h_f \cdot \bar{u}_f = \dot{V}_f/w_f \text{ and } \tau_W = 2\mu_f \frac{\bar{u}_f}{h_f} \tag{6}$$

Note that the velocity distribution of shear-driven liquid film is assumed to be linear (i.e., $u_{\mathrm{fs}} = 2\bar{u}_f$, where $u_{\mathrm{fs}}$ is the film surface velocity). The wall roughness is evaluated by using the following relations [19]:

$$k_s = \psi_\tau h_f \tag{7}$$

$$\psi_\tau = 1.47 + 0.01851 \tau_W \tag{8}$$

The boundary conditions for the low-Reynolds-number turbulent model that are used on the smooth wall of the duct are $u = v = k = 0$, $\varepsilon = 2\nu k_p/y_p^2$ at the wall. In the high-Reynolds-number turbulent model, the boundary conditions that are applied at $y_p$ consisted of $u_p$ that is computed from the logarithmic law of the wall (Eq. (4)), and $\varepsilon_p = c_\mu^{3/4} k_p^{3/2}/\kappa' y_p$, while the boundary conditions for $v$ and $k$ are applied at the wall as $\partial v/\partial y = 0$, $\partial k/\partial y = 0$. The inlet velocity distribution of the gas flow was equivalent to fully developed turbulent flow, and the exit conditions were taken as fully developed. The shear stress at $p$, which is considered to be constant between $p$ and the rough wall, is evaluated using Eq. (5) and the simulated gas flow results.

**5.2 Film Flow Model.** The liquid film flow is simulated by using the laminar boundary layer flow approximation that is governed by the following simplified Navier–Stokes equation:

$$\rho_f \left( u_f \frac{\partial u_f}{\partial x} + v \frac{\partial u_f}{\partial y} \right) = \frac{\partial \tau}{\partial y} \tag{9}$$

Assuming a linear velocity distribution through the film, and using the integral method (i.e., integrating the above momentum equation together with continuity equation (Eq. (2)) in the $y$ direction from 0 to $h(x)$), yields the following ordinary differential equation for the surface film velocity:

$$\frac{du_{\mathrm{fs}}(x)}{dx} = \frac{3}{2\rho_f \dot{V}_f} (\tau_p - \tau_W) \tag{10}$$

where $\tau_p$ is evaluated from Eq. (5) and $\tau_W$ is evaluated from Eq. (6). A fourth-order Runge–Kutta integration scheme with adaptive stepsize control is used to determine the local surface film velocity from Eq. (10), and from these results, the local film thickness is evaluated and used to evaluate the average film thickness over the length of the calculation domain. The resulting average film thickness is used to update the effective wall roughness, and this new wall roughness is used to start a new gas flow simulation. This iterative procedure is repeated until the difference between the evaluated shear stress at the first grid point $p$ for two iterations, $(\tau_p^n - \tau_p^{n+1})$, is smaller than $10^{-6}$. At that state, $\tau_p$ becomes equal to $\tau_W$ for most of the simulated domain downstream except for the injection region of the liquid film. A starting film thickness is needed to initiate the computation of the film flow and that film thickness is updated after every iteration during the coupling iteration process.

**5.3 Model Validation and Results.** To verify our numerical simulation code using the rough wall model, a reproduction of the experiment described by Wittig et al. [10] was performed. The experimental configuration was similar to the one used in this study in that a shear-driven film was established on a plate. However, the gap height between the bottom plate and the top plate of the test section was only 0.4 cm, compared to 2 cm for this work. As expected, the rough wall model developed for this work produced results quite similar to those reported by Wittig et al. [10] and matched well to their reported experimental measurements, as shown by the film thickness and surface velocity data shown in Fig. 6. Note that this was not a validation of the shear-driven film model of Sattelmayer and Wittig [9], which has been performed and presented in the literature [10,11], but instead was a verification of the simulation code used to obtain the film thickness and average film velocity as inputs for the developed force balance model.

Finally, Fig. 7 shows typical results of the simulations for the test section and fluid described in Sec. 4. The simulations were performed for the film introduction section and the corner section up to but not including the corner. The purpose of the simulations was to provide reasonable estimates for the average film velocity and the average film thickness at the corner, for input into the film separation criteria. The simulation results show that for a fixed inlet air velocity, the liquid film thickness and its velocity, increase as the liquid flow rate (or $\mathrm{Re}_f$) increases for this two-dimensional simulation. On the other hand, for a fixed liquid flow rate ($\mathrm{Re}_f$), the liquid film thickness decreases but its average velocity increases as the inlet air velocity increases.

## 6 Separation Prediction by Analytical Force Balance

When the liquid film flow reaches the sharp corner, the bulk of the liquid may separate from the wall and then break up into droplets by the aerodynamic force of the gas or turn the corner and remain attached to the inclined wall, depending on the flow conditions of both the gas and liquid phase. To determine the behavior of the bulk film at the corner, an appropriate separation

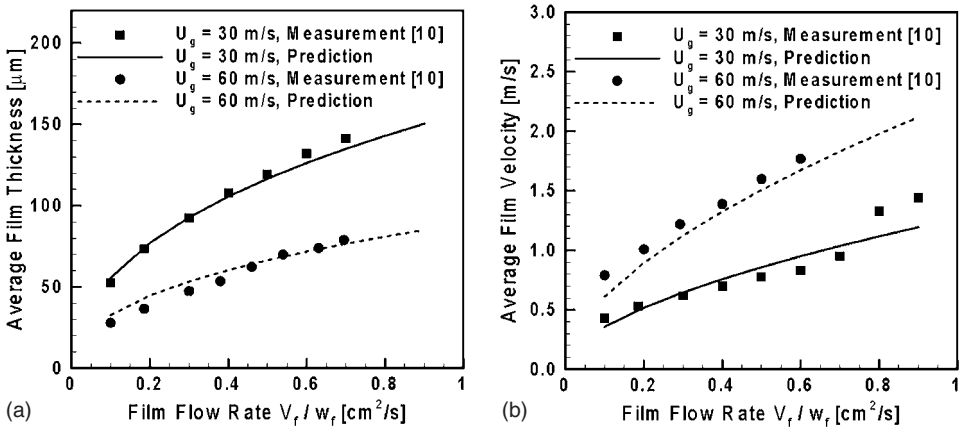


**Fig. 6 Comparison of the results of the rough wall model developed for this work and the experimental results reported by Wittig et al. [10]**

criterion needs to be established. For the analysis here, the forces considered are film inertia, surface tension, and body forces.

To consider this balance of forces at the corner, an approach similar to that of Hartley and Murgatroyd [20], Murgatroyd [21], and Penn et al. [22] for the analysis of dry patches on flat surfaces is used. A two-dimensional control volume is drawn around the liquid film, in this case at the point of separation, and a linear momentum conservation law is written for the control volume.

As shown in Fig. 8, a control volume, represented by dashed lines, is chosen perpendicular to the film flow at the corner and surrounding the presumed separated film after the corner at an angle of $\beta$ from the horizontal. The surface expands at an angle $\theta$ with the horizontal. The force balance is made perpendicular to the film, in the $p$-direction, to ascertain the equilibrium position of the separated film by balancing the perpendicular forces on the film. External forces considered are the surface tension force at the top of the film $F_s$, the surface tension force at the bottom of the film $F_c$, as well as a gravitational force $W$. The surface tension force at the bottom of the film $F_c$ is presumed to act perpendicular to the control surface, in the negative $p$-direction, at the meniscus between the separated liquid and the film that remains on the wall.

When the film approaches the corner, the effect of its momentum is to drive the film to separate from the corner that is balanced by the two surface tension forces as well as the gravitational force. This balance is established by considering conservation of linear momentum for steady conditions for the $p$-direction. Beginning with

$$\int\int_{cs} \rho_f u_f (\mathbf{V} \cdot \mathbf{n}) dA = \rho \mathbf{g} \forall + \mathbf{F}_{\text{ex}} \tag{11}$$

the momentum flux entering the control volume in the $p$-direction, assuming uniform flow at the mean film velocity $u_f$ is given by

$$-\rho_f \dot{\forall}_f u_f \sin\beta \tag{12}$$

There is no momentum flux in the $p$-direction exiting the control volume. For the external forces $F_{\text{ex}}$, acting on the control volume, the surface tension force on the upper surface $F_s$ is

$$-\sigma w_f \sin\beta \tag{13}$$

while for the lower surface, the surface tension force $F_c$ acts in the negative $p$-direction and is given by

$$-\sigma w_f \tag{14}$$

To consider the magnitude of the gravitational force, a characteristic length of the film after the corner $L_b$ must be established. Using the experimental correlations of Arai and Hashimoto [23] for thin sheet breakup, a characteristic breakup length is given by

$$L_b = 0.0388 h_f^{0.5} \text{Re}_f^{0.6} \text{We}_{\text{rel}}^{-0.5} \tag{15}$$

For this correlation, the Reynolds number of the film is defined as

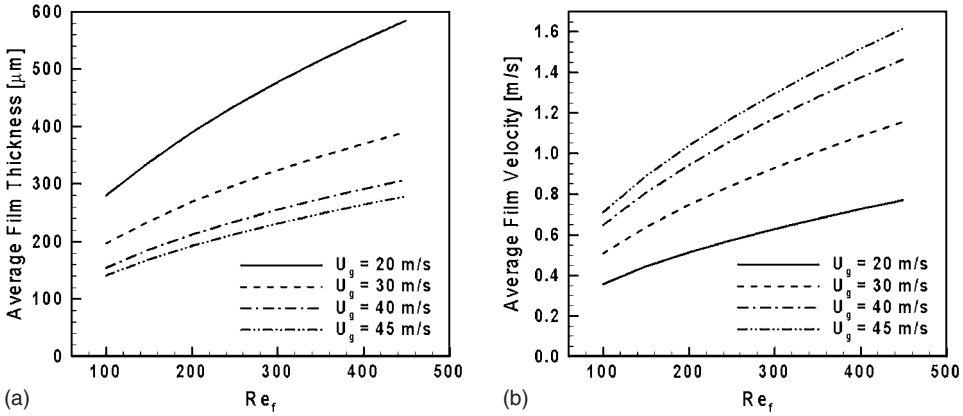


**Fig. 7 Typical results from the rough wall model used to predict film characteristics before the corner in the test section**

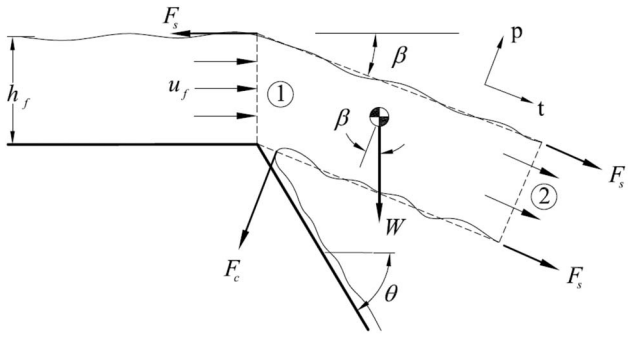


**Fig. 8 Momentum analysis for a control volume**

$$\mathrm{Re}_f = \frac{h_f u_f \rho_f}{\mu_f} \tag{16}$$

and the Weber number is based on the relative velocity between the gas phase and the liquid film

$$\mathrm{We}_{\mathrm{rel}} = \frac{h_f \rho (U_g - u_f)^2}{2\sigma} \tag{17}$$

where $\rho$ is the gas phase density. Given that the film volumetric flow is

$$\dot{\forall}_f = u_f w_f h_f \tag{18}$$

and combining the external forces, the $p$-direction linear momentum balance, per unit width, results in

$$\rho_f u_f^2 h_f \sin\beta = \sigma \sin\beta + \sigma + \rho_f g h_f L_b \cos\beta \tag{19}$$

The above relation provides a means by which the film angle $\beta$ can be determined that balances the film momentum flux with the external forces of surface tension and weight. This "equilibrium" film angle should provide a measure, when compared to the corner angle $\theta$, of whether the bulk of the liquid film will separate. However, measuring this equilibrium film angle is very difficult experimentally due to the characteristic unsteadiness in the flow.

If film separation is considered to exist for any $\beta$ less than $\theta$, then a critical force ratio can be obtained by setting $\beta = \theta$. Doing so in Eq. (19) and normalizing by the surface tension, one finds the following ratio of the inertial force to the surface tension and gravitational forces:

$$\text{force ratio} = \left\{ \frac{\rho_f u_f^2 h_f \sin\theta}{\sigma \sin\theta + \sigma + \rho_f g h_f L_b \cos\theta} \right\} \tag{20}$$

or nondimensionalizing gives

$$\text{force ratio} = \left\{ \frac{\mathrm{We}_f}{1 + \dfrac{1}{\sin\theta} + \mathrm{Fr}_{h_f} \mathrm{We}_f \left(\dfrac{L_b}{h_f}\right)\left(\dfrac{1}{\tan\theta}\right)} \right\} \tag{21}$$

where $\mathrm{We}_f = \rho_f u_f^2 h_f / \sigma$, $\mathrm{Fr}_{h_f} = g h_f / u_f^2$, and $\mathrm{Re}_f = \rho u_f h_f / \mu$. This force balance is effectively a Weber number modified by the wall angle due to the surface tension at the lower surface and a gravitational force effect. This differs from previous Weber number models [24] in the inclusion of the effects of the wall angle as well as body forces on the separation process. It differs from the force analysis of Owen and Ryley [25] by the inclusion of additional surface tension forces, which provide the wall angle dependence experimentally seen. Arguably, when the force ratio becomes greater than 1, the inertial force becomes great enough for the film to begin to separate from the wall. Hence, a force ratio of 1 can be used as a criterion for the onset of film separation. Clearly, since the unsteady nature of the film surface has not been considered, as displayed in Fig. 4, one could not expect all of the liquid film to separate at this point. If, however, the appropriate forces have been captured, for force ratios greater than 1, some measurable film mass should be separated since sufficient film inertia exists, whereas below 1, all the film mass should remain attached to the wall.

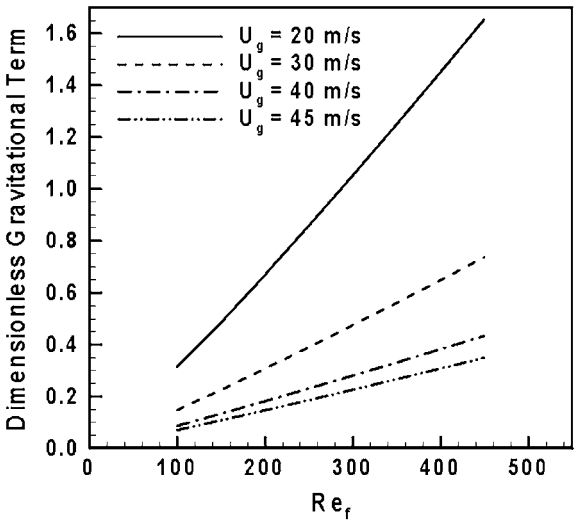


**Fig. 9 Dimensionless gravitational term from Eq. (16) as a function of $\mathrm{Re}_f$**

The various dimensionless terms in Eq. (21) can be calculated knowing the film thickness and velocity along with the fluid properties. To observe the general behavior of the various force terms, the film velocity and thickness are calculated using the rough wall model, for example, as shown in Fig. 7. With these predictions, Fig. 9 shows the variation of the dimensionless gravitational force term

$$\mathrm{Fr}_{h_f} \mathrm{We}_f \left(\frac{L_b}{h_f}\right)\left(\frac{1}{\tan\theta}\right) \tag{22}$$

in the denominator of Eq. (21) as a function of $\mathrm{Re}_f$. Clearly, the gravitational effect becomes more significant at higher $\mathrm{Re}_f$, which from Fig. 7 corresponds to thicker films. The film $\mathrm{We}_f$, shown in Fig. 10, captures the force balance between the surface tension and the film inertia at the corner. As expected, the $\mathrm{We}_f$ increases with $\mathrm{Re}_f$ due to the increase in film inertia.

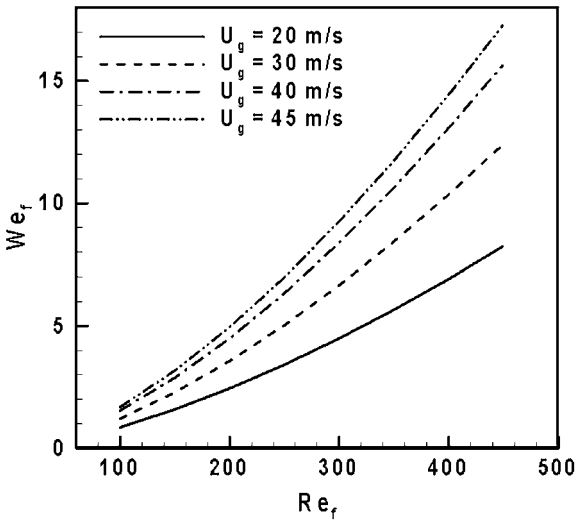


**Fig. 10 Film Weber number as a function of $\mathrm{Re}_f$**

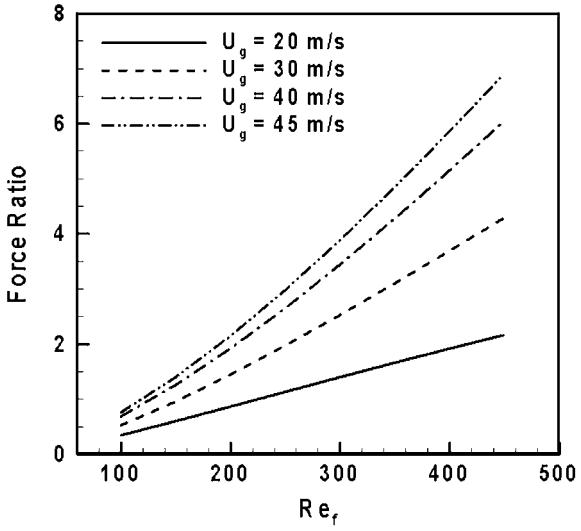


**Fig. 11 Dimensionless force ratio as a function of $Re_f$**

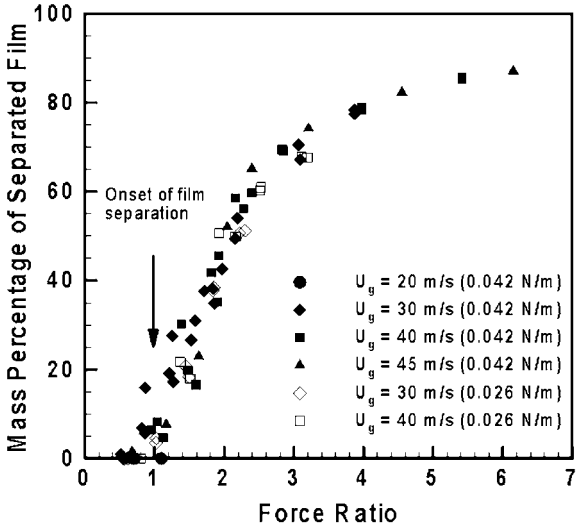


**Fig. 12 Experimentally measured film separation by mass correlated to the calculated force ratio for various gas phase and liquid phase flow conditions; surface tension shown in parentheses**

Finally, the force ratio defined in Eq. (21) is shown as a function of the $Re_f$ for various gas phase velocities in Fig. 11. The rather significant difference in the force ratio for different gas phase velocities at higher $Re_f$ seems to be driven by the gravitational term, as shown in Fig. 9, which becomes significant at these higher $Re_f$. If the above force balance captures the appropriate physics, then the film should begin to separate from the wall when the force ratio in Eq. (21) becomes greater than 1. Figure 11 suggests, then, that films with lower $Re_f$ would be more likely to stay attached to the wall. Similarly, films driven by lower gas phase velocities would also tend to stay attached. Based on Figs. 7 and 11, films would need to be quite thick at lower gas phase velocities (leading to higher relative film velocities) to begin to separate from the wall. To test the viability of the above force balance to predict the onset of film separation, film separation experiments were conducted.

## 7 Experimental Results

**7.1 Validation of Film Separation Criterion.** Film separation experiments were made for gas phase velocities between 20 m/s and 45 m/s and $Re_f$ between 100 and 400. Validation of the separation criterion was performed by measuring the percent of liquid mass that remained attached to the wall after the corner. For each experimentally determined gas phase velocity and $Re_f$, as established by the liquid flow rate and film width, the rough wall model was used to predict the film velocity $u_f$ and film thickness $h_f$. This provided sufficient information for calculating the force ratio, as per Eq. (21).

Results for 68 different flow conditions are shown in Fig. 12. For each gas phase velocity, several liquid film flow rates were established, with the film width and liquid mass attached to the wall measured for each set point. Two water-surfactant mixtures were used to study the effect of surface tension. Two important features should be noted from these results. First, the force ratio appears to reduce the results from a wide range of experimental conditions into a common trend. The results varied from cases where no liquid was separated from the wall (i.e., the film remained attached) to approximately 90% of the liquid mass separated from the wall near the corner. The second important observation is that the force balance performed for this analysis appears to capture quite well the onset of the film separation process. For the range of conditions examined, the start of the film separation process begins when the inertial film force is greater than the restoring forces, i.e., at a force ratio of 1. As the force ratio increases from 1, a continual increase in the mass of the film separated from the corner was observed. A determination of when the film is "separated" versus "not separated" is not made here as this determination is a bit arbitrary. In fact, the results show that under many flow conditions, a "partial separation" occurs where a fraction of the liquid mass separates with the remainder staying attached to the wall. However, as can be seen in Fig. 12, the force ratio model predicts quite well the onset of film separation from the corner at a force ratio of near 1, with approximately 50% of the liquid mass separating at a force ratio of 2 for most flow conditions.

The ability of a force balance at the corner to capture the onset of the film separation process suggests that the appropriate forces are being included, at least over the range of flow conditions studied. This suggests that the model established by O'Rourke and Amsden [12] is inconsistent with this work in that it argues the importance of the gas phase pressure on either side of the film and does not include surface tension effects. Clearly, the nature of the gas phase shear, particularly the shear layer and recirculation zones as depicted in Fig. 1, will impact the breakup process. However, the separation process only appears to be affected by the gas phase field through the film inertia, established by the shear-driven boundary condition.

Although the flow conditions and fluid properties were quite different than those considered in this study, a few comments can be made in regard to the force balance developed here and the experimental observations of Steinhaus et al. [16]. Steinhaus et al. [16] observed that higher film flow rates (i.e., $Re_f$) generally resulted in more film separation, which agrees with the trends shown in Fig. 11. However, they commented that the film flow rate seemed to have a relatively small effect. This may be due to the fact that their study considered only very high gas phase velocities (between roughly 70 m/s and 200 m/s), which resulted in very thin films (less than 100 $\mu$m) for the liquid considered. With $Re_f$ all well less than 100 in their experiments, the decreasing slope shown in the force ratio at low $Re_f$ in Fig. 11 would suggest a lessening dependence on $Re_f$. Steinhaus et al. [16] also noted that very high gas phase velocities (greater than 200 m/s) were necessary to "preferentially strip" the liquid film for low liquid flow rates ($Re_f < 10$) for a 45 deg wall angle. Again, this observation fits well with the trend shown in the force ratio of Fig. 11, which suggests that gas phase velocities would need to far exceed the 45 m/s considered here for the onset of separation (force ratio=1) at a wall angle of 60 deg.

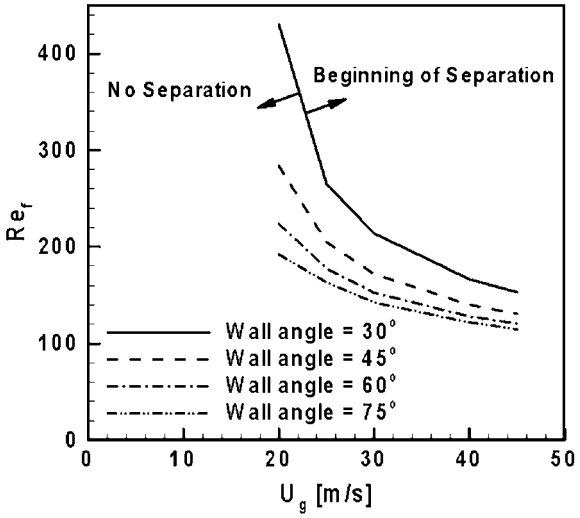


**Fig. 13 Predicted effects of the wall angle of the onset of film separation for various gas phase and liquid phase flow conditions**

**7.2 Prediction of Wall Angle Effects.** It is important to note that the ability of the force ratio to capture the onset of film separation leads to a predictive capability. For example, using the rough wall film model, the force ratio can be calculated for a given set of gas phase velocity, liquid flow rate, and wall angle. Considering those conditions that provide a unity force ratio for a chosen wall angle, prediction of the onset of film separation can be established, as shown in Fig. 13. As indicated in the figure, to the right of the curves are flow conditions that result in a force ratio larger than 1 for the given wall angle and would suggest the occurrence of some degree of film separation; to the left of the curves are force ratios less than 1, which would imply no separation. The results suggest that the wall angle has a lesser effect on film separation for steeper wall angles. Additionally, the impact of the wall angle on the separation process is more significant for lower gas phase velocities and of lesser importance for higher gas phase velocities.

## 8 Summary and Conclusions

An experimental test facility to study the development of a shear-driven liquid film and its subsequent separation at an expanding corner has been developed. Built into the test section is the ability to measure the liquid mass that stays attached to the wall after the corner. An analytical force balance was developed to serve in a predictive sense as a criterion for the onset of film separation. Required for the force balance is knowledge of the film thickness and velocity at the corner, which for this study were determined using a simple rough wall film propagation model.

The force balance of the major liquid phase forces acting at the corner, including surface tension, film inertia, and gravity, correlated well to the onset of film separation as measured in the experiment. Unlike previous Weber number models, effects of the wall angle on film separation are included. Additionally, the mass fraction of the liquid film that separates from the wall correlates to the force ratio over a wide range of experimental test conditions. The correlation of the separated mass to the liquid film force balance suggests that the gas phase impacts the separation process only through its effect on the liquid film momentum. It is surmised, however, that the inclusion of gas phase effects in the shear layer and recirculation zone will be necessary to consider the breakup of the film.

## Acknowledgment

This work was supported in part by NSF Grant No. CTS-0352135.

## Nomenclature

$A$ = area
CS = control surface
$F_c$ = surface tension force at the bottom of the film
$F_{ex}$ = external force
$Fr_{hf}$ = film Froude number
$F_s$ = surface tension force at the top of the film
$g$ = gravitational constant
$h_f$ = film thickness
$k$ = turbulent kinetic energy
$k_s$ = wall roughness
$L_b$ = characteristic length of the film after the corner
$\mathbf{n}$ = normal vector
$Re_f$ = film Reynolds number
$Re_{ks}$ = roughness Reynolds number
$S_\phi$ = source term
$U_g$ = gas phase velocity
$\bar{u}_{in}$ = initial fluid velocity vector
$u_f$ = film velocity
$u_{fs}$ = film surface velocity
$u$ = fluid velocity component
$v$ = fluid velocity component
$\mathbf{V}$ = velocity vector
$\dot{V}_f$ = film volumetric flow rate
$W$ = gravitational force
$We_f$ = film Weber number
$We_{rel}$ = relative Weber number
$w_f$ = film width
$\beta$ = separated film angle from the horizontal
$\Gamma_\phi$ = effective diffusion coefficient
$\varepsilon$ = dissipation
$\theta$ = surface corner angle from the horizontal
$\kappa'$ = von Karman constant
$\mu_f$ = film viscosity
$\rho_f$ = film density
$\sigma$ = surface tension
$\tau$ = shear stress
$\phi$ = corresponding variable
$\psi_\tau$ = efficiency factor of film roughness
$\nabla$ = gradient
$\forall$ = volume

### Subscripts

$p$ = first grid point
$w$ = wall

## References

[1] Felton, P. G., Kyritsis, D. C., and Fulcher, S. K., 1995, "Visualization of Liquid Fuel in the Intake Manifold During Cold Start," Society of Automotive Engineering, Technical Paper No. 952464.
[2] Dawson, M., and Hochgreb, S., 1998, "Liquid Fuel Visualization Using Laser-Induced Fluorescence During Cold Start," Society of Automotive Engineering, Technical Paper No. 982466.
[3] Landsberg, G., Heywood, J., and Cheng, W., 2001, "Contribution of Liquid Fuel to Hydrocarbon Emissions in Spark Ignition Engines," Society of Automotive Engineering, Technical Paper No. 2001-01-3587.
[4] Stanglmaier, R., Li, J., and Matthews, R., 1999, "The Effects of In-Cylinder Wall Wetting Location on the H. C. Emissions From S. I. Engines," Society of Automotive Engineering, Technical Paper No. 1999-01-0502.
[5] 1994, "Multiphase Flows: An Assessment With a View to the Future," *Colloquium*, eds. T. J. Hanratty, T. Theofanous, University of Illinois at Urbana-Champaign, Nov. 5–6.
[6] Chang, H.-C., 1994, "Wave Evolution on a Falling Film," Annu. Rev. Fluid Mech., **26**, pp. 103–136.
[7] Kriegsmann, J. J., Miksis, M. J., and Vanden-Broeck, J. M., 1998, "Pressure Driven Disturbances on a Thin Viscous Film," Phys. Fluids, **10**(6), pp. 1249–1255.

[8] Lightfoot, M. D. A., 2006, "Atomization of Wall-Bounded Two-Phase Flows," *ILASS Americas, Proceedings of the 19th Annual Conference on Liquid Atomization and Spray Systems*, Toronto, Canada, May.
[9] Sattelmayer, T., and Wittig, S., 1986, "Internal Flow Effects in Prefilming Airblast Atomizers: Mechanisms of Atomization and Droplet Spectra," ASME J. Eng. Gas Turbines Power, **108**, pp. 465–472.
[10] Wittig, S., Himmelsbach, J., Noll, B., Feld, H. J., and Samenfink, W., 1992, "Motion and Evaporation of Shear-Driven Liquid Films in Turbulent Gases," ASME J. Eng. Gas Turbines Power, **114**, pp. 395–400.
[11] Himmelsbach, J., Noll, B., and Wittig, S., 1994, "Experimental and Numerical Studies of Evaporating Wavy Fuel Films in Turbulent Air Flow," Int. J. Heat Mass Transfer, **37**, pp. 1217–1226.
[12] O'Rouke, P. J., and Amsden, A. A., 1996, "A Particle Numerical Model for Wall Film Dynamics in Port-Injected Engines," Society of Automotive Engineering, Technical Paper No. 961961.
[13] Maroteaux, F., Llory, D., Le Coz, J.-F., and Habchi, C., 2002, "Liquid Film Atomization on Wall Edges-Separation Criterion and Droplets Formation Model," ASME J. Fluids Eng., **124**, pp. 565–575.
[14] Maroteaux, F., Llory, D., Le Coz, J.-F., and Habchi, C., 2003, "Potential of Inertial Instabilities for Fuel Film Separation in Port Fuel Injection Engine Conditions," Int. J. Engine Res., **4**(1), pp. 11–26.
[15] Gubaidullin, A., 2007, "Comments on "Liquid Film Atomization on Wall Edges-Separation Criterion and Droplets Formation Model," J. Fluids Eng., **129**, pp. 665–666.
[16] Steinhaus, B. C., Ghandhi, J. B., and Shedd, T. A., 2007, "Experimental Investigation of Liquid Film Stripping at a Sharp Corner," *ILASS Americas, Proceedings of the 20th Annual Conference on Liquid Atomization and Spray Systems*, Chicago, IL, May.
[17] Thiruvengadam, M., Armaly, B. F., and Drallmeier, J. A., 2008 "Shear Driven Liquid Film in a Duct," ASME J. Fluids Eng., accepted.
[18] Tao, W. Q., *Numerical Heat Transfer*, 2001, 2nd ed., Xi'an Jiaotong University Press, Xi'an, China.
[19] Gerendas, M., and Wittig, S., 2001, "Experimental and Numerical Investigation on the Evaporation of Shear-Driven Multi-Component Liquid Wall Films," ASME J. Eng. Gas Turbines Power, **123**, pp. 580–588.
[20] Hartley, D. E., and Murgatroyd, W., 1964, "Criteria for the Break-Up of Thin Liquid Layers Flowing Isothermally Over Solid Surfaces," Int. J. Heat Mass Transfer, **7**, pp. 1003–1015.
[21] Murgatroyd, W., 1965, "The Role of Shear and Form Forces in the Stability of a Dry Patch in Two-Phase Film Flow," Int. J. Heat Mass Transfer, **8**, pp. 297–301.
[22] Penn, D. G., Lopez de Bertodano, M., Lykoudis, P. S., and Beus, S. G., 2001, "Dry Patch Stability of Shear Driven Liquid Films," ASME J. Fluids Eng., **123**, pp. 857–862.
[23] Arai, T., and Hashimoto, H., 1985, "Disintegration of a Thin Liquid Sheet in a Concurrent Gas Stream," *Proceedings of the Third International Conference on Liquid Atomization and Spray Systems*, London.
[24] Wang, Y.-P., Thiruvengadam, M., Drallmeier, J. A., and Armaly, B. F., 2005, "A Comparison of Models for Shear-Driven Liquid Film Separation Around a Corner," *ILASS Americas, Proceedings of the 18th Annual Conference on Liquid Atomization and Spray Systems*, Irvine, CA, May.
[25] Owen, I., and Ryley, D. J., 1985, "The Flow of Thin Liquid Films Around Corners," Int. J. Multiphase Flow, **11**(1), pp. 51–62.

# On the Interaction of Water Waves With a Surface-Parallel Vortex

**Amy Warncke Lang**
Department of Aerospace Engineering
& Mechanics,
University of Alabama,
Box 870280,
Tuscaloosa, AL 35487

**William D. Thacker**
Department of Physics & Center for Fluids
at All Scales,
Saint Louis University,
3450 Lindell Boulevard,
St. Louis, MO 63103

*An experimental study was performed to investigate the interaction of water waves with a surface-parallel oriented vortex at a free surface. Shadowgraph images were obtained visualizing surface deformations. The role of vortex strength and the direction of approach of the waves were investigated. For favorable waves, with flow velocity at crests parallel to vortex flow, surface deformations were weaker, lasted longer than for a vortex without waves, and were characterized at late times by the appearance of surface-normal vortices. For unfavorable waves incident on the vortex from the other side, surface deformations were stronger and dissipated more quickly.* [DOI: 10.1115/1.2907430]

*Keywords: water waves, turbulence, free-surface flows, vortex breakdown*

## 1 Background

The exchange of energy between water waves and underlying turbulence is an important fluid phenomenon to understand. Turbulence generated under a quiescent air-water interface will result in pressure fluctuations that generate free-surface water waves. In the presence of surface waves, turbulence can act as a damping influence, draining the energy downward to the region below the wave motion [1]. Large-scale coherent vortex structures may also dissipate or scatter the wave energy. For example, in the case of a whale footprint, the large-scale vortex structure of the wake shed from a diving whale, with consequent upwelling of flow, causes a calm spot on the ocean surface to appear and last for several minutes. Another such example is that of a ship wake, where in an otherwise rough sea calmer conditions at the water surface in the wake persist over many miles [2].

The problem of wave-turbulence interaction is further complicated by the presence of surfactants, which are known to damp underlying turbulence [3] and alter the interaction of vortex filaments with a free surface [4,5]. In the case of the ship wake, the harvesting of surfactants by bubbles can also play a role as their presence will also contribute to the wave damping. The specific case of surface-parallel vorticity interacting at a water surface, for both the clean and contaminated surface cases, was studied by Hirsa and Willmarth [6] and Willert and Gharib [7] among others. An excellent overview of many of these studies, as well as a discussion of the interaction of vorticity with a free surface, has been given by Sarpkaya [8].

Brocchini and Peregrine [2] gave an excellent overview of the dynamics of turbulence at free surfaces. They discussed the fact that "water wave generation by weak turbulence requires a reasonable match of length and time scales between the turbulent motion and free waves." The problem is further complicated by the minimum phase velocity of water waves (about 23 cm/s at a wavelength of 1.7 cm). In addition, surface waves are strongly damped in the regime where their wavelength is similar to, or smaller than, the dominant length scale in the turbulence.

Kitaigorodskii and Lumley [9] also considered the effects of the relative length and time scales of the turbulence and wave motion. When the time scale of the turbulence is small compared to that of the surface waves, the turbulence equation based on phase averaging is appropriate. When the turbulence time and length scales are very large, on the other hand, the turbulence is "frozen" on the time scale of the orbital wave motion and expected to have little dynamical effect. In the case of random surface waves, the primary effect of wave-turbulence interaction is the downward transport of energy and the main contribution to this effect comes from turbulent motions with time and length scales comparable to those of the wave motion.

An additional complexity to the problem comes from considering whether the vorticity, with which the waves are interacting, is oriented vertically or normally to the free surface. Two theoretical studies [10,11] have discussed the scattering effect that vertical vorticity can have on surface waves. In this case, no downward surface current exists to carry the wave energy further below the free surface.

Perhaps most relevant to the current case was a computational study of the interaction of a submerged vortex pair with free-surface waves performed by Fish and von Kerczek [12]. They pointed out the importance of the vortex-induced surface current in the interaction of the vortex flow with ambient waves. In a related experimental study, Fish [13] presented flow visualizations of a counter-rotating vortex pair ascending toward a free-surface containing waves. The vortex that was upstream with respect to the waves was observed to remain near the surface while the downstream vortex rebounded to a deeper level. Fish attributed these observations to the influence of a near-surface drift current produced by the waves.

In the current experimental study, the generic problem of wave-turbulence interaction is broken down in complexity to isolate the interaction between surface waves and the flow field of a large-scale surface-parallel vortex. A surface-parallel vortex was generated and surface waves were directed into the flow field. The directional effect of the side of approach of the waves impinging on the vortex was also isolated. Vortices of two different sizes and circulations were used. The surface wavelengths studied were comparable to the diameters of the vortices and the orbital motion induced by the waves, about an order of magnitude smaller than the wavelength of the waves at the surface, decreased with depth. The wavemaker was operated at two different settings. The lower frequency setting produced a packet with wavelengths ranging from 2.0 to 4.3 cm accompanied by a 30 cm wavelength progressive wave, while for the higher frequency setting only 2.0 cm wavelength waves were observed.

Shadowgraph visualizations of the free-surface deformations show the ability of the vortex flow field to inhibit the motion of the surface waves, as well as the generic tendency for the wave

Contributed by the Fluids Engineering Division of ASME for publication in the JOURNAL OF FLUIDS ENGINEERING. Manuscript received June 14, 2006; final manuscript received February 26, 2008; published online April 29, 2008. Review conducted by Joseph Katz.

motion acting on the vortex flow field to induce a change in the vortex location relative to the free surface. In addition, observations showed a greater tendency for vortex filaments within the vortex flow to be reoriented to the surface-normal direction, during the later stages of the flow field evolution, with the presence of surface waves.

## 2 Theory

Surface waves in water are driven by a balance between the inertia of the fluid and the restoring forces of gravity and surface tension [14]. The waves in this study, with wavelengths ranging from 2.0 cm to 4.3 cm, fall into the ripple regime where both gravity and surface tension are significant. For sinusoidal waves of wave number $k$ in deep water of density $\rho$ the stiffness characterizing the restoring force is $\rho g$, due to gravity, plus $Tk^2$, due to surface tension $T$, while the generalized inertia of a fluid column is $\rho k^{-1}$. The ratio of stiffness to generalized inertia gives the angular frequency

$$\omega^2 = (g + \rho^{-1}Tk^2)k \tag{1}$$

the phase velocity,

$$c = \frac{\omega}{k} = [(g + \rho^{-1}Tk^2)/k]^{1/2} \tag{2}$$

and the group velocity,

$$c_g = \frac{d\omega}{dk} = \frac{1}{2}\frac{g + 3\rho^{-1}Tk^2}{[gk + \rho^{-1}Tk^3]^{1/2}} \tag{3}$$

The phase and group velocities relevant in this study range from $c=23$ cm/s and $c_g=22$ cm/s for wavelength 2.0 cm to $c=28$ cm/s and $c_g=18$ cm/s for wavelength 4.3 cm, while the 30 cm wavelength wave has $c=69$ cm/s and $c_g=34.5$ cm/s. For deep water waves of amplitude $a \ll \lambda$, fluid particles follow circular orbits of radius $ae^{kz}$ and orbital speed $a\omega e^{kz}$, where $z \leq 0$ is the vertical coordinate measured from the undisturbed surface. Superimposed on their circular motion, the fluid particles undergo a second order mean drift, called the Stokes drift, which results in a mean velocity in the direction of wave propagation that exponentially decays with depth below the surface.

The surface-parallel vortex in this study can be modeled as a cylindrical vortex tube or Rankine vortex [15] with axis perpendicular to the direction of wave propagation. In this study, the weak vortex has radius $R_1=1.25$ cm and surface velocity $U_1=3.2$ cm/s giving it a circulation $\Gamma_1=2\pi R_1 U_1=25$ cm$^2$/s, while the strong vortex has radius $R_2=3.1$ cm, surface velocity $U_2=6.4$ cm/s, and circulation $\Gamma_2=125$ cm$^2$/s. The fluid particle velocities in the vortices are significantly less than the phase and group velocities of the surface waves.

In their study of wave-turbulence interactions, Kitaigorodskii and Lumley [9] specified a wave layer, or depth below the free surface into which a wave causes motion of the fluid. They characterize this to be on the order of the inverse of the wave number, $k^{-1}$, or $\lambda/2\pi$, where $\lambda$ is the wavelength. In the cases studied here, the wavelayer depths associated with the smaller (2.0–4.3 cm) waves ranged from 0.32 cm to 0.68 cm, considerably less than the vortex diameters. However, the cases with the approximate 30 cm wavelength wave produced a wave layer of approximately 4.8 cm, which is of the same order of magnitude as the vortex diameters. Therefore, as this larger wave interacts with the vortex the stretching/compressing action of the wave on the flow field must be considered.

Kitaigorodskii and Lumley [9] also discussed the decomposition of the whole spectrum of wave-turbulent interactions into four categories based on the length scale ($L_t$) and (inverse) time scale ($\Omega_t$) of the turbulence and the length scale ($\Lambda$) and frequency ($\sigma$) of the waves. These are long ($L_t > \Lambda$), short ($L_t < \Lambda$), rapid ($\Omega_t > \sigma$), and slow ($\Omega_t < \sigma$). The present study deals with large-scale coherent vorticity interacting with waves that have wavelengths of size comparable to or smaller than the vortex. As calculated above, all the cases studied can be considered to fall within the long category. Based on the assertion by Kitaigorodskii and Lumley [9] that "long fluctuations are the most effective for transporting wave energy downward, since they are able to cross the whole wave layer," one would expect an absorption of the wave energy by the vortex flow field to be observed within this study.

Rood [16] gave a theoretical overview of the interaction and production of vorticity at a free surface. A free surface is defined as an interface between two fluids, such as air and water, in which one of the fluids (quiescent air) produces no tangential stress and has negligible dynamical effect on the flow of the other fluid (water). A free surface, by definition, allows for free deformation of this interface and satisfies the condition that the tangential stress is zero and normal stress is constant at all times. This stress-release condition at a free surface has a dramatic effect on the dynamics of nearby vorticity that is different than that produced by a no-slip boundary. While vorticity must be normal to a flat free surface, surface-parallel vorticity must be present at a curved surface even when the flow underneath is irrotational. For example, in a progressive gravity wave, the bulk flow has zero vorticity and nonvanishing viscous stress, while at the free surface the stress-free condition results in the production of surface-parallel vorticity, which is positive for the concave portion of the wave and negative for the convex portion [16,17].

Rood [16] discussed the interactions between the primary vortices and free surfaces, which are characterized by the deformation of vortical structures due to the pressure at the free surface and the diffusion of vorticity constrained by the free surface. Rood [16] pointed out that the vortical structure interacting at a free surface, in particular, that of a surface-parallel vortex, will have its vorticity distribution modified by the pressure of the free surface. The vortex core will take on an oblong shape as it is flattened by the interaction with the free surface. This flattening of the vortex core was observed in the present study during dye visualization of the vortex flow field as it interacted with a calm free surface. A primary vortex can also generate secondary vorticity at a free surface associated with the curvature of the induced surface-parallel flow. Vortex disconnection is another important interaction in which segments of vorticity from the primary vortex move toward and merge with the free surface leaving vortex lines terminating vertically at the surface.

The present study is concerned with the interaction between a surface-parallel vortex and surface waves on water. When the waves encounter the surface current of velocity $U$ produced by the vortex, the Doppler effect must be taken into account by replacing the observed frequency $\omega$ in dispersion relation (1) by the intrinsic frequency $\sigma = \omega - kU$ in the rest frame of the current. Since the wave source (wavemaker) and observer are in the same (laboratory) frame, the frequency $\omega$ remains constant while the wave number and the corresponding wavelength are modified by the current $U$. Phillips [18] showed that curvature and centripetal acceleration of the surface current can be taken into account by replacing $g$ by the effective gravitational acceleration

$$g' = g\cos\theta + \frac{U^2}{R} \tag{4}$$

where $\theta$ is the angle between the surface tangent and the horizontal, and $R$ is the radius of curvature. Shyu and Phillips [19] considered the blockage of short gravity-capillary waves by longer waves and by currents that may have vorticity. Wave blockage occurs when the convective velocity of the current cancels the group velocity

$$U + \frac{d\sigma}{dk} = 0 \tag{5}$$

In this process, the blocked wave is reflected as an extremely short capillary and then rapidly dissipated by viscosity [19].

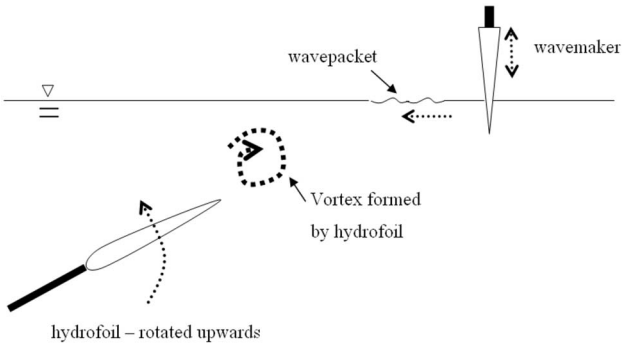


**Fig. 1 Diagram of the experimental setup showing the case for unfavorable waves**

## 3 Method of Approach

The experiment was conducted in the test section of the Parks College water tunnel. With the tunnel turned off, this allowed for the test section (15 in. wide by 20 in. high by 60 in. in length) to be used as a tank facility. A plunger type wavemaker (spanning the width of the test section), employed to generate progressive water waves, was operated at two different settings. At the first setting, the wavemaker generated packets with observable wavelengths of 2.0–4.3 cm superposed with a much larger approximately 30 cm wavelength wave that could be measured in the side view whole field video of the wave generation process. At the second setting, only 2.0 cm wavelength waves were observed. A flat plate inclined to the free surface served as a simulated beach at the far end of the test section such that minimal wave reflection would occur back into the test area. In addition, all waves were generated to move parallel to the test section walls and minimal reflection of the waves off the walls was observed during the experiments.

To visualize the free-surface deformations and obtain qualitative observations of the flow field during the experiment, a shadowgraph system was used. A fiber optic light source (continuous Cuda Products I-250) was focused into a beam of collimated light using a spherical mirror of 8 in. diameter and a focal length of 24 in.. The collimated light was shone upward through the test section, where it then passed through the water surface and onto a white glass screen. A digital camera (Canon Powershot) was focused onto the screen and images of the free-surface deformation field during each experimental run were obtained. The exposure time was adjusted to acquire bright images with no blurring due to the fluid motion. The bright circle covering almost the entire image defines the length scale as it corresponds to the 8 in. diameter beam of collimated light that was shone up through the test section. These images, shown in the Results section, are gray scale images where the light and dark regions correspond to variations of the slope of the free surface. Specifically, lighter regions are areas where the free surface has focused the light and thus correspond to convex regions at the water surface. Likewise, darker regions correspond to depressions or concave regions on the water surface. The darker areas, when approximately circular in shape, correspond to the connection of a vortex tube to the free surface as the lower pressure at the center of the vortex pulls the surface downward.

A hydrofoil, with a length of 13 in. and thus spanning almost the entire width of the test section, was rotated upward to generate a single vortex, which interacted with the water surface. Figure 1 shows a diagram of the experimental setup. The rate of rotation of the hydrofoil was varied to generate vortices of two different strengths, and the final resting point of the hydrofoil at the end of rotation was approximately 4 in. below the water surface. In the absence of surface waves, characteristics of the vortices were determined. Using the buoyant particles at the water surface, and imaging their motion with the time difference known between images, a characteristic or average surface velocity $U$ for each vortex strength was measured (3.2 cm/s and 6.4 cm/s for the weak and strong vortices, respectively). A characteristic diameter $d$ of the vortex was obtained from the shadowgraph images, where the depressed region (dark region in shadowgraph images) of the flow characterizing the low pressure core of the vortex was used, giving $d=2.5$ cm for the weak vortex and 6.2 cm for the strong one. Based on other dye visualization results, this value was consistent with the core size observed during vortex generation. Thus, a Reynolds number ($\mathrm{Re}=Ud/\nu=\Gamma/\nu$) and Froude number ($\mathrm{Fr}=U^2/gd$) for each vortex was calculated. These values are $\mathrm{Re}=779$ and $\mathrm{Fr}=0.004$ for the weak vortex, and $\mathrm{Re}=3940$ and $\mathrm{Fr}=0.01$ for the strong vortex. Dye visualization of the vortex core was observed during the interaction process and all observations given in the results with respect to the depth of the vortex below the free surface were confirmed with the video sequence of the dye studies.

To ensure repeatability of the experimental conditions and strength of the vortex during various runs, a programmable logic controller (PLC) was used to control the motion of both the wavemaker and hydrofoil. The PLC also allowed for the timing of the formation of waves to be repeatable with respect to the initiation time of the vortex. By changing the position of the wavemaker, waves could be generated that impinge on the vortex from either direction. The cases where the waves impinged on the vortex in such a way that the surface velocity induced by the vortex (left to right as in Fig. 1) was opposite to that at the crests of the wave motion are herein referred to as unfavorable waves. The cases where the waves impinged on the vortex from the other side, such that the surface velocity induced by the vortex and motion at the crests of the waves were in the same direction, are referred to as favorable waves. Taking the phase velocity of the incoming waves as positive, the surface current velocity $U$ produced by the vortex is positive in the favorable and negative in the unfavorable case. Finally, before each run, it was ensured that approximately 10 min or more had elapsed since the previous run so that the fluid in the tunnel was motionless before the hydrofoil motion was initiated.

The last aspect of this particular experiment that should be mentioned is the level of free-surface contamination. Before each run, the water surface in the test area was vacuumed, over several minutes, to remove impurities. However, due to the fact that tap water was used in the tunnel and other possible factors, the water surface could not be brought to what would be considered a clean state. Observations showed that some surface contamination was present during the runs. This was evident from the formation of a Reynolds ridge within the field of view to the left of the vortex during the cases where just the vortex was observed to interact at the surface without the presence of the waves. The Reynolds ridge was formed due to the strong surface current from the vortex, cleaning the water surface and forming a line of demarcation between the clean and contaminated regions. The ridge was not noticeable though during the cases with surface waves present in the flow field. This is a sign that the waves sufficiently disturbed the surface to prevent the localized buildup of surface contaminants to form the ridge, and also pointed to the fact that the surface contamination was kept to a low level. Even though surface contamination was a factor in the experiment, the results still focus on the observed differences between the cases with and without water waves with the same surface conditions. In addition, runs were obtained showing the waves propagating through the test area without the presence of the vortex, showing that the wave energy, over the wavelengths measured, was not significantly damped by the presence of surfactants.

## 4 Results

Figure 2 shows a characteristic sequence of shadowgraph images for the case of the weak vortex interacting at a calm free

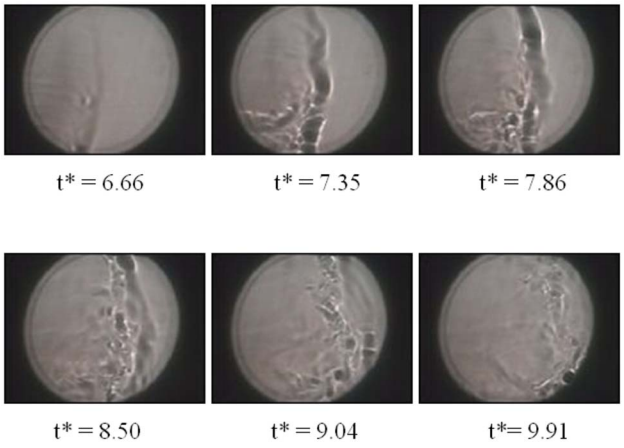


**Fig. 2 Characteristic time sequence of shadowgraph images for the weak vortex interacting with a calm surface**

surface. Time $t^*=0$ is considered in all images to be the moment when the hydrofoil was put into motion to generate the vortex, and all subsequent times are nondimensionalized by the corresponding velocity and vortex radius for the weak or strong case, respectively. The surface deformation induced by the vortex is visible as an elongated shadow at early times. For the weak case, by $t^*=8.5$, instabilities have set in and the process of vortex disconnection (Rood 1995) is evident, where segments of vorticity break off the primary vortex and vertically merge with the surface. In the later slides, regions of vorticity terminating normal to the surface are visible as circular shadows. Figure 3 shows a similar series of images for the strong vortex. Note that the entire sequence of events in Fig. 3 occurs at significantly earlier times than that in Fig. 2; therefore, this implies that the stronger vortex interacts earlier with the surface. Also in Fig. 3 at the two earliest times, one can see evidence of streamwise vortex structures. These are most likely due to the formation process of the vortex, with vorticity trailing behind the vortex as the hydrofoil is brought to the end of its motion. These striations are only visualized at the free surface for the higher Re vortex case. In the case of the strong vortex, evidence of vortex instability is also seen in the surface striations across the vortex core. One could possibly consider this to be an instability mechanism similar to that observed by Leweke and Williamson [20].

Figures 4 and 5 show the shadowgraph images for the case of the weak vortex interacting with the unfavorable and favorable

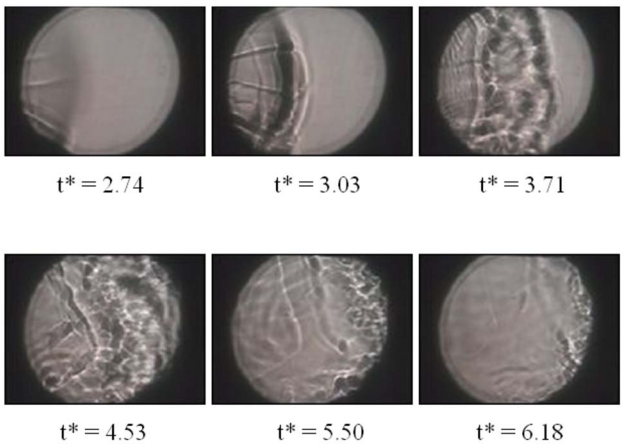


**Fig. 3 Characteristic time sequence of shadowgraph images for the strong vortex interacting with a calm surface**

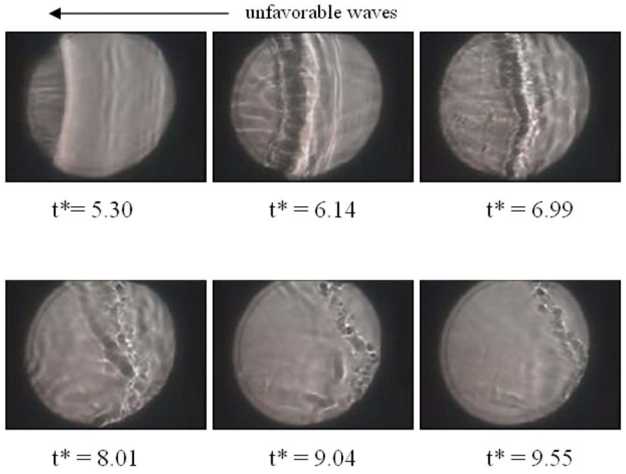


**Fig. 4 Characteristic time sequence of shadowgraph images for a weak vortex interacting with unfavorable waves of 4.3 cm and less in wavelength**

waves, respectively. The plunger used for these cases (Figs. 4 and 7) generated a wave packet of measurable waves ranging in a wavelength from 2 cm to 4.3 cm in addition to the larger than view wave of approximately 30 cm wavelength. In the case of the favorable waves, the interaction time of the vortex with the free surface was longer, and the vortex also moved to the right of the imaging area to a greater degree. This prompted additional image sequences of the characteristic flow fields to be obtained by moving the area imaged in the test section approximately 7 in. to the right. The experiment was repeated with the new viewing area to confirm the result. Both of these cases showed an apparent widening of the area over which the vortex interacted with the surface in the presence of waves. One difference between the favorable and unfavorable wave cases is that the surface deformations associated with the vortex, which appear as rough light and dark areas in the shadowgraph images, appear earlier and are more pronounced in the presence of unfavorable waves, and are weaker in the presence of favorable waves during the initial stages of interaction, when compared to the case of no surface waves. However, although the initial surface deformations were weaker in the fa-

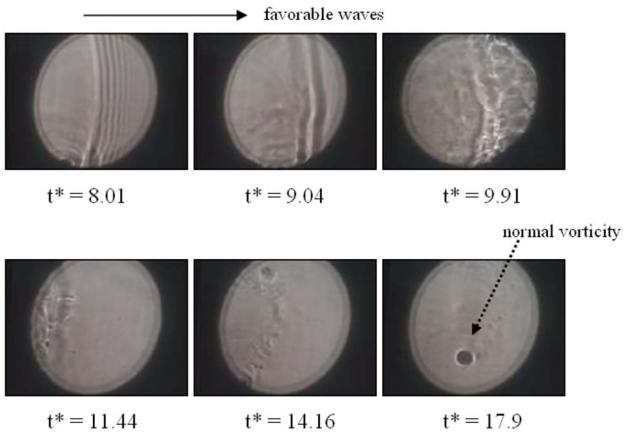


**Fig. 5 Characteristic time sequence of shadowgraph images for a weak vortex interacting with favorable waves of 4.3 cm and less in wavelength. Note that at $t^*=11.44$ the field of view in the test area was moved to the right with respect to the previous images. At $t^*=17.9$, note the dark circle that is a representative of the connection of a strong vortex filament to the free surface.**

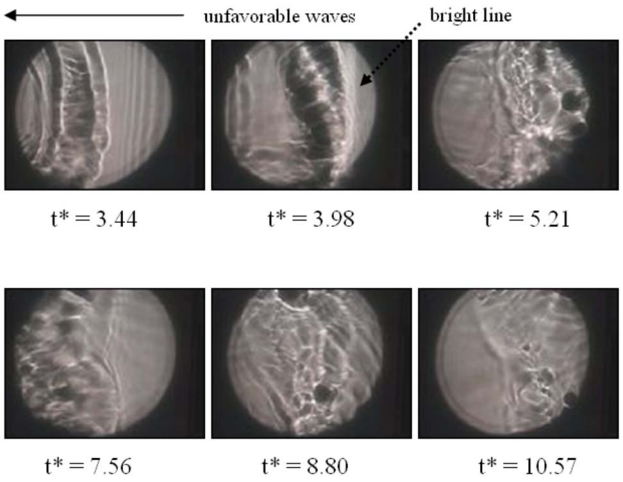


**Fig. 6 Characteristic time sequence of shadowgraph images for a strong vortex interacting with unfavorable waves of 4.3 cm and less in wavelength. Note that at $t^*=17.56$, the field of view in the test area was moved to the right with respect to the previous images.**

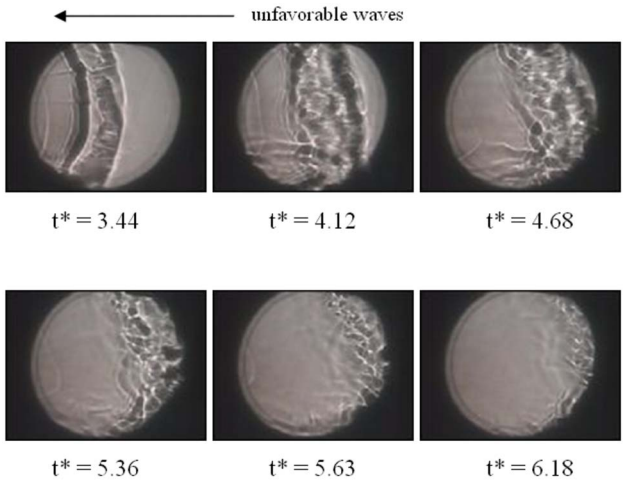


**Fig. 8 Characteristic time sequence of shadowgraph images for a strong vortex interacting with unfavorable waves of 2.0 cm wavelength**

vorable case, it appears that at late times a significant portion of the vorticity has been reoriented to the vertical direction as evidenced by the large whirl, or normal vortex connection, observed to persist at $t^*=17.9$. Another difference between the favorable and unfavorable cases can be seen in the behavior of the waves. Note that the favorable waves have already passed over the vortex by $t^*=8.5$ while unfavorable waves appear to be blocked by the vortex and there is no evidence of them on the downstream (left) side.

Figures 6 and 7 show comparable cases for the strong vortex, resulting in similar observations as previously discussed but for a larger scale vortex flow field. These figures highlight the influence that vortex intensity has on the surface deformation and the time scale of the interaction. For both favorable and unfavorable waves, the stronger vortex is more unstable and shows increased evidence of surface-normal vorticity. Note in the unfavorable case the bright line on the right side of the vortex indicating large convex surface deformations where the impinging waves appear

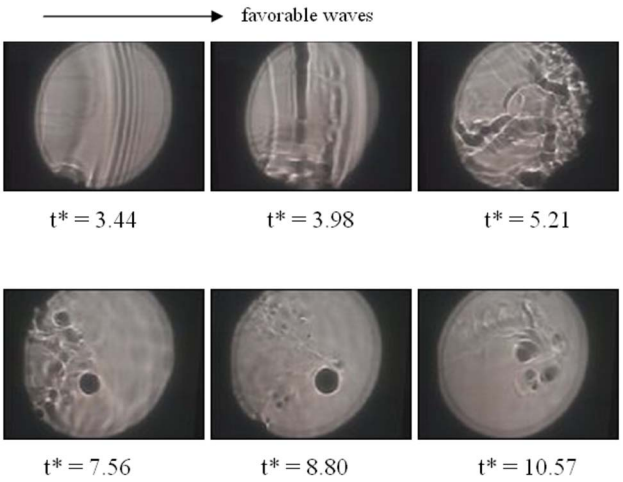


**Fig. 7 Characteristic time sequence of shadowgraph images for a strong vortex interacting with favorable waves of 4.3 cm and less in wavelength. Note that at $t^*=17.56$, the field of view in the test area was moved to the right with respect to the previous images.**

to be absorbed (between $t^*=3.44$ and 3.98). This bright line (pointed out in Fig. 6) is visible in the other figures showing unfavorable wave cases and appears to be characteristic of the case that the waves propagate in the direction opposite to the vortex-induced surface velocity. Also, the overall disturbance of the free surface persists longer for the strong vortex and vortex reconnection at the surface is evident at later times for both the favorable and unfavorable wave cases.

In order to avoid the presence of the 30 cm wave evident in the above cases, the runs were repeated with a smaller plunger angle to produce smaller wavelength waves. This resulted in wavetrains where only 2.0 cm wavelength waves were observed. Results were similar to the above cases but with less of an overall impact on the vortex flow field. These characteristics, along with some exceptions, are evidenced by the cases shown in Figs 8 and 10. Figure 8 shows the unfavorable waves impinging on a strong vortex (note, however, that the waves actually impinge on the vortex flow some time between $t^*=3.44$ and $t^*=4.12$ and are not visible in the slides). The results show the strong vortex to be less disturbed by the waves than in the previous cases, and to resemble more the calm case as in Fig. 3. However, one can still observe the bright line on the right side of the vortex, indicating the result of waves impinging on the vortex flow. Figure 9 shows the case of favorable waves interacting with a weak vortex. One notes, in particular, the reduced interaction of the vortex at the free surface in the initial stages of the flow field along with what appears to be a greater coherency of the vortex core. However, in the later stages of the flow field, a significant portion of the vortex (as the ring diameter is comparable in size to the width of the vortex as it approaches the surface in the earlier frames) has been vertically reoriented. It appears that the ends of the vortex filament have connected to the free surface to form a half-ring. The last overall characteristic observed is the earlier and more significant interaction of the weak vortex for the unfavorable waves (shown in Fig. 10), as compared to a delayed interaction of the weak vortex with smaller surface deformations for the favorable waves (Fig. 9).

## 5 Conclusions

The interaction of a surface-parallel vortex with a free surface is significantly altered by the presence of surface waves and dramatic differences were observed between the favorable and unfavorable wave cases. These differences in the effects of the waves were most apparent for the weaker vortex. In the case of the unfavorable waves, the entire interaction between vortex and free surface initially displayed larger deformations, which then de-

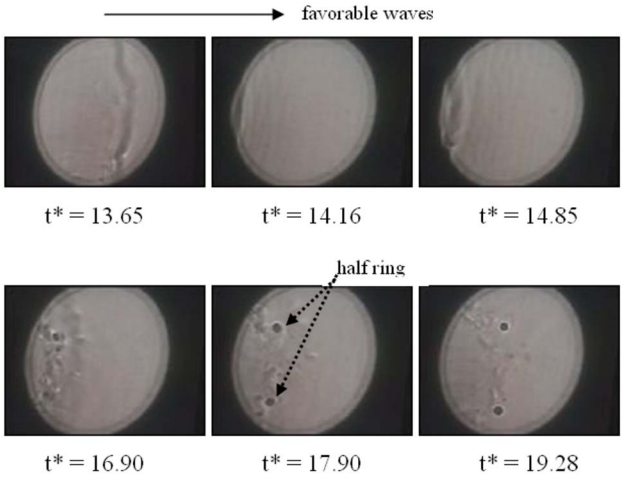


**Fig. 9 Characteristic time sequence of shadowgraph images for a weak vortex interacting with favorable waves of 2.0 cm wavelength. Note that at $t^*=14.16$, the field of view in the test area was moved to the right with respect to the previous image.**

cayed faster than for either the initially calm surface or the favorable waves. The surface deformations were more intense and began to significantly appear earlier, the vortex then appeared to break up and form surface-normal vortices, and finally the surface structures disappeared much earlier. In the case of favorable waves, on the other hand, the entire vortex/free-surface interaction took place on a much longer time scale than for the initially calm surface. The vortex could not be seen to deform the surface in the favorable wave case long after the structures had begun to appear in the other two cases, and when surface deformations did appear they were weaker. However, in the later stages of the interaction, large surface-normal vortices appeared and persisted to the end of the image sequences. For the strong vortex, the surface deformations appeared earlier, were generally more intense, and the difference in time scale of the vortex/free-surface interaction for the three cases (favorable, unfavorable, and no waves) was less obvious. However, it was still apparent that the surface deformations were significantly weaker for favorable waves and dominated by surface-normal vortices at later times.

Another important difference between the favorable and unfavorable cases can be seen in the behavior of the waves. For the favorable waves the surface current $U>0$ has the same direction as the wave propagation and the waves appear to be easily convected over the vortex. The unfavorable waves meet an adverse current $U<0$ and appear to be blocked by the vortex. However, based on the wave group velocities and vortex current velocities given in Sec. 2, the wave blockage condition (5) cannot be satisfied. This remains the case even when surface curvature is taken into account in the reduced effective gravity (4). The blocking of waves in this study appears to be a different effect perhaps better described as wave absorption. This effect appears to be more pronounced in the presence of the greater surface deformation induced by the strong vortex and may be associated with the downward convection of wave energy.

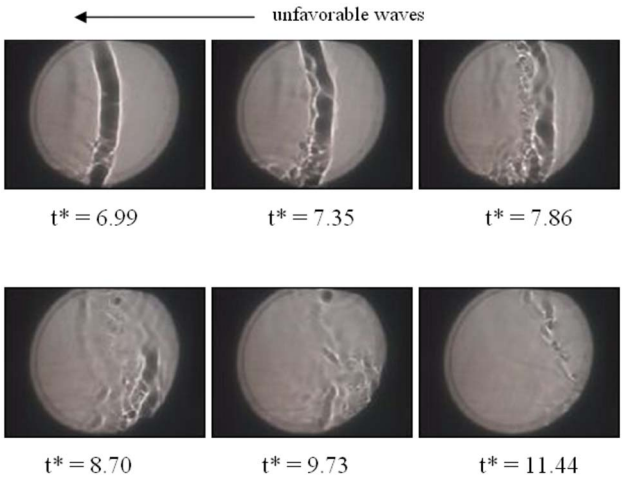


**Fig. 10 Characteristic time sequence of shadowgraph images for a weak vortex interacting with unfavorable waves of 2.0 cm wavelength**

The fact that the vortex-induced surface deformations were relatively strong and appeared early in the case of unfavorable waves suggests that the absorption of wave energy has a destabilizing effect on the vortex. Sarpkaya [8] described, how the surface-parallel vortex undergoes centrifugal instability with patches of helical vorticity spiraling out from its edges and normally attaching in isolated patches to the free surface, ultimately leading to the dissolution of the vortex. Evidently, the straining action of the waves as they are convected downward and absorbed by the vortex accelerates this process.

In the case of favorable waves, on the other hand, the waves pass right over the vortex without being absorbed and the interaction of the vortex with the free surface is delayed even compared to the case of no surface waves. The passage of surface waves over the vortex causes it to remain deeper below the surface for a longer period of time. The study of Fish [13] provides a possible mechanism for this phenomenon. He observed that in his experiment the upstream vortex encounters unfavorable waves and remains at the surface, while the same wave train is favorable with respect to the downstream vortex and causes it to rebound from the surface and move to a deeper level. Fish [13] attributed this effect to the drift current produced by the surface waves. Measurements of the mean flow in Fish [13] showed a profile indicative of Stokes drift, where the streamwise velocity increased with vertical coordinate until very near the surface and then the mean velocity rapidly reduced to zero in a thin shear layer. According to Fish [13], the thin shear layer at the surface is caused by the combined action of surface tension gradient and viscous forces. The placement of the vortices in the favorable and unfavorable cases can then be understood in terms of the tendency of a vortex, demonstrated in previous simulations [21,22] to be sustained in a shear layer of same signed vorticity and to rapidly decay in a shear layer of opposite signed vorticity. Favorable waves produce a Stokes layer with vorticity of the same sign as the vortex, sustaining it below the surface.

This observation also appears to be consistent with the intermediate Froude number case numerically studied by Ohring and Lugt [23]. They observed that secondary vorticity can cause a rebounding of the vortex from the free surface. In the experiment herein described though, vorticity is introduced by the presence of the waves. However, the role of the Stokes layer could not be confirmed by the present study.

The observation of persistent surface-normal vortices at late times in the favorable wave cases suggests that the two ends of the initial vortex may bend around forming a half-ring with two patches of vertical vorticity that join the surface. Figure 9 clearly shows a pair of surface-normal vorticity patches suggestive of a half-ring, while in other favorable wave cases only a single patch remains in the field of view. Further studies using other methods such as particle image velocimetry are needed to confirm the existence of the half-ring vortex.

The role of surface waves as an instability on the vortex flow was particularly pronounced in the cases where the larger 30 cm wave was present. The stress field induced by this larger wave appeared to cause a greater disruption to the vortex core.

Overall, the experiment showed significant interactions be-

tween a surface-parallel vortex and impinging surface waves with wavelengths of similar magnitude to the vortex diameter. The vortex can absorb wave energy carried by the orbital motion of the fluid particles. In addition, the fluctuation of the flow field induced by the wave acts as an instability mechanism on the vortex and causes enhanced reorientation of the vortex filaments in the flow field to the surface-normal direction.

## Acknowledgments

The authors would like to acknowledge the support of this work through Saint Louis University. First, the award of a SLU 2000 Research Assistantship to the Department of Aerospace and Mechanical Engineering paid the tuition and stipend of MS student Ana de Leon who carried out much of the experimental work. Second, we would also like to acknowledge the help of Ed Ising and Frank Coffey in designing and building the experimental apparatus.

## References

[1] Olmez, H., and Milgram, J., 1992, "An Experimental Study of Attenuation of Short Water Waves by Turbulence," J. Fluid Mech., **239**, pp. 133–156.
[2] Brocchini, M., and Peregrine, D., 2001, "The Dynamics of Turbulent Free Surfaces. Part 1. Description," J. Fluid Mech., **449**, pp. 225–254.
[3] Davies, J. T., 1966, "The Effects of Surface Films in Damping Eddies at a Free Surface of a Turbulent Liquid," Proc. R. Soc. London, Ser. A, **290**, pp. 515–526.
[4] Gharib, M., and Weigand, A., 1996, "Experimental Studies of Vortex Disconnection at a Free surface," J. Fluid Mech., **321**, pp. 59–86.
[5] Lang, A. W., and Gharib, M., 2000, "Experimental Study of the Wake Behind a Surface-Piercing Cylinder for a Clean and Contaminated Free Surface," J. Fluid Mech., **402**, pp. 109–136.
[6] Hirsa, A., and Willmarth, W., 1994, "Measurements of Vortex Pair Interaction With a Clean or Contaminated Free Surface," J. Fluid Mech., **259**, pp. 25–45.
[7] Willert, C., and Gharib, M., 1997, "The Interaction of Spatially Modulated Vortex Pairs With Free Surfaces," J. Fluid Mech., **345**, pp. 227–250.
[8] Sarpkaya, T., 1996, "Vorticity, Free Surface, and Surfactants," Annu. Rev. Fluid Mech., **28**, pp. 83–128.
[9] Kitaigorodskii, S., and Lumley, J., 1983, "Wave-Turbulence Interactions in the Upper Ocean. Part I: The Energy Balance of the Interacting Fields of Surface Wind Waves and Wind-Induced Three-Dimensional Turbulence," J. Phys. Oceanogr., **13**, pp. 1977–1987.
[10] Coste, C., Lund, F., and Umeki, M., 1999, "Scattering of Dislocated Wave Fronts by Vertical Vorticity and the Aharonov–Bohm Effect. I. Shallow Water," Phys. Rev. E, **60**(4), pp. 4908–4916.
[11] Fabrikant, A., and Raevsky, M., 1994, "The Influence of Drift Flow Turbulence on Surface Gravity Wave Propagation," J. Fluid Mech., **262**, pp. 141–156.
[12] Fish, S., and von Kerczek, C., 1991, "Submerged Vortex Pair Influence on Ambient Free Surface Waves," *18th Symposium on Naval Hydrodynamics*, National Academy, Washington, DC, pp. 491–501.
[13] Fish, S., 1991, "Vortex Dynamics in the Presence of Free Surface Waves," Phys. Fluids A, **3**, pp. 504–506.
[14] Lighthill, J., 1978, *Waves in Fluids*, Cambridge University Press, New York.
[15] Saffman, P. G., 1992, *Vorticity Dynamics*, Cambridge University Press, New York.
[16] Rood, E., 1995, "Vorticity Interactions With a Free Surface," *Fluid Vortices*, S. I. Green ed., Kluwer Academic, Netherlands, Chap. 16.
[17] Longuet-Higgins, M. S., 1992, "Capillary Rollers and Bores," J. Fluid Mech., **240**, pp. 659–679.
[18] Phillips, O. M., 1981, "The Dispersion of Short Wavelets in the Presence of a Dominant Long Wave," J. Fluid Mech., **107**, pp. 465–485.
[19] Shyu, J. H., and Phillips, O. M., 1990, "The Blockage of Gravity and Capillary Waves by Longer Waves and Currents," J. Fluid Mech., **217**, pp. 115–141.
[20] Leweke, T., and Williamson, C., 1998, "Cooperative Elliptic Instability of a Vortex Pair," J. Fluid Mech., **360**, pp. 85–119.
[21] Bilanin, A., Teske, M., and Hirsh, J., 1978, "Neutral Atmospheric Effects on the Dissipation of Aircraft Vortex Wakes," AIAA J., **16**(9), pp. 956–961.
[22] Robins, R. E., and Delisi D. P., 1990, "Numerical Study of Vertical Shear and Stratification Effects on the Evolution of a Vortex Pair," AIAA J., **28**, pp. 661–669.
[23] Ohring, S., and Lught, H., 1991, "Interaction of a Viscous Vortex Pair With a Free Surface," J. Fluid Mech., **227**, pp. 47–70.

# A Moving Boundary Analysis for Start-Up Performance of a Nuclear Steam Generator

**S. Paruya**
Department of Chemical Engineering,
Haldia Institute of Technology,
Haldia 721 657, India
e-mail: swapanparuya@rediffmail.com

**P. Bhattacharya**
Department of Chemical Engineering,
Jadavpur University,
Kolkata 700 032, India
e-mail: pinaki_che@yahoo.com

*Thermohydraulic phenomena of a steam-water natural-circulation (SWNC) system are very complicated, particularly, during its start-up and shutdown. Its performance strongly depends on the circulation inside it. Accurate quantification of the flow, void fraction, two-phase level, boiling boundary, etc., is difficult at both steady state and transient states like load variation, start-up, and shutdown. Attempts have been made to develop a high-fidelity thermohydraulic model (five-equation scheme) that caters to nonhomogeneous and thermal nonequilibrium flow to derive the dynamic effect of heating rate on the performance of the SWNC loop of steam generator of an Indian nuclear reactor during steaming-up period. The proposed work also attempts to predict boiling height, flow reversal, and density-wave oscillation (DWO). The boiling channel of the SWNC loop is modeled based on the moving boundary analysis using finite volume method. In this moving boundary problem, both control volumes of single-phase zone and two-phase zone change with time. Numerical results have been presented in this paper. The results indicate that both circulation flow variation and two-phase level variation in steam drum have strong dependency on void fraction in the boiling channel. Flow-reversal phenomenon is identified during the initial stage of boiling. Two-phase swelling and collapse that occur during the start-up are predicted. Above a critical heating rate, DWO has been observed. All these phenomena have been explained.*
[DOI: 10.1115/1.2911684]

*Keywords: two-phase natural circulation, moving boundary analysis, finite volume method, start-up simulation*

## Introduction

Simulation of steam generator (SG) unit in a power plant with respect to different process parameters, viz., pressure, steam drum (SD) level, steam generation rate, void fraction, boiling height, and circulation flow rate $R$ of liquid water, has been mandatory from the safety point of view for any fossil or nuclear power plant (NPP). For power plant simulation, thermohydraulic models for boiling steam-water mixture flow have been referred in literatures [1–3], which include formulations based on homogeneous equilibrium model (HEM), drift-flux model, and two-fluid model. Poon [4] studied the transient response of a natural-circulation boiler perturbed by a sudden drop of boiler pressure and used lumped-parameter approach to develop linearized model of a SG in Laplace domain. The response equations developed by Poon were verified using the data of laboratory-scale boiler experiment. He came to an important conclusion that the circulation velocity greatly reduces and becomes reverse due to the formation of steam in the downcomer. Recently, Paruya et al. [5,6] presented a rigorous model of SG of an Indian nuclear reactor (Kaiga-1). The unique feature of the model is that it can simulate the transient behavior of natural circulation during reactor trip; feeder pipe break and SG tube leakage based on HEM and quasisteady boiling boundary model.

A few improved equations for a natural-circulation steam-water loop have also been reported [7–10]. Paniagua et al. [7] developed a TWOPHASE computer code for thermal hydraulics to simulate the geysering instability during the start-up of a natural-circulation system from subcooled conditions and to assess the impact of the system pressure and channel inlet subcooling on the inception of the instability. For theoretical formulation of nonhomogeneous and thermal nonequilibrium two-phase flow, they considered four-equation scheme (vapor mass balance, liquid mass balance, mixture momentum balance, and mixture energy balance) and drift-flux model. During the start-up of a natural-circulation loop, Manera [8] also experimentally observed flashing-induced flow oscillations and formulated the problem using a different four-equation scheme (vapor mass balance, mixture mass balance, mixture momentum balance, and mixture energy balance) and drift-flux model. They identified the flashing phenomenon based on the experience of the steep rise of void fraction in adiabatic riser, and concluded that it was the result of enthalpy transportations. Furuya et al. [9] experimentally studied flashing-induced instability on a natural-circulation boiling water reactor (SIRIUS-N) at pressures of 0.1–0.5 MPa. The time period of oscillations was correlated with the transit time of the fluid required for traveling adiabatic riser (RI). They found that the period is approximately 1.5–2.0 times of the transit time regardless of the system pressure, heat flux, and inlet subcooling. Li et al. [10] developed a computer program based on a HEM of a two-phase flow to study the start-up performance of a fossil boiler while they carried out the fixed-boundary analysis by using finite difference method (FDM). Frepoli et al. [11] solved the moving thermal quench front and forth in the core cooling during the blowdown phase of large loss-of-coolant accidents (LOCAs) using FVM implemented in a thermal-hydraulic code COBRA-TF/FHMG, which demonstrates increased accuracy over FDMs. Moving boundary models of the SWNC loop have also been formulated by various investigators [12–14] by using four-equation scheme and simplified boiling boundary models (assumption of saturated condition at the boiling boundary), and subsequently deriving the solutions of the whole set of model equations through the use of FDM. Chang et al. [12] developed a one-dimensional moving-nodal model to analyze the

Contributed by the Fluids Engineering Division of ASME for publication in the JOURNAL OF FLUIDS ENGINEERING. Manuscript received March 8, 2007; final manuscript received November 30, 2007; published online May 5, 2008. Assoc. Editor: Malcolm J. Andrews.

  

chaotic instabilities in the natural-circulation boiling water reactors (BWR) loop at constant pressures using HEM formulation and assumption of saturation condition at the boiling boundary. van Bragt et al. [13] formulated a moving-nodal model of a two-phase flow by using HEM for predicting flashing-induced density instability of a natural-circulation BWRs at low pressures assuming an equilibrium condition at the boiling boundary (liquid attains a saturation temperature). Lee et al. [14] also developed a nonlinear model for a double-channel two-phase natural-circulation loop on the basis of HEM and used a Galerkin nodal approximation method for the moving-nodal analysis to determine the stability boundary.

The above literature survey suggests that an appreciable extent of the moving boundary analysis of the SWNC loop has been carried out in simplistic forms to predict the start-up phenomena of the loop using HEM, four-equation scheme with drift-flux model (for nonhomogeneous and thermal nonequilibrium flow), and FDM for the solution of model equations. With the four-equation scheme, one has to assume the vapor temperature or liquid temperature at the state of saturation to incorporate the effect of thermal nonequilibrium between the phases. In the present work, attempts have been made to simulate the thermohydraulic phenomena such as flow reversal and DWO during the start-up of the SWNC loop of a SG of an Indian NPP by carrying out the moving boundary analysis using a more realistic thermohydraulic model that involves a five-equation scheme along with the drift-flux model. The study also considers a more realistic boiling boundary model. The essential feature of the proposed model is that assuming the vapor temperature or liquid temperature at the state of saturation is not required. Computation of both vapor temperature and liquid temperature in the five-equation scheme has been carried out by considering two energy equations. The proposed moving boundary analysis has been carried out with the help of FVM, instead of FDM, since the former technique was observed to be more befitting in the present case [15]. Subsequently, Gear's method for stiff ordinary differential equations (ODEs) was followed. In addition, the model for the boiling boundary has been developed incorporating the effect of thermal nonequilibrium at the boiling boundary to eliminate the assumption of saturated condition at the boundary. The phenomena predicted by the present model have been validated by the experimental observations available in literatures. The present investigation is the modification of the previous work [6] in which HEM formulation and simplified boiling boundary model have been considered.

## System Model Equations

**Conservation Equations.** Basic mathematical formulations of a two-phase flow dynamics based on conservation equations called field equations are well described by Wallis [16] and Ishii [17]. More complicated formulations are also found in literatures [1,2,18,19]. Eulerian–Eulerian approach of Ishii [17] has been adopted in the present study to discretize partial differential equations (PDEs) obtained during the formulation of the problem. According to this approach, both liquid phase and vapor phase separately behave as a continuous phase. The continuity (local one or instantaneous one) formulation of a quantity being conserved is usually made through space or time averaging of the quantity. This leads to the equations for a two-phase flow in terms of space averaged or time averaged or both the averaged flow variables. A five-equation model involving conservation equations of mass, momentum, and energy of mixture, mass conservation equation of vapor, and energy conservation equation of liquid is presented below with the following simplifying assumptions: (1) The flow is one dimensional, (2) an average of products is approximated by the product of averages over cross section, (3) dry-out conditions are not considered, (4) heat and momentum conduction in phases and viscous dissipation are neglected, (5) evaluation of thermophysical properties is based on a uniform pressure throughout the cross section, and (6) bubbles are spherical and its diameter remains unchanged during the start-up period. In addition, one may note that the energy balance in the present case considers only the thermal energy equation, which can be obtained by subtracting the equation of kinetic energy from the total energy equation consisting of internal energy and kinetic energy. This was elegantly discussed by Bird et al. [20]. Contribution of potential energy and kinetic energy has been neglected because part of interests of the present investigation is only on heat transfer phenomenon and their magnitudes are insignificantly low compared to internal energy.

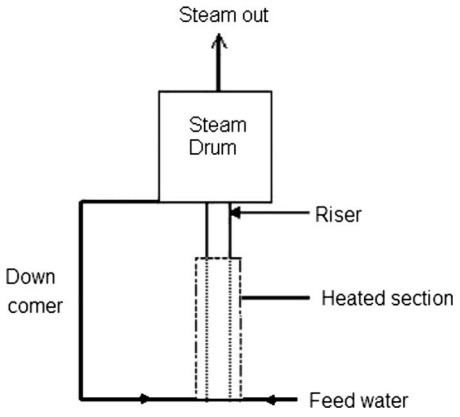


**Fig. 1 Schematic of the SWNC loop**

The SWNC loop is described in Fig. 1. The integral forms of conservation equations for the boiling channel (BC) consisting of heated section (HS) and RI are presented below with reference to Fig. 2.

In mixture mass balance,

$$\int_{\lambda}^{L_j} \frac{\partial}{\partial t}[(1-\alpha)\rho_l + \alpha\rho_g]_j dz + \int_{\lambda}^{L_j} \frac{\partial}{\partial z}[(1-\alpha)\rho_l v_l + \alpha\rho_g v_g]_j dz = 0 \tag{1}$$

In vapor mass balance,

$$\int_{\lambda}^{L_j} \frac{\partial}{\partial t}(\alpha\rho_g) dz + \int_{\lambda}^{L_j} \frac{\partial}{\partial z}(\alpha\rho_g v_g) dz = \int_{\lambda}^{L_j} \Gamma_v dz \tag{2}$$

In mixture momentum balance,

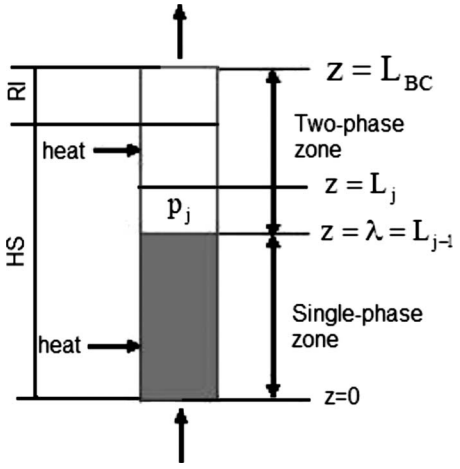


**Fig. 2 Schematic of BC**

$$\int_{\lambda}^{L_j} \frac{\partial}{\partial t}[(1-\alpha)\rho_l v_l + \alpha\rho_g v_g]_j dz + \int_{\lambda}^{L_j} \frac{\partial}{\partial z}[(1-\alpha)\rho_l v_l v_l + \alpha\rho_g v_g v_g]_j dz = -\int_{\lambda}^{L_j} \left\{ \frac{\partial p}{\partial z} + g[(1-\alpha)\rho_l + \alpha\rho_g]\sin\theta + \Delta p_{ft} \right\} dz \quad (3)$$

$\theta$ is the angle between axes of the flow channel and the horizontal plane. Its value is 90 deg for the vertical flow channel (as used in the present application). $\Delta p_{\mathrm{ft}}$ is the total frictional pressure loss per unit length of the flow channel.

In mixture energy balance,

$$\int_{\lambda}^{L_j} \frac{\partial}{\partial t}[(1-\alpha)\rho_l h_l + \alpha\rho_g h_g]_j dz + \int_{\lambda}^{L_j} \frac{\partial}{\partial z}[(1-\alpha)\rho_l h_l v_l + \alpha\rho_g h_g v_g]_j dz = \int_{\lambda}^{L_j} \frac{\partial p_j}{\partial t} dz + \int_{\lambda}^{L_j} [(1-\alpha)v_l + \alpha v_g]_j \frac{\partial p_j}{\partial z} dz + \int_{\lambda}^{L_j} Q_j dz \quad (4)$$

In liquid energy balance,

$$\int_{\lambda}^{L_j} \frac{\partial}{\partial t}[(1-\alpha)\rho_l h_l]_j dz + \int_{\lambda}^{L_j} \frac{\partial}{\partial z}[(1-\alpha)\rho_l h_l v_l]_j dz = \int_{\lambda}^{L_j} (1-\alpha)\frac{\partial p_j}{\partial t} dz + \int_{\lambda}^{L_j} [(1-\alpha)\rho_l v_l]_j \frac{\partial p_j}{\partial z} dz + \int_{\lambda}^{L_j} Q_{lj} dz \quad (5)$$

$Q_{lj}$ is the net heat transfer to liquid phase, contributed by the wall heat transfer to the liquid phase and bubble condensation. $Q_j$ is the net heat transfer to the $2-\phi$ mixture consisting of heat transfer due to boiling, bubble condensation, and convective heat transfer to the $1-\phi$ liquid. $L_j$ is shown in Fig. 2 where $j$th node is immediately after the $1-\phi$ zone. $\lambda$ is the boiling height. In the steam-water system, $\Gamma_v$ is the net vapor generation rate that accounts for boiling ($\Gamma_{\mathrm{boil}}$) and condensation ($\Gamma_{\mathrm{cond}}$), and it is calculated by

$$\Gamma_v = \Gamma_{\mathrm{boil}} - \Gamma_{\mathrm{cond}} \quad (6)$$

It is important to mention that for RI, Eqs. (1)–(6) are subjected to the limits of integration from $z=L_{j+k}$ to $z=L_{j+k+1}$.

**Total Frictional Loss.** The total frictional pressure loss $\Delta p_{\mathrm{Tf}}$ over a certain length of the flow channel (say, $L_j - L_{j-1}$ in Fig. 2) is given by Eq. (7). Subscript $m$ is for the mixture. $G$ is the mass velocity and $D_h$ is the hydraulic diameter. $\Sigma k$ is the sum of the loss factor for piping, valves, and fittings.

$$\Delta p_{\mathrm{Tf}} = \left( \frac{4 f_m (L_j - L_{j-1})}{D_h} + \sum k \right) \frac{|G_m| G_m}{2\rho_m} \quad (7)$$

As shown in Eq. (7), the first term within brackets takes care of wall friction calculated using Fanning's equation [21] and $f$ is the Fanning friction factor while the second term is for form friction. $2-\phi$ friction factor ($f_m$) is the product of $1-\phi$ friction factor ($f_l$) and two-phase multiplier ($\phi^2_{\mathrm{Lo}}$) where $f_l$ is calculated using $G_l$ equal to $G_m$. The phenomenal correlation for $\phi^2_{\mathrm{Lo}}$ was first proposed by Lockhart and Martinelli [22] for isothermal and separated flow based on the following considerations: (1) The individual phases are assumed to separately flow in a flow channel with insignificant phase interactions and flow regimes are classified based on viscous ($v$) and turbulent ($t$) flows of phases ($v$-$v$, $v$-$t$, $t$-$v$, and $t$-$t$) and (2) frictional pressure drops in individual phases are the same irrespective of flow regimes, neglecting the contributions of gravitation and acceleration. Collier [23] discussed the limitations of the correlation in detail. The correlation limits its uses in flow channels of a large flow area and vertical orientation and in high-pressure applications. Another important correlation $\phi^2_{\mathrm{Lo}}$ presented below was given by Becker et al. [24], which has been extensively used for steam-water flow in a tube. The essential feature of the correlation is that it takes less computational effort to calculate $\phi^2_{\mathrm{Lo}}$.

$$\phi^2_{\mathrm{Lo}} = 1.48623 \times 10^8 \left( \frac{x}{p} \right)^{0.96} + 1 \quad (8)$$

$p$ in Eq. (8) is the system pressure in $\mathrm{N/m^2}$ and $x$ is the steam quality of the steam-water flow. Equation (8) has been used in the present study. Paniagua et al. [7] validated their simulation results of the start-up transients of a SWNC loop by using Eq. (8).

**Moving Boundary Analysis of Boiling Channel.** The BC of the SWNC loop is modeled based on the moving boundary analysis by using finite volume method. In this moving boundary problem, both control volumes of $1-\phi$ zone and $2-\phi$ zone change with time. Accurate simulation of the problem requires sound mathematical techniques for solving relevant model equations. Solutions of moving boundary problems are generally found by moving-grid methods (MGMs) and fixed-grid methods (FGMs). Fixed numbers of computation grids are chosen in both methods. Li et al. [25] outlined the advantages and the disadvantages of each method. FGMs such as front-tracking methods [26,27], volume of fluid [28,29], and level-set method [30,31] enable one to work out the problems of surface-tracking, volume-tracking, accurate simulation of very complex interface. In contrast to FGMs, MGMs employ the algorithm of automatic grid refinements (grid redistributions) and offers power tool for relatively accurate treatment of boundary conditions at moving interface. One specific advantage of MGMs over FGMs is that the moving boundary (physical coordinates) coincides with numerical grids (computation coordinates), leading to more accurate prediction of very complex interface motion compared to that using FGMs. With mesh redistribution and transformation of computation coordinates to physical coordinates, MGMs allow more grids to be concentrated in the region of singularities [32]. Thus, they have been found to be very useful for the problems with localized dynamic singularities.

FGMs rely on logical coordinates spread over space, by which interface needs to be explicitly traced. Unlike MGMs, they get rid of rigorous computations of mesh redistribution, coordinate transformation, and grid generation at each time step [33]. Thus, they find efficient uses in real-time computations. Exploitation of sufficient computing time is not desired in a real-time LOCA simulation in which both time-step size and number of computational grids are required to be optimized to achieve acceptable accuracy and run the simulator in real time [5].

*Determination of Mixture Volumetric Flux* ($J_m$). Integrating both vapor mass and liquid continuity equations from $z=\lambda$ to $z=L$ (arbitrarily chosen) using Leibnitz's integral formula, one obtains the following equation for volumetric flux $J$:

$$J_m(L) = J_m(\lambda)\frac{\rho_l(\lambda)}{\rho_l(L)} + \Phi \quad (9)$$

where

$$J_m(L) = J_l(L) + J_g(L) \quad (10)$$

In Eq. (10), $J_l$ and $J_g$ are volumetric fluxes of liquid phase and vapor phase, respectively. By mathematical manipulation, $\Phi$ is found to substantially depend on $\Gamma_v$, velocity of boiling boundary $d\lambda/dt$, density change (if phase change takes place), and void propagation velocity. For single phase liquid, $J_l$ is expressed as

**Table 1 Ishii correlations for $C_0$ and $V_{gj}$**

| Flow regime | $V_{gj}$ | $C_0$ |
|---|---|---|
| Bubbly flow $(0<\alpha<0.25)$ | $\sqrt{2}\left(\frac{g\sigma(\rho_l-\rho_g)}{\rho_l^2}\right)^{1/4}(1-\alpha)^{1.75}$ | $\left(1.2-0.2\sqrt{\frac{\rho_g}{\rho_l}}\right)(1-e^{-18\alpha})$ |
| Slug flow | $0.35\left(\frac{g\sigma(\rho_l-\rho_g)}{\rho_l^2}\right)^{1/4}$ | $1.2-0.2\sqrt{\frac{\rho_g}{\rho_l}}$ |
| Churn flow | $\sqrt{2}\left(\frac{g\sigma(\rho_l-\rho_g)}{\rho_l^2}\right)^{1/4}$ | $1.2-0.2\sqrt{\frac{\rho_g}{\rho_l}}$ |

$$J_l(L) = J_l(\lambda)\frac{\rho_l(\lambda)}{\rho_l(L)} \tag{11}$$

*Drift-Flux Model and Computation of Mixture Mass Flux* ($G_m$). Drift flux represents the volumetric flux of a component relative to a surface moving at the average velocity. Zuber–Findlay's drift-flux formulation [34] gives the following expressions of $J_l$ and $J_g$:

$$\langle J_l\rangle = \langle 1-\alpha\rangle\langle v_l\rangle = (1-\alpha C_0)\langle J_m\rangle - \alpha V_{gj} \tag{12}$$

$$\langle J_g\rangle = \langle \alpha\rangle\langle v_g\rangle = \alpha C_0\langle J_m\rangle + \alpha V_{gj} \tag{13a}$$

In Eqs. (12) and (13*a*)–(13*c*), $\langle\cdot\rangle$ is the area average of a quantity and it is defined by

$$\langle v\rangle = \frac{1}{A}\int_A\int v(A)dA \tag{13b}$$

$C_0$ is the void-distribution coefficient and $V_{gj}$ is the drift velocity. $V_{gj}$ is defined as

$$V_{gj} = v_g - J_m \tag{13c}$$

Correlations for $V_{gj}$ and $C_0$ given by Ishii [3] have been used in the present work and the same are presented in Table 1 for various flow regimes. One may express $G_m(L)$ in the following form by combining Eqs. (10), (12), and (13*a*)–(13*c*):

$$G_m(L) = B_1(L)J_m(L) + B_2(L) \tag{14}$$

In Eq. (14), $B_1$ is defined by $\rho_l-\alpha C_0(\rho_l-\rho_g)$ and $B_2$ by $-\alpha V_{gj}(\rho_l-\rho_g)$. The expressions of $B_1(L)$ and $B_2(L)$ may be obtained by comparing Eq. (14) and the combined form of Eqs. (12) and (13*a*)–(13*c*). Now, Eq. (15) is obtained from Eqs. (9) and (14).

$$G_m(L) = B_2(L) + \left\{\frac{G_m(\lambda)-B_2(\lambda)}{B_1(\lambda)}\right\}\frac{\rho_l(\lambda)}{\rho_l(L)}B_1(L) + \Phi B_1(L) \tag{15}$$

*Calculation of Circulation Flow Rate*. As SG under investigation is natural circulating type, the flow is density driven. It depends on the difference between the density at the exit of the downcomer and that at the exit of RI. It is convenient to calculate the circulation flow rate $R$ (the liquid flow rate at the station a in Fig. 3) by using loop momentum balance equation derived in the following manner [5]. Now, one may obtain Eq. (16) for a flow in a closed loop by using Eq. (3) in various pressure nodes in the loop.

$$\sum_j L_j\frac{dG_{mj}}{dt} + \sum_j\left([G_g v_g + G_l v_l]_{j,\text{out}} - [G_g v_g + G_l v_l]_{j,\text{in}}\right) + \sum_j\frac{(4f_jL_j + k_j)|G_{mj}|G_{mj}}{2\rho_m D_{hj}} + \sum_j L_j\rho_{mj}g = 0 \tag{16}$$

The simplified forms of Eq. (16) are given below, which calculate the total loop momentum ($M_T$) of the fluid.

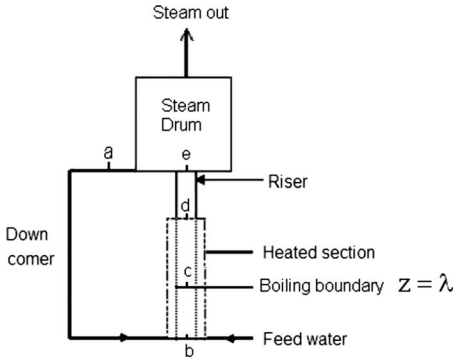


**Fig. 3 Nodalization of the SWNC loop**

$$\frac{dM_T}{dt} = -\Omega \tag{17}$$

$$\frac{dM_T}{dt} = \sum_j\frac{dG_{mj}L_j}{dt} \tag{18}$$

$\Omega$ accounts for the friction pressure drop, gravity force, and inertia force. $R$ is computed by using the value of $M_T$ determined from Eq. (17).

*Boiling Height* ($\lambda$) *Computation*. The 1-$\phi$ liquid height above which the liquid starts to boil is known as the boiling height. Complexities lie in determining $\lambda$ because of its moving nature. $\lambda$ changes during the start-up of a SWNC loop because of the change of $R$, enthalpy at the inlet of BC, system pressure, and heat input. A quasisteady state is assumed at the inlet boundary and the outlet boundary of the 1-$\phi$ zone. Based on FVM, the integral form of the resulting equation obtained by coupling 1-$\phi$ liquid energy balance equation and 1-$\phi$ continuity equation is given below.

$$\int_{\lambda_1(t)}^{\lambda_2(t)}\frac{\partial h}{\partial t}dz + \int_{\lambda 1(t)}^{\lambda 2(t)} v_l\frac{\partial h}{\partial z}dz = \int_{\lambda 1(t)}^{\lambda 2(t)} q_w dz \tag{19}$$

$q_w$ is the volumetric heat transfer rate to the 1-$\phi$ liquid zone and it is in W/kg. Now, 1-$\phi$ zone is divided into $N$ number of computational grids shown in Fig. 4. 1-$\phi$ liquid energy balance has been formulated based on the following assumptions: (1) The flow is incompressible and one dimensional, (2) viscous dissipation is negligible, (3) energy transfer due to molecular transport (conduction) is very small compared to that due to bulk flow, (4) energy involved due to pressure variation with time and, space is negligible, and (5) potential energy and kinetic energy are neglected. Assumptions (1) and (4) limit their validity in high-pressure and high-temperature applications. Equation (19) is integrated using Leibnitz's integral rule from $n=1$ to 2 (Fig. 4) to obtain Eq. (20)

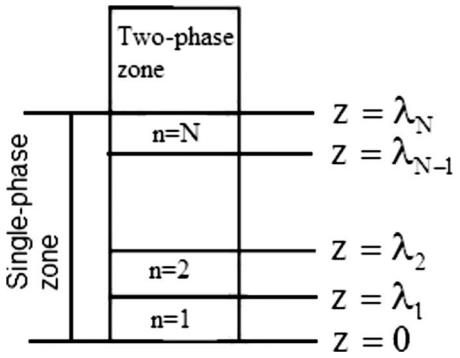


**Fig. 4 Computational cells in the single-phase zone**

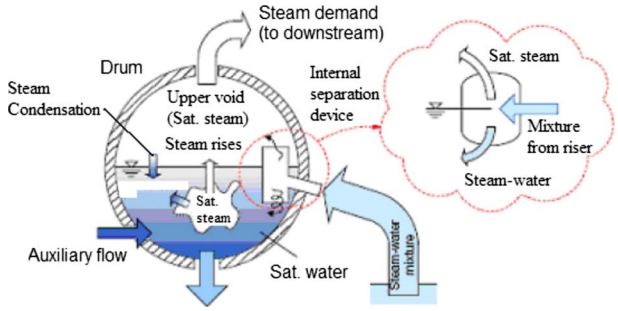


**Fig. 5 Steam drum (steam-water separator)**

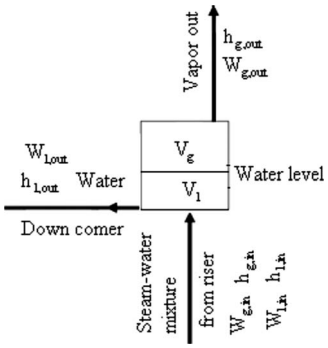


**Fig. 6 Schematic of steam-water separator**

based on the following assumptions: (1) Pressures at the inlet of BC and $q_w$ are quasisteady and (2) enthalpy change is linear from the inlet to the net vapor generation (NVG) point.

$$\frac{d\lambda_{n+1}}{dt} = 2v_l - \frac{2q_w(\lambda_{n+1} - \lambda_n)}{h_{n+1} - h_n} - \frac{d\lambda_n}{dt} \tag{20}$$

The number of the nodes ($N$) in the 1-$\phi$ liquid zone is based on the calculation of the critical frequency, which is defined as the ratio of $v_1$ at the BC inlet to $\lambda(0)$ [35]. Instead of assuming saturation enthalpy of liquid at the NVG point, liquid enthalpy at the point ($h_\lambda$) is computed from the phenomenological correlation of Saha and Zuber [36]. Paruya et al. [15] presented detailed derivation and dynamics of boiling boundary by introducing the concept of thermal nonequilibrium. For $n=1$ to $N$ nodes in single phase, $N$ numbers of ODEs obtained using Eq. (20) have been simultaneously solved by using implicit Euler's method [15].

*Void Fraction* ($\alpha$) *Calculation*. Given the value of $\Gamma_v$, $J_m$ in the, 2-$\phi$ region of BC can be readily obtained using Eq. (9). $v_g$ can then be evaluated using Eqs. (13*a*)–(13*c*). Finally, the result of integration of Eq. (2) computes $\alpha$ assuming $\alpha$ equal to zero at the NVG point.

*Pressure Calculation*. The local pressure at which nucleation occurs in BC is computed by solving mixture energy balance (Eq. (4)).

**Modeling of Steam Drum Level.** Dynamics of nonisothermal volume-type components such as nonisothermal constant stirred tank reactor (CSTR), nonisothermal mixing tank, nonisothermal separator, etc., are analyzed by overall mass balance (or component mass balance for multicomponent mixture) and overall thermal energy balance. The present model was formulated for water-level dynamics for drum-type boiler where steam bubbles rise through water with the help of the overall mass balance and overall energy balance along with drift-flux correlations. Kim et al. [37] showed that incorporation of the drift-flux model predicted properly the dynamics of level variation for the steam drum into which steam-water mixture enters at the bottom and rise of bubbles through water takes place. Bell and Astrom [38] studied the nonlinear dynamics of steam drum of natural-circulation boiler by solving nonlinear mass and energy balance equations. The steam-water separator drum under investigation is presented in Fig. 4(*a*). The bubble rise through water, as it happens in the present SD, is taken care of during modeling the drum by using the drift-flux model of Ishii [3]. In addition, the thermal capacitance of the drum-wall material was taken care of for more realistic simulation.

In the steam-water separator drum presented in Fig. 5, a saturated steam phase exists above the water level, and water and steam bubbles below the level. The internal separation device of efficiency of $\eta$ ($0 < \eta < 1$) is shown in Fig. 5. If $\eta$ is 1, the whole steam from RI goes to the upper part, which is intended for other applications. If $\eta=0$, the whole steam flows into the water phase. So, one may consider three control volumes: steam phase above the water level, water phase, and steam phase below the level. The following material balance equations (Eqs. (21)–(23)) and overall internal energy balance equation (Eq. (24)) may be given by assuming no auxiliary flow. For material balance, two control volumes were considered inside the drum (one above the water level and another below the level), while for energy balance, one control volume for the whole volume of the drum was considered. Based on the schematic of the SD (Fig. 6), the following model equations for the SD are presented.

In steam-phase mass balance above the water level,

$$V_T \frac{d(\rho_g \alpha_D^+)}{dt} = \eta W_{g,\text{in}} + W_{g,i} - W_{g,\text{out}} \tag{21}$$

In steam-phase mass balance below the water level,

$$V_T \frac{d(\rho_g \alpha_D^-)}{dt} = (1-\eta) W_{g,\text{in}} - W_{g,i} - W_c \tag{22}$$

In water-phase mass balance below the water level,

$$V_T \frac{d[\rho_l(1-\alpha_D^- - \alpha_D^+)]}{dt} = W_{l,\text{in}} + W_c - W_{l,\text{out}} \tag{23}$$

In overall enthalpy energy balance equation,

$$V_T \frac{d[\rho_l(1-\alpha_D^- - \alpha_D^+)h_l + \rho_g(\alpha_D^- + \alpha_D^+)h_g]}{dt}$$

$$= W_{l,\text{in}} h_{l,\text{in}} - W_{l,\text{out}} h_{l,\text{out}} + V_T \frac{dp}{dt} - m_w C_w \frac{dT_w}{dt} \tag{24}$$

In Eqs. (21)–(24), $\alpha_D^-$ and $\alpha_D^+$ are steam volume fractions below the water level $\chi$ and above, respectively. $V_T$ is the total volume of the drum. $W_{l,\text{in}}$ and $W_{l,\text{out}}$ are water mass flow rates to the drum and from the drum, respectively, and $W_{g,\text{in}}$ and $W_{g,\text{out}}$ are steam mass flow rates to the drum and from the drum, respectively. $W_{g,i}$ is the steam rising rate through the interface. $h_{l,\text{in}}$ and $h_{l,\text{out}}$ are water enthalpies at the drum inlet and at the drum outlet, respectively, and $h_{g,\text{in}}$ and $h_{g,\text{out}}$ are steam enthalpies at the drum inlet and at the drum outlet, respectively. $C_w$ is the thermal capacitance of the drum-wall material, $T_w$ is the drum-wall temperature, and $m_w$ is the mass of the drum material.

Calculation of $\alpha^-$ requires the drift-flux relation given by Eqs. (13*a*)–(13*c*). From Eqs. (13*a*)–(13*c*) one obtains

$$v_g = \frac{J_g}{\alpha_D^-} = V_{gj} + C_0 J_m = V_{gj} + C_0(J_g + J_l) \tag{25}$$

So, one obtains from the above equation,

$$J_g = \frac{\alpha_D^-(V_{gj} + C_0 J_l)}{1 - C_0 \alpha_D^-} \tag{26}$$

In the steam flow rate across $W_{g,i}$, the level interface is given by

$$W_{g,i} = A_i \rho_g \left( J_g - \frac{d\chi}{dt} \right) \tag{27}$$

The condensation rate $W_c$ is given by

$$W_c = \frac{1}{h_{fg}} \left\{ \alpha_D V_T \rho_g \frac{dh_g}{dt} + \rho_l [V_T (1 - \alpha_D)] \frac{dh_l}{dt} + V_T \frac{dp}{dt} - m_w C_w \frac{dT_w}{dt} \right\} \tag{28a}$$

where the total volume fraction of the steam with respect to the total volume drum $\alpha_D$ is given by

$$\alpha_D = \alpha_D^+ + \alpha_D^- \tag{28b}$$

Simultaneous solution of Eqs. (21), (22), and (24) gives $p$, $\alpha_D$. The overall mass balance equation and overall internal energy balance equation are the ODEs of stiff nature. The stiff nature is due to the nonlinear variation of saturation properties $(\rho, h)$ of water and steam with pressure or temperature. For solving those stiff equations, multistep Gear's method [39] was found to be more suitable than the implicit Runge–Kutta method because of the provision in the former method for calculating step size based on the criteria that compromise between stability and convergence.

Now, the water-level (surface) movement is computed based on the water-volume balance as presented below:

$$A_i \frac{d\chi}{dt} = \frac{W_{l,\text{in}}}{\rho_{l,\text{in}}} + \frac{W_{g,\text{in}}}{\rho_{g,\text{in}}} - \frac{W_{l,\text{out}}}{\rho_{l,\text{out}}} - \frac{\eta W_{g,\text{in}}}{\rho_{g,\text{in}}} - \frac{W_{g,i}}{\rho_g} \tag{29}$$

## Solution Scheme

The solution schemes of field equations for a two-phase flow are well addressed in literatures [40–42] in which implicit and semi-implicit schemes using FDM have been detailed. In the present work of the moving boundary analysis, and FVM scheme followed by multistep Gear's method for stiff ODEs has been proposed. Multistep Gear's method has been outlined in the Appendix.

**Overall Solution Scheme.** For the overall solution scheme for a large set of model equations, modular approach has been adopted. The sequential steps are presented below, showing the computational algorithm in new time step.

(1) Given boundary conditions (heat flux) and given initial conditions computed at previous time step.
(2) Calculation of heated-wall temperature, boiling heat flux, and convective heat flux to single phase.
(3) Solution of boiling boundary model in BC using Eq. (20).
(4) Calculation of $\Gamma_v$.
(5) Solution of model equations (equations of mass, momentum, and energy) of BC for $(J_m, p, h_l, h_g, \alpha)$ for two-phase flow and for $(v_l, p, h_l)$ for single-phase liquid flow. Single-phase zone and two-phase zone are separately solved by using and implicit scheme of Gear's method. The stiff ODE set is obtained for a computation grid by integrating finite-volume forms of conservation equations using Leibnitz's rule. For a two-phase flow, Eqs. (1)–(5) have been simultaneously solved.
(6) Solution of model equations (equations of single-phase liquid mass, momentum, and energy) of downcomer for $(v_l\ p\ h_l)$.
(7) Solution of loop momentum balance equations (Eqs. (17) and (18)) for $R$.
(8) Calculation of local mass flow rate and velocities of phases using Eqs. (12), (13*a*)–(13*c*), and (15).
(9) Solution of model equations (Eqs. (21), (22), and (24)) for the SD for $(p, \alpha_D)$ by Gear's method.

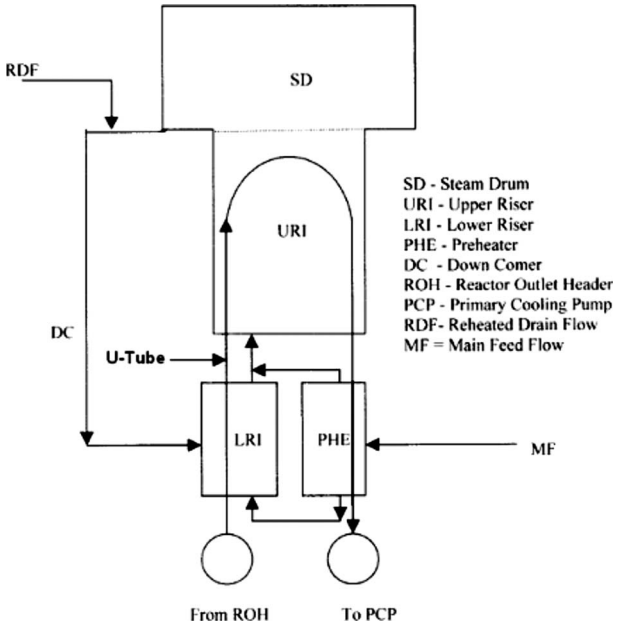


**Fig. 7 Schematic diagram of the nuclear steam generator loop**

## Results and Discussion

**Description of Nuclear Steam Generator Loop.** In the Kaiga-1 preheat SG whose schematic is presented in Fig. 7 and its simplified scheme shown in Fig. 1, pressurized heavy water flows through the U-tube heat exchanger of the primary side and gives up its heat to the light water, which flows over the tubes in the shell side. The two legs of the U-tube bundle are known as hot leg and cold leg, the former being the leg in which the primary fluid is at a relatively higher temperature than that of the fluid in the latter. Demineralized feed water (approximately 90% of total feed water flow) is preheated in the heat exchanger or preheater located at the bottom of the cold-leg side of the tubes. In the preheater section, the feed water flow is equally split into two parts. One part flows upward and the other part downward. This lower part of the flow then mixes with the recirculating water from the downcomer and the resulting mixture enters the lower riser (LRI) section (the main boiling section of the SG). The upward portion of the flow from the preheater gets mixed with all the fluid coming from the LRI of the SG and enters the upper riser (URI). Maximum heat transfer from the tube side to the shell side takes place in this URI and a steam-water mixture with high void fraction exits from the top of the URI. The saturated water from the SD is recirculated through the downcomer after mixing with about 10% feed water (auxiliary feed) and reheated drain flow in the upper downcomer region. It is required to mention that HS of this SG consists of LRI and a part of URI, which add to get a height of U-tube. The rest of URI was treated as adiabatic section.

**Simulation Results.** Given the system configuration (Fig. 1 and Table 2) and initial conditions (Table 3), the SG of an Indian NPP (Kaiga-1) was allowed to be steaming up from the ambient temperature of 25 °C and pressure of 6.0 bars. Total mass inventory in the SG was kept unchanged. One may note that no feed water was allowed to flow into SG because the present work caters to only initial phase of the start-up of SG and no strategy for drum-level control was adopted. The present investigation reports the open-loop response of SG subjected to heating-power ramp. The power factor is ramped up at the rate of 0.1%/s. HS was assumed to uniformly receive the heat at periphery, and the total amount of heat received by the section linearly changes with axial length exposed to the heating medium. The computed results are shown in Figs. 5–11 from the instant just before the inception of vapor.

**Table 2 Geometrical configuration of SG loop**

| Sl. No. | Item | Dimension |
|---|---|---|
| 1 | SD length | 4.585 m |
| 2 | SD diameter | 2.4 m |
| 3 | Total length of RI and HS | 12.11 m |
| 4 | Diameter of RI and HS | 1.343 m |
| 5 | Down comer length | 12.11 m |
| 6 | Down comer diameter | 0.8320 m |

Figure 8 shows variation of SG pressure in terms of SD pressure. The rate of pressurization depends on the heating rate in this study. However, numerical experiment shows that the stability of the system improves at high pressures. The variation of the 2-$\phi$ level in SD is presented in Fig. 9. Given the constant inventory in SG, SD level variation indicates 2-$\phi$ swelling (volume expansion due to bubble nucleation) and collapse (condensation of steam bubbles due to subcooled water) in BC of the SG loop and it is consistent with the progressive change of $\alpha$ (Fig. 11). The phenomena of two-phase swelling and collapse were experimentally observed by Poon [4], maintaining constant total mass inventory of the loop. Poon also measured the degree of swelling or collapse by SD level indication in real-time operation. The variation of net steam generation rate (NSGR) presented in Fig. 10 reflects that the steam generation rate remains approximately unchanged between 21 s and 32 s, and beyond 32 s, it rises again. This is explained by the fact that high $R$ during the period (Fig. 13) causes the liquid temperature to drop (bubble condensation enhanced) despite the increased heat input and so $\alpha$ in BC decreases. Furthermore, $R$ diminishes because of the void dependency of the driving force due to density difference. The liquid temperature again starts to rise when the flow goes down below a certain value and NSGR again increases.

**Table 3 Initial conditions and other parameters**

| Sl. No. | Item | Values |
|---|---|---|
| 1 | Initial pressure | 6.0 bars |
| 2 | Initial temperature | 25°C |
| 3 | Initial SD level | 0.64 m |
| 4 | Time step | 10 ms |
| 5 | Power (100%) | 188.0 MW |
| 6 | Pressure at 100% power | 41.0 bars |
| 7 | Feed water flow rate at 100% power | 92.35 kg/s |
| 8 | Feed water temperature at 100% power | 148.0°C |
| 9 | Recirculation ratio at 100% power | 3.6 |
| 10 | Power factor ramp-up rate | $10^{-3}$/s |
| 11 | Bubble diameter | $10^{-3}$ m |

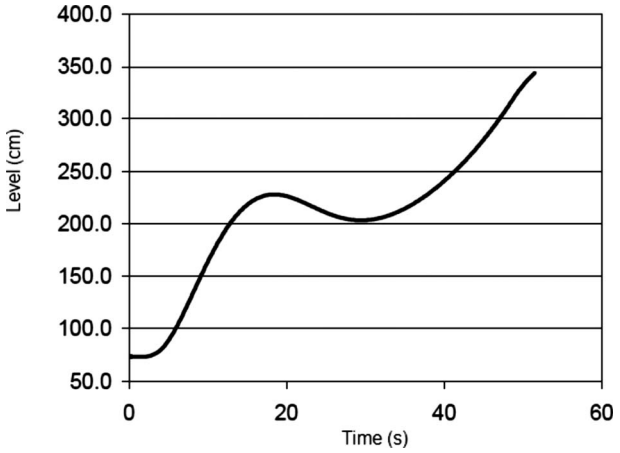


**Fig. 9 Variation of the steam drum level**

The variation of $\alpha$ in the channel is shown in Fig. 11. Increase or decrease in $\alpha$ explains the reason of 2-$\phi$ swelling or collapse. The swelling effect allows the 2-$\phi$ level in SD to rise and the bubble-collapse causes the decrease in the level. It is important to note in Fig. 11 that at 23.5 s, $\alpha$ starts to decrease after reaching a high value of 0.676. Decrease in $\alpha$ is due to the temperature drop of fluid caused by high circulation flow. Figure 12 shows the variation of boiling height, and this variation starts at 2.2 s after the start of the simulation. At this instant of time, a boiling phenomenon starts. The starting value of the boiling height (3.04 m) was calculated by using Eq. (20) in the steady-state form, which has been obtained by equating the time-derivative term to zero. With this starting value, computation of the boiling height by using dynamic model (Eq. (20)) was carried out. The figure also indicates that the variation is mostly due to the hydrodynamic effect although both hydrodynamic effect and thermal effect are present. The change is consistent with the variation of circulation flow, which is presented in Fig. 13. However, the boiling boundary is about to disappear after 49.5 s because of inappreciable subcooling effect at the inlet of BC. It is worthwhile to mention

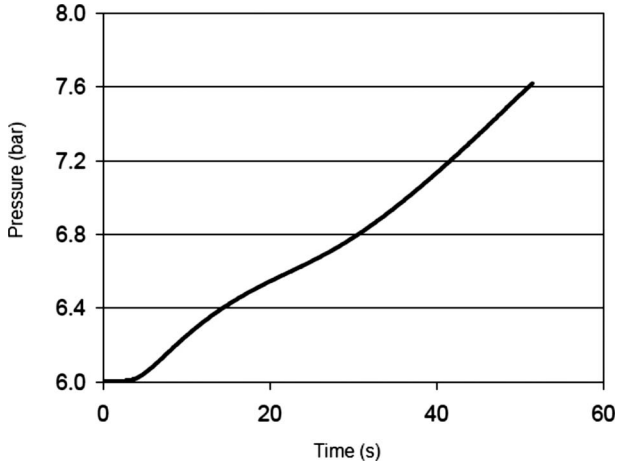


**Fig. 8 Variation of the steam drum pressure**

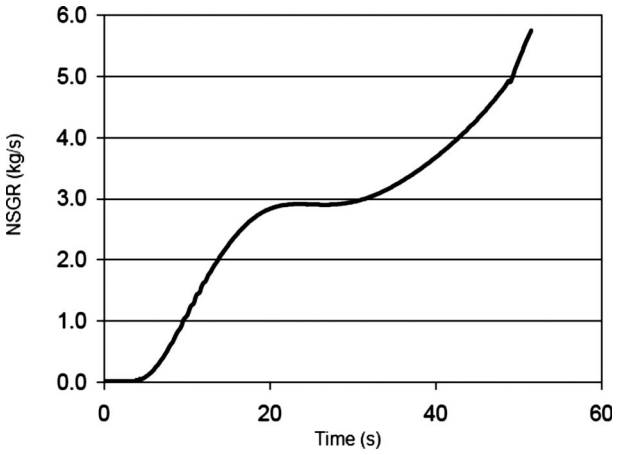


**Fig. 10 Variation of the net steam generation rate**

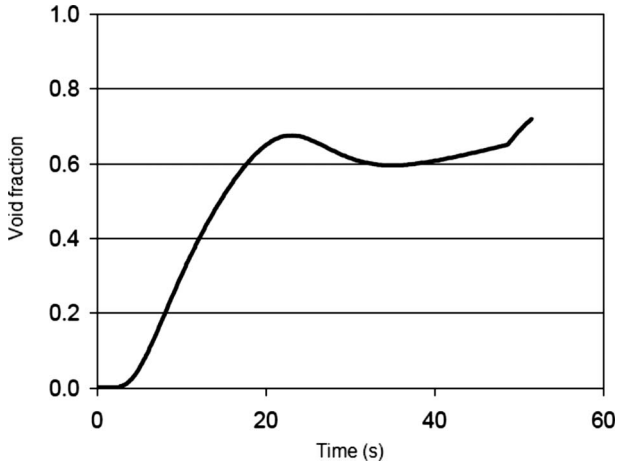


**Fig. 11 Variation of void fraction in riser**

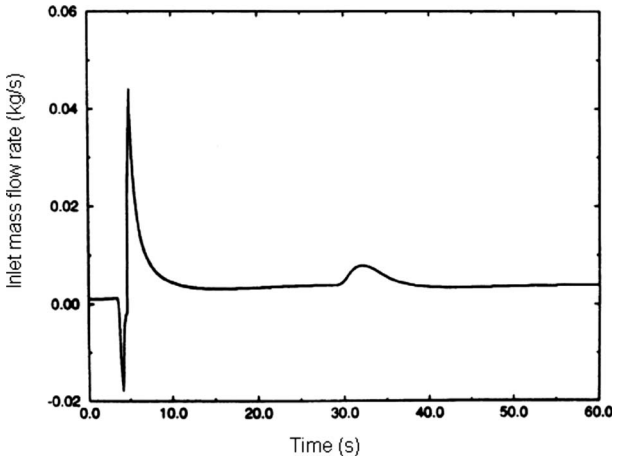


**Fig. 14 Channel inlet mass flow rate at 3 atm, 6 kW, and 60°C inlet subcooling [7]**

that after 49.5 s, the boiling height becomes negligibly small (of the order of 15–25 mm as the numerical results were examined) for which it is not reflected in the plot (Fig. 12). Due to low subcooling, bubbles rigorously form in BC increasing buoyancy force and circulation flow rate steeply increases after 49.5 s (Fig. 13).

In Fig. 13, the circulation flow (flow rate at station a in Fig. 3)

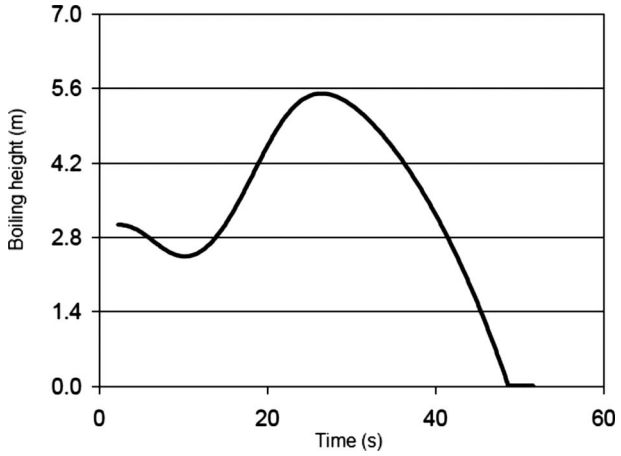


**Fig. 12 Variation of boiling height**

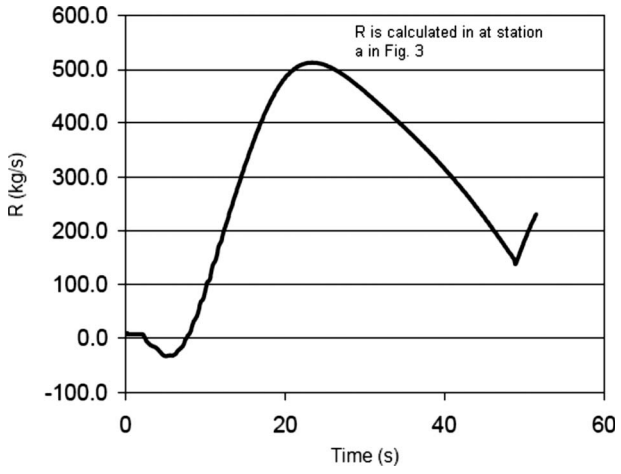


**Fig. 13 Variation of circulation flow rate in the SWNC loop**

starts to decrease at the time of bubble inception in BC due to increased frictional pressure drop of the 2-$\phi$ mixture flow compared to that of the 1-$\phi$ flow when the driving force for circulation has not increased enough initially. At a particular instant, the circulation flow becomes reverse, which is an unsafe operation region experimentally observed by Poon [4]. Walter and Linzer [43,44] also identified flow-reversal phenomenon during the start-up of a natural-circulation boiler as a result of uneven distribution of heat in BCs. Paniagua et al. [7] observed the flow-reversal phenomenon during the start-up of a laboratory-scale single-loop natural-circulation system at various operating pressures (3 atm and 5 atm) based on the computation with TWOPHASE code developed by them. As a result of the computation, Figs. 14 and 15 are presented, which show time-dependent variation of the inlet flow rate to the heated channel (these flows are from the downcomer). Each of the variations indicates the reverse flow as the bubbles incept in BC. In the figures, it is also important to note that given the condition of a heating rate of 6 kW and an inlet subcooling of 60°C, the extent of the flow reversal decreases with pressure. This is due to the fact that the difference between liquid density and vapor density significantly varies with pressure. Influence of buoyancy force, therefore, reduces with pressure. So, one may clearly conclude that the stability nature of the natural-circulation loop improves with an increase in operating pressure. The limitations of the theoretical investigation carried out by Paniagua et al. [7] are that they assumed the vapor temperature at the

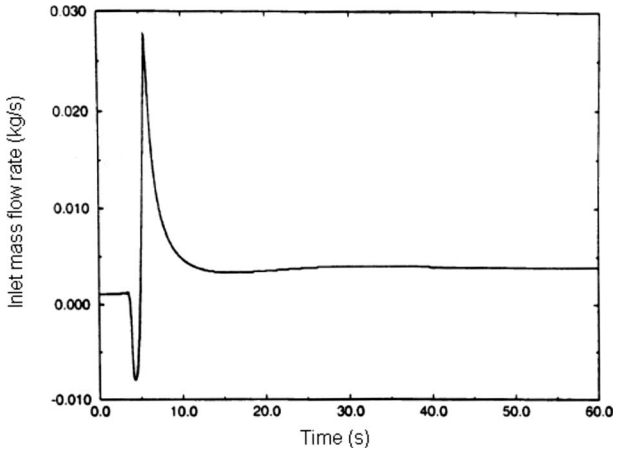


**Fig. 15 Channel inlet mass flow rate at 5 atm, 6 kW, and 60°C inlet subcooling [7]**

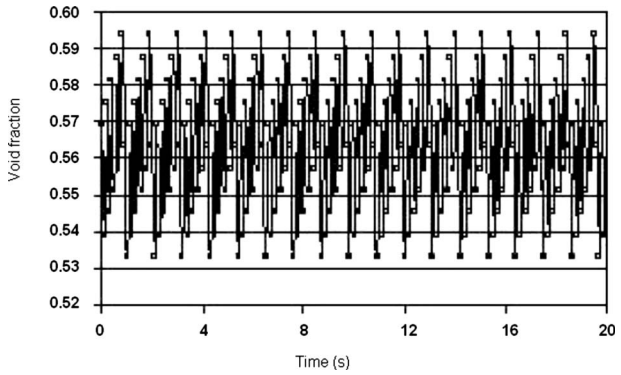


**Fig. 16 DWO in RI at 50% steady-power level**

state of saturation (a four-equation scheme was used) and adopted fixed-boundary method that uses FDM for the solution of model equations.

In the present study, the flow-reversal phenomenon is observed to be an overall result of thermal-hydraulic effects as experienced in the SWNC loop. The unique modeling features as adopted in the present study and the subsequent solutions of PDEs using FVM can clearly describe the flow reversal observed experimentally and theoretically. This evidently indicates the usefulness of the proposed model equations. It is also observed that as SG gets pressurized, flow-reversal phenomenon dies out. So, the present study evidently establishes the fact that the system stability improves with the progress of pressurization and confirms the observations of Paniagua et al.. It is also important to note in Fig. 13 that after 6.1 s, $R$ starts to increase due to increased buoyancy force (as the void fraction rapidly increases). When $R$ reaches a high value of 512.6 kg/s, frictional pressure drop becomes dominant over the pressure drop due to gravity (buoyancy force) and $R$ starts to decrease at 23.5 s. As mentioned earlier, at the same instant of 6.1 s, $\alpha$ also reaches a high value and starts to decrease at 23.5 s. It, therefore, can be mentioned that time-dependent variations of $\alpha$ and $R$ take place without time delay and they are strongly coupled.

At a 50% steady power level (critical heating rate), DWO (in terms of $\alpha$-variation in RI) is found to originate and presented in Fig. 16. Increased heating rate has led to such kind of oscillations even enough pressurization of SG has been achieved. This indicates that the system stability is sensitive to the heating rate too. Regarding the identification of DWO, literature reviews suggest that there are three kinds of DWOs: flashing-induced DWO [8,9,13,45], Type-I DWO, and Type-II [46,47]. Flashing types take place at low pressures and are induced by increased vapor generation as a result of change of saturation enthalpy of liquid with pressure (which is particularly experienced in an RI in which the hydrostatic head reduces as the fluid flows upward). Type-I DWO occurs at low flow qualities, in which gravitational pressure drop becomes dominant. Type-II DWO takes place at high flow qualities, in which frictional pressure drop becomes dominant. So, the observed DWO in the present investigation falls within the familiar group of Type-I DWO. Simulation results at the critical heating rate also indicate that the flow quality is not so significant to cause Type-II DWO to induce and more importantly, the system pressure is fairly large enough to restrict flashing-induced DWO to occur. The observed DWO are also self-sustained due to the thermohydraulic feedbacks and are of high frequency. In addition, some secondary oscillations are also observed, which are not necessarily periodic.

## Conclusions

The proposed study reveals that the start-up operation of SWNC loop progresses through various instability phenomena like flow reversal and DWO as a result of impressing power ramp. As bubbles incept in BC, the flow reversal occurs but it cannot persist due to the SG pressurization, indicating the improvement of system stability with pressure. At a critical heating rate of 50% of steady power level, DWO is observed. So, the study shows that the stability of SWNC loop is influenced by pressure and heating rate. In addition to that, the developed model is capable of predicting two-phase swelling and collapse for a given inventory. Variation of the 2-$\phi$ level is consistent with progressive variation of void fraction. Both circulation flow variation and 2-$\phi$ level variation are found to have strong functionality of $\alpha$ in the BC. It is also important to mention that nonhomogeneous and nonequilibrium model gives better predictions of the phenomena that occur during the start-up operation of the loop, which were not considered in the previous study carried out by the authors [6] using HEM and simplified quasisteady model for boiling boundary which could not explain density-wave instabilities. It is, however, felt that there is enough scope for improving the model equations so that they can explain geysering phenomenon. Although the study reveals the possibility of Type-I DWOs, experimental investigation on the characterization of the density-wave instabilities obtained is still required to determine numerical uncertainties of the present model.

## Acknowledgment

The authors are highly grateful to M/s Flotherm Consultants (P) Limited, Kolkata for extending their help by providing some valuable information for this study, particularly the geometry of the SG under investigation.

## Nomenclature

$A$ = area of cross section, $m^2$
$C_0$ = void-distribution parameter, dimensionless
$C$ = thermal capacitance, J/kg K
$D$ = diameter of the flow channel, m
$f$ = Fanning's friction factor, dimensionless
$\mathbf{F}$ = vector of functions defined in Eq. (A2)
$G$ = mass flux, $kg/m^2$ s
$g$ = acceleration due to gravity, 9.81 $m/s^2$
$h$ = enthalpy, J/kg
$\mathbf{I}$ = identity matrix
$h_{fg}$ = latent heat of vaporization, J/kg
$J$ = volumetric flux, $m^3/m^2$ s
$(\partial \mathbf{F}/\partial \mathbf{Y})$ = Jacobian matrix
$k$ = loss coefficient, dimensionless
$L_j$ = length as shown in Fig. 2, m
$m_w$ = metal mass of steam drum, kg
$M$ = momentum, kg $m/m^2$ s
$N$ = number of computation cells in single-phase liquid zone, dimensionless
$p$ = pressure, $N/m^2$
$\Delta p_{Tf}$ = total frictional pressure drop, $N/m^2$
$\Delta p_{fT}$ = total frictional pressure drop per unit length, $N/m^3$
$Q$ = heat transfer rate, $W/m^3$
$q$ = heat transfer rate, W/kg
$q''$ = heat flux ($W/m^2$)
$R$ = circulation flow rate, kg/s
$T$ = temperature, K
$t$ = time, s
$V$ = volume, $m^3$
$V_{gj}$ = drift velocity, m/s
$v$ = phase velocity, m/s
$W$ = mass flow rate, kg/s
$x$ = flow quality, dimensionless
$\mathbf{Y}$ = vector of variables to be solved
$y$ = = variables to be solved

$z$ = axial length, m

**Greek**

$\alpha$ = void fraction, dimensionless
$\eta$ = separation efficiency, dimensionless
$\Gamma_v$ = net vapor generation rate, $kg/m^3\,s$
$\Gamma_{boil}$ = vapor generation rate due to boiling, $kg/m^3\,s$
$\Gamma_{cond}$ = vapor condensation rate, $kg/m^3\,s$
$\rho$ = density, $kg/m^3$
$\lambda$ = boiling height, m; eigenvalue
$\chi$ = water level in steam drum, m
$\phi^2_{Lo}$ = two-phase multiplier, dimensionless
$\Delta$ = differential

**Subscripts**

$D$ = drum
$l$ = liquid
$g$ = vapor
$h$ = hydraulic
$i$ = interface
$j$ = pressure node/computation node
$k$ = iteration counter, integers
$m$ = mixture
$n$ = node no.
$T$ = total
$\lambda$ = boiling boundary
$w$ = wall
in = inlet/inflow
out = outlet/outflow

**Superscripts**

$+$ = above water level
$-$ = below water level

**Abbreviations**

DWO = density-wave oscillation
SWNC = steam-water natural circulation
FVM = finite volume method

## Appendix

Multistep Gear's method. It is supposed that the following stiff ODE set is to be integrated using implicit Euler scheme. Gear [39] outlined the following method to solve the system.

$$\frac{dy_1}{dt} = f_1(y_1, y_2) \tag{A1a}$$

$$\frac{dy_2}{dt} = f_2(y_1, y_2) \tag{A1b}$$

Now considering $\mathbf{Y} = \begin{bmatrix} y_1 \\ y_2 \end{bmatrix}$ and $\mathbf{F} = \begin{bmatrix} f_1 \\ f_2 \end{bmatrix}$, the above ODE set may be reduced to

$$\frac{d\mathbf{Y}}{dt} = \mathbf{F} \tag{A2}$$

The backward difference formula of $d\mathbf{Y}/dt$ is given by

$$\left(\frac{d\mathbf{Y}}{dt}\right)_{k+1} = \frac{\mathbf{Y}_{k+1} - \mathbf{Y}_k}{\Delta t} \tag{A3}$$

$$\mathbf{Y}_{k+1} = \mathbf{Y}_k + \Delta t\left(\frac{d\mathbf{Y}}{dt}\right)_{k+1} = \mathbf{Y}_k + \Delta t\mathbf{F}_{k+1} \tag{A4}$$

Linearizing $\mathbf{F}$, one obtains

$$\mathbf{F}_{k+1} = \mathbf{F}_k + \left(\frac{\partial \mathbf{F}}{\partial \mathbf{Y}}\right)_k (\mathbf{Y}_{k+1} - \mathbf{Y}_k) \tag{A5}$$

$\left(\frac{\partial \mathbf{F}}{\partial \mathbf{Y}}\right)_k$ in Eq. (A5) is the Jacobian matrix and defined as follows:

$$\left(\frac{\partial \mathbf{F}}{\partial \mathbf{Y}}\right)_k = \begin{bmatrix} \left(\frac{\partial f_1}{\partial y_1}\right)_k & \left(\frac{\partial f_1}{\partial y_2}\right)_k \\ \left(\frac{\partial f_2}{\partial y_1}\right)_k & \left(\frac{\partial f_2}{\partial y_2}\right)_k \end{bmatrix} \tag{A6}$$

Now, substituting the linearized form of $\mathbf{F}_{k+1}$ in Eq. (A5) and doing mathematical manipulation further, one solves

$$\mathbf{Y}_{k+1} = \frac{\mathbf{Y}_k\left[\mathbf{I} - \Delta t\left(\frac{\partial \mathbf{F}}{\partial \mathbf{Y}}\right)_k\right] + \Delta t\mathbf{F}_k}{\mathbf{I} - \Delta t\left(\frac{\partial \mathbf{F}}{\partial \mathbf{Y}}\right)_k} \tag{A7}$$

$\mathbf{I}$ is the identity matrix. Equation (A7) clearly indicates that if $\Delta t \to \infty$, $\mathbf{Y}_{k+1} \to 0$, and the scheme is absolutely stable for linear system. Selection of integration interval ($\Delta t$) is also a crucial as the numerical error of solution with respect to the exact solution, and the solution stability is concerned. If $\lambda$'s are the eigenvalues of $(\partial \mathbf{F}/\partial \mathbf{Y})_k$, $[1 - \Delta t\lambda]^{-1}$ are the eigenvalues of $[\mathbf{I} - \Delta t(\partial \mathbf{F}/\partial \mathbf{Y})_k]^{-1}$ and $|[1 - \Delta t\lambda]^{-1}|$ is less than unity. Equation (A7) clearly indicates that if $\Delta t \to \infty$, $\mathbf{Y}_{k+1} \to 0$, and the scheme is absolutely stable for linear or linearized systems at the cost of low-order accuracy. Gear [39] also determined the criterion for time-step size for desired accuracy and stability based on which the step size for future time can be predicted.

## References


[1] Ranson, V. H., and Wagner, R. J., 1984, RELAP5/MOD2 Manual, EGG-SAM-6377, INEL, Id, Apr.
[2] Lahey, R. T., Jr., and Moody, F. J., 1993, *The Thermal-Hydraulics of a Boiling Water Nuclear Reactor*, 2nd ed., American Nuclear Society Press, Lagrange Park, IL.
[3] Ishii, M., 1977, "One-Dimensional Drift-Flux Model and Constitutive Equations for Relative Motion Between Phases in Various Two-Phase Flow Regimes," Argonne National Laboratory, Report No. ANL-77-47.
[4] Poon, K. L., 1975, "Effect of Rapid Steam Take-Off in Natural Circulation and Water Level in Boiling," ASME J. Eng. Power, **97**, pp. 645–654.
[5] Paruya, S., Dhur, G. M., Guha, C., and Saha, P., 1998, "Documentation of Kaiga-1 Real-Time LOCA Simulation Software I: Simulation Methodologies," Flotherm Consultants (p) Ltd., Kolkata, India, Dec.
[6] Paruya, S., and Bhattacharya, P., 2004, "Simulation of the Effect of Boiling Boundary on Startup Performance of a Steam Generator," *Proceedings of National Seminar on Technology Upgradation in Process Industries*, Haldia Institute of Technology, Haldia, India, Aug. 6.
[7] Paniagua, J., Rohatgi, U. S., and Prasad, V., 1999, "Modeling of Thermal Hydraulic Instabilities in Single Heated Channel Loop During Startup Transients," Nucl. Eng. Des., **193**, pp. 207–226.
[8] Manera, A., 2003, "Experimental and Analytical Investigations on Flashing-Induced Instabilities in Natural Circulation Two-Phase Systems—Applications to the Startup of Boiling Water Reactors," Ph.D. thesis, Delft University of Technology, Delft, Netherlands.
[9] Furuya, M., Inadaa, F., and van der Hagen, T. H. J. J., 2005, "Flashing-Induced Density Wave Oscillations in a Natural Circulation BWR—Mechanism of Instability and Stability Map," Nucl. Eng. Des., **235**, pp. 1557–1569.
[10] Li, B., Chen, T., and Yang, D., 2005, "DBSSP—A Computer Program for Simulation of Controlled Circulation Boiler and Natural Circulation Boiler Start Up Behavior," Energy Convers. Manage., **46**, pp. 533–549.
[11] Frepoli, C., Mahaffy, J. H., and Hochreiter, L. E., 2002, "A Moving Subgrid Model for Simulation of Reflood Heat Transfer," *Proceedings of Tenth International Conference on Nuclear Engineering*, Arlington, VA, Apr. 14–18.
[12] Chang, C.-J., and Lahey, R. T., 1997, "Analysis of Chaotic Instabilities in Boiling Systems," Nucl. Eng. Des., **167**, pp. 307–334.
[13] van Bragt, D. D. B., de Kruijf, W. J. M., Manera, A., van der Hagen, T. H. J. J., van Dam, H., 2002, "Analytical Modeling of Flashing-Induced Instabilities in a Natural Circulation Cooled Boiling Water Reactor," Nucl. Eng. Des., **215**, pp. 87–98.
[14] Lee, J. D., and Pan, C., 2005, "Nonlinear Analysis for a Double-Channel Two-Phase Natural Circulation Loop Under Low-Pressure Conditions," Ann. Nucl. Energy, **32**, 299–329.
[15] Paruya, S., and Bhattacharya, P., 2006, "A Moving Boundary Problem in Steam Generator-Choice of Suitable Solution Method," *Proceedings of National Conference on Advances in Energy Research*, IIT, Mumbai, India, Dec. 5–6.
[16] Wallis, G. B., 1969, *One-Dimensional Two-Phase Flow*, McGraw-Hill, New York.
[17] Ishii, M., 1975, *Thermo-Fluid Dynamic Theory of Two-Phase Flow*, Eyrolles, Paris.
[18] Drew, D. A., 1983, "Mathematical Modeling of Two-Phase Flow," Annu. Rev.

Fluid Mech., **15**, pp. 261–291.
[19] Boure, J. A., and Delhaye, J. M., 1982, "General Equations and Two-Phase Flow Modeling," *Handbook of Multiphase Systems*, G. Hedsorni ed., McGraw-Hill, New York.
[20] Bird, R. B., Stewart, W. E., and Lightfoot, E. N., 1960, *Transport Phenomena*, Wiley, New York.
[21] Fanning, J. T., 1877, *A Practical Treatise on Water-Supply Engineering*, Van Nostrand, New York.
[22] Lockhart, R. W., and Martinelli, R. C., 1949, "Proposed Correlation of Data for Isothermal Two Phase, Two Component Flow in Pipes," Chem. Eng. Prog., **45**, pp. 39–48.
[23] Collier, J. G., 1972, *Convective Boiling and Condensation*, McGraw-Hill, London.
[24] Becker, K., Hernborg, M., and Bode, M., 1962, "An Experimental Study of Pressure Gradients for Flow of Boiling Water in Vertical Round Duct," January, Parts 1–3, AE 69, 70 and, 85, AB Atomenergi, Studsvik.
[25] Li, J., Hesse, M., Ziegler, J., and Woods, A. W., 2005, "An Arbitrary Lagrangian Eulerian Method for Moving-Boundary Problems and Its Application to Jumping Over Water," J. Comput. Phys., **208**, pp. 289–314.
[26] Unverdi, S. O., and Tryggvason, G., 1992, "A Front-Tracking Method for Viscous, Incompressible, Multi-Fluid Flows," J. Comput. Phys., **100**, pp. 25–37.
[27] Tryggvason, G., Bunner, B., Esmaeeli, A., Juric, D., Al-Rawahi, N., Tauber, W., Han, J., Nas, S., Jan, Y.-J., 2001, "A Front-Tracking Method for the Computations of Multiphase Flow," J. Comput. Phys., **169**, pp. 708–759.
[28] Hirt, C. W., and Nichols, B. D., 1981, "Volume of Fluid (VOF) Method for the Dynamics of Free Boundaries," J. Comput. Phys., **39**, pp. 201–225.
[29] Ride, W. J., and Kothe, D. B., 1998, "Reconstructing Volume Tracking," J. Comput. Phys., **141**, pp. 112–152.
[30] Osher, S. J., and Fedkiw, R., P., 2002, *Level Set Methods and Dynamic Implicit Surfaces*, Springer-Verlag, Berlin.
[31] Sethian, J. A., 1996, *Level Set Methods and Fast Marching Methods: Evolving Interfaces in Geometry, Fluid Mechanics, Computer Vision, and Material Science*, Cambridge University Press, Cambridge.
[32] Tan, Z., Tao, T., and Zhang, Z., 2006, "A Simple Moving Mesh Method for One- and Two-Dimensional Phase-Field Equations," J. Comput. Appl. Math., **190**, pp. 252–269.
[33] LeVeque, R., Russell, R. D., and Ruuth, S., 2003, *Conference on Computational Techniques for Moving Interfaces*, Banff, AB, Canada, Aug. 23–28, Final Report.
[34] Zuber, N., Findlay, J. A., 1965, "Average Volumetric Concentration in Two-Phase Flow System," ASME J. Heat Transfer, **87**, pp. 453–468.
[35] Benedek, S., and Drew, D. A., 1998, "An Analytical Study for Determining the Dynamics of Boiling Boundary," Int. J. Heat Mass Transfer, **41**, pp. 2735–2742.
[36] Saha, P., and Zuber, N., 1974, "Point of Net Vapor Generation and Vapor Void Fraction in Subcooled Boiling, *Proceedings of the Fifth International Heat Transfer Conference*," Tokyo, Japan, Vol. 4, pp. 175–179.
[37] Kim, H., and Choi, S., 2005, Int. Commun. Heat Mass Transfer, **32**, pp. 786–796.
[38] Bell, R. D., and Astrom, K. J., 2000, "Drum-Boiler Dynamics," Automatica, **36**, pp. 363–378.
[39] Gear, C. W., 1971, *Numerical Initial Value Problems in Ordinary Differential Equations*, Series in Automatic Computation, Prentice Hall, New York.
[40] Harlow, F. H., and Amsden, A. A., 1975, "Numerical Calculation of Multiphase Fluid Flow," J. Comput. Phys., **17**, pp. 19–52.
[41] Travis, J. R., Harlow, F. H., and Amsden, A. A., 1976, "Numerical Calculation of Two-Phase Flows," J. Comput. Phys., **61**, pp. 1–10.
[42] Liles, D. R., and Reed, W. H., 1978, "Semi-Implicit Method for Two-Phase Fluid Dynamics," J. Comput. Phys., **26**, pp. 390–407.
[43] Walter, H., and Linzer, W., 2005, "The Influence of the Operating Pressure on the Stability of Natural Circulation Systems," Appl. Therm. Eng., **25**, pp. 327–340.
[44] Walter, H., and Linzer, W., 2003, "Flow Reversal in Natural Circulation System," Appl. Therm. Eng., **23**, pp. 2363–2372.
[45] Wissler, E., Isbin, H. S., and Amudson, N. R., 1956, "Oscillatory Behavior of Two-Phase Natural Circulation Loop," AIChE J., **2**, pp. 157–162.
[46] Fukuda, K., Kobori, T., 1979, "Classification of Two-Phase Flow Stability by Density-Wave Oscillation Model," J. Nucl. Sci. Technol., **16**, pp. 95–108.
[47] van der Hagen, T. H. J. J., Stekelenburg, A. J. C., and van Bragt, D. D. B., 2000, "Reactor Experiments on Type-I and Type-II BWR Stability, Nucl. Eng. Des.," **200**, pp. 177–185.

# Design and Validation of a Scale-Adaptive Filtering Technique for LRN Turbulence Modeling of Unsteady Flow

**W. Gyllenram**

**H. Nilsson**

Division of Fluid Dynamics,
Department of Applied Mechanics,
Chalmers University of Technology,
SE-412 96 Gothenburg, Sweden

*An adaptive low-pass filtering procedure for the modeled turbulent length and time scales is derived and applied to Wilcox' original low reynolds number k-ω turbulence model. It is shown that the method is suitable for complex industrial unsteady flows in cases where full large eddy simulations (LESs) are unfeasible. During the simulation, the modeled length and time scales are compared to what can potentially be resolved by the computational grid and time step. If the modeled scales are larger than the resolvable scales, the resolvable scales will replace the modeled scales in the formulation of the eddy viscosity. The filtered k-ω model is implemented in an in-house computational fluid dynamics (CFD) code, and numerical simulations have been made of strongly swirling flow through a sudden expansion. The new model surpasses the original model in predicting unsteady effects and producing accurate time-averaged results. It is shown to be superior to the wall-adpating local eddy-viscosity (WALE) model on the computational grids considered here, since the turbulence may not be sufficiently resolved for an accurate LES. Because of the adaptive formulation, the filtered k-ω model has the potential to be successfully used in any engineering case where an LES is unfeasible and a Reynolds (ensemble) averaged Navier–Stokes simulation is insufficient.*
[DOI: 10.1115/1.2911685]

## 1 Introduction

The standard two-equation eddy viscosity turbulence models are designed to predict the influence of all turbulent scales. In doing this, they have a strong damping influence on any resolved turbulence or unsteady structures in the flow field. This is desireable in steady calculations, in which the influence of any unsteadiness on the mean flow field must, by definition, be modeled. However, when unsteady information about the flow field is necessary, the turbulence model must be able to distinguish between resolvable and nonresolvable scales. In this paper, it will be shown that this ability can be achieved by applying a low-pass filter to the modeled turbulent length and time scales.

There are many interesting strategies for unsteady turbulence modeling. Spalart [1] gave an overview and discussion about the advantages and limitations of many of these. As the Reynolds numbers of most engineering flows are usually very large, large eddy simulation (LES) is very seldom an option for a full scale industrial simulation. On the other hand, traditional statistical turbulence models developed for the Reynolds (ensemble) averaged Navier–Stokes (RANS) equations do not distinguish between unsteadiness and turbulence. This problem partly arises from the fact that most industrial closure models for the RANS equations are tuned for steady flow, in which the model must predict the influence of all turbulent time scales and, subsequently, all turbulent length scales. In a time-resolved computation, there is a potential in resolving large turbulent time scales. In addition, the grid is usually capable of resolving the largest turbulent length scales, at least outside boundary layers. In a numerical simulation of an unsteady internal (wall-bounded) flow, in which the boundary layer is not fully resolved, models that are tuned to steady flow usually behave very well in the near-wall region. Statistical turbulence models are generally quite accurate in their prediction of wall shear stress. However, there is also a conceptual aspect of the aforementioned problem with statistical turbulence models. In general, there is no way to mathematically distinguish unsteadiness from turbulence. Although the uniqueness of a solution to the three-dimensional Navier–Stokes equations has yet to be mathematically proven [2], it is generally accepted to believe that the solution is completely determined by the initial and boundary conditions. If this is the case, there are no such things as randomness or independent events in the flow. The lack of coherence we observe in a turbulent flow field only gives us a hint of our limited perception. Hence, the concept of ensemble averaging is questionable in unsteady computational fluid dynamics (CFD), simply because one expects to get the same solution repeatedly if one uses the same boundary conditions and the same computer. The ensemble average of an infinite number of direct numerical simulations would thus still be an unsteady and turbulent flow field. The filtering approach of LES is physically more appealing, compared to the concept of ensemble averaging. The limitations of LES are related to a large extent to the simple turbulence models that are used. These models are calibrated to give accurate results if most energy-containing eddies are resolved everywhere, which means that the computational grid has to be extremely fine near walls. Usually, they do not provide any information about how turbulence is convected through the domain. This information is assumed to be carried by the resolved flow field.

There is obviously a need for a turbulence model that can distinguish between what can be resolved and what is not, at the same time as it produces an accurate estimate of the wall shear stress. One method to accomplish this is to introduce a filtering procedure that limits the influence of the statistical turbulence model on the unsteady mean flow field. This is sometimes called very large eddy simulation (VLES) and may be viewed as a combination of the LES and RANS approaches to turbulence modeling. Other common acronyms for the combination of LES and

Contributed by the Fluids Engineering Division of ASME for publication in the JOURNAL OF FLUIDS ENGINEERING. Manuscript received June 11, 2007; final manuscript received; January 11, 2008 published online April 29, 2008. Assoc. Editor: Paul Durbin.

  

RANS methods are detached eddy simulation (DES), limited numerical scales (LNSs), extra large eddy simulation (XLES), flow simulation methodology (FSM), or simply hybrid LES-RANS. In a full LES, the Navier–Stokes equations are filtered in space in order to avoid the need of computing the smallest turbulent scales. The equations are usually averaged (filtered) over the control volumes of the grid, and the unresolved scales are regarded as subgrid turbulence. In contrast to LES, where the mean length scales of all unresolved turbulence are assumed proportional to the local grid spacing, VLES is usually based on statistical turbulence models where the turbulent length scale is calculated and will depend on the flow field. Consequently, the filtering procedure can be formulated in a more dynamic and general way compared to the static spatial filtering of a LES. It can be activated locally in the space-time domain depending on the ratio between an estimation of the resolved turbulent length scales and the magnitude of the modeled turbulent length scales. There are many ways of formulating this dynamical filter. Speziale [3,4] and Fasel et al. [5] arbitrarily defined an exponential filter function, $f(\Delta, L_t) = (1 - \exp(\beta\Delta / L_t))^n$, that depends on a predefined length scale, $\Delta$ (presumably proportional to the local grid spacing), and a modeled turbulent length scale, $L_t$, where subscript $t$ denotes turbulence. The exponential function will allow a smooth transition between the RANS and LES modes of the simulation. The function is multiplied to the modeled Reynolds stress tensor before solving the averaged momentum equations in order to limit the effect of the turbulence model on the mean flow field in regions where parts of the tensor can be resolved. As noted by Fasel et al. [5], other forms of the filter function that are more universally applicable may be defined. Another approach to filtering is to limit the length scales in the transport equations for turbulent quantities, as done by Spalart et al. [6], Menter et al. [7,8], Kok et al. [9], and Menter and Egerov [10]. Spalart et al. [6] defined a maximum length scale, $\tilde{L} = \min\{L_{\text{wall}}, C_{\text{DES}}\Delta\}$, to be used in the denominator of the destruction term of the Spalart–Allmaras transport equation for eddy viscosity. In this formulation, $L_{\text{wall}}$ is the normal distance to the wall and $\Delta$ is again proportional to the local grid spacing. $C_{\text{DES}}$ is a model coefficient that must be calibrated. When $L_{\text{wall}} < C_{\text{DES}}\Delta$, the simulation will run in RANS mode. Away from walls, the destruction term in the equation for the eddy viscosity will be significantly larger than in the original formulation, and the simulation will be forced to run in a LES mode. This approach is aptly called DES. Menter et al. [8] used a similar filtering procedure for the shear stress transport (SST) turbulence model. However, as the SST model, is a two-equation model from which a modeled turbulent length scale can be obtained, the filter is formulated in a more dynamic way by comparing the modeled scales of the simulation to the predefined length scale, $\Delta$. This approach is taken a step further by Menter et al. [7] and Menter and Egerov [10], where instead the von Karman length scale is computed from the resolved velocity field and replaces the predefined length scale. In the latter case, all information from both the resolved and unresolved turbulent length scales is obtained from either the resolved velocity field or the turbulence model. Another interesting hybrid LES-RANS method was recently proposed by Templeton et al. [11], in which precomputed lookup tables for the RANS eddy viscosity are used to define wall functions for coarse grid LES. The eddy viscosity that is active in the solution of the LES equations in the near-wall region is here taken as the difference between the RANS eddy viscosity and an averaged resolved eddy viscosity. However, because the resolved eddy viscosity must be averaged, the method is not entirely straightforward if the flow lacks homogeneous directions.

The filtering approach in this work may in some sense be considered converse to the filtering approach that is used in LES. Instead of solving the filtered equations to avoid the computation of the small scales, the modeled length and time scales are filtered in order to supress their negative influence on unsteady flow field. This approach was initially developed by Willems [12] and is similar to the approach of Speziale [3,4] and Fasel et al. [5], because the filter is applied directly to the Reynolds stress tensor and the turbulence model is left unchanged. However, in this work, the functional form of the filter is derived from the relation between filtered and nonfiltered turbulent length and time scales. The modeled length and time scales are being compared to what can potentially be resolved by the computational grid and time step. If the modeled scales are larger than the resolvable scales, the resolvable scales will replace the modeled scales in the formulation of the eddy viscosity. To distinguish between large- and small-scale turbulences, the upper limit of the length scales of nonresolved turbulence is made proportional to the local grid spacing or the product of the local velocity magnitude and the time step of the simulation. The latter constraint will only be active for large Courant, Friedrich, and Levy (CFL) numbers. There is no lower limit because the mean nonresolved turbulent length scale may be much smaller than the local grid spacing, especially close to walls. This will allow a much coarser grid resolution than in LES. The filter will allow large-scale unsteady structures in the flow, and the model will still produce a wall shear stress comparable to what is produced by a standard RANS model. In this work, the filtering technique is applied to the Wilcox' [13] $k$-$\omega$ model, and the results are validated with experimental data (Dellenback et al. [14]) and compared to LES.

## 2 Filtered Navier–Stokes Equations

There are various filtering approaches for unsteady CFD. They all give rise to new unknowns in the Navier–Stokes equations that must be modeled. The main issue in eddy viscosity models is to determine which length and time scales should be used. It is important to realize that the local value of modeled scales is the *local mean value* of all nonresolved turbulent scales, and the distribution and magnitude of the eddy viscosity are the only parameters that separate a LES from an unsteady RANS simulation. The local mean value may be defined either as an ensemble average (RANS) or a local volume average (LES). The governing equations will nevertheless be identical in their form. However, for conceptual reasons (see Sec. 1), the local volume average is preferable. John [2] made a review of several volume-averaging (filtering) techniques of the Navier–Stokes equations, including estimates of the errors that are associated with the new formulation. The volume-averaged Navier–Stokes equations can be expressed as

$$\partial_0 \bar{u}_i + \bar{u}_j \partial_j \bar{u}_i = -\frac{1}{\rho}\partial_i \bar{p} + \nu \partial_j \partial_j \bar{u}_i - \partial_j \mathcal{R}_{ij} \tag{1}$$

where $\bar{u}_j$ is the resolved (volume-averaged) velocity vector and $\bar{p}$ is the resolved pressure. The Reynolds stress tensor, $\mathcal{R} = -\bar{u}_i\bar{u}_j + \overline{u_i u_j}$, can be expanded into

$$\mathcal{R}_{ij} = -\bar{u}_i\bar{u}_j + \overline{\bar{u}_i\bar{u}_j} + \overline{\bar{u}_i u_j'} + \overline{u_i'\bar{u}_j} + \overline{u_i' u_j'} \tag{2}$$

where Reynolds decomposition, $u_i = \bar{u}_i + u_i'$, has been used. Here, $u_i$ is the exact solution and $u_i'$ denotes a fluctuation from the resolved velocity vector. The turbulence model that will replace the Reynolds stress tensor, $\mathcal{R}_{ij}$, in a numerical simulation must predict a nonresolved turbulent length scale, $\ell_t$, that is *smaller or equal* to the averaging length scale, or filter width, $\Delta_f$, which is usually chosen to be proportional to the local grid spacing. Zero- and one-equation subgrid models always use a length scale, $\ell_t$, that is proportional to the local grid spacing. However, the length scale, $\ell_t$, of the unknown, $u_i'(\mathbf{x}, t)$, does not generally correspond to the length scales of the grid. In near-wall regions, $\ell_t \ll \Delta$, unless the local grid spacing is extremely fine, i.e., near the resolution required for a direct numerical simulation (DNS). Obviously, there is a need for a closure model that can predict length scales that are smaller than the grid spacing, if necessary.

## 3 Turbulence Modeling

The $k$-$\omega$ model of Wilcox [13], with the addition of the realizability constraint derived by Durbin [15], has been used as the basic turbulence model in this work. The main advantage of this model over, e.g., $k$-$\varepsilon$ models, is that it can be integrated all the way to the wall without damping or correction functions. The model is a two-equation eddy viscosity model, and it is coupled to the averaged Navier–Stokes equations by the Boussinesq assumption,

$$-\mathcal{R}_{ij} = 2\nu_t S_{ij} - \tfrac{2}{3}k\delta_{ij} \tag{3}$$

where $S_{ij}=(\partial_j U_i+\partial_i U_j)/2$ and $k=\overline{u_i' u_i'}/2$ is the turbulent kinetic energy. The Boussinesq assumption introduces the concept of a turbulent eddy viscosity, $\nu_t$. It suggests that the influence of turbulence on the mean flow is dominated by a mixing process. The eddy viscosity has the same dimension as the kinematic viscosity of the fluid and is assumed to be proportional to a function of the local turbulent length and time scales, i.e.,

$$\nu_t \sim L_t^2/T_t \tag{4}$$

The turbulent length and time scales are unknown local properties of the turbulent flow and must be modeled. If transport equations for, e.g., the modeled turbulent kinetic energy, $k$, and dissipation rate, $\varepsilon$, or specific dissipation rate, $\omega$, are solved, a measure of the turbulent length and time scales can be obtained from these variables by dimensional analysis, see Sec. 3.1.

**3.1 Consistent Derivation of the Filter Function.** The filtering approach of Willems [12] has earlier been successfully employed by Helmrich et al. [16] and Ruprecht et al. [17]. This filter is applied to the turbulence model in order to allow the existence of resolvable turbulent scales in the solution of the flow field. Willems derived the form of the filter function from the two-point correlation tensor and applied it to the $k$-$\varepsilon$ model. In the present paper, the same form of the filter function is derived by simple dimensional analysis. It is also shown that the novel generalization of the approach to other eddy viscosity models than the $k$-$\varepsilon$ model requires that the filter is applied to the turbulent length and time scales and not only to the turbulent kinetic energy, as in Willems' work.

The local turbulent length and time scales may be obtained from a dimensional analysis of $k$ and $\omega$. It follows that

$$L_t \sim k^{1/2}/\omega \tag{5}$$

$$T_t \sim 1/\omega \tag{6}$$

The filter width, $\Delta_f$, is the upper limit of the modeled turbulent length scale. This corresponds exactly to the lower limit of the resolved turbulent length scale and will in this work be a function of time step $\delta t$ and local cell volume $\Delta$. Hence, the largest length scale that needs to be a part of the eddy viscosity formulation is

$$\ell_t = \min\{L_t, \Delta_f\} \tag{7}$$

where

$$\Delta_f = \alpha \max\{|\mathbf{U}|\delta t, \Delta^{1/3}\} \tag{8}$$

Coefficient $\alpha > 1$ takes into account the need for a limited number of cells to actually resolve a turbulent structure. In the study by Gyllenram and Nilsson [18], a value of $\alpha \geqslant 3$ was necessary to obtain accurate results. The product $|\mathbf{U}|\delta t$, in Eq. (8), is a measure of the shortest distance, over which a fluid particle can be traced in an unsteady computation, for which reason the computational time step may also set a lower limit to the resolved length scale. This temporal constraint is especially important in complex geometries, as discusseed by Batten et al. [19], who also noted that a steady RANS calculation would correspond to an infinite time step, for which $\ell_t = L_t$, always. The upper limit on the modeled length and time scales can also be defined in terms of the filtered (nonresolved) variables, i.e.,

$$\ell_t \sim \hat{k}^{1/2}/\hat{\omega} \tag{9}$$

$$t_t \sim 1/\hat{\omega} \tag{10}$$

The specific dissipation rate, $\omega$, is related to the dissipation rate, $\varepsilon$, by the relation

$$\omega = \frac{\varepsilon}{\beta^* k} \tag{11}$$

where $\beta^* = 0.09$. The filtered specific dissipation rate can be written as

$$\hat{\omega} = \frac{\hat{\varepsilon}}{\beta^* \hat{k}} \tag{12}$$

The dissipation rate, $\varepsilon$, is never resolved in anything cheaper than a DNS, because it takes action at the Kolmogorov scale, the very smallest turbulent length scale. Hence,

$$\hat{\varepsilon} = \varepsilon \tag{13}$$

and it follows from Eqs. (11)–(13), that

$$\hat{\omega} = \frac{\omega k}{\hat{k}} \tag{14}$$

It is straightforward to show that Eqs. (5), (9), and (14) yield an expression for the filtered turbulent kinetic energy according to

$$\hat{k} = g(\ell_t, L_t)k \tag{15}$$

where the equality follows from the assumption that the constants of proportionality in Eqs. (5) and (9) are equal. The filter function, $g(\ell_t, L_t)$, is defined as

$$g \equiv (\ell_t/L_t)^{2/3} \tag{16}$$

in which $\ell_t$ is computed from Eq. (7) and the modeled turbulent length scale, $L_t$, is taken as $L_t = \sqrt{k}/(\beta^*\omega)$. In regions where turbulence cannot be resolved, i.e., where $L_t < \Delta_f$ in Eq. (7), the filter function, Eq. (16), is unity and $\hat{k}=k$ in Eq. (15). However, there is no need to compute the filtered turbulent variables explicitly. A filtered eddy viscosity can be constructed directly from the nonresolvable turbulent length and time scales, i.e.,

$$\hat{\nu}_t \sim \ell_t^2/t_t \tag{17}$$

It follows from Eqs. (9), (10), (14), and (15) that

$$\hat{\nu}_t = g^2 \frac{k}{\omega} \tag{18}$$

where the equality must hold in order to recover the original (nonfiltered) eddy viscosity formulation, $\nu_t = k/\omega$, in regions where the filter is inactive. Note that the only modification to the original eddy viscosity formulation is the factor $g^2$, i.e., the square of the filter function. The filter function can be derived and applied using *any* two-equation turbulence model. It will always obtain the same functional form as in Eq. (16) and it will always end up as squared when used in the formulation of the eddy viscosity.

There will obviously be an explicit grid dependence in the eddy viscosity formulation, Eq. (18), when $\Delta_f < L_t$ in Eq. (7). However, the derivative of $g^2$ with respect to the filter width,

$$\frac{\partial(g^2)}{\partial \Delta_f} = \frac{4}{3}\left(\frac{\Delta_f}{L_t}\right)^{1/3} \tag{19}$$

will vanish in the fine grid limit, $\Delta_f \to 0$, because

$$\left.\frac{\partial(g^2)}{\partial \Delta_f}\right|_{\Delta_f \to 0} \to 0 \tag{20}$$

This shows that the eddy viscosity asymptotically approaches a constant in the fine grid limit, as long as the model equations for $k$ and $\varepsilon$ do not explicitly depend on the local grid spacing them-

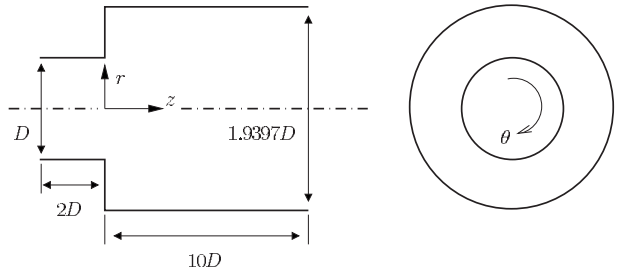


**Fig. 1 Geometry of the test case. The inlet swirl is clockwise in the *z* direction.**

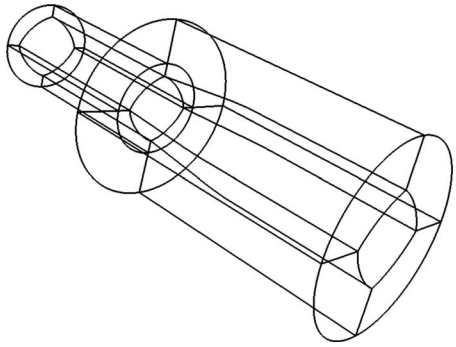

**Fig. 2 Block structure. Only 10 out of 15 blocks are shown.**

selves. Actually, as the eddy viscosity is limited by the filter, there will also be less production of modeled turbulent kinetic energy, $k$, and specific dissipation rate, $\omega$. This is natural, because the resolved turbulent kinetic energy and specific dissipation should increase. The importance of the novel approach of applying the filter to the length and time scales of the eddy viscosity formulation instead of only to the turbulent kinetic energy, as in the work of Willems [12], is now obvious. If the filter was applied only to the turbulent kinetic energy, the square of the filter function $g(\ell_t, L_t)$ in Eq. (18) would vanish and the filter would not have the proper behavior in the fine grid limit according to Eq. (20).

*3.1.1 Near-Wall Asymptotics*. There could be an obvious risk in applying a filter width that is too small in boundary layers because, if $\Delta_f < L_t$ in Eq. (7), the eddy viscosity can be written as

$$\hat{\nu}_t = \beta^* \Delta_f^{4/3} (\beta^* \omega k)^{1/3} \tag{21}$$

This expression does not have the proper asymptotical behavior in the near-wall limit unless the grid is abnormally stretched. In the limit $n \to 0$, where $n$ is the wall-normal coordinate, $\hat{\nu}_t \sim n^{1/3}$, while a proper functional behavior of the eddy viscosity would be $\nu_t \sim n^3$, at least in a time-averaged sense [20]. However, the purpose of the filtering approach is to avoid the need of an extremely fine near-wall resolution and, indeed, the wall boundary condition for the turbulent kinetic energy, $k_{\text{wall}}=0$, is expected to limit the modeled turbulent length scale and thereby inactivate the filter before the wall limit is reached. Nevertheless, too small a filter width ($\alpha$) may, as shown by Gyllenram and Nilsson [18], cause the filter to be activated all the way to the wall and the results to deteriorate. However, on a computational grid with a wall $y^+ \sim 2$, the modeled turbulent length and time scales obtained from the $k$-$\omega$ model are small enough to inactivate the filter near the wall using $\alpha=3$ in Eq. (8), as will be shown in Sec. 5. In other words, the filter should not be active close to walls. Instead, the underlaying RANS model should take care of the near-wall modeling.

## 4 Test Case and Computational Setup

A swirling flow through a sudden expansion has been investigated, see Fig. 1. Measurements courtesy of Dellenback et al. [14] have been used to validate the results. The swirl number, defined as

$$S = \frac{\int_0^R V_\theta V_z r^2 dr}{R \int_0^R V_z^2 r dr} \tag{22}$$

is approximately 0.6, based on the inlet radius, $R=D/2$. $V_\theta$ and $V_z$ denote the time-averaged tangential and axial velocities, respectively. The Reynolds number, based on the inlet diameter, $D$, and bulk velocity, $U_b$, is 30,000. The case has earlier been studied numerically by Schlüter et al. [21] and Gyllenram et al. [22]

**4.1 Code.** The CALC-PMB [23] CFD software was used to simulate the flow. The code was developed at the Division of Fluid Dynamics, Department of Applied Mechanics, at Chalmers University of Technology, Göteborg, and is based on the finite volume method. The pressure-velocity coupling is solved using the SIMPLEC algorithm developed by Van Doormaal and Raithby [24]. Conformal block-structured, boundary-fitted coordinates are used, and two ghost cells are employed at the block interfaces to enable different first- and second-order discretization schemes. The code is parallelized by domain decomposition. Message passing interface (MPI) is used for the exchange of information between the different processes/blocks. To avoid spatial oscillations of the pressure field over the collocated (nonstaggered) grid arrangement, Rhie and Chow interpolation is applied for convections through the cell faces. For the discretized and linearized system of equations, TDMA (also known as Thomas' algorithm) and biconjugated gradient solvers are implemented. For this work, a parallelized version of TDMA was used.

**4.2 Grids and Numerics.** Two different block-structured grids were used in this work. The sizes of the grids were 1,711,424 and 3,356,640 nodes. The two grids will in the following be referred to as the coarse and fine grids, respectively. Each grid consisted of 15 blocks. The block structure is shown in Fig. 2. Each block of the coarse grid consisted of $N_i \times N_j \times N_k = 44 \times 68 \times 44$ nodes except the four wall-bounded blocks of the inlet pipe section, which sum up to $44 \times 68 \times 22$ nodes. The corresponding block sizes of the fine grid are $56 \times 81 \times 51$ and $56 \times 81 \times 31$. For the wall-bounded blocks, $N_i$, $N_j$, and $N_k$ refer to the tangential, axial, and radial directions, respectively. The first cell centers normal to the wall were placed at $y^+ \approx 2$ in both grids. Consequently, the coarse grid has larger grid stretching in the wall-normal direction, especially in the inlet pipe section and in the near-wall region just downstream of the sudden expansion. The fine grid has an axial resolution of $\Delta z^+ \approx 50$ and a tangential resolution of $\Delta \theta^+ \approx 20$. The axial and tangential resolutions of the coarse grid are $z^+ \approx 60$ and $\theta^+ \approx 25$, respectively. The approximate values are estimated from a snapshot of the simulation. Both grids are considered fine enough for RANS simulations. The resolution of the fine grid is considered merely adequate for LES. All simulations were made using a second-order central differencing scheme for the momentum and pressure correction equations. The transport equations for $k$ and $\omega$ were discretized using the van Leer [25] scheme. The second-order implicit Crank–Nicholson time integration scheme was used. For time-accurate numerical results, a CFL number of CFL $< 1$ is preferable. With this requirement, nondimensional time steps, $\delta t^* = \delta t \times U_b / D$, of 0.0027 and 0.0036 were sufficient for the fine and coarse grids, respectively, yielding a maximum CFL number of approximately 0.8. Thanks to the larger time step and the smaller grid size, a simulation on the coarse grid is more than twice as fast as a simulation on the fine grid for a specific simulated real-time interval. Time series of the wall pressure at several locations were sampled during the simulations. The

solutions were considered as converged when the pressure levels were fluctuating around a steady mean value (i.e., when the flow was fully developed) and all normalized residuals were of the order of $10^{-3}$ in each time step. The residuals of the momentum equation were normalized by the global convection and the residuals of the continuity equation were normalized by the mass flow rate. The filtered version of the $k$-$\omega$ model requires slightly more CPU time than the original formulation. Nevertheless, it is expected to be computationally cheaper than most other two-equation models because of the simplicity of the original formulation. The additional cost of computing the function $g$, Eq. (16), can be compared to that of, e.g., adding a damping function to the eddy viscosity. Furthermore, the convergence rate of the filtered model was much better than the convergence rate of the original model.

**4.3 Boundary Conditions and Turbulence Model Constants.** Spline curves based on the measured data of Dellenback et al. [14] were used as the inlet boundary condition for the mean velocities. The experimental data taken along two counter-directed radial lines were averaged to obtain a fully symmetric inflow condition. A boundary layer based on the log-law was added between the (radially) outermost measuring point and the wall. Earlier numerical investigations by Schlüter et al. [21] showed that the resolved turbulence level of the inlet boundary conditions has a great effect on the mean velocity profiles for low swirl levels. However, the swirl level in the present study is high enough for a fast transition to turbulence. Hence, to add unsteadiness at the steady inlet boundary condition is superfluous. A constant inlet turbulent intensity of 10% was chosen, and the inlet boundary condition for $\omega$ was approximated by $\omega=\sqrt{k}/(\beta^* R)$, where $R$ is the radius of the inlet and a crude estimate of the turbulent length scale. The assumption of a turbulent intensity of 10% was based on the levels of axial and tangential Reynolds normal stresses, as measured by Dellenback et al. [14]. The turbulent intensity of 10% was estimated from measurements by Dellenback et al. The simulations using the filtered $k$-$\omega$ model are not expected to be sensible to the values of turbulent quantities at the inlet boundary. If the imposed length scale is too large, the filter will activate and automatically decrease the production of turbulence via the eddy viscosity, according to Eq. (7). However, this matter has not yet been studied in detail. At the outlet, a homogeneous Neumann boundary condition was used for all variables. A no-slip condition was used for the velocity at the walls, where the turbulent kinetic energy also vanishes. The wall boundary condition for the specific dissipation was set at the first interior node as $\omega=6\nu/(\beta^* y^2)$, see Ref. [20].

Two turbulence models have been considered, i.e., the $k$-$\omega$ model by Wilcox [13] and the wall-adapting local eddy-viscosity (WALE) zero-equation subgrid model by Nicoud and Ducros [26]. The filtering technique derived in Sec. 3.1 was applied only to the former model. A filter width of $\alpha=3$ was chosen for the $k$-$\omega$ model, and $C_w=0.5$ for the WALE model.

## 5 Results

The purposes of the novel filtering technique are to allow large-scale unsteady structures in the resolved flow field and to give accurate time-averaged results on a typical RANS grid. In order to see what results can be obtained from a LES on the same grid, a simulation using the WALE subgrid turbulence model, derived by Nicoud and Ducros [26], was also made. The WALE model is known to perform very well in complex flows as long as all energy-containing turbulent structures are sufficiently resolved. As will be shown in Sec. 5.2, the grid resolution is, as expected, not fine enough to actually justify the use of the WALE subgrid model. Especially the wall-normal resolution must be higher.

The main features of the flow are visualized and discussed in Sec. 5.1. The time-averaged results of the computations are compared to experiments done by Dellenback et al. [14] in Sec. 5.2.

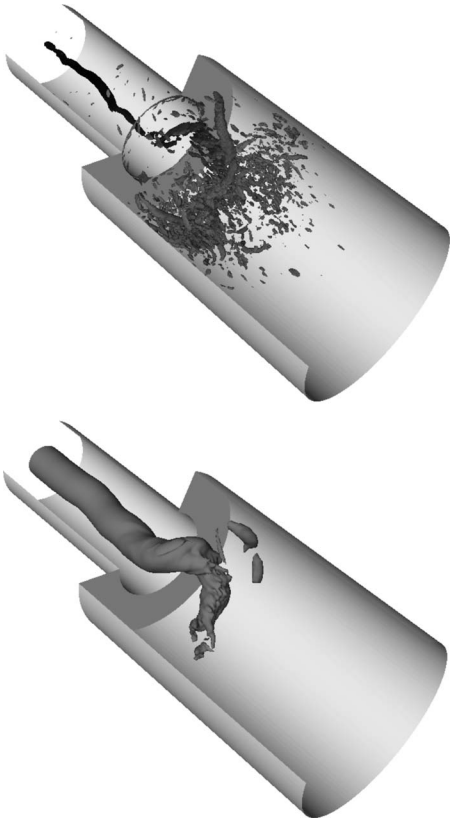

**Fig. 3 Snapshot of the precessing vortex core visualized by isosurfaces of the nondimensional second invariant of the velocity gradient, $II^*_{\partial_j U_i}=480$ (top) and static pressure (bottom). Both methods predict the same location and shape of the vortex core. The results are obtained from a simulation using the filtered $k$-$\omega$ model on the fine grid. Only a part of the computational domain is shown. The helicoidal vortex structure is formed immediately after the expansion and propagates upstream almost all the way up to the inlet. It dominates the flow until a point approximately one and a half diameters downstream of where it is formed. At this point, the flow returns to a quasisymmetric mode.**

The filter function and the eddy viscosity are examined in Sec. 5.2.2, while the resolved and modeled turbulent kinetic energies are discussed in Sec. 5.2.3. The unsteadiness of the flow is analyzed in Sec. 5.3.

**5.1 Visualization of Resolved Structures.** A snapshot of the flow is presented in Fig. 3. The vortical structures are visualized by isosurfaces of the nondimensional second invariant of the velocity gradient tensor and pressure. The second invariant of the velocity gradient tensor is normalized by the factor $(R/U_b)^2$ and will in the following be referred to as $II^*_{\partial_j U_i}$. It can be physically interpreted as the source term for the pressure equation, see Ref. [27] for further details. A local maximum of $II^*_{\partial_j U_i}$ is located inside each small volume that is bounded by an isosurface, and corresponds to local pressure minimum. The vortex that is defined at the inlet breaks down near the sudden expansion. A helicoidal vortex core is formed. The vortex core rotates around the geometrical axis of symmetry with a well defined frequency. Other counter-rotating vortex structures are formed in the near-wall recirculation zone just downstream of the expansion. These structures give rise to other frequencies. There is also a recirculation zone along the axis of symmetry, i.e., the flow on the inside of the helicoidal structure is reversed.

A comparison of the results obtained from using different grid

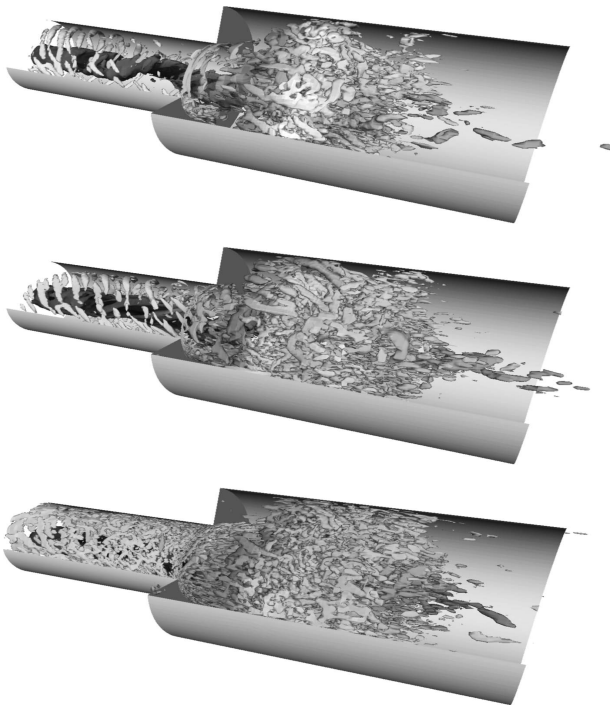

**Fig. 4 Isosurfaces of the normalized second invariant of the velocity gradient tensor, $II^*_{\partial_j U_i}=120$, using the filtered $k$-$\omega$ model and the WALE model. Top: filtered $k$-$\omega$, coarse grid. Center: filtered $k$-$\omega$, fine grid. Bottom: WALE model, fine grid. The isosurfaces are shaded by the static pressure. A darker shade denotes a lower pressure. As expected, the fine grid resolves a larger part of very small scale turbulence. However, the strongest and largest vortices are well resolved on any of these grids. An even higher density of small-scale turbulence is obtained using the WALE model.**

sizes and turbulence models is presented in Fig. 4, where instantaneous isosurfaces of $II^*_{\partial_j U_i}=120$ are shown in Fig. 4. Large torus-shaped vortices are formed near the sudden expansion. The main vortex core is very well defined near the axis of symmetry in the upstream part of the domain. The simulation using the filtered $k$-$\omega$ model on the fine grid resolves a larger part of the small-scale turbulence, as compared with the result of using the same model on the coarse grid, as expected. The WALE model is less dissipative than the filtered $k$-$\omega$ model, resulting in an even higher density of small-scale turbulence.

**5.2 Velocity Profiles and Time-Averaged Results.** The time-averaged results are based on 1480 samples, which correspond to a nondimensional sampling time of $t^*_S=40$, as there were ten time steps between each sample. This is approximately equivalent to 20 vortex core revolutions or four mean flow residence times. The axisymmetry of the computional domain also allows circumferential averaging, and thus the time-averaged profiles at four circumferential locations were averaged once again. This yields a virtual sampling time of $t^*_S=160$. The evolutions of the axial and tangential velocity distributions and the swirl angle ($\arctan(V_\theta/V_z)$) near the sudden expansion are shown in Fig. 5. The experimental data shown are for each $z/D$ the averages of measurements taken along two counterdirected radial lines.

The agreement between the results obtained from using the filtered $k$-$\omega$ model and the experimental data is excellent. The WALE model also performs quite well. The main differences in the prediction of the axial velocity profiles are found in the most unsteady region, where the vortex breaks down. The swirl velocity far downstream is overestimated by the simulation using the WALE model. On the other hand, the grid resolution may not be at a level that fully justifies the use of this model.

As the length scale of the local grid spacing appears explicitly in the filter function, Eq. (16), it is expected that the instantaneous solution is influenced by a grid refinement. However, the time-averaged solutions should ideally not be sensitive to the grid refinement. Figure 5 suggests that the grid dependence seems not to be a major issue. The results obtained when the filtered $k$-$\omega$ model is used on the coarse grid actually agree better with experimental data than the results obtained from using the WALE model on the fine grid. No study of the performance of the WALE model on the coarse grid has been carried out, simply because it is not applicable. It should be borne in mind that the filtered $k$-$\omega$ simulations on the coarse grid for a specific real-time interval are completed in less than half of the time, as compared to the simulations on the fine grid. The simulations using the WALE model on the fine grid are approximately 30–50% faster than the filtered $k$-$\omega$ approach on the same grid, because fewer equations are being solved.

The original (nonfiltered) $k$-$\omega$ model fails to predict reasonable results. The simulation converges to a steady flow even if an unsteady velocity field obtained from using the filtered $k$-$\omega$ model is used as an initial (starting) condition. Nevertheless, the axial velocity profiles show good agreement with the other simulations near the wall, and the tangential velocity profiles near the suddden expansion, Fig. 5 (second row, to the left), show very good agreement at $r/D>0.5$. The results deteriorate closer to the centerline. Figure 5 (second row, to the right) shows that the rate of decay of swirl is far too high.

It can be shown that the original $k$-$\omega$ model is insensitive to rotation, see, e.g., Ref. [20]. Furthermore, the turbulence model tends to damp out unsteady fluctuations during the simulation. It is clear that the filtering procedure of the turbulent length and time scales removes these inherent shortcomings of the turbulence model, while retaining its good near-wall characteristics.

*5.2.1 Reattachment Length.* The flow enters the wider pipe section as a swirling jet. The flow separates from the wall at the sudden expansion and a large region of entraining and recirculating flows is formed near the wall of the wider pipe section. The mean axial flow reattaches to the wall at some distance a few (inlet) diameters downstream of the sudden expansion. This distance is called the reattachment length.

Dellenback et al. [14] measured the reattachment length of the flow and obtained a value of $z_r/h=2.5$, where $h$ is the step size, i.e., the difference between the outlet and inlet radii. The average reattachment length obtained from using the filtered $k$-$\omega$ model on the fine grid is $z_r/h=2.5$, in full agreement with the experimental result. A reattachment length of approximately $x_r/h=3.3$ was obtained when using the WALE model. The reattachment length obtained when using the filtered $k$-$\omega$ model on the coarse grid is almost 15% larger compared to the simulation on the fine grid, i.e., $z_r/h\approx 2.9$. The longer reattachment length is directly connected to the slight overshoot of the axial velocity profile at $z/D=1$ and $r/D\approx 0.5$. This can probably be explained in part by the larger grid stretching that was applied in the design of the coarse grid. Nevertheless, as can be seen in Fig. 5, the velocity profiles agree quite well with the experimental data.

*5.2.2 Eddy Viscosity and the Filter Function.* The time-averaged square of the filter function, Eq. (16), and the filtered eddy viscosity is shown in Fig. 6. The filter function is always inactive near the wall region and sometimes in the strong shear layer near the sudden expansion. In these regions, the modeled turbulent length scales are small enough to pass through the filter. The small turbulent length scales of the shear layer partly originate from the wall boundary layer of the upstream pipe section. The distribution of eddy viscosity is directly influenced by the shape of the filter function. Figure 6 (left) shows that the filter function behaves approximately the same on both grids. The rea-

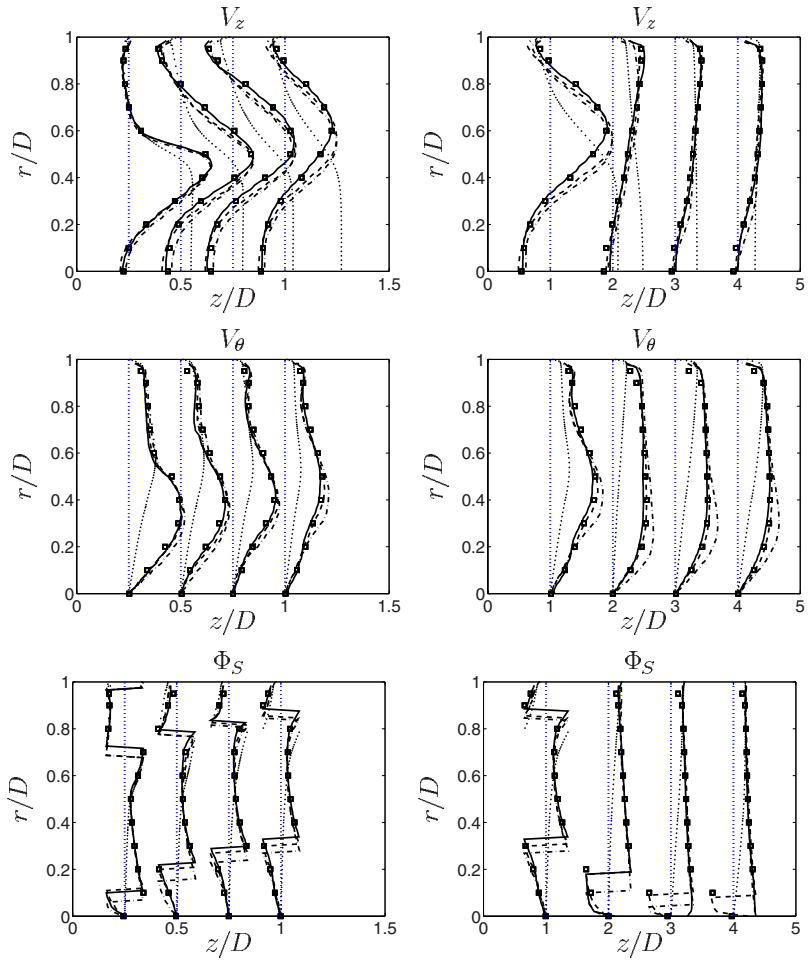


**Fig. 5 Radial distributions of averaged axial velocity (top row), tangential velocity (center row), and swirl angle (bottom row) at different cross sections. (—) Filtered *k-ω* model, fine grid. (– – –) Filtered *k-ω* model, coarse grid. (· –) WALE model, fine grid. (···) Standard *k-ω* model, coarse grid. (□) Experiment. The scaling between the left and right columns is given by the profiles at *z/D* =1. The standard *k-ω* model fails to predict reasonable results. It converges to a steady solution. The WALE model performs well considering the grid resolution. However, the agreement between the results obtained using the filtered *k-ω* model and the experimental data is excellent, especially on the fine grid.**

sons for this are that less turbulence is modeled on the fine grid and that the denominator of Eq. (16) has decreased in proportion to the nominator, i.e., the filter width. The eddy viscosity, shown in Fig. 6 (to the right), is very dependent on the grid resolution, however. This is actually the advantage of the present approach. When the grid is not fine enough to resolve the turbulent structures, their effect must instead be present through the modeled part of the turbulence. The maximum value of the nondimensional filtered eddy viscosity that is shown in Fig. 6 (to the right) is $\hat{\nu}_t^* = \hat{\nu}_t/\nu = 75$. It is found at $z/D = 0.5$ using the coarse grid. At that location, the fine grid gives a maximum value of $\hat{\nu}_t^* = 59$.

*5.2.3 Turbulent Kinetic Energy*. Figure 7 shows the distributions of the modeled and the (time-averaged) resolved turbulent kinetic energy (TKE) for the two different grids at two different cross sections, obtained with the filtered $k$-$\omega$ model. The resolved TKE is computed as $K = (\langle \bar{u}_i \bar{u}_i \rangle - U_i U_i)/2$, where $\bar{u}_i$ and $U_i$ are the resolved (instantaneous) and time-averaged velocity vectors, respectively, and $\langle(\cdot)\rangle$ denotes time average. The weak grid dependence of the resolved TKE, $K$, suggests that it is dominated by large-scale fluctuations. The maximum of resolved turbulent kinetic energy in Fig. 7 (to the left), at $r/D \approx 0.4$, corresponds to the location of the rotating vortex core. Further downstream, at $z/D = 2$, the resolved turbulent kinetic energy is quite evenly distributed.

The grid dependence of the (nonfiltered) modeled TKE, $k$, is explained by the fact that the filtered eddy viscosity is used in the production term, $P_k$, in the transport equation for $k$, i.e., $P_k = 2\hat{\nu}_t S_{ij} \partial_j \bar{u}_i$, where $S_{ij}$ is the strain rate tensor, see, e.g., Ref. [20]. Consequently, the finer the grid, the less turbulence will be modeled.

The distribution of filtered modeled TKE, $\hat{k}$, as defined in Eq. (15), is determined by length and time scales smaller or equal to what can be resolved. It is the only part of the modeled turbulent kinetic energy that is fed to the momentum equations, via the eddy viscosity. From Fig. 7, it is clear that the filtered modeled TKE obtained on the fine grid is approximately one order of magnitude smaller than the resolved TKE, $K$. In Sec. 5.2.2, it was shown that the filter is inactive in the near-wall region, i.e., $g^2 = 1$ in Eq. (18). Hence, the filtered modeled TKE, $\hat{k}$, is identical to the nonfiltered modeled TKE, $k$, in the near-wall region. Note that a local maxi-

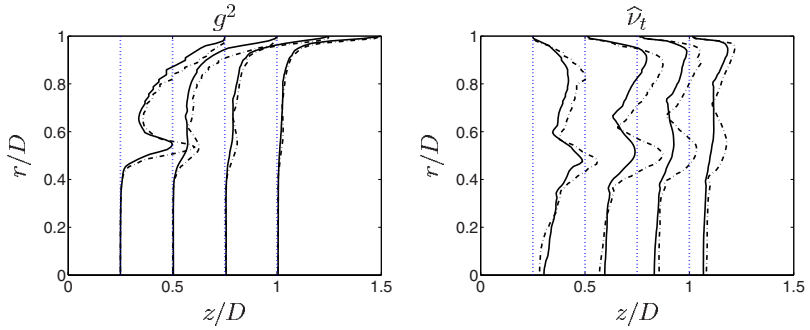


**Fig. 6 Radial distribution of the time-averaged squared filter function, $g^2$ (left), and the (nondimensional) filtered eddy viscosity, $\hat{\nu}_t^* = \hat{\nu}_t/\nu$ (right), obtained with different grids. (· –) Coarse grid. (—) Fine grid. The filter is inactive near the wall where it reaches the value of 1, and (often) in the strong shear layer near the sudden expansion. The filtered eddy viscosity is much larger on the coarse grid, because the less that is resolved, the more must be modeled. The maximum (time-averaged) value of the filtered eddy viscosity, $\hat{\nu}_t^* = 75$, is found at $z/D = 0.5$ (coarse grid).**

mum of the filtered modeled TKE occurs at $r/D \approx 0.5$. The maximum coincides with the local maximum of the filter function in Fig. 6 (to the left). It is explained by the fact that nonresolved TKE of the inlet boundary layer is convected downstream into the larger pipe section. This flow-history effect could not have been predicted by anything but a transport model for turbulence.

**5.3 Frequency Analysis.** The fluctuations of the wall pressure as a function of the nondimensional time are shown in Fig. 8 (to the left). As can be seen, the time series obtained from the two grids are quite similar. The fluctuations are somewhat larger in the simulation on the fine grid. Fourier transforms of the wall pressure were used to analyze the large-scale unsteadiness of the flow. The Fourier transforms of 6609 overlapping segments of length $2^{13}$ were averaged in order to get rid of the noise. Each segment from the simulation on the fine grid, in which a nondimensional time step of 0.0027 was used, corresponds to a nondimensional sampling time $t^* \approx 22$. Figure 8 (to the right) shows that the resolution seems not to play a major role in determining the main frequency. The most distinct nondimensional frequency is at Strouhal number $\mathrm{St} = f \times U_b/D = 0.6$. This frequency corresponds to the rotational speed of the helicoidal vortex core.

Figure 9 shows the spectral density of the wall pressure sampled at four different downstream locations. Near the expansion, the solution obtained using the filtered $k$-$\omega$ model shows exactly the same frequency as the solution obtained by using the WALE model. This is expected, as the vortex core is fully resolved in both simulations. The lower frequencies most likely correspond to the bursting of large turbulent structures in the recirculation zone near the wall, just after the expansion, as these structures are convected downstream. As the vortex core does not propagate further downstream than to where the flow reattaches, only the lower frequencies are present downstream $z/D \approx 1.25$. Because of the limited sampling time, the lowest frequencies are not well resolved. Hence, the model and grid dependency of the lowest frequencies cannot be analyzed.

Figure 10 shows the normalized frequency spectra of resolved

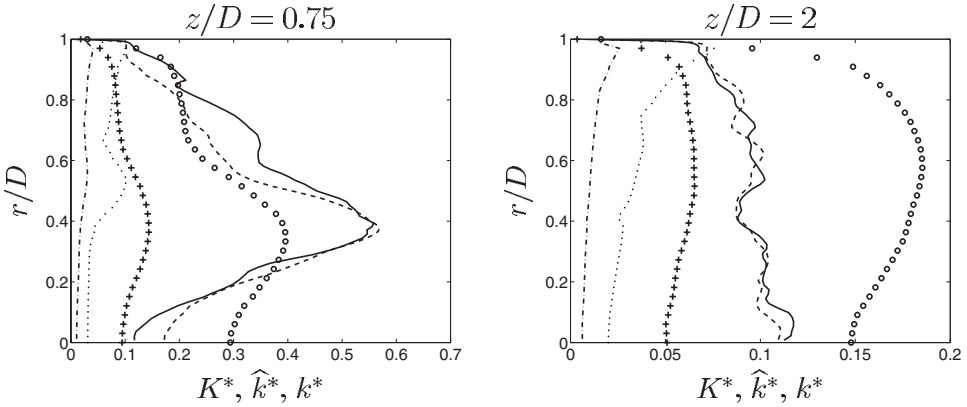


**Fig. 7 Radial distribution of nondimensional turbulent kinetic energy (TKE) at $z/D = 0.75$ (left) and $z/D = 2$ (right) obtained with the filtered $k$-$\omega$ model on two different grids. All quantities marked by superscript asterisks (*) are normalized by $U_b^2$. (– –) Resolved TKE ($K^*$), coarse grid. (—) Resolved TKE ($K^*$), fine grid. (···) Filtered modeled TKE ($\hat{k}^*$), coarse grid. (-·) Filtered modeled TKE ($\hat{k}^*$), fine grid. (○) Modeled TKE ($k^*$), coarse grid, (+) Modeled TKE ($k^*$), fine grid. The resolved TKE is dominated by large-scale turbulent structures that only weakly depend on grid resolution. The distribution of filtered modeled turbulent kinetic, $\hat{k}^*$, is determined by length and time scales smaller or equal to what can be resolved. Consequently, it depends heavily on grid resolution.**

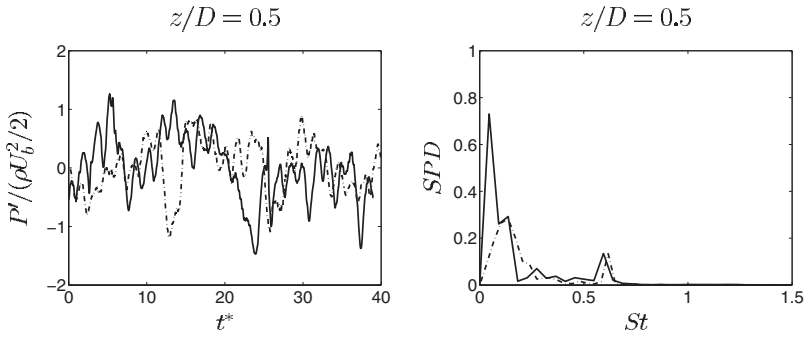


**Fig. 8 Left: time series of nondimensional wall pressure fluctuations at $z/D = 0.5$ obtained with the filtered $k$-$\omega$ model. (—) Fine grid. (– –) Coarse grid. Note that the end points of the time series are quite arbitrary, and thus no correlation between the two series is expected. Right: spectral power density of the wall pressure at $z/D = 0.5$ obtained from using the filtered $k$-$\omega$ model. (—) Fine grid. (– –) Coarse grid. The predicted rotational speed (St=0.6) of the vortex core is not sensitive to the resolution.**

axial velocity fluctuations at $z/D=2$ and $r/D=0.25$, obtained using the filtered $k$-$\omega$ model on different grids. The largest scales of turbulence are resolved on both grids, as already seen in Fig. 7. However, there is a difference in the prediction of intermediate- and small-scale turbulences. At the locations $z/D=2$ and $r/D=0.25$, the grids are not fine enough to resolve turbulent structures with frequencies higher than St$\sim$20. The results for higher frequencies are accordingly not included in Fig. 10.

## 6 Conclusions

Numerical simulations of unsteady turbulent flow can be significantly improved by applying an adaptive low-pass filter to the modeled turbulent length and time scales predicted by a two-equation low Reynold number (LRN) turbulence model. The filter limits the damping effect of the turbulent viscosity on the resolved flow field away from walls. Large-scale unsteady turbulent structures are resolved, and the time-averaged results correspond very well to experimental data. On the computational grids considered in this work, the filtered $k$-$\omega$ model surpasses the WALE LES model in accuracy, while the results are equivalently unsteady. The main frequency of the simulated flow is not sensitive to the choice of model or grid size, while the amplitude of the largest pressure fluctuations is. The difference in the prediction of the largest scales is most likely connected to the difference in the prediction of the reattachment length. While the simulation using the filtered $k$-$\omega$ model agrees very well with experimental results

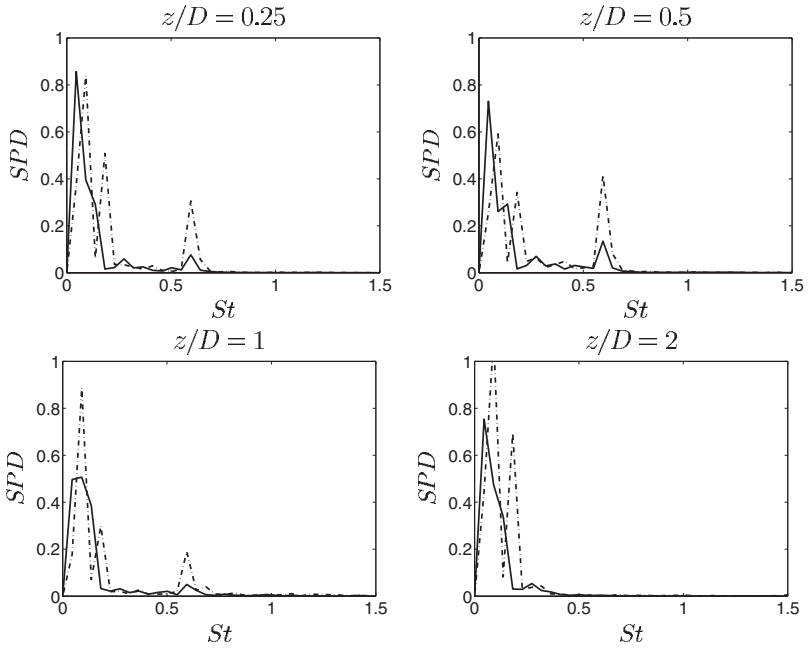


**Fig. 9 Spectral power density of the wall pressure fluctuations at $z/D = 0.25$ (top left), $z/D = 0.5$ (top right), $z/D = 1$ (bottom left), and $z/D = 2$ (bottom right). (—) Filtered $k$-$\omega$ model, fine grid. (· –) WALE model, fine grid. The most distinct frequency is at St=0.6 and corresponds to the rotational speed of the vortex core. The strong lower frequencies most likely correspond to unsteady structures that are formed in the recirculation zone near the wall, just after the expansion.**

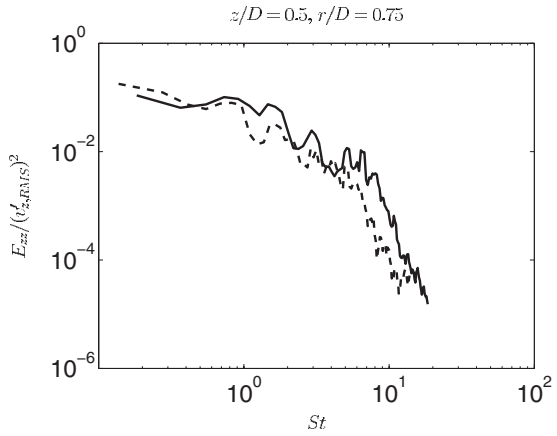


**Fig. 10 Normalized frequency spectra of resolved axial velocity fluctuations at $z/D=2$ and $r/D=0.75$ using the filtered $k$-$\omega$ model on two grids. (—) Fine grid. (– –) Coarse grid. (· –) Note the higher density of high frequencies obtained when using the fine grid.**

in this respect as well, the estimate of the reattachment length obtained from the simulation using the WALE model is not satisfactory.

It was shown by Gyllenram and Nilsson [18] that the degree of unsteadiness in the resolved velocity field is inversely related to the size of the filter width, i.e., model coefficient $\alpha$. However, too small a filter width may cause the results to deteriorate because there will be a spectral gap between the filtered scales and the scales that can potentially be resolved. Furthermore, it is preferable for the filter width to be large enough to enable the original asymptotic near-wall behavior of the turbulence model. The positive effects of introducing the filtering technique to the present test case most likely owe to a more accurate prediction of the large-scale unsteadiness. As shown by Gyllenram et al. [22], the turbulence is, at least in a time-averaged sense, extremely anisotropic in the shear layer near the sudden expansion. However, most of the anisotropy lies in the largest scales. If the large anisotropic scales are accurately resolved in space and time, a simple turbulence model is sufficient for estimating the influence of small-scale turbulence on the mean flow.

A study of the influence of the grid resolution was carried out. The local grid resolution is explicitely used in the formulation of the eddy viscosity when the filter is active. This will obviously introduce a grid dependence in the instantaneous flow field, and the time-averaged results are also expected to be affected. In spite of this, the grid dependence of the time-averaged results seems surprisingly weak and may just as well be a numerical issue. Neither were the main unsteady effects sensitive to the spatial resolution.

## Acknowledgment

This project was financed by SVC:[1] Swedish Energy Agency, ELFORSK, Svenska Kraftnät. The authors would also like to thank Dr. Ruprecht at IHS, University of Stuttgart, for support during the development of the model, and Dr. Paul A. Dellenback at the University of Wyoming, USA, for providiing the experimental data.

[1]Companies involved: CarlBro, E.ON Vattenkraft Sverige, Fortum Generation, GE Energy (Sweden), Jämtkraft, Jönköping Energi, Mälarenergi, Skellefteå Kraft, Sollefteåforsens, Statoil Lubricants, Sweco VBB, Sweco Energuide, SweMin, Tekniska Verken i Linköping, Vattenfall Research and Development, Vattenfall Vattenkraft, Waplans, and VG Power and Öresundskraft. Universities involved: Chalmers University of Technology, Luleå University of Technology, Royal institute of Technology, and Uppsala University.

## References

[1] Spalart, P. R., 2000, "Strategies for Turbulence Modeling and Simulations," Int. J. Heat Fluid Flow, **21**, pp. 252–263.
[2] John, V., 2006, "Short Review of Some Aspects in LES and VMS," Appl. Math. (Germany), **51**, pp. 321–353.
[3] Speziale, C. G., 1998, "Turbulence Modeling for Time-Dependent RANS and VLES: A Review," AIAA J., **36**, pp. 173–184.
[4] Speziale, C. G., 1998, "A Combined Large-Eddy Simulation and Time-Dependent RANS Capability for High-Speed Compressible Flows," J. Sci. Comput., **13**(3), pp. 253–274.
[5] Fasel, H. F., Seidel, J., and Wernz, S., 2002, "A Methodology for Simulations of Complex Turbulent Flows," J. Fluids Eng., **124**, pp. 933–942.
[6] Spalart, P. R., Jou, W.-H., Strelets, M., and Allmaras, S. R., 1997, "Comments on the Feasibility of LES for Wings, and on a Hybrid RANS/LES Approach," *Advances in DNS/LES, First AFOSR International Conference on DNS/LES*, Ruston, LA, Aug. 4–8, C. Liu and Z. Liu, eds. Greyden, Columbus, OH.
[7] Menter, F., Kuntz, M., and Egerov, Y., 2003, "A Scale Adaptive Simulation Model for Turbulent Flow Predictions," 41st AIAA Aerospace Sciences Meeting and Exhibit, Reno, NV, Vol. AIAA-2003-0767.
[8] Menter, F. R., Kuntz, M., and Langtry, R., 2003, "Ten Years of Industrial Experience With the SST Turbulence Model," in *Turbulence, Heat and Mass Transfer*, Begell House, New York, Vol. 4.
[9] Kok, J. C., Dol, H. S., Oskam, B., and van der Ven, H., 2004, "Extra-Large Eddy Simulation of Massively Separated Flows," 42nd AIAA Aerospace Meeting, Reno, NV, pp. 1–12.
[10] Menter, F. and Egerov, Y., 2005, "A Scale Adaptive Simulation Model Using Two-Equation Models," 45th AIAA Aerospace Sciences Meeting and Exhibit, Reno, NV, Vol. AIAA-2005–1095.
[11] Templeton, J. A., Medic, G., and Kalitzin, G., 2005, "An Eddy-Viscosity Based Near-Wall Treatment for Coarse Grid Large-Eddy Simulation," Phys. Fluids, **17**, p. 105101.
[12] Willems, W., 1996, "Numerische Simulation Turbulenter Scherströmungen mit einem Zwei-Skalen Turbulenzmodell," Ph.D. thesis, Rheinish-Westfälischen Technischen Hochschule, Aachen, Germany.
[13] Wilcox, D. C., 1988, "Reassessment of the Scale-Determining Equation for Advanced Turbulence Models," AIAA J., **26**(11), pp. 1299–1310.
[14] Dellenback, P. A., Metzger, D. E., and Neitzel, G. P., 1987, "Measurements in Turbulent Swirling Flow Through an Abrupt Expansion," AIAA J., **26**(6), pp. 669–681.
[15] Durbin, P. A., 1995, "On the $k$-$\varepsilon$, Stagnation Point Anomaly," Int. J. Heat Fluid Flow, **17**, pp. 88–89.
[16] Helmrich, T., Buntic, I., and Ruprecht, A., 2002, "Very Large Eddy Simulation for Flow in Hydraulic Turbo Machinery," *Classics and Fashion in Fluid Mechanics*, Belgrade, Yugoslavia, October 18–20.
[17] Ruprecht, A., Helmrich, T., and Buntic, I., 2003, "Very Large Eddy Simulation for the Prediction of Unsteady Vortex Motion," *Conference on Modeling Fluid Flow, CMFF'03*, 12th International Conference on Fluid Flow Technologies, Budapest, Hungary, September 3–6.
[18] Gyllenram, W. and Nilsson, H., 2006, "Very Large Eddy Simulations of Draft Tube Flow," 23rd IAHR Symposium, Yokohama, Japan, Oct., Vol. 1.2, pp. 1–10.
[19] Batten, P., Goldberg, U., and Chakravarthy, S., 2002, "LNS—An Approach Towards Embedded LES," 40th AIAA Aerospace Sciences Meeting and Exhibit, Reno, NV, Vol. AIAA-2002-0427.
[20] Wilcox, D. C., 2002, *Turbulence Modeling for CFD*, 2nd ed., DCW Industries Inc., La Cañada, CA.
[21] Schlüter, J. U., Pitsch, H., and Moin, P., 2004, "Large Eddy Simulation Inflow Conditions for Coupling With Reynolds-Averaged Flow Solvers," AIAA J., **42**(3), pp. 478–484.
[22] Gyllenram, W., Nilsson, H., and Davidson, L., 2006, "Large Eddy Simulation of Turbulent Swirling Flow Through a Sudden Expansion," 23rd IAHR Symposium, Yokohama, Japan, Oct., Vol. 1.2, pp. 1–10.
[23] Nilsson, H., 2002, "Numerical Investigations of Turbulent Flow in Water Turbines," Ph.D. thesis, Chalmers University of Technology, Göteborg, Sweden.
[24] Van Doormaal, J. P. and Raithby, G. D., 1984, "Enhancements of the SIMPLE Method for Predicting Incompressible Fluid Flows," Numer. Heat Transfer, **7**, pp. 147–163.
[25] van Leer, B., 1974, "Towards the Ultimate Conservative Difference Scheme Monotonicity and Conservation Combined in a Second Order Scheme," J. Comput. Phys., **14**, pp. 361–370.
[26] Nicoud, F. and Ducros, F., 1999, "Subgrid-Scale Stress Modelling Based in the Square of the Velocity Gradient Tensor," Flow, Turbul. Combust., **62**, 183–200.
[27] Jeong, J., and Hussain, F., 1995, "On the Identification of a Vortex," J. Fluid Mech., **285**, pp. 69–94.

# Linear Stability of Weakly Forced Taylor-Vortex Flow

**Roger E. Khayat**
Department of Mechanical and Materials Engineering,
The University of Western Ontario,
London, ON, N6A 5B9, Canada
e-mail: rkhayat@uwo.ca

*Linear stability analysis of fully developed axisymmetric steady spatially modulated Taylor–Couette flow (TCF) is carried out in the narrow-gap limit. In contrast to unforced TCF, only the vortical base flow is possible in the forced case. It is found that the forcing tends to generally destabilize the base flow, especially around the critical point corresponding to unforced flow. Both the critical Taylor number and wave number are found to essentially linearly decrease with modulation amplitude.*
[DOI: 10.1115/1.2907411]

## 1 Introduction

One of the simplest geometric perturbations of Taylor–Couette flow (TCF) is when one or two of the cylindrical boundaries are allowed to have an axially periodic radius. Besides the work on the effect of localized radius variation [1,2], the only work on extended (periodic or random) radius variation known to us is the experimental work by Koschmieder [3], Ikeda and Maxworthy [4], and Painter and co-workers [5,6]. More recently, Khayat and co-workers [7,8] theoretically examined the effect of cylinder spatial modulation on the onset of vortex flow. Their work was, however, limited to steady state flow.

The current study considers a geometry consisting of two coaxial cylinders such that the outer smooth cylinder is stationary while the inner rotating cylinder has an axisymmetric wavy surface. This geometry can be considered as an extension of Wimmer's cone-cylinder configuration [9], and is closely related to the flow in an hourglass geometry [10]. The spatial modulation of cylindrical flow is also closely analogous to the presence of end effects in TCF. In both cases, the forcing makes itself felt at precritical values of the Taylor number, $\mathrm{Ta}_c$, and the periodicity of the vortex pattern is dictated by the spacing of the cylinder ends and modulation wave number. It is well established that vortices adjacent to the end plates form far below $\mathrm{Ta}_c$ [11]. When the precritical Taylor number ($\mathrm{Ta}<\mathrm{Ta}_c$) is gradually increased, additional vortices form on top of each other until the vortices coming from the (symmetric) top and bottom plates meet in the middle of the column, at the critical Taylor number predicted by linear analysis.

In close connection with the present problem, Li and Khayat [7] theoretically examined the steady modulated axisymmetric Taylor-vortex flow, with weak forcing. The present work addresses the important question regarding the stability of the steady states previously computed [7].

## 2 Problem Formulation and Solution Procedure

Consider the flow of an incompressible Newtonian fluid, of density $\rho$ and kinematic viscosity $\nu$, between the two concentric infinite cylinders. The inner cylinder is assumed to be sinusoidally modulated along the axial direction, with amplitude $A_i$, and the outer cylinder is straight. The inner cylinder is assumed to rotate at constant angular velocity, $\Omega_i$, while the outer cylinder is at rest. The radii of the inner and outer cylinders are denoted by $R_i$ and $R_o$, and $\bar{R}_i$ is the mean radius of the inner cylinder. The conservation equations are reduced to the narrow-gap limit by introducing dimensionless coordinates, $x$ and $z$, in the radial and axial directions, respectively, time $t$, pressure $p$, and velocity components $u$, $v$, $w$, in the radial, azimuthal, and axial directions, respectively. After nondimensionlization, the conservation equations in the narrow-gap limit are obtained, namely [7],

$$u_x + w_z = 0 \tag{1a}$$

$$u_t + uu_x + wu_z = \mathrm{Ta}\, v^2 + u_{xx} + u_{zz} - p_x \tag{1b}$$

$$v_t + uv_x + wv_z = v_{xx} + v_{zz} \tag{1c}$$

$$w_t + uw_x + ww_z = w_{xx} + w_{zz} - p_z \tag{1d}$$

A subscript denotes partial differentiation. The Taylor number Ta is defined in terms of the Reynolds number Re and the average gap-to-radius ratio, $\delta$. Thus,

$$\mathrm{Ta} = \mathrm{Re}^2\,\delta, \quad \mathrm{Re} = \frac{\bar{R}_i \Omega_i \bar{D}}{\nu}, \quad \delta = \frac{\bar{D}}{\bar{R}_i} \tag{2}$$

where $\bar{D}=R_o-\bar{R}_i$ is the mean gap width. The dimensionless physical domain is defined by $(x,z)\in[-1/2+\varepsilon\sin(\alpha z),1/2]\times(-\infty,+\infty)$, where $\varepsilon=A_i/\bar{R}_i$ is a measure of the dimensionless modulation amplitude, and $\alpha$ is the modulation wave number (in units of $\bar{D}$). Note that $\varepsilon=A_i/\bar{R}_i=(A_i/\bar{D}\bar{D}/\bar{R}_i)=(A_i/\bar{D})\delta$. Thus, $A_i/\bar{D}=\varepsilon/\delta$, which is assumed to be small. In this case, $\varepsilon\ll\delta$, and is taken as the small parameter in the problem. Following the methodology in Ref. [7], Eqs. (1*a*)–(1*d*) are solved by first mapping the physical domain in the $(x,z)$ plane onto the rectangular domain $(\eta,\xi)\in[-1/2,1/2](-\infty,+\infty)$. In this case, the mapping is given by

$$\tau(x,z,t)=t, \quad \eta(x,z,t)=\left(\frac{1}{1-\varepsilon\sin(\alpha z)}\right)\left(x-\frac{\varepsilon\sin(\alpha z)}{2}\right)$$

and $\xi(x,z,t)=z$. Adherence conditions are assumed at the cylinders. A regular perturbation expansion is used for the velocity and pressure. Here, Ta, $\varepsilon$, and $\alpha$ are the only similarity parameters in the present problem.

The steady base flow solution $(\mathbf{u}^s,p^s)$, where $\mathbf{u}^s(u^s,v^s,w^s)^T$, is the same as in Ref. [7], and will therefore not be detailed here. To leading order in $\varepsilon$, the solution that corresponds to the flow between the two straight cylinders is recovered. The equations to $O(\varepsilon)$ is a set of nonhomogenous ordinary differential equations, which together with the corresponding homogeneous boundary conditions constitute a boundary-value problem of the two-point type [7].

Linear stability analysis is carried out by imposing infinitesimal disturbances in velocity and pressure on the mean flow. Since the base flow is periodic $\xi$ with wavelength $2\pi/\alpha$, the disturbance equations are transformed into ordinary differential equations using Floquet theory [12]. Thus, the disturbance flow is considered as a superposition of the cylinder wall modulation, with wave number $\alpha$, and perturbation wave with wave number $\beta$: In this case,

$$\mathbf{u}(\eta,\xi,\tau)=\mathbf{u}^s(\eta,\xi)+\sum_{n=-N}^{N}\mathbf{u}^{(n)}(\eta)e^{i[(n\alpha+\beta)\xi-\lambda\tau]}$$

Contributed by the Fluids Engineering Division of ASME for publication in the JOURNAL OF FLUIDS ENGINEERING. Manuscript received February 19, 2007; final manuscript received December 3, 2007; published online April 25, 2008. Assoc. Editor: Paul Durbin.

  

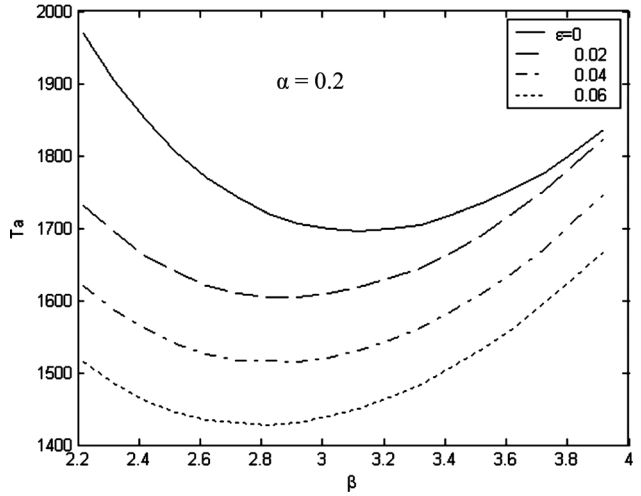


**Fig. 1 Neutral stability curves in the ($\beta$-Ta) plane. Here, $\alpha$ =0.2 and $\varepsilon$=0,0.02,0.04,0.06.**

$$p(\eta,\xi,\tau) = p^s(\eta,\xi) + \sum_{n=-N}^{N} p^{(n)}(\eta) e^{i[(n\alpha+\beta)\xi-\lambda\tau]} \tag{3}$$

where $N$ is the number of modes. The $\eta$ dependent amplitudes $(\mathbf{u}^{(n)}, p^{(n)})$ must be determined. In addition, $\lambda$ is the complex eigenvalue. Upon substituting expressions (3) into (1*a*)–(1*d*), projecting onto the various modes and neglecting terms of $O(\varepsilon^2)$, Eqs. (1*a*)–(1*d*) are reduced to a linearized system for the disturbance coefficients $\mathbf{u}^{(n)}$ and $p^{(n)}$. Obviously, the resulting homogenous system (and boundary conditions) is far more complicated than the classical stability problem in the absence of modulation ($\varepsilon$=0). However, the problem is reduced to an infinite set of linear homogenous ordinary differential equations that can be solved in a similar manner to the classical problem. The selection of the solution method is important and will be addressed next.

## 3 Results and Discussion

An obvious limit case of the modulated flow is the flow between straight cylinders ($\varepsilon=\alpha=0$), which will be taken as reference to validate the current solution methodology. In this limit, the critical Taylor number and corresponding wave number are computed and found to be $\mathrm{Ta}_c$=1695 and $\beta_c$=3.12, respectively, which are in good agreement with the values in the literature [11]. This critical threshold is also taken as the starting point in the computations for modulated flow. The critical Taylor number $\mathrm{Ta}_{cr}$ and corresponding wave number $\beta_{cr}$, for the loss of stability of the modulated base flow, are calculated for various wall modulation amplitudes. Note that $\mathrm{Ta}_c=\mathrm{Ta}_{cr}(\varepsilon=0,\alpha=0)$ and $\beta_c=\beta_{cr}(\varepsilon=0,\alpha=0)$.

The influence of wall modulation on the overall stability picture is typically illustrated in Fig. 1. The neutral stability curves are plotted in the (Ta-$\beta$) plane for $\alpha$=0.2 and different values of $\varepsilon$. In the absence of modulation ($\varepsilon$=0), the neutral stability curve for conventional Taylor-vortex flow is recovered. The neutral stability curves for $\varepsilon>0$ appear all to be below that corresponding to $\varepsilon$=0, for any $\beta$ value. However, at small modulation amplitude, the drop in threshold Taylor number is not uniform (with respect to $\beta$). Indeed, the two curves corresponding to $\varepsilon$=0 and $\varepsilon$=0.02 show that there a relatively significant drop in Ta for small $\beta$ (roughly 15% at $\beta$=2.2), but hardly any drop for $\beta>4$. Thus, there is a significant coupling between the effects of wall amplitude and wall wave number. The lack of influence of the wall modulation on the critical Taylor number for large wave number suggests that when a large number of vortices are about to form, the size of the modulation becomes irrelevant; the small vortex still sees the wall modulation as having a large (infinite) wavelength.

Linear Stability of Weakly Forced Taylor-Vortex Flow

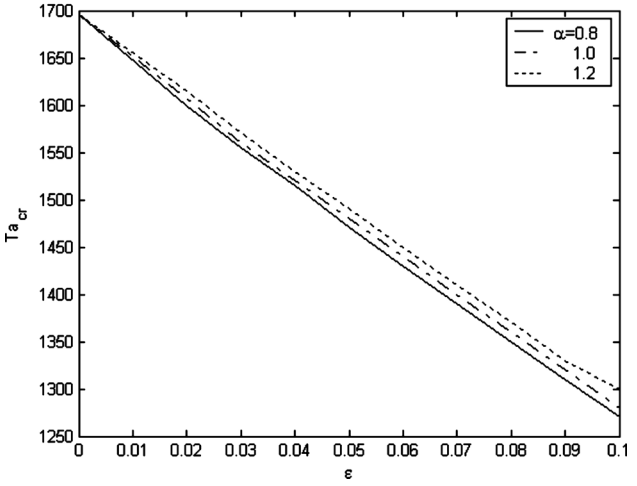


**Fig. 2 Variation of the critical Taylor number with modulation amplitude $\varepsilon$, for $\alpha$=0.8,1.0,1.2**

The drop in Ta becomes more uniform for larger $\varepsilon$. Additional calculations show that the drop in Ta essentially becomes uniform when the modulation wave number is small ($\alpha<0.05$). The marginal stability curves are expected to collapse onto the $\varepsilon$=0 curve. This apparent similarity can be further confirmed upon examining the governing equations in the limit $\alpha\rightarrow 0$. In this limit, the base modulated flow is the same as that corresponding to the flow between the straight cylinders. It is not difficult to show in this case that the linear stability problem has exactly the same form as that corresponding to the flow between cylinders of dimensionless

Linear Stability of Weakly Forced Taylor-Vortex Flow

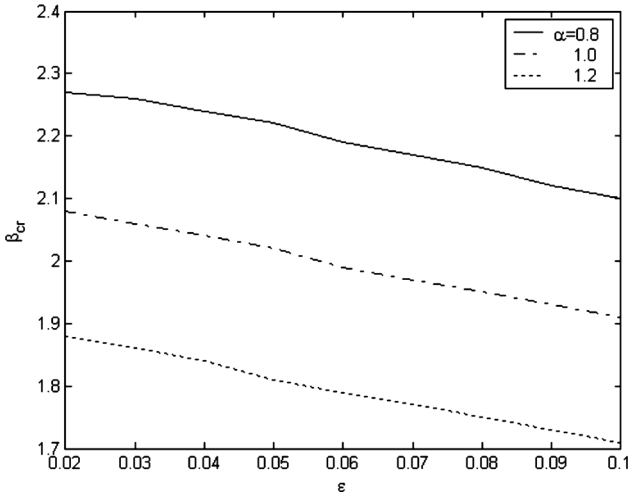


**Fig. 3 Variation of the critical disturbance wave number with modulation amplitude $\varepsilon$, for $\alpha$=0.8,1.0,1.2**

gap $1-\varepsilon\alpha\xi$. This gap linearly decreases with $\xi$ (assuming $\xi \geqslant 0$). The effective Taylor number in this case decreases with $\varepsilon$, making the flow unstable.

The influence of wall modulation on criticality is illustrated in Figs. 2 and 3, where the critical Taylor number and critical disturbance wave number are plotted against $\varepsilon$ for different $\alpha$, respectively. In this case, both $\mathrm{Ta}_{\mathrm{cr}}$ and $\beta_{\mathrm{cr}}$ monotonically decrease with $\varepsilon$. The decrease is essentially linear, reflecting the similarity character as discussed above, particularly at small $\alpha$. This linear dependence on $\varepsilon$ is somewhat unexpected for large $\alpha$ given the trend shown in Fig. 1. Indeed, that figure clearly shows the nonlinear dependence in general, especially at large $\beta$. It is also interesting to observe that $\beta_{\mathrm{cr}}$ appears to linearly decrease with $\varepsilon$ regardless of the value of $\alpha$. Moreover, both critical numbers more rapidly decrease at smaller $\alpha$. This means that smaller modulation wavenumbers tend to be more destabilizing [13,14].

## 4 Conclusion

The linear stability analysis of spatially modulated TCF is examined in this study. The inner cylinder wall is sinusoidally modulated and rotating, while the outer cylinder is straight and at rest. Floquet theory is used to solve the stability problem. The modulated flow is always vortical no matter how small Ta is. It is found that cylinder modulation tends to destabilize the base vortex flow. However, the decrease in Taylor number corresponding to the onset of instability is not the same for any disturbance wave number. The critical Taylor and wave numbers tend to linearly decrease with modulation amplitude. Finally, it is shown that the results for the modulated flow are collapsible onto those of unforced Taylor–Couette for small modulation wave number.

## References


[1] Eagles, P. M., and Eames, K., 1983, "Taylor Vortices Between Almost Cylindrical Boundaries," J. Eng. Math., **17**, pp. 263–280.

[2] Ning, L., Ahlers, G., and Cannell, D. S., 1990, "Wave-Number Selection and Traveling Vortex Waves in Spatially Ramped Taylor–Couette Flow," Phys. Rev. Lett., **64**, pp. 1235–1238.

[3] Koschmieder, E. L., 1975, "Effect of Finite Disturbances on Axisymmetric Taylor Vortex Flow," Phys. Fluids, **18**, pp. 499–503.

[4] Ikeda, E., and Maxworthy, T., 1994, "Spatially Forced Corotating Taylor–Couette Flow," Phys. Rev. E, **49**, pp.5218–5224.

[5] Painter, B. D., and Behringer, R. P., 1998, "Effects of Spatial Disorder on the Transition to Taylor Vortex Flow," Europhys. Lett., **44**, pp. 599–605.

[6] Zimmermann, W., Painter, B. D., and Behringer, R. P., 1998, "Pattern Formation in an Inhomogeneous Environment," Eur. Phys. J. B, **5**, pp. 757–770.

[7] Li, Z., and Khayat, R. E., 2004, "Pattern Formation in Weakly Forced Taylor–Couette Flow," Phys. Rev. E, **69**, 046305.

[8] Zhang, J., and Khayat, R. E., 2006, "Finite-Amplitude Modulated Taylor–Couette Flow," Phys. Fluids, **18**, 044105.

[9] Wimmer, M., 1995, "An Experimental Investigation of Taylor Vortex Flow Between Conical Cylinders," J. Fluid Mech., **292**, pp. 205–227.

[10] Wiener, R. J., Snyder, G. L., Prange, M. P., Frediani, D., and Diaz, P. R., 1997, "Periodic-Doubling Cascade to Chaotic Phase Dynamics in Taylor Vortex Flow With Hourglass Geometry," Phys. Rev. E, **55**, pp. 5489–5497.

[11] Koschmieder, E. L., 1992, *Bénard Cells and Taylor Vortices* (Cambridge University Press, London).

[12] Codington, S. A., and Levinson, N., 1965, *Theory of Ordinary Differential Equations*, McGraw-Hill, New York.

[13] Peyret, R., 2002, *Spectral Methods for Incompressible Viscous Flow* (Applied Mathematics Science), Springer, New York, Vol. 148.

[14] Ache, G. A., and Cores, D., 1995, "Note on the Two-Point Boundary Value Solution of the Orr–Sommerfeld Stability Equation," J. Comput. Phys., **116**, pp. 180–183.

# Fluid Flow in an Annular Microchannel Subjected to Uniform Wall Injections

**Mohammad Layeghi**
Ph.D.
Department of Wood & Paper Science & Technology,
University of Tehran,
P.O. Box 31485-77871,
Tehran, Karaj, Iran
e-mail: mlayeghi@nrf.ut.ac.ir

**Hamid Reza Seyf**
B.S. student
Karaj Islamic Azad University,
P.O. Box 31485-313,
Tehran, Karaj, Iran

*Analytical analysis of fluid flow in an annular microchannel subjected to uniform wall injection at various Reynolds numbers is presented. The classical Navier–Stokes equations are used in the present study. Mathematically, using an appropriate change of variable, Navier–Stokes equations are transformed to a set of nonlinear ordinary differential equations. The governing equations are analytically solved using series solution method. Some analytical results are given for the prediction of velocity profiles and pressure distributions in annular microchannels. The agreement between the computational fluid dynamics and the analytical predictions is very good. However, the analytical results are valid in a limited range of radius ratios and needs more study.*
[DOI: 10.1115/1.2911655]

*Keywords: laminar and incompressible fluid flow, annular microchannel, Navier–Stokes equations, analytical method*

## Introduction

Analysis of fluid flow in annular microchannels has great importance in design and utilization of microfluidic devices. Generally, these devices have applications in many areas of engineering, including propulsion and power generations, microsatellites, microaerial vehicles, inkjet printer heads, and bioanalytical or medical instruments [1,2]. Novel electrical devices [3,4] and annular micromixers are good examples [5,6] with high technological innovation. Annular microchannels can also be used in chemical and heat transfer applications including microreactors or microheat pipes [7–9].

Investigations of low-Reynolds number hydrodynamics naturally fall into the fluid dynamics realm of long interest to the chemical and mechanical engineering community [10,11]. The most important new themes introduced by the small length scales of microfluidic devices are the significant role of surface forces. Fluid motions in these small-scale systems are usually driven by applied pressure differences, electric fields, capillary forces, gradients in interfacial tension, etc. [12,13].

Some discrepancies have been reported between flow measurements made in small channels and experiences from classical theory based on solutions to the Navier–Stokes equations. However, a careful consideration of the experimental results for pressure driven flows of liquids demonstrates that in almost all cases there are no significant discrepancies [14].

For gases, the theory is in excellent agreement with experiment if compressibility and finite wall slip are properly accounted for [15]. Furthermore, at the scale of hundreds of nanometers, at least for surfaces that are essentially atomically smooth, there is evidence for slip [16]. Thus, it is our understanding that for small molecule liquids, such as water, the familiar continuum description remains an appropriate starting point for analysis of microdevices.

There is substantial amount of work done on analytic solutions of similar flows [17–20]. The earliest studies of steady flows across permeable and stationary walls can be traced back to Berman [17]. He investigated the laminar, two-dimensional flow of a viscous incompressible fluid driven by uniform injection or suction in a rectangular channel with porous walls. In that study, he assumed that the transverse velocity component is independent of the streamwise coordinate. He reduced the Navier–Stokes equations to a single, nonlinear, fourth-order, ordinary differential equation with four boundary conditions. Numerous studies of channel flows with permeable walls have been followed after Berman [17]. The other most important works have been done by Terrill [18,19], who extended Berman's small Reynolds number solution, and Zlnchenko and Fedorova [20], who studied flow in an annular duct with large injection at the walls.

The basic idea of this paper is to present an innovative exact solution of Navier–Stokes equations, which seems to be valid in wide ranges of dimensions including nano-, micro-, and higher scales and wide ranges of Reynolds numbers. The Navier–Stokes equations are solved for the study of fluid flow in an annular microchannel subjected to uniform wall injections. The presented analytical results can also be used for the analysis of vapor flow in annular channels. This work may be considered as an extension of the previous work of the first author about cylindrical microchannels [21].

## Governing Equations

The axisymmetric motion of a fluid flow in a cylindrical microchannel subjected to uniform wall injection is considered here (Fig. 1).

The present model is based on the following assumptions:

(1) The vapor flow is laminar and in steady state and the fluid is incompressible.
(2) The Knudsen number $\mathrm{Kn}=\lambda/l$, where $\lambda$ is the mean free path of the fluid, is small enough in such a way that the continuum model or Navier–Stokes equations with no-slip boundary conditions are applicable [22].
(3) The properties of the fluid are assumed to be constant.
(4) Uniform injection occurs at the inner and outer walls from $z=0$ to $z=L$ along the annular microchannel (Fig. 1).
(5) The left end of the microchannel ($z=0$) is closed.

The governing equations for the conservation of mass, $z$-momentum, and $r$-momentum can be written as

$$\frac{\partial w}{\partial z}+\frac{1}{r}\frac{\partial}{\partial r}[rv]=0 \tag{1}$$

$$\rho\left(w\frac{\partial w}{\partial z}+v\frac{\partial w}{\partial r}\right)=-\frac{\partial P}{\partial z}+\mu\left[\frac{\partial^2 w}{\partial z^2}+\frac{1}{r}\frac{\partial}{\partial r}\left(r\frac{\partial w}{\partial r}\right)\right] \tag{2}$$

$$\rho\left(w\frac{\partial v}{\partial z}+v\frac{\partial v}{\partial r}\right)=-\frac{\partial P}{\partial r}+\mu\left[\frac{\partial^2 v}{\partial z^2}+\frac{1}{r}\frac{\partial}{\partial r}\left(r\frac{\partial v}{\partial r}\right)-\frac{v}{r^2}\right] \tag{3}$$

where $w$ and $v$ are the velocity components in the $z$ and $r$ directions, respectively, and $P$ is the fluid pressure. $\rho$ and $\mu$ are the

Contributed by the Fluids Engineering Division of ASME for publication in the JOURNAL OF FLUIDS ENGINEERING. Manuscript received June 10, 2007; final manuscript received January 15, 2008; published online May 1, 2008. Assoc. Editor: Dimitris Drikakis.

  

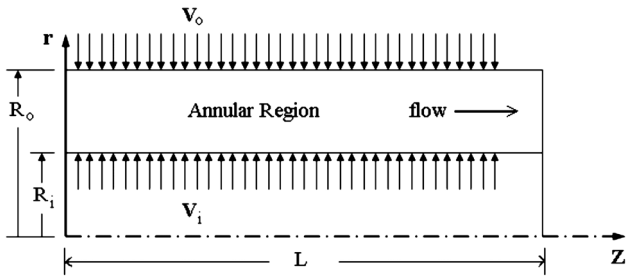


**Fig. 1 Fluid flow in an annular microchannel subjected to uniform wall injections along with coordinate system**

density and viscosity of the fluid, respectively. The boundary conditions are defined as follows:

$$w(0,r) = v(0,r) = 0 \tag{4a}$$

$$w(z,R_i) = 0 \tag{4b}$$

$$v(z,R_i) = V_i \tag{4c}$$

$$w(z,R_o) = 0 \tag{4d}$$

$$v(z,R_o) = V_o \tag{4e}$$

$$P(0,r) = 0 \tag{4f}$$

where $L$ is the injection length on the microchannel and $R_i, R_o$ are the inner and outer radii of the annular microchannel, respectively.

## Method of Solution

The governing equations can be transformed to a set of nonlinear ordinary differential equations using appropriate change of variables based on the physics of fluid flow in annular microchannels. Only one symmetrical half of the microchannel longitudinal section is considered in the present analysis. It can be easily shown that the axial and radial velocity components can be expressed as

$$w(z,r) = zG(r) \tag{5a}$$

$$v(z,r) = H(r) \tag{5b}$$

Equation (5*a*) can be obtained from the conservation of mass and boundary conditions for the axial velocity. Equation (5*b*) can be obtained from Eq. (1) by considering that $\partial w/\partial z$ is independent of $z$. Equations (5*a*) and (5*b*) are valid in a wide range of radial Reynolds numbers and for various microchannel radius ratios.

Substitution of Eqs. (5*a*) and (5*b*) into Eqs. (1)–(3) gives the following set of ordinary differential equations:

$$G + \frac{1}{r}H + H' = 0 \tag{6a}$$

$$\frac{\partial P}{\partial z} = \left\{ \mu\left[\frac{1}{r}G' + G''\right] - \rho[G^2 + HG']\right\} z \tag{6b}$$

$$\frac{\partial P}{\partial r} = \mu\left(H'' + \frac{1}{r}H' - \frac{1}{r^2}H\right) - \rho HH' \tag{6c}$$

where $\vartheta$ is the kinematic viscosity of the fluid. Combining Eqs. (6*b*) and (6*c*) and removing the pressure gives

$$\frac{d}{dr}\left\{ \mu\left[\frac{1}{r}G' + G''\right] - \rho[G^2 + HG']\right\} = 0 \tag{7}$$

Substitution of function $G$ from Eq. (6*a*) in terms of function $H$ into Eq. (7) gives

$$\begin{aligned}\vartheta(r^4H^{(iv)} + 2r^3H''' - 3r^2H'' + 3rH' - 3H) \\ = r^4H'''H - r^3H''H - r^4H''H' - r^3H'^2 - 3r^2H'H + 4rH^2\end{aligned} \tag{8}$$

Equation (8) is a fourth-order nonlinear differential equation and therefore, four boundary conditions are needed for its solution. The associated boundary conditions in terms of $H(r)$ are obtained from Eqs. (4*b*)–(4*d*) as

$$H(r = R_i) = V_i \tag{9a}$$

$$H(r = R_o) = V_o \tag{9b}$$

$$\left(\frac{1}{r}H + H'\right)_{r=R_i} = 0 \tag{9c}$$

$$\left(\frac{1}{r}H + H'\right)_{r=R_o} = 0 \tag{9d}$$

Equation (8) with boundary conditions (9*a*)–(9*d*) is solved using a series solution method. The solution procedure is as follows:

(1) Apply a change of variable: $\omega = r - R_i$ to Eqs. (8) and (9*a*)–(9*d*).
(2) Solve Eq. (8) to find $H(\omega)$ and then find $H(r)$.
(3) Use Eq. (6*a*) to find $G(\omega)$ and then find $w(z,r) = zG(r)$.
(4) Find pressure drop using Eqs. (6*b*) and (6*c*).

Applying the change of variable to Eqs. (8) and (9*a*)–(9*d*) gives

$$\begin{aligned}\vartheta((\omega + R_i)^4H^{(iv)} + 2(\omega + R_i)^3H''' - 3(\omega + R_i)^2H'' \\ + 3(\omega + R_i)H' - 3H) \\ = (\omega + R_i)^4H'''H - (\omega + R_i)^3H''H - (\omega + R_i)^4H''H' \\ - (\omega + R_i)^3H'^2 - 3(\omega + R_i)^2H'H + 4(\omega + R_i)H^2\end{aligned} \tag{10}$$

$$H(\omega = 0) = V_i \tag{11a}$$

$$H(\omega = R_o - R_i) = V_o \tag{11b}$$

$$\left(\frac{1}{R_i}H + H'\right)_{\omega=0} = 0 \tag{11c}$$

$$\left(\frac{1}{R_o}H + H'\right)_{\omega=R_o-R_i} = 0 \tag{11d}$$

In order to solve Eq. (10), a series solution in the following form is used.

$$H(\omega) = a_0 + a_1\omega + a_2\omega^2 + a_3\omega^3 + a_4\omega^4 + \ldots \tag{12}$$

Inserting the above series with the first five terms into Eqs. (10) and (11*a*)–(11*d*) gives

$$a_0 = V_i \tag{13a}$$

$$a_1 = -V_i/R_i \tag{13b}$$

$$a_2 = \alpha - (R_o - R_i)a_3 - (R_o - R_i)^2a_4 \tag{13c}$$

$$a_3 = \frac{\gamma_2(\beta - \alpha) + \beta_2(\alpha - \gamma) + (R_o - R_i)^2(\gamma - \beta)}{(\gamma_2\beta_1 - \beta_2\gamma_1) + (\beta_2 - \gamma_2)(R_o - R_i) + (\gamma_1 - \beta_1)(R_o - R_i)^2} \tag{13d}$$

$$a_4 = \frac{\beta_1(\gamma - \alpha) + (R_o - R_i)(\beta - \gamma) + \gamma_1(\alpha - \beta)}{(\gamma_2\beta_1 - \beta_2\gamma_1) + (\beta_2 - \gamma_2)(R_o - R_i) + (\gamma_1 - \beta_1)(R_o - R_i)^2} \tag{13e}$$

where in the above equations

$$\alpha = -\frac{V_o + V_i[2 - 1/\kappa]}{(R_o - R_i)^2}, \quad \beta = \frac{2V_i}{R_i R_o[3 - \kappa]}, \quad \gamma = -\frac{3V_i(\vartheta + R_i V_i)}{R_i^2(V_i R_i^2 + 3\vartheta)}$$

$$\beta_1 = \frac{4 - \kappa}{3 - \kappa}(R_o - R_i), \quad \beta_2 = \frac{5 - \kappa}{3 - \kappa}(R_o - R_i)^2 \tag{14}$$

$$\gamma_1 = -\frac{6\vartheta R_i}{(V_i R_i^2 + 3\vartheta)}, \quad \gamma_2 = -\frac{12\vartheta R_i^2}{(V_i R_i^2 + 3\vartheta)}, \quad \kappa = \frac{R_i}{R_o}$$

After finding $H(\omega)$, the function $G$ is obtained using Eq. (6*a*) as

$$G(r) = -\frac{a_0}{r} - a_1\left(2 - \frac{R_i}{r}\right) - a_2(r - R_i)\left(3 - \frac{R_i}{r}\right) - a_3(r - R_i)^2\left(4 - \frac{R_i}{r}\right) - a_4(r - R_i)^3\left(5 - \frac{R_i}{r}\right) - \ldots \tag{15}$$

Finally, the velocity components $w, v$ can be obtained as

$$w(z,r) = z\left(-\frac{a_0}{r} - a_1\left(2 - \frac{R_i}{r}\right) - a_2(r - R_i)\left(3 - \frac{R_i}{r}\right) + \ldots\right) \tag{16a}$$

$$v(r) = a_0 + a_1(r - R_i) + a_2(r - R_i)^2 + \ldots \tag{16b}$$

It is important to note that this solution is an approximate series solution. It can be easily shown that by considering more terms in the series (12), a bifurcation occurs in the series coefficients and more than one solution is obtained. Furthermore, by a number of comparisons with computational fluid dynamics (CFD) results, it has been found that this solution is acceptable at large radius ratios, namely, $R_i/R_o \geqslant \delta_{\min}$ in a wide range of radial Reynolds numbers where $\delta_{\min}$ seems to be dependent on the ratio of radial injection velocities $V_i$ and $V_o$.

The pressure drop can be easily obtained by the integration of Eq. (6*b*) along the annular microchannel. Substitution of functions $G$ and $H$ into Eq. (6*b*) and integration from $z=0$ to $z=L$ gives

$$P(z,r) - P(0,r) = \frac{z^2}{2}\left\{\frac{c_{-3}}{r^3} + \frac{c_{-2}}{r^2} + \frac{c_{-1}}{r} + c_0 + c_1 r + \ldots + c_6 r^6\right\} \tag{17}$$

where in the above equation

$$c_{-3} = -\mu(a_2 R_i^2 + a_4 R_i^4 + 2V_i - a_3 R_i^3)$$

$$c_{-2} = -\rho(a_2^2 R_i^4 - 2a_2 a_3 R_i^5 + a_3^2 R_i^6 + 2a_2 a_4 R_i^6 - 2a_3 a_4 R_i^7 + a_4^2 R_i^8 + 5a_2 V_i R_i^2 - 5a_3 V_i R_i^3 + 5a_4 V_i R_i^4 + 6V_i^2)$$

$$c_{-1} = -\mu(3a_2 - 9a_3 R_i + 18a_4 R_i^2) - \rho\left(-8a_2^2 R_i^3 + 20a_2 a_3 R_i^4 - 12a_3^2 R_i^5 - 24a_2 a_4 R_i^5 + 28a_3 a_4 R_i^6 - 16a_4^2 R_i^7 - 21a_2 V_i R_i + 29a_3 V_i R_i^2 - 37a_4 V_i R_i^3 - 10\frac{V_i^2}{R_i}\right)$$

$$c_0 = -16\mu(a_3 - 4a_4 R_i) - \rho\left(23a_2^2 R_i^2 - 73a_2 a_3 R_i^3 + 54a_3^2 R_i^4 + 107a_2 a_4 R_i^4 - 150a_3 a_4 R_i^5 + 100a_4^2 R_i^6 + 27a_2 V_i - 51a_3 V_i R_i + 86a_4 V_i R_i^2 + 4\frac{V_i^2}{R_i^2}\right)$$

$$c_1 = -45\mu a_4 - \rho\left(-24a_2^2 R_i + 117a_2 a_3 R_i^2 - 117a_3^2 R_i^3 - 224a_2 a_4 R_i^3 + 401a_3 a_4 R_i^4 - 320a_4^2 R_i^5 + 37a_3 V_i - 9a_2\frac{V_i}{R_i} - 86a_4 V_i R_i\right)$$

$$c_2 = -\rho\left(6a_2^2 - 77a_2 a_3 R_i + 129a_3^2 R_i^2 + 229a_2 a_4 R_i^2 - 591a_3 a_4 R_i^3 + 591a_4^2 R_i^4 + 39a_4 V_i - 8a_3\frac{V_i}{R_i}\right)$$

$$c_3 = -\rho\left(13a_2 a_3 - 63a_3^2 R_i - 104a_2 a_4 R_i + 474a_3 a_4 R_i^2 - 656a_4^2 R_i^3 - 5a_4\frac{V_i}{R_i}\right)$$

$$c_4 = -\rho(8a_3^2 + 12a_2 a_4 - 177a_3 a_4 R_i + 418a_4^2 R_i^2), \quad c_5 = -\rho(17a_3 a_4 - 128a_4^2 R_i),$$

$$c_6 = -\rho(10a_4^2) \tag{18}$$

Equation (17) must be used with care for the prediction of pressure drop in an annular microchannel. It may not be accurate when used for large scale annular channels or small radius ratios.

## Results and Discussion

The saturated water vapor flow in an annular microchannel subjected to uniform water vapor flow injection is investigated here as a test case.

The saturated vapor properties at temperature $T_{\text{sat}}=373.15$ K are $\mu=120.3e-7$ Pa s, $\rho=0.5974$ kg/m$^3$, $C_p=2.034$ kJ/kg K, $h_{fg}=2251.2$ kJ/kg, $\gamma=1.3$, and $R_g=0.4615$ kJ/kg K. $C_p$ and $h_{fg}$ are the heat capacity of the vapor and the latent heat of vaporization, respectively, and $R_g$ is the vapor gas constant. Furthermore, assume an annular microchannel with radii: $R_o=100$ $\mu$m and $R_i=80$ $\mu$m, and injection length of $L=10$ cm subjected to two sets of radial Reynolds numbers: $(\text{Re}_{r,i}, \text{Re}_{r,i})=(0.6e-6, 3.0e-6)$ and $(\text{Re}_{r,i}, \text{Re}_{r,i})=(2.4e-6, 3.0e-6)$. It can be easily shown that the maximum Mach number in the microchannel occurs at $z=L$ and is smaller than 0.3 and the Knudsen number is about $10^{-3}$ in these two sets of radial Reynolds numbers. Therefore, the vapor can be assumed to be incompressible and the Navier–Stokes equations with no-slip boundary conditions are applicable [22].

Figure 2 shows the velocity profiles along the microchannel for these two sets of radial Reynolds numbers. It can be seen that as the radial Reynolds number increases the model works well and shows the evolution of the velocity profiles reasonably.

The vapor pressure distributions along the inner and outer walls of the microchannel for two sets of radial Reynolds numbers are shown in Fig. 3. It can be seen that pressure distributions are parabolic with small differences between the inner and outer walls. Similar parabolic distribution has been observed in a cylindrical microchannel [21]. However, the approximate solution discussed in this paper may not be valid in some other situations.

Figure 4 shows a comparison between the numerically predicted velocity profiles using a computer code [23] and the analytical results using Eq. (16*a*) at several stations along the annular channel. Three different meshes $40\times80$, $60\times120$, and $80\times160$ have been used for obtaining grid independent numerical results. It can be seen that the analytical and numerical results are very close together, particularly near the beginning ($z=0$) of the channel. The maximum difference between the analytical and numerical velocity profiles has been found 2% in the worst case at $z=0.2$ m and near $r=0.044$ m. Similar results are obtained at higher radial Reynolds numbers.

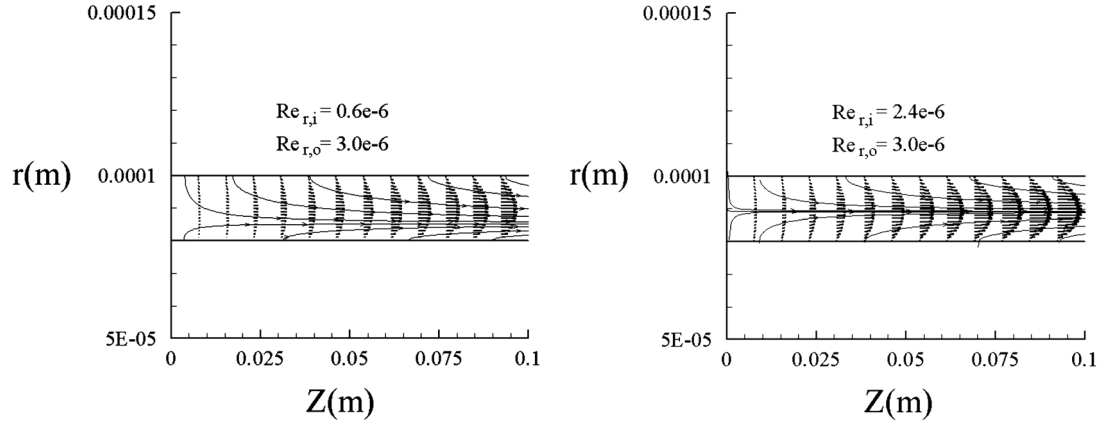


**Fig. 2 Velocity profiles in an annular microchannel subjected to uniform wall injection at two different sets of radial Reynolds numbers**

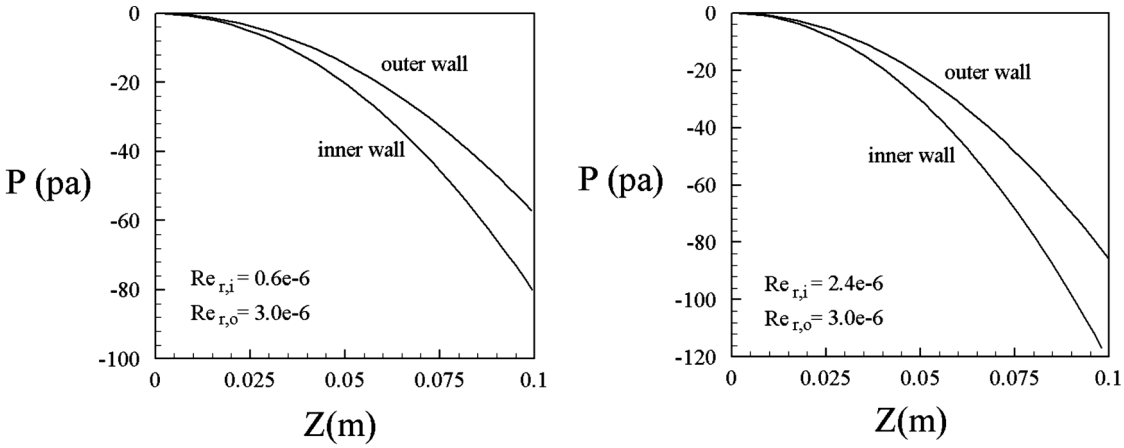


**Fig. 3 Pressure distributions on the inner and outer walls of an annular microchannel subjected to uniform wall injection at two different sets of radial Reynolds numbers**

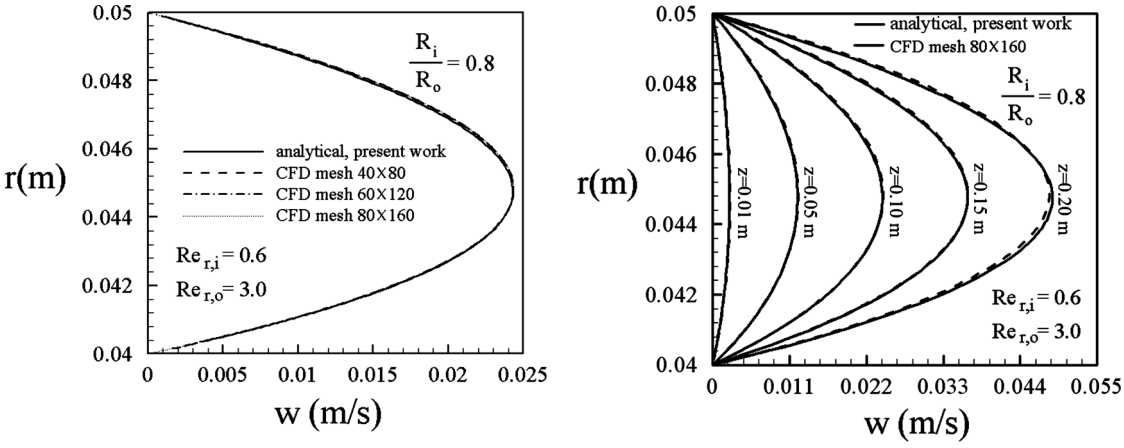


**Fig. 4 Comparison between numerical (CFD) and analytical velocity profiles at several stations along the annular channel and grid independency**

## Conclusion

Analytical analysis of fluid flow in annular microchannels subjected to uniform wall injection at various Reynolds numbers has been presented. The classical Navier–Stokes equations have been used in the present study. Mathematically, using an appropriate change of variable, Navier–Stokes equations have been transformed to a set of nonlinear ordinary differential equations. The governing equations have been analytically solved using series solution method. It has been shown that the laminar and incompressible fluid flow in an annular microchannel can be simulated

using the present model in a limited range of inner and outer wall radius ratios. It has also been demonstrated that the model works well for the prediction of saturated water vapor flow velocity profile and pressure distribution in annular channels and presents reasonable results at larger scales. However, further studies are needed to determine the limitations of the present model. The present analysis can be easily used for the study of vapor flow in microannular heat pipes.

## Nomenclature

$C_p$ = heat capacity at constant pressure
$h_{fg}$ = heat of vaporization
Kn = Knudsen number
$L$ = injection length
$P$ = pressure
$R_g$ = gas constant
$R_i$ = microchannel inner wall radius
$R_o$ = microchannel outer wall radius
$\mathrm{Re}_{r,i}$ = radial Reynolds number for the inner wall ($=V_i R_i/\vartheta$)
$\mathrm{Re}_{r,o}$ = radial Reynolds number for the outer wall ($=V_o R_o/\vartheta$)
$r$ = radial coordinate
$T$ = temperature
$V_i$ = inner wall injection velocity
$V_o$ = outer wall injection velocity
$v$ = radial velocity
$w$ = axial velocity
$z$ = axial coordinate

### Greek Symbols

$\gamma$ = specific heat ratio
$\mu$ = dynamic viscosity
$\lambda$ = mean free path
$\rho$ = density
$\vartheta$ = kinematic viscosity

### Subscripts

$g$ = gas
sat = saturation
$r$ = radial
$z$ = axial

## References


[1] Stone, H. A., and Kim, S., 2001, "Microfluidics: Basic Issues, Applications, and Challenges," AIChE J., **47**(6), pp. 1250–1254.
[2] Meinhart, C. D., Wereley, S. T., and Santiago, J. G., 1999, "PIV Measurement of a Microchannel Flow," Exp. Fluids, **27**(5), pp. 414–419.
[3] Jensen, K. F., 1999, "Micromechanical Systems: Status, Challenges, and Opportunities," AIChE J., **45**(10), pp. 2051–2054.
[4] Happel, J., and Brenner, H., 1983, *Low Reynolds Number Hydrodynamics*, Martinus Nijhoff, Kluwer, Boston.
[5] Gelb, A., Gleeson, J. P., West, J., and Roche, O. M., 2004, "Modelling Annular Micromixers," SIAM J. Appl. Math., **64**(4), pp. 1294–1310.
[6] Chang, M. H., and Chen, C. K., 1999, "Hydro-Magnetic Stability of Current-Induced Flow in a Small Gap Between Concentric Cylinders," ASME J. Fluids Eng., **121**, pp. 548–554.
[7] http://www.chem.tue.nl/scr
[8] Erickson, D., and Li, D., 2004, "Integrated Microfluidic Devices," Anal. Chim. Acta, **507**(1), pp. 11–26.
[9] Nouri-Borujerdi, A., and Layeghi, M., 2005, "A Review of Concentric Annular Heat Pipes," Heat Transfer Eng., **26**(6), pp. 45–58.
[10] Langer, R., 2000, "Biomaterials: Status, Challenges, and Perspectives," AIChE J., **46**(7), pp. 1286–1289.
[11] Kim, S., and Karrila, S. J., 1991, *Microhydrodynamics Principles and Selected Applications*, Butterworth-Heinemann, Stoneham, MA.
[12] Gallardo, B. S., Gupta, V. K., Eagerton, F. D., Jong, L. I., Craig, V. S., Shah, R. R., and Abbott, N. L., 1999, "Electrochemical Principles for Active Control of Liquids on Submillimeter Scales," Science, **283**(5396), pp. 57–60.
[13] Chang, H. C., 2001, *Bubble/Drop Transport in Microchannels* (CRC Handbook of MEMS) M. Gad-el-Hak, ed., CRC, New York, p. 11-1.
[14] Sharp, K. V., Adrian, R. J., Santiago, J. G., and Molho, J. I., 2001, *Liquid Flow in Microchannels* (CRC Handbook of MEMS) M. Gad-el-Hak, ed., CRC Press, New York, pp. 6-1–6-38.
[15] Arkilic, E. B., Schmidt, M. A., and Breuer, K. S., 1997, "Gaseous Slip Flow in Long Microchannels," J. Microelectromech. Syst., **6**(2), pp. 167–178.
[16] Pit, R., Hervet, H., and Leger, L., 2000, "Direct Experimental Evidence of Slip in Hexadecane: Solid Interfaces," Phys. Rev. Lett., **85**(5), pp. 980–983.
[17] Berman, A. S., 1953, "Laminar Flow in Channels With Porous Walls," J. Appl. Phys., **24**(9), pp. 1232–1235.
[18] Terrill, R. M., 1964, "Laminar Flow in a Uniformly Porous Channel," Aeronaut. Q., **15**(3), pp. 299–310.
[19] Terrill, R. M., 1982, "An Exact Solution for Flow in a Porous Pipe," ZAMP, **33**(4), pp. 547–552.
[20] Zlnchenko, V. I., and Fedorova, O. P., 1976, "Analysis of Flow in an Annular Duct With Large Injection at the Walls," Fluid Dyn., **11**(3), pp. 458–461.
[21] Layeghi, M., 2004, "Fluid Flow in Cylindrical Microchannels Subjected to Uniform Wall Injection," *Proceeding of American Physical Society, 57th Annual Meeting of the Division of Fluid Dynamics*, Seattle, WA, Nov. 21–23, Paper No. NC009.
[22] Gad-el-Hak, M., 2001, "Flow Physics in MEMS," Mec. Ind., **2**, pp. 313–341.
[23] Nouri-Borujerdi, A., and Layeghi, M., 2004, "A Numerical Analysis of Vapor Flow in Concentric Annular Heat Pipes," ASME J. Fluids Eng., **126**(3), pp. 442–448.